The Effects of Load Ratio on Threshold Fatigue Crack Growth of Aluminum Alloys

John A. Newman

Dissertation submitted to the Faculty of the
Virginia Polytechnic Institute and State University
in partial fulfillment of the requirements for the degree of

Doctor of Philosophy
in
Engineering Mechanics

Norman E. Dowling, Chair
Robert S. Piascik
John C. Duke
Surot Thangjitham
Stephen L. Kampe

17 October 2000
Blacksburg, Virginia

Keywords: Fatigue crack growth, Threshold, Load ratio, R, Fatigue crack closure, Crack-tip damage, Humidity, Roughness-induced crack closure, Plasticity-induced crack closure, Oxide-induced crack closure, Microvoids, Microcracks, Crack-tip process zone, K_{max}, Aluminum alloys.

Copyright 2000, John Andrew Newman

The Effects of Load Ratio on Threshold Fatigue Crack Growth of Aluminum Alloys

John Andrew Newman

(ABSTRACT)

The integrity of nearly all engineering structures are threatened by the presence of cracks. Structural failure occurs if a crack larger than a critical size exists. Although most well designed structures initially contain no critical cracks, subcritical cracks can grow to failure under fatigue loading, called fatigue crack growth (FCG). Because it is impossible or impractical to prevent subcritical crack growth in most applications, a damage tolerant design philosophy was developed for crack sensitive structures. Design engineers have taken advantage of the FCG threshold concept to design for long fatigue lives. FCG threshold (ΔK_{th}) is a value of ΔK (crack-tip loading), below which no significant FCG occurs. Cracks are tolerated if ΔK is less than ΔK_{th}. However, FCG threshold is not constant. Many variables influence ΔK_{th} including microstructure, environment, and load ratio. The current research focuses on load ratio effects on ΔK_{th} and threshold FCG. Two categories of load ratio effects are studied here: extrinsic and intrinsic. Extrinsic load ratio effects operate in the crack wake and include fatigue crack closure mechanisms. Intrinsic load ratio effects operate in the crack-tip process zone and include microcracking and void production. To gain a better understanding of threshold FCG load ratio effects (1) a fatigue crack closure model is developed to consider the most likely closure mechanisms at threshold, simultaneously, and (2) intrinsic load ratio mechanisms are identified and modeled.

An analytical fatigue crack closure model is developed that includes the three closure mechanisms considered most important at threshold (PICC, RICC, and OICC). Crack meandering and a limited amount of mixed-mode loading are also considered. The rough crack geometry, approximated as a two-dimensional sawtooth wave, results in a mixed-mode crack-tip stress state. Dislocation and continuum mechanics concepts are used to determine mixed-mode crack face displacements. Plasticity induced crack closure is included by modifying an existing analytical model, and an oxide layer in the crack mouth is modeled as a uniform layer. Finite element results were used to verify the analytical solutions for crack-tip stress intensity factor and crack face displacements. These results indicate that closure for rough cracks can occur at two locations: (1) at the crack-tip, and (2) at the asperity nearest the crack-tip. Both tip contact and asperity contact must be considered for rough cracks. Tip contact is more likely for high K_{max} levels, thick oxide layers, and shallow asperity angles, α. Model results indicate that closure mechanisms combine in a synergistic manner. That is, when multiple closure mechanisms are active, the total closure level is greater than the sum of individual mechanisms acting alone. To better understand fatigue crack closure where multiple closure mechanisms are active (*i.e.* FCG threshold), these interactions must be

considered. Model results are well supported by experimental data over a wide range of ΔK, including FCG threshold.

Closure-free load ratio effects were studied for aluminum alloys 2024, 7050, and 8009. Alloys 7050 and 8009 were selected because load ratio effects at FCG threshold are not entirely explained by fatigue crack closure. It is believed that closure-free load ratio mechanisms occur in these alloys. Aluminum alloy 2024 was selected for study because it is relatively well behaved, meandering most load ratio effects are explained by fatigue crack closure. A series of constant K_{max} threshold tests on aluminum alloys were conducted to eliminate fatigue crack closure at threshold. Even in the absence of fatigue crack closure load ratio (K_{max}) effects persist, and are correlated with increased crack-tip damage (*i.e.* voids) seen on the fatigue crack surfaces. Accelerated FCG was observed during constant K_{max} threshold testing of 8009 aluminum. A distinct transition is seen the FCG data and is correlated with a dramatic increase in void production seen along the crack faces. Void production in 8009 aluminum is limited to the specimen interior (plane-strain conditions), promoting crack tunneling. At higher values of K_{max} ($\geq$ 22.0 MPa$\sqrt{m}$), where plane-stress conditions dominate, a transition to slant cracking occurs at threshold. The transition to slant cracking produces an apparent increase in FCG rate with decreasing ΔK. This unstable threshold behavior is related to constraint conditions. Finally, a model is developed to predict the accelerated FCG rates, at higher K_{max} levels, in terms of crack-tip damage.

The effect of humidity (in laboratory air) on threshold FCG was studied to ensure that environmental effects at threshold were separated from load ratio effects. Although changes in humidity were shown to strongly affect threshold FCG rates, this influence was small for ambient humidity levels (relative humidity between 30% and 70%). Transient FCG behavior, following an abrupt change in humidity level, indicated environmental damage accumulated in the crack-tip monotonic plastic zone. Previous research implies that hydrogen (a component of water vapor) is the likely cause of this environmental damage. Analysis suggests that bulk diffusion is not a likely hydrogen transport mechanism in the crack-tip monotonic plastic zone. Rather, dislocation-assisted diffusion is presented as the likely hydrogen transport mechanism.

Finally, the (extrinsic) fatigue crack closure model and the (intrinsic) crack-tip damage model are put in the context of a comprehensive threshold model. The ultimate goal of the comprehensive threshold model is to predict fatigue lives of cyclically loaded engineering components from (small) crack nucleation, through FCG, and including failure. The models developed in this dissertation provide a basis for a more complete evaluation of threshold FCG and fatigue life prediction.

The research described in this dissertation was performed at NASA-Langley Research Center in Hampton, Virginia. Funding was provided through the NASA GSRP program (Graduate Student Researcher Program, grant number NGT-1-52174).

DEDICATION

This dissertation is dedicated to my maternal grandfather, Virgil Lawrence Catron (1920-1998), who died while this research was in progress. The close relationship my grandfather and I shared (which I miss dearly) is not the primary motivation for this dedication. (I prefer not to share such feelings.) Instead, this dedication is motivated by my grandfather's role as a teacher. Although he was not college educated, the lessons learned from my grandfather enabled my successful completion of the Ph.D. degree and this dissertation. He taught me to be patient, persistent, and to have pride in my work. Much of his advice I initially did not understand. As my life goes on his words develop new meaning, and reveals what an immensely knowledgeable and mature man my grandfather was. I guess that I am still learning from my granddad. In his final days, my granddad told me that he "knew I had what it takes" to complete the Ph.D. degree and that he was proud of me. His approval helped me persevere when "the going got tough." I've heard that the best measure of a teacher is the quality of his or her students. I hope my work has made my granddad as proud of me as I am of him.

ACKNOWLEDGEMENTS

Although this dissertation represents my individual scientific efforts, I was fortunate to have assistance from others. Because the research described in this dissertation was performed at NASA-Langley Research Center while a student at Virginia Tech, I was fortunate to have two advisors. Norman E. Dowling was my academic advisor at Virginia Tech and Robert S. "Bob" Piascik was my research advisor at NASA-Langley Research Center. Their advice and guidance is greatly appreciated and I have enjoyed working with these "world class" researchers. Additionally, the time and efforts of the other committee members (John C. Duke, Surot Thangjitham, and Stephen L. Kampe) are appreciated.

During my time at NASA-Langley Research Center I have enjoyed a unique research environment and interactions with well-known researchers in the field of fatigue and fracture mechanics. I have had the privilege of working with two recent Ph.D. graduates ("post-docs") at NASA-Langley, Stephen "Steve" W. Smith and William "Will" T. Riddell. My research has benefited a great deal from technical discussions with Steve and Will.

Finally, I would like to acknowledge the sacrifices made by my family while I was a graduate student. Although I have enjoyed my graduate school experience, I regret spending so much time away from family (and friends). Thanks to my wife, daughter, mother, father, and grandmother for putting up with me the past few years.

TABLE OF CONTENTS

ABSTRACT ii
DEDICATION iv
ACKNOWLEDGEMENTS v
LIST OF FIGURES x
LIST OF TABLES xxii
NOMENCLATURE xxiii

PART I – Introduction and Objectives 1

CHAPTER 1 – INTRODUCTION 2
1.1 – INTRODUCTION TO FATIGUE CRACK GROWTH 2
1.2 – FATIGUE CRACK GROWTH BEHAVIOR OF ENGINEERING METALS 3
1.3 – DAMAGE TOLERANT DESIGN 4
1.4 – FATIGUE CRACK GROWTH LOAD RATIO EFFECTS 5
1.5 – PROBLEM STATEMENT 6
1.6 – LITERATURE REVIEW 7
1.6.1 – Threshold testing procedures 7
1.6.2 – Fatigue crack closure 8
1.6.3 – Closure-free load ratio effects 8
1.6.4 – Short crack issues 10
1.6.5 – Other influences to consider 12

CHAPTER 2 – RESEARCH MOTIVATION, OBJECTIVES, AND APPROACH 13
2.1 – MOTIVATION FOR RESEARCH 13
2.2 – RESEARCH OBJECTIVES 14
2.3 – TECHNICAL APPROACH 16
2.4 – PITFALLS TO AVOID 17

PART II – Research 18

CHAPTER 3 – FATIGUE CRACK CLOSURE MODEL 19
3.1 – INTRODUCTION 19
3.2 – MODEL DEVELOPMENT 20
3.2.1 – Consideration of RICC and crack meandering 20
3.2.2 – Stress intensity factors 21
3.2.3 – Elastic crack face displacements 23
3.2.4 – Consideration of crack-tip plasticity and PICC 23
3.2.5 – Consideration of OICC 28

3.3 – NUMERICAL VERIFICATION OF STRESS INTENSITY FACTORS AND CRACK FACE DISPLACEMENTS 28
3.4 – EVALUATION OF CLOSURE LEVELS 31
3.5 – MODEL RESULTS 33
3.5.1 – Straight crack results 34
3.5.2 – Rough crack results 41
3.6 – EXPERIMENTAL VERIFICATION 54
3.6.1 – Plasticity induced crack closure (PICC) 55
3.6.2 – Plasticity and oxide induced crack closure (PICC and OICC) 56
3.6.3 – Roughness induced crack closure (RICC) 63
3.7 – FRACTOGRAPHY 72
3.8 – SUMMARY 76

CHAPTER 4 – INTRINSIC LOAD RATIO EFFECTS 79
4.1 – INTRODUCTION 79
4.2 – TEST PROCEDURE AND RESULTS 79
4.2.1 – Aluminum alloy 2024 80
4.2.2 – Aluminum alloy 7050 83
4.2.3 – Aluminum alloy 8009 85
4.3 – FRACTOGRAPHY 93
4.4 – CRACK-TIP DAMAGE MODEL 101
4.4.1 – Model development 101
4.4.2 – Evaluation of fatigue crack growth rates 104
4.4.3 – Model results 106
4.5 – SUMMARY 109

PART III – Analysis of Results and Conclusions 110

CHAPTER 5 – DISCUSSION OF RESULTS 111
5.1 – DISCUSSION OF CLOSURE MODEL RESULTS 111
5.1.1 – Interaction of closure mechanisms 112
5.1.2 – Sliding mode crack closure (SMCC) 115
5.1.3 – Crack-tip plasticity (slip) 117
5.1.4 – Closure model limitations 119
5.2 – DISCUSSION OF INTRINSIC LOAD RATIO (K_{max}) EFFECTS 119
5.2.1 – High K_{max} crack-tip damage in aluminum alloys 2024 and 7050 120
5.2.2 – Unusual threshold behavior of 8009 aluminum 120
5.2.3 – Plane-strain dominance 122
5.2.4 – Crack-tip damage model 124
5.3 – HUMIDITY EFFECTS AT THRESHOLD 124
5.4 – COMPREHENSIVE THRESHOLD MODEL 125

CHAPTER 6 – CONCLUDING REMARKS 127
6.1 – SUMMARY OF RESEARCH RESULTS 127
6.1.1 – Fatigue crack closure 127
6.1.2 – Intrinsic load ratio effects 128
6.1.3 – Effects of humidity on threshold behavior 128
6.2 – FUTURE RESEARCH TOPICS 129

PART IV – Appendices 131

APPENDIX A – LITERATURE REVIEW 132
A.1 – THRESHOLD FATIGUE CRACK GROWTH 132
A.1.1 – Microstructure 132
A.1.2 – Environment 133
A.1.3 – Short crack behavior 133
A.2 – THRESHOLD FATIGUE CRACK CLOSURE 134
A.2.1 – Crack closure mechanisms 134
A.2.2 – Crack closure models 136
A.3 – INTRINSIC K_{max} EFFECTS AT THRESHOLD 138
A.3.1 – Effects of constituent particles 139
A.3.2 – Effects of grain boundaries 141

APPENDIX B – MECHANICAL TESTING PROCEDURES 142
B.1 – FATIGUE CRACK GROWTH TESTING 142
B.2 – ENVIRONMENT CONTROL 146
B.3 – FRACTOGRAPHIC AND ENERGY DISPERSIVE X-RAY SPECTROSCOPY (EDX) ANALYSES 147

APPENDIX C – CRACK CLOSURE MEASUREMENT TECHNIQUES 148
C.1 – VISIBLE LIGHT TRANSMITTED THROUGH THE CRACK OPENING 148
C.2 – COMPLIANCE TECHNIQUES 150
C.3 – DIGITAL IMAGE DISPLACEMENT SYSTEM (DIDS) 152

APPENDIX D – ALLOYS AND SPECIMENS 157
D.1 – ALUMINUM ALLOYS 157
D.1.1 – Aluminum alloy 2024 157
D.1.2 – Aluminum alloy 7050 159
D.1.3 – Aluminum alloy 8009 160
D.2 – NITINOL (SHAPE MEMORY ALLOY) 161
D.3 – FATIGUE CRACK GROWTH SPECIMENS 165

APPENDIX E – THRESHOLD FATIGUE CRACK GROWTH HUMIDITY EFFECTS 167
E.1 – INTRODUCTION 167
E.2 – TEST PROCEDURE AND RESULTS 168
E.3 – HYDROGEN DIFFUSIVITY 174
E.4 – SUMMARY 177

APPENDIX F – BASIC COMPUTER CODES FOR MODEL EVALUATION 179
F.1 – FATIGUE CRACK CLOSURE MODEL 179
F.2 – K_{MAX} DAMAGE MODEL 182

APPENDIX G – REFERENCES 184

VITA 197

LIST OF FIGURES

Chapter 1 – Introduction

Figure 1.1 – Schematic of constant amplitude load cycles, where the crack-tip stress intensity factor, K, is plotted against time. 3

Figure 1.2 – Schematic of typical FCG data. Plotted as log (d*a*/dN) versus log (ΔK), the FCG behavior is divided into three regions (threshold, Paris, and unstable FCG). 4

Figure 1.3 – Schematic of ΔK plotted against K_{max}, used to demonstrate the philosophy of damage tolerant design. 5

Figure 1.4 – Schematic of typical FCG data, plotted as log (d*a*/dN) versus log (ΔK) for three values of load ratio, R. 6

Figure 1.5 – Schematic of ΔK plotted against K_{max}, used to demonstrate the influence of K_{max} (or R) on FCG threshold and damage tolerant design. 7

Figure 1.6 – Schematics of the three closure mechanisms most likely at FCG threshold; (a) PICC, (b) RICC, and (c) OICC. 9

Figure 1.7 – Schematic of unstable FCG threshold behavior observed during constant K_{max} threshold testing of titanium alloys. 10

Figure 1.8 – Schematic of typical short fatigue crack data (increasing ΔK) compared with long crack data (decreasing ΔK). (This figure is modified from Tokaji [25].) 11

Chapter 2 - Research Goals and Approach

Figure 2.1 – Schematic of a generic crack-tip region used to define extrinsic and intrinsic FCG load ratio effects. 14

Figure 2.2 – Chart of extrinsic and intrinsic FCG load ratio mechanisms considered most likely to affect FCG threshold. 15

Chapter 3 – Fatigue Crack Closure Model

Figure 3.1 – Idealized two-dimensional crack profiles. A schematic of the sawtooth configuration of previous models is shown in part (a). For this model the sawtooth is allowed to meander, as shown in part (b). 20

Figure 3.2 – Schematics of two crack configurations for which analytical solutions are used; (a) an angled, straight crack and (b) a straight crack with a kinked crack-tip. A schematic illustrating the simultaneous application of these solutions is shown in part (c). 22

Figure 3.3 – Plot of singular shear stress, $\tau_{r\theta}$, and corresponding plastic zone. In part (a) a plot of the singular shear stress is given, as a function of θ, for $\alpha = 45^o$, $\gamma = 10^o$, $K_{IIg} = 0$. A schematic of the corresponding plastic is given in part (b). 25

Figure 3.4 – Definition of the crack wake compression factor, ξ. The crack wake compression factor, ξ, is schematically defined in part (a) for a straight crack. A plot of ξ versus $R_{applied}$, obtained from Budiansky and Hutchinson, is shown in part (b). 27

Figure 3.5 – Typical (deformed) mesh used for finite element analyses. Taking advantage of symmetry, for the nominally mode I case, only half of a specimen is analyzed, as shown, and symmetry is enforced with appropriate boundary conditions. Arrows point to higher magnification images of the crack-tip region. For this mesh, $\alpha = 45^o$ and $g/a = 0.05$. 29

Figure 3.6 – Stress intensity factors for sawtooth cracks under mode I loading (K_{Ig}) for asperity angles $\alpha = 0^o$, 15^o, 30^o, and 45^o. 30

Figure 3.7 – Crack face displacements of sawtooth cracks. This crack configuration is illustrated by the schematic. These displacements are plotted against r/g for $g/a = 0.10$ and 0.01, and are indicated by open symbols, for α = (a) 30° and (b) 45° are shown. Solid, dashed, and dotted curves correspond to displacements of Equations 3.4 (model results), and those expected of a straight crack, respectively. 31

Figure 3.8 – Geometric configuration of crack faces at potential contact points. The most likely places for crack face contact are at the crack-tip and at the first asperity behind the crack-tip. A sawtooth crack is schematically shown at the top of the figure. High magnification sketches of the first asperity behind the crack-tip and the crack-tip region are shown at the bottom left and bottom right of the figure, respectively. The shaded region represents an oxide layer. 32

Figure 3.9 – Plots of closure levels for straight cracks. In part (a) R_{cl} is plotted against ξ. Since ξ is related to the applied R, $R_{applied}$ (see Figure 3.4), R_{cl} is related to $R_{applied}$, as shown in part (b). The dotted line corresponds to closure at the minimum load, so that no closure is expected below this line. Experimental results, using back face strain data, are shown in part (b) for aluminum alloy 8009 tested at $\Delta K = 6.6$ MPa$\sqrt{m}$ in laboratory air. 35

Figure 3.10 – Closure behavior for straight cracks with an oxide layer. In part (a) closure levels, R_{cl}, are plotted against K_{max} for three different values of oxide layers; 0, 100, and 500 Å. In part (b) the fully closed conditions are indicated as a function of K_{max} and t. 37

Figure 3.11 – Closure levels, R_{cl}, are plotted against Δa for (a) $K_{max} = 2$ MPa$\sqrt{m}$, (b) $K_{max} = 4$ MPa$\sqrt{m}$, and (c) $K_{max} = 6$ MPa$\sqrt{m}$. Model results for no oxide layer ($R_{cl} = 0.252$) are indicated by a horizontal dotted line on each plot. 38

Figure 3.12 – Model results of Figure 3.11 are re-plotted, here for (a) t = 0, (b) t = 100 Å, and (c) t = 500 Å. 39

Figure 3.13 – Variation of transition crack length, Δa_{trans}, for a straight crack. In part (a) Δa_{trans} is plotted against oxide layer thickness for three different K_{max} (2,4, and 6 MPa$\sqrt{m}$). In part (b) Δa_{trans} is plotted against K_{max} for three different oxide thickness (125, 250, and 500 Å). 40

Figure 3.14 – Closure levels, for three different values of K_{max} (2, 4, and 6 MPa$\sqrt{m}$) are plotted against asperity angle, α, for (a) t = 0, (b) t = 100 Å, (c) t = 250 Å, and (d) t = 500 Å. 42

Figure 3.15 – Model results presented in Figure 3.14 are re-plotted for (a) $K_{max} = 2$ MPa$\sqrt{m}$, (b) $K_{max} = 4$ MPa$\sqrt{m}$, and (c) $K_{max} = 6$ MPa$\sqrt{m}$. 43

Figure 3.16 – Model results are plotted here for a rough crack (2024 aluminum model parameters) with a 100 Å oxide layer. Both tip contact and asperity contact are considered. 44

Figure 3.17 – Plots of α_{fc} and α_{trans} versus K_{max} for several oxide layers. These parameters are plotted as solid and dashed curves, respectively, and separate each plot into three regions of crack closure behavior. 45

Figure 3.18 – Plot of the relationship between $K_{max\,cr}$ and oxide layer thickness, t. Below the curve no asperity contact occurs. Above the curve, asperity contact will occur for some values of α. 46

Figure 3.19 – Closure levels versus α, are plotted for three values of K_{max} (2, 4, and 6 MPa$\sqrt{m}$) and γ (10^o, 20^o, and 30^o) for t = 100 Å. Model parameters for 2024 aluminum were used. 47

Figure 3.20 – Plot of closure level versus α for a meandering rough crack. Both tip contact and asperity contact are considered for $\gamma = 20^o$ and t = 0. 48

Figure 3.21 – Plots of the relationship between $K_{max\ fc}$ and $K_{max\ trans}$, and α. These parameters are plotted as solid and dashed curves respectively, which divide the plots into three regions of crack closure behavior. 49

Figure 3.22 – Plot of the relationship between α_o and γ. Above the curve, the crack is always fully closed. Below the curve, the crack may be partially open for some values of K_{max}. 50

Figure 3.23 – Plot of closure level, R_{cl}, versus K_{max} as typically presented in literature. Results for R = 0.05 and two values of oxide thickness, t = 0 and 500 Å, are shown. 51

Figure 3.24 – Plots of closure level versus K_{max} for variable (a) yield stress, (b) asperity length, and (c) meandering angle. 52

Figure 3.25 – Plots of closure levels against (a) yield stress, (b) asperity length, and (c) meandering angle. 53

Figure 3.26 – Experimental closure data obtained from aluminum alloy 8009 tested at R = 0.05 in both UHV and laboratory air. Closure measurements using DIDS (near-tip) and back-face strain data are shown. The horizontal dotted line corresponds model results. Additional data for 8009 (T-L) is shown as cross-hair symbols (+) [57]. 56

Figure 3.27 – Experimental closure data obtained from aluminum alloy 8009 tested at R = 0.05 in laboratory air, after (a) 0.05 μm and (b) 0.30 μm alumina particles were inserted into the crack. Model results are indicated as a solid curve. 58

Figure 3.28 – Plot of closure level versus K_{max} for steel specimens tested in brine solution. Results for increasing and decreasing K_{max} are shown as open and closed symbols, respectively. Model results are indicated for several oxide layers as line curves. 59

Figure 3.29 – Closure levels, R_{cl}, plotted against the change in crack length after the addition of oxide into the crack, are shown here. Results in the figures correspond to aluminum alloy 8009, as a fatigue crack grew away from 0.05 μm alumina particles at R = 0.05, and (a) K_{max} = 4.4 MPa$\sqrt{m}$ and (b) K_{max} = 4.95 MPa$\sqrt{m}$, and in laboratory air. 61

Figure 3.30 – Crack face contact data, $R_{contact}$, plotted against distance behind the crack-tip is shown here. The conditions for this data correspond to that of point A in Figure 3.30b. The model prediction is indicated by the horizontal dotted line (R_{cl} = 0.252), while the compliance datum is shown as a horizontal dashed line (R_{cl} = 0.506). 62

Figure 3.31 – Schematic illustrating (possible) behavior of plastic strain (shown as hatched regions) before and after annealing shape memory alloy specimen. 64

Figure 3.32 – Experimental data for Nitinol 50-50 before and after the specimen was annealed to recover crack wake plasticity. Cyclic loading was applied at K_{max} = 8.8 MPa√m, R = 0.05, and 11 Hz in UHV. 65

Figure 3.33 – Measured closure levels before and after application of an overload, and before and after subsequent annealing, of Nitinol 50-50. 66

Figure 3.34 – Fatigue crack closure results for Nitinol, before and after annealing. Data after annealing suggest that closure mode changes from asperity contact to tip contact as K_{max} increases. 67

Figure 3.35 – Crack contact levels ($R_{contact}$) as a function of distance behind the crack-tip. Tip contact and asperity contact are expected in part (a) and part (b), respectively, at points A and B, respectively. 69

Figure 3.36 – Closure data for course and fine grained microstructures of (a) AISI 1080 steel and (b) INCONEL 718. 71

Figure 3.37 – Aluminum alloy 2024 closure data for constant R threshold tests and constant ΔK tests, at R = 0.1. 72

Figure 3.38 – Micrographs of crack surfaces after 0.05 μm particles were injected into the crack mouth. Conditions where particles are not expected to reach the crack-tip (K_{max} = 3.3 MPa√m) are shown in the left column. Particles are expected to reach the crack-tip for K_{max} = 7.7 MPa√m (right column). In the top row, both specimen surfaces can be seen along the top and bottom of both micrographs. The crack front at fracture (A) and dense regions of particles near the specimen surface (B) are indicated. High magnification images of regions labeled C are shown in the bottom row. 73

Figure 3.39 – Micrographs of crack surfaces after 0.30 μm particles were injected into the crack mouth. Conditions where particles are not expected to reach the crack-tip (K_{max} = 7.7 MPa√m) are shown in the left column. Particles are expected to reach the crack-tip for K_{max} = 15.4 MPa√m (right column). In the top row, both specimen surfaces can be seen along the top and bottom of both micrographs. The crack front at fracture (A) and dense regions of particles near the specimen surface (B) are indicated. High magnification images of regions labeled C are shown in the bottom row. 74

Figure 3.40 – Micrographs of a fatigue crack surface (K_{max} = 7.7 MPa√m and R = 0.05) after 0.30 μm particles were injected into the crack mouth. Images of the specimen interior and near the specimen edge are indicated in the left and right columns, respectively. Top and bottom rows correspond to near crack-tip (within 60 μm) and approximately 1.6 mm behind the crack-tip, respectively. Individual and agglomerated particles are labeled A and B, respectively. 76

Figure 3.41 – Micrograph of agglomerated (0.05 μm) alumina particles approximately 5 mm behind the crack-tip (labeled A). Fatigue loads here are K_{max} = 5.5 MPa√m and R = 0.05. A few individual particles are also labeled (B). 77

Figure 3.42 – Fatigue crack surface produced before and after 0.05 μm particles were injected into the crack mouth. Applied fatigue loads were K_{max} = 4.4 MPa√m and R = 0.05. The divergence of a_{vis} and a_{comp} are a result of crack tunneling. 77

Chapter 4 -Intrinsic Load Ratio Effects

Figure 4.1 – FCG data for constant-K_{max} threshold tests of aluminum alloy 2024-T3. Testing was performed in laboratory air at 11 Hz. Closure affected data would lie within the hatched region. The ASTM suggested threshold rate (10^{-10} m/cycle) is indicated by the horizontal dotted line. 81

Figure 4.2 – Plot of threshold FCG parameters m^* and ΔK_{th} for 2024 aluminum. Threshold FCG data shown in part (a) is used to determine m^* and ΔK_{th}, which are plotted in part (b). 82

Figure 4.3 – FCG rate versus ΔK data of alloy 7050-T6 for constant-K_{max} threshold tests. FCG data where closure was detected (not shown) occurred within the shaded region. The ASTM suggested threshold rate (10^{-10} m/cycle) is indicated by the horizontal dotted line. Testing was performed in laboratory air, at 11 Hz. 84

Figure 4.4 – Plot of threshold FCG parameters m^* and ΔK_{th} for 7050 aluminum. 85

Figure 4.5 – FCG rate versus ΔK data of alloy 8009 for constant-K_{max} threshold tests. Closure-affected FCG data (not shown) would have occurred within the shaded region. The ASTM suggested threshold rate (10^{-10} m/cycle) is indicated by the horizontal dotted line. Testing was performed in laboratory air, at 11 Hz. 86

Figure 4.6 – Plot of constant K_{max} threshold data for K_{max} levels of 5.5 MPa√m and 11.0 MPa√m. Transitions to accelerated FCG are indicated. 87

Figure 4.7 – Plot of constant K_{max} threshold data for K_{max} levels of 11.0 and 22.0 MPa√m. Transitions to accelerated FCG and unstable threshold behavior for K_{max} = 22.0 MPa√m are indicated. 88

Figure 4.8 – Schematic comparing (a) flat crack and (b) slant crack geometries. 89

Figure 4.9 – Plot of threshold FCGparameters m^* and ΔK_{th} for 8009 aluminum. 90

Figure 4.10 – Crack length plotted as a function of (a) cycles and (b) time, for alloy 8009 subject to constant K_{max} = 5.5 and ΔK = 0.77 MPa√m loading in lab air at 11, 5, and 1 Hz. FCG rates corresponding to each condition are indicated in the figures. 91

Figure 4.11 – FCG rate versus ΔK data for constant-K_{max} = 5.5 and 11.0 MPa√m threshold tests on 8009 aluminum, loaded at 11 Hz, in both lab air (open symbols) and UHV (<$5x10^{-7}$ Pa, as closed symbols). The ASTM suggested threshold rate (10^{-10} m/cycle) is indicated by the horizontal dotted line. Testing was performed at 11 Hz, using C = -0.8 mm^{-1}. Transitions in FCG behavior are indicated where appropriate. 92

Figure 4.12 – Crack length as a function of (a) cycles and (b) time for alloy 8009 subject to constant K_{max} = 5.5 and ΔK = 1.21 MPa√m loading in UHV (<$5x10^{-7}$ Pa) at 11, 5, and 1 Hz. FCG rates corresponding to each condition are indicated. 93

Figure 4.13 – SEM fractographs of alloy 2024-T3 fatigue crack surfaces produced by constant-K_{max} = (a) 5.5 and (b) 22.0 MPa√m threshold tests, (c) quasi-static fracture (K_c = 42 MPa√m), and (d) a high magnification fractograph of a typical microvoid produced on the fatigue crack surface of Figure 4.13b. For Figures 4.13a-c, microvoids are marked by white circle (or ovals) on the right, but unmarked on the left. 94

Figure 4.14 – SEM fractographs of alloy 7050-T6 fatigue crack surfaces produced by constant-K_{max} = (a) 5.5 and (b) 22.0 MPa√m threshold tests, (c) quasi-static fracture (K_c = 35 MPa√m), and (d) a high magnification fractograph of a typical region labeled A on the fatigue crack surface shown in part (b). Regions labeled A in parts (a) and (b) are outlined in white, while regions B in the figures remain unmarked. Figure 4.14c is almost completely consumed with regions previously denoted as A. 95

Figure 4.15 – SEM fractographs of alloy 8009 fatigue crack surfaces produced by a constant-K_{max} = 5.5 MPa√m threshold test; (a) the entire fatigue crack surface, (b) high magnification fractograph of region A in part (a), and (c) high magnification fractograph of region B in Figure 4.9a. Figures 4.15b and 4.15c correspond to FCG rates just before and just after point A in Figure 4.7. (Recall threshold tests performed with decreasing ΔK.) 96

Figure 4.16 – SEM fractographs of alloy 8009 fatigue crack surfaces produced by a constant-K_{max} = 11.0 MPa√m threshold test; (a) the entire fatigue crack surface, (b) high magnification fractograph of region A in part (a), and (c) high magnification fractograph of region B in part (a). Figures 4.16b and 4.16c correspond to FCG rates just before and just after point B in Figure 4.6. 97

Figure 4.17 – Schematic illustrating the difference between concave surfaces produced by void coalescence and boundary cracking mechanisms. 98

Figure 4.18 – Photographs of crack-tip damage along the plastic crack wake (MPZ) generated at K_{max} = 22.0 MPa√m, and ΔK = 0.77 MPa√m for aluminum alloy 7050. Surfaces are shown unetched and the FCG direction is indicated by an arrow. 100

Figure 4.19 – Schematics of crack configurations used to develop the crack tip damage model. In part (a) a simplified form of the Meguid model is shown. An infinite row of microcracks is shown in part (b). 102

Figure 4.20 – Geometry of the crack-tip damage model developed here. An infinite row of microcracks is added to the (simplified) Meguid model. 104

Figure 4.21 – Plot of baseline data used for the crack-tip damage model. Results are presented for (a) 2024 aluminum and (b) 7050 aluminum. 105

Figure 4.22 – Comparison of experimental data and model results for aluminum alloy 2024. 107

Figure 4.23 – Comparison of experimental data and model results for aluminum alloy 7050. 108

Chapter 5 - Discussion of Results

Figure 5.1 – Table of schematics, active closure mechanisms, and closure levels for four crack configurations, used to show interactions between closure mechanisms for FCG at K_{max} = 3.5 MPa$\sqrt{m}$ and R = 0.05. 113

Figure 5.2 – Schematic illustrating sliding mode crack closure (SMCC). Under mode II loading, crack faces (a) initially move perpendicular to each other. When asperities touch (b), the rough crack features tend to slide past each other producing opening mode displacements of the crack surfaces. Arrows indicate direction of crack face movement. 115

Figure 5.3 – Crack face displacement data from finite element analyses are shown for $\alpha = 45^{o}$, plotted against r/g. 116

Figure 5.4 – Possible sources of mixed-mode displacements for a straight crack due to asymmetry of the slip system; (a) unequal slip lengths due to barrier in dislocation motion and (b) unequal angles of slip planes due to geometry of microstructure dependent preferred slip planes. 118

Figure 5.5 – Linear plot of FCG conditions associated with the first threshold transition in 8009 aluminum. The parameters, ΔK_{trans} (open symbols, using left vertical axis), and da/dN_{trans} (closed symbols, using right vertical axis), are plotted against K_{max}. 122

Figure 5.6 – Chart illustrating how current models fit in with comprehensive threshold FCG model. 126

Appendix A - Literature Review

Figure A.1 – Comparison of (a) faceted Stage I and (b) striated Stage II crack paths. 133

Figure A.2 – Schematic illustrating remote closure due to load history. 136

Figure A.3 – FCG threshold, ΔK_{th}, versus (a) R and (b) K_{max} for 2024 aluminum. In part (a) a horizontal line is fitted through the closure-free data, as done by Schmidt and Paris. ΔK_{th} is plotted with K_{max} in part (b), as done by Doker and Bachmann. 139

Figure A.4 – Possible ways slip paths interact with constituent particles. 141

Appendix B - Mechanical Testing Procedures

Figure B.1 – Photograph of the equipment and computer system used to perform K-controlled FCG tests. The servo-hydraulic testing machine, microscope, and the computer used to control FCG tests, are indicated..... 142

Figure B.2 – Schematic used to show how compliance at the back face changes with increasing crack length, *a*. 143

Figure B.3 – A schematic of compliance, dP/dε, as a function of crack length, *a*. Once the compliance is known (as indicated by the horizontal dotted line), this relationship can be used to determine crack length (indicated by the vertical dotted line). 144

Figure B.4 – A schematic of two types of threshold tests are shown; (a) constant K_{max} and (b) constant R (load ratio). 145

Figure B.5 – Plot of crack length versus applied cycles for aluminum alloy 8009 tested in laboratory air at K_{max} = 3.3 MPa$\sqrt{m}$ and R = 0.05. The slope of the fitted line is the steady state FCG rate. 146

Figure B.6 – A photo of the vacuum chamber is shown here, which is mounted on a servo-hydraulic testing machine. 147

Appendix C - Crack Closure Measurement Techniques

Figure C.1 – A high magnification photograph of light transmitted through the mouth of an 8009 aluminum fatigue crack. Initially, the crack grew at K_{max} = 5.5 MPa$\sqrt{m}$ and R = 0.05. At the location indicated, the load was abruptly reduced to K_{max} = 3.3 MPa$\sqrt{m}$ and R = 0.05. 148

Figure C.2 – Photograph of crack wake removal using a jeweler saw. The specimen, clamp, and jeweler saw are indicated in the figure. 149

Figure C.3 – A schematic used to illustrate how the effective crack length, a_{eff} changes during crack closure. The schematic in part (a) is of a fully open crack, while part (b) corresponds to a partially closed crack. 150

Figure C.4 – Schematics are shown here of the change of (a) compliance during the load cycle and (b) the reduced compliance technique. 151

Figure C.5 – Data for aluminum alloy 8009 (K_{max} = 3.3 MPa$\sqrt{m}$ and R = 0.05) used to demonstrate the reduced compliance technique. 152

Figure C.6 – A photograph of the DIDS setup. The testing machine, long-focal-length microscope, digital camera, and computer are labeled. 153

Figure C.7 – Photograph of the speckle pattern on the surface of an ESET specimen. The speckle pattern is oriented perpendicular to the loading axis and centered on the machined notch where crack propagation occurs. 154

Figure C.8 – A digital image captured during the loading cycle is shown here. The direction of FCG is indicated by an arrow in the legend. The crack tip is indicated on the right side of the figure. A typical image pair used for DIDS analyses are also indicated (one on each crack side). 154

Figure C.9 – Schematics of the required steps to prepare a specimen for DIDS analysis are shown here. Each sketch (a-f) corresponds to events in the respective steps (a-f). 156

Appendix D - Alloys and Specimens

Figure D.1 – Orthogonal metallurgical cube for aluminum alloy 2024-T3. 158

Figure D.2 – Orthogonal metallurgical cube for aluminum alloy 7050-T6. 160

Figure D.3 – Orthogonal metallurgical cube for aluminum alloy 8009. 161

Figure D.4 – Schematic of thremo-plastic hysteresis loop for typical shape memory alloys, including Nitinol 50-50. 162

Figure D.5 – Schematics of stress-strain plots are shown here for Nitinol 50-50 in (a) martensite and (b) austenite phases. 163

Figure D.6 – Orthogonal metallurgical cube for Nitinol 50-50 (as tested). 164

Figure D.7 – Photographs of (a) compact tension (CT) and (b) eccentrically loaded edge notch tension (ESET) specimens. 165

Appendix E - Threshold Fatigue Crack Growth Humidity Effects

Figure E.1 – Humdity and temperature measurements of laboratory air. RH and temperature are plotted in parts (a) and (b), respectively, for one week. These data were used to determine the ambient range of humidity and temperature (ΔRH and ΔT, respectively), bounded by horizontal dotted lines in the plots. 168

Figure E.2 – Photograph of test setup to perform FCG tests in controlled RH. The specimen is shown inside a plastic bag where two air hoses, a humidity probe, pullrods, and a strain gage wire is allowed to penetrate the bag. Holes in the bag are sealed with tape. A warm beaker of water is used to humidify the compressed air, as shown. 169

Figure E.3 – Plot of crack length versus cycle count used to determine steady state FCG rate. 170

Figure E.4 – Steady state FCG rate plotted as a function of RH for aluminum alloy 7050-T6. Test results correspond to $\Delta K = 1.0$ MPa$\sqrt{m}$ and $K_{max} = 5.5$ (closed symbols) or 11.0 MPa$\sqrt{m}$ (open symbols). The FCG data are plotted (on a linear plot) against RH (bottom horizontal axis). The corresponding partial pressure of water vapor is shown along the top horizontal axis. 172

Figure E.5 – Plots of crack length versus cycle count for $K_{max} = 5.5$ MPa$\sqrt{m}$ as humidity was (a) decreased and (b) increased. Transient behavior occurred until the crack grew approximately one MPZ in part (a). No transition was observed in part (b). 174

Figure E.6 – Plots of crack length versus cycle count for $K_{max} = 11.0$ MPa$\sqrt{m}$ as humidity was (a) decreased and (b) increased. Transient behavior occurred until the crack grew approximately one MPZ in part (a). No transition was observed in part (b). 175

Figure E.7 – Schematics of (a) planar interface of environment and clean metal surface and (b) interaction of environment at a crack-tip. These configurations are used to model the concentrations of hydrogen in the MPZ of a fatigue crack. 177

LIST OF TABLES

Table 3.1 – Model parameters for specific alloys. 33

Table 5.1 – Changes in threshold FCG behavior with K_{max}. 120

Table 5.2 – Limits of plane-strain dominance, $K_{\varepsilon\ max}$, for each alloy. 123

Table A.1 – Comparison of threshold and Paris FCG. (Modified from Suresh [83].) 132

Table D.1 – Mechanical properties of aluminum alloys. 158

Table D.2 – Specimen configuration and geometry of FCG specimens. 166

Table E.1 – Expected hydrogren (normalized) concentration at edge of MPZ. ... 177

NOMENCLATURE

a – crack length
a_{eff} – effective crack length (see Appendix C)
a_{vis} – crack length, as measured visually
a_{comp} – crack length, as measured using compliance
ASTM – American Society for Testing of Materials
B – total amount of slip along a given slip plane (see Section 3.2.4)
b – magnitude of the Burger's vector, slip contribution of a single dislocation (see Section 3.2.4)
C – K-gradient; prescribes the rate of ΔK reduction (see Equation B.1)
CG – course-grained microstructure (see Section 3.6.3)
CPZ – cyclic plastic zone; crack-tip region where cyclic plasticity occurs
CT – compact tension FCG specimen
CTOD – crack-tip opening displacement (see Section 3.2.4)
CTSD – crack-tip sliding displacement (see Section 3.2.4)
da/dN – FCG rate with respect to load cycle count
da/dt – FCG rate with respect to time
DIDS – Digital image displacement system (see Section C.3)
E – elastic modulus
EDX – energy dispersion x-ray spectroscopy
ESET – eccentrically-loaded-single-edge tension FCG specimen
FCG – fatigue crack growth
FG – fine-grained microstructure (see Section 3.6.3)
g – asperity length for rough cracks (see Section 3.2)
K – stress intensity factor
K_c – critical value of K corresponding to fracture
K_{cl} – value of K corresponding to crack closure on unloading
K_I – mode I stress intensity factor
K_{II} – mode II stress intensity factor
$K_{I\,Local}$ – mode I stress intensity factor in local coordinates (see Section 3.2.2)
$K_{II\,Local}$ – mode II stress intensity factor in local coordinates (see Section 3.2.2)
K_{Ic} – plane-strain value of K_c
K_{Ig} – mode I stress intensity factor in global coordinates (see Section 3.2.2)
K_{IIg} – mode II stress intensity factor in global coordinates (see Section 3.2.2)
$K_{\varepsilon\,max}$ – maximum K for plane-strain dominance (see Equation 5.8)
$K_{max\,fc}$ – value of K_{max} below which the crack is completely closed, *i.e.* $R_{cl} = 1$
$K_{max\,trans}$ – value of K_{max} at the transition between tip contact and asperity contact
K_{max} – maximum value of K during constant amplitude loading (see Section 1.1)
K_{min} – minimum value of K during constant amplitude loading (see Section 1.1)
m – slope of FCG curve in the Paris regime (see Section 1.2)
m^* – slope of FCG curve between 10^{-9} m/cycle and 10^{-10} m/cycle (see Section 4.2)
MPZ – monotonic plastic zone; crack-tip region where tensile plasticity occurs
OICC – oxide-induced crack closure (see Section 1.6.2)
PICC – plasticity-induced crack closure (see Section 1.6.2)
PM – powder metallurgy; descriptor of 8009 aluminum

r – distance behind the crack-tip (see Section 3.2)
r_p – plastic zone radius determined from elastic solution (see Equation 3.5a)
r_p^* – plastic zone radius considering crack-tip plasticity (see Equation 3.5b)
R – applied load ratio, defined as K_{min}/K_{max} (see Section 1.1)
$R_{applied}$ – applied load ratio; same meaning as R but used to distinguish R from R_{cl}
R_{cl} – value of load ratio corresponding to crack closure on unloading
RH – relative humidity (see Appendix E)
RICC – roughness-induced crack closure (see Section 1.6.2)
SEM – scanning electron microscope
SMCC – sliding mode crack closure (see Sections 5.1.2 and A.2)
t – thickness of the oxide layer (see Section 3.2)
UHV – ultra-high vacuum (see Section B.2)
u – elastic mode II crack face displacement
v – elastic mode I crack face displacement
u^* – normalized elastic mode II crack face displacement (see Figure 3.7)
v^* – normalized elastic mode I crack face displacement (see Figure 3.7)
u^{**} – normalized elastic mode II crack face displacement (see Figure 5.3)
v^{**} – normalized elastic mode I crack face displacement (see Figure 5.3)
α – crack-tip asperity angle for rough cracks (see Section 3.2)
α_{fc} – value of α above which the crack is completely closed, *i.e.* $R_{cl} = 1$
α_{trans} – value of α at which tip contact and asperity contact occur simultaneously
Δa – change in crack length as a crack grows away from oxide (see Section 3.5.1)
Δa_{comp} – value of Δa measured by compliance
Δa_{trans} – value of Δa where crack wake oxide no longer contributes to closure
Δa_{vis} – value of Δa measured visually
ΔK – cyclic range of K during constant amplitude loading (see Section 1.1)
ΔK_{eff} – the effective (closure-free) portion of ΔK (see Section 1.6.2)
ΔK_I – cyclic range of mode I stress intensity factor
ΔK_{II} – cyclic range of mode II stress intensity factor
ΔK_{th} – threshold value of ΔK estimated by ASTM procedures (see Appendix B)
ΔK_{trans} – value of ΔK corresponding to a transition in FCG
γ – crack meandering angle (see Section 3.2)
ν – Poisson's ratio
θ – angular measurement with respect to the crack-tip direction (see Section 3.2)
σ_o – yield stress
ξ – ratio of residual crack wake plasticity to $CTOD_{max}$ (see Section 3.2.4)

PART I – Introduction and Objectives

CHAPTER 1 — INTRODUCTION

The topic of this study, threshold fatigue crack growth load ratio effects, is introduced in this chapter. Typical fatigue crack growth behavior (including the influence of load ratio) and practical design issues are discussed. A brief literature review of topics relevant to this dissertation is also presented.

1.1 — INTRODUCTION TO FATIGUE CRACK GROWTH

Cracks compromise the integrity of engineering materials and structures. Under applied stress, a crack exceeding a critical size will suddenly advance breaking the cracked member into two or more pieces. This failure mode is called fracture. Even sub-critical cracks may propagate to a critical size if crack growth occurs during cyclic (or fatigue) loading. Crack growth resulting from cyclic loading is called fatigue crack growth (FCG). Because all engineering materials contain microstructural defects that may produce fatigue cracks, a damage tolerant design philosophy was developed to prevent fatigue failure in crack sensitive structures. Damage tolerant design acknowledges the presence of cracks in engineering materials and is used when cracks are expected. Both sudden fracture, and fracture after FCG, must be considered as failure modes. Because initial critical defects are rare in well-designed engineering structures [1], FCG is of primary concern here.

The stress intensity factor, K, was initially used to quantify crack-tip damage for fracture scenarios. Fracture was shown to occur when the crack-tip stress intensity factor reached a critical value, K_c,[1] independent of crack size or net applied stress[2] [2]. This observation led to the concept of crack similitude, *i.e.* cracks of different length will fracture at the same K_c. Fracture mechanics analysis and crack similitude were modified for fatigue cracks by Paris [3]. Fatigue crack growth rates (increment of crack growth per load cycle, d*a*/dN) were related to ΔK, the cyclic range of crack-tip stress intensity, for constant amplitude loading. A schematic of typical constant amplitude load cycles are shown in Figure 1.1, where the stress intensity factor, K, is plotted as a function of time. As indicated by the solid curve, the stress intensity factor oscillates between minimum and maximum values, K_{min} and K_{max}, respectively. Arrows indicate change in K with increasing time. ΔK is shown schematically on the right side of the figure and is defined as $K_{max} - K_{min}$. Another useful parameter to describe constant amplitude loading is the load ratio, R, defined in the figure (lower right corner) as the ratio of K_{min} and K_{max}. Paris implied that similitude exists for fatigue cracks subject to the same ΔK.[3] In other words, fatigue cracks of different length but subject to the same ΔK will grow at the same FCG rate, d*a*/dN. Therefore, FCG data obtained from laboratory specimens (of convenient size) can be used to predict the FCG response for any crack configuration.

---

[1] The fracture toughness, K_c, depends on specimen thickness (due to plane-stress conditions at the specimen surface). The plane-strain fracture toughness, K_{Ic}, is constant and a material property.

[2] Validity of the stress intensity factor depends on small-scale yielding and is not expected to be meaningful as the net applied stress approaches the (large scale) yield stress, σ_o.

[3] Other influences on FCG rates will be discussed later, most notably the effect of R.

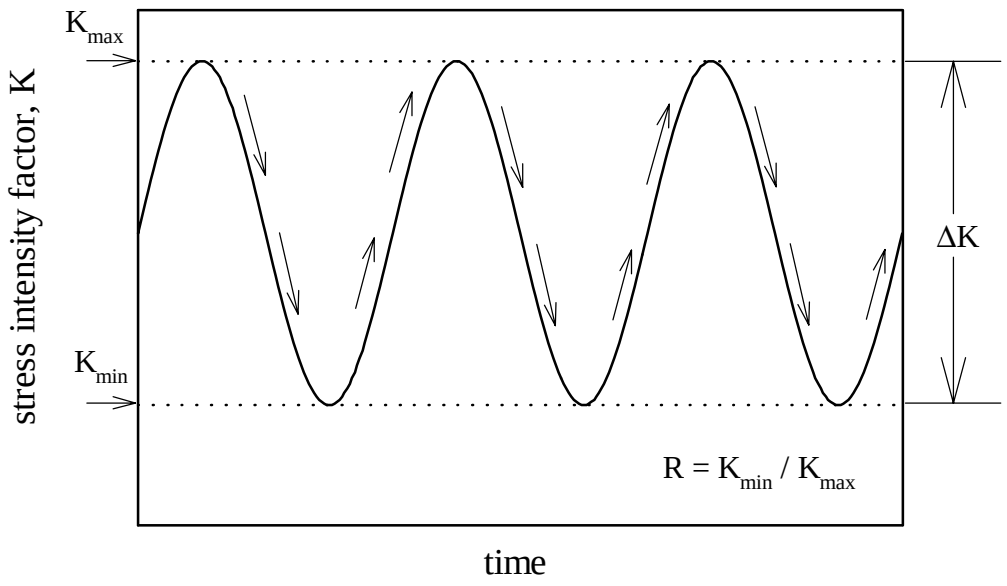

Figure 1.1 – Schematic of constant amplitude load cycles, where the crack-tip stress intensity factor, K, is plotted against time.

1.2 — FATIGUE CRACK GROWTH BEHAVIOR OF ENGINEERING METALS

A schematic of typical (constant R) FCG behavior for engineering metals is shown in Figure 1.2, where the logarithm of FCG rate, log (d*a*/dN), is plotted against log (ΔK). FCG behavior, indicated by the solid curve, is divided into three regions by vertical dotted lines in the figure. At intermediate values of ΔK, (typically between 5 and 20 MPa√m for aluminum alloys at R = 0) the FCG curve is nearly linear on log-log plots. This region, called the Paris regime, is labeled in Figure 1.2. Taking advantage of this linear relation, Paris presented an equation relating FCG rates (d*a*/dN) to ΔK using two empirical parameters (C and m) as shown in Equation 1.1 [3]. The slope of the FCG curve in the Paris regime, m, is shown on the figure and ranges from 2 to 4 for most engineering metals. As ΔK increases beyond the Paris regime, unstable crack growth occurs. This region is shown to the right of the Paris regime in Figure 1.2. Here, the FCG curve becomes steep (*i.e.* d*a*/dN increases rapidly with increasing ΔK) as K_{max} approaches the fracture toughness, K_c, or large scale yielding occurs.

$$da/dN = C(\Delta K)^m \qquad (1.1)$$

As ΔK decreases into the threshold region, the FCG curve becomes steep as d*a*/dN rapidly decreases with ΔK reduction. Presumably, a threshold ΔK is reached, ΔK_{th}, below which no detectable FCG occurs. Threshold FCG is the focus of this research (as indicated by the boxed region in Figure 1.2) and is of practical interest for two reasons. First, the concept of FCG threshold is useful from a design standpoint. For applications where initial cracks or defects are unavoidable, FCG (ultimately leading to failure) can be avoided if $\Delta K < \Delta K_{th}$. Second, under constant cyclic loads a (naturally forming) fatigue

crack grows faster as crack length increases, so the majority of fatigue life is spent propagating a small crack under threshold conditions. Paris and unstable FCG behavior are typically limited to a small portion of the total fatigue life.

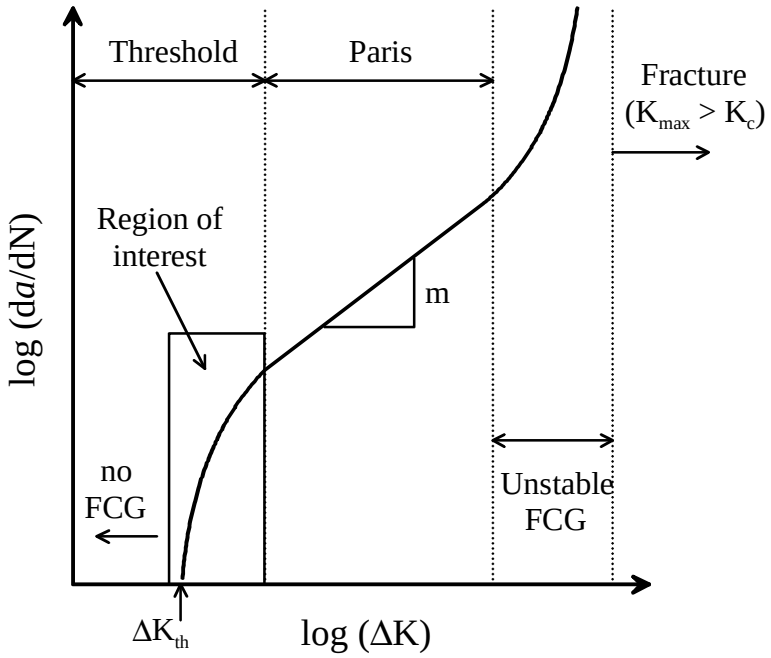

Figure 1.2 – Schematic of typical FCG data. Plotted as log (d*a*/dN) versus log (ΔK), the FCG behavior is divided into three regions (threshold, Paris, and unstable FCG regions).

1.3 — DAMAGE TOLERANT DESIGN

Damage tolerant design was developed to prevent structural failure of components where fatigue cracking is likely. Fatigue life is calculated using service conditions, known FCG behavior, and crack sizes found by careful inspection procedures. If no crack is found, the most damaging flaw or crack that cannot be reliably detected is assumed to exist. This conservative design philosophy has been successfully used when FCG and fracture limits the service life of a structure. Using damage tolerant analysis, failure can be prevented by two means; (1) limiting service life to the cycles required for the longest crack to propagate to failure or (2) ensuring that the most damaging (longest) crack will not propagate, *i.e.* $\Delta K < \Delta K_{th}$. The latter option is most attractive when designing for long fatigue lives, and is the subject of this discussion. In these cases, ΔK_{th} and K_c are used as design parameters for FCG and fracture, respectively. An idealized schematic of ΔK versus K_{max} is shown in Figure 1.3. Values corresponding to ΔK_{th} and K_c are labeled in the figure. If K_{max} exceeds K_c, fracture will occur as indicated on the right side of Figure 1.3. At ΔK greater than ΔK_{th}, FCG will occur (likely leading to fracture) as shown at the top of the figure. A safe region exists where, $\Delta K < \Delta K_{th}$ and $K_{max} < K_c$, indicated by the shaded region at the bottom of Figure 1.3. Existing cracks are considered benign if the crack-tip stress state lies within these safe bounds.

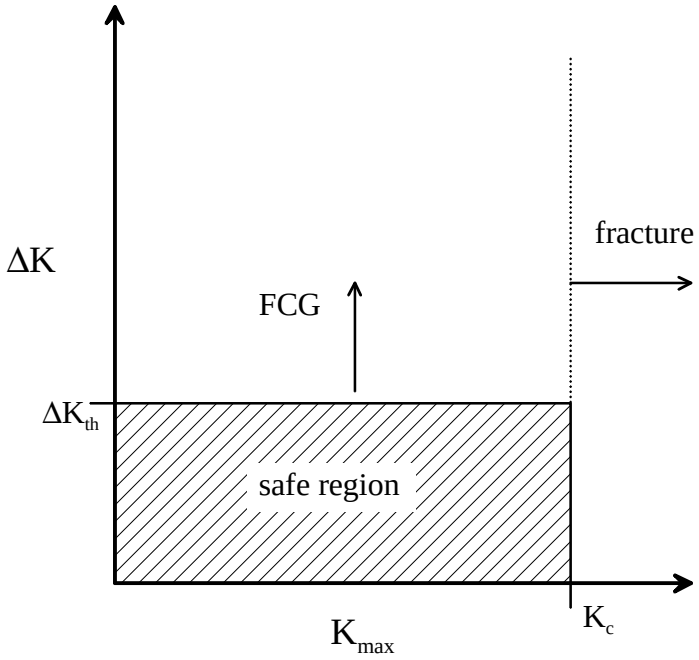

Figure 1.3 – Schematic of ΔK plotted against K_{max}, used to demonstrate the philosophy of damage tolerant design.

Damage tolerant design has been used to decrease structural weight (reducing cost and increasing performance) without sacrificing safety. The most common way to reduce ΔK (below ΔK_{th}) in an engineering component is to decrease stress levels. Because stress reduction is normally accomplished by increasing the load bearing area, increased weight results as an undesirable by-product. Weight increases are especially troublesome for aircraft and spacecraft applications where lightweight, durable structures are essential. Optimal design (between weight and fatigue criteria) of high-performance lightweight structures requires service loads to be just within safe limits. For fatigue loading, it is advantageous for ΔK (service loading) to approach, but not exceed, ΔK_{th}. Such a design criterion requires an appropriate value for ΔK_{th}, and a good understanding of the variables that influence threshold FCG. Any variation of ΔK_{th} is potentially dangerous.

1.4 —FATIGUE CRACK GROWTH LOAD RATIO EFFECTS

Threshold FCG behavior for three different values of load ratio ($R_1 < R_2 < R_3$) are schematically plotted as log (d*a*/dN) versus log (ΔK) in Figure 1.4. Increases in R produce increases in FCG rate, as indicated by the arrow labeled 'R'. The effect of R in the Paris regime (an increase in FCG rate) is labeled Δ(d*a*/dN) in the figure. FCG threshold occurs at ΔK_{th1} and ΔK_{th3} for R_1 and R_3, respectively. If ΔK_{th1} was used as a safe design parameter, but service loads corresponded to R_3, FCG would occur at or below the assumed threshold (ΔK_{th1}). The resulting FCG at ΔK_{th1} for R_3 is indicated by 'Δ' in Figure 1.4. For this example, the appropriate ΔK_{th} is ΔK_{th3} instead of ΔK_{th1}. The difference between is ΔK_{th1} and ΔK_{th3} is indicated by $\Delta(\Delta K_{th})$ in Figure 1.4. Because

ΔK_{th} is a function of R, great care must be taken to (1) accurately predict service loads and (2) choose a ΔK_{th} appropriate for design analysis.

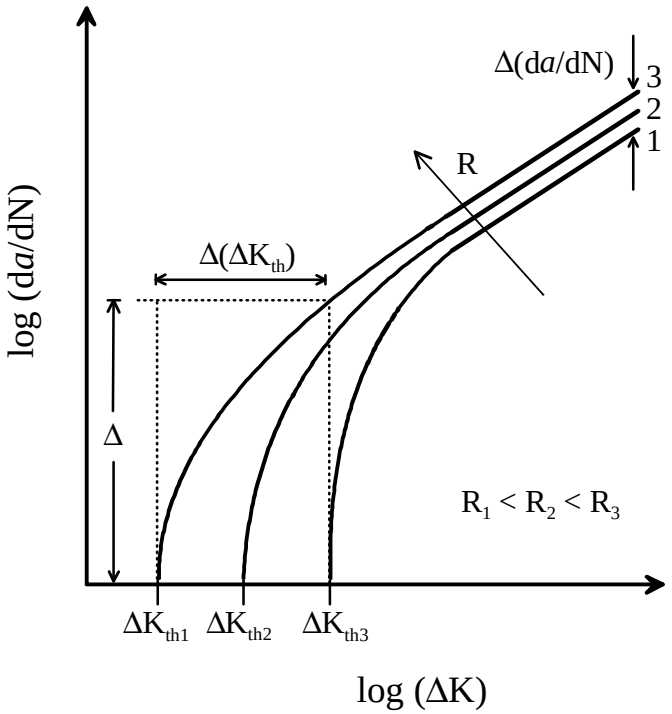

Figure 1.4 – Schematic of typical FCG data, plotted as log (d*a*/dN) versus log (ΔK), for three values of load ratio, R.

1.5 — PROBLEM STATEMENT

Threshold load ratio effects complicate damage tolerant design. Because ΔK_{th} decreases with increasing R, Figure 1.3 should be modified as shown in Figure 1.5. The values ΔK_{th1} and ΔK_{th3} from Figure 1.4 are indicated along with their corresponding K_{max} values (K_{max1} and K_{max3}, respectively). FCG occurs below ΔK_{th1} at high K_{max}, indicated below the horizontal dotted line in the figure. The upper bound of the shaded (safe) region is ΔK_{th} as a function of K_{max}. (Although the upper bound of the safe region is shown as a straight line, this does not imply any specific relation between ΔK_{th} and K_{max} other than ΔK_{th} decreases with increasing K_{max}.) Conditions to the right of threshold in Figure 1.4, (for all cases) lie above the shaded region in Figure 1.5, indicating that FCG occurs. For high-performance lightweight structural design, it is advantageous to approach the limits of the safe region.[4] For conditions outside the safe region, premature mechanical failure will result. If a design is too conservative, and lies too deep within the safe region, the performance of the structure will suffer. For example, overly conservative design may eliminate fatigue problems for an airplane, but performance may suffer due to increased weight. A poor understanding of threshold FCG behavior limits the confidence of design

[4] A factor of safety is normally applied so conservative (safe) results are obtained.

engineers to optimize structures in terms of cost, performance, and safety. The solution of this problem is to better understand threshold FCG, which is the ultimate goal of this research.

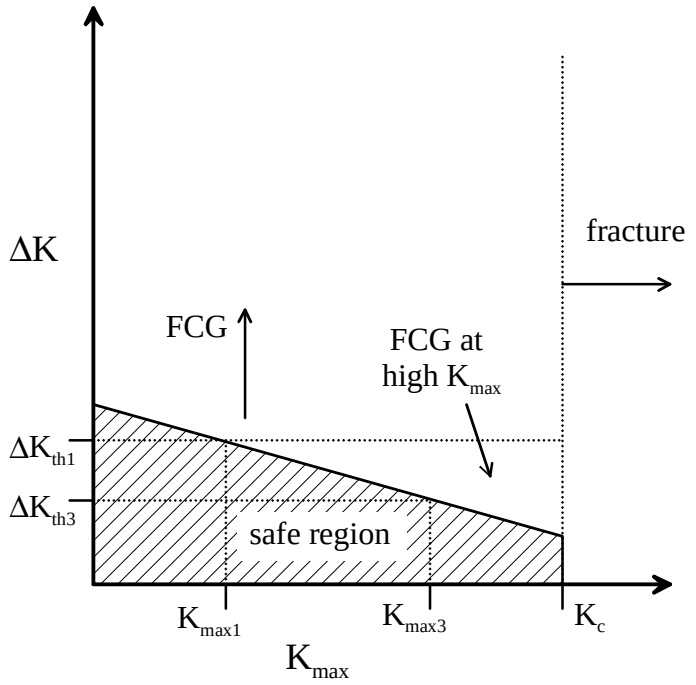

Figure 1.5 – Schematic of ΔK plotted against K_{max}, used to demonstrate the influence of K_{max} (or R) on FCG threshold and damage tolerant design.

1.6 — LITERATURE REVIEW

A brief literature review is given here to present the most important concepts related to this research. Included is a description of threshold testing procedures. A more detailed literature review is presented in Appendix A. Details of the threshold testing procedures, used to produce the FCG data presented in this dissertation, are described in Appendix B.

1.6.1 — Threshold testing procedures

Using the concept of crack-tip similitude, FCG is normally studied using laboratory specimens of a convenient size, geometry, and crack length. Although generally associated with short cracks (< 1 mm), threshold FCG is studied with long crack (> 5 mm) specimens. Threshold conditions are achieved for long fatigue cracks by reducing the crack-tip driving force, ΔK, as the crack propagates. FCG threshold is reached when the crack stops growing. Because load reduction occurs gradually as the crack grows, no true threshold is reached in a practical amount of time. Instead, a working definition for ΔK_{th} is used as very low FCG rates are achieved (10^{-10} m/cycle has been suggested) [4]. Standard FCG test procedures have been established (by ASTM, American Society for Testing and Materials) to eliminate load history effects and ensure consistent results [4]. However, recent evidence suggests these standards are insufficient [5, 6].

1.6.2 — Fatigue crack closure

During cyclic loading, fatigue crack closure occurs when crack faces contact before minimum load. It is assumed that no crack-tip damage occurs while crack faces are in contact, so this portion of the load cycle is ineffective in terms of FCG. Thus, FCG rates are related to an effective cyclic stress intensity range, ΔK_{eff}, as defined in Equations 1.2, where K_{cl} is the stress intensity corresponding to crack face contact. Because a greater portion of the load cycle is expected to be ineffective (*i.e.* below K_{cl}) at low R, closure is used to explain the influence of load ratio on FCG rates.

$$\Delta K_{eff} = K_{max} - K_{cl} \tag{1.2a}$$

$$da/dN = f(\Delta K_{eff}) \tag{1.2b}$$

Elber, the first to propose fatigue crack closure, suggested that premature crack face contact resulted from residual plastic deformation in the crack wake [7]. This mechanism was coined plasticity-induced crack closure (PICC) as other closure mechanisms were suggested. Voluminous oxide debris in the crack mouth has been suggested as a closure mechanism called oxide-induced crack closure (OICC) [8-10]. Misalignment of rough crack surfaces upon unloading has been suggested as another closure mechanism, roughness-induced crack closure (RICC) [8, 11, 12]. Other closure mechanisms have been suggested but are not discussed here because PICC, OICC, and RICC are considered the most likely mechanisms at FCG threshold. Schematics of PICC, RICC, and OICC are given in Figure 1.6. In Figure 1.6a, the plastic stretch in the crack wake causes crack face contact at the crack-tip (PICC). Contact of rough crack asperities (RICC) is shown in Figure 1.6b. Finally, oxide debris or an oxide layer in the crack mouth can prop a fatigue crack open (OICC), as indicated in Figure 1.6c. For most engineering alloys, PICC is the dominant closure mechanism, especially in the Paris regime [13]. The significance of RICC and OICC is generally limited to threshold conditions where crack opening displacements are small and crack paths become more torturous [14]. Although typically studied individually, it is likely that all three mechanisms (PICC, RICC, and OICC) contribute at threshold.

1.6.3 — Closure-free load ratio effects

Not all R effects are explained by closure, especially at high values of R [15]. This suggests that closure-free load ratio mechanisms exist. Load ratio effects on FCG rates tend to be more dramatic at threshold than in the Paris regime [16]. A closure-free mechanism has been proposed to explain R effects in the unstable FCG (see Figure 1.2). At high ΔK (as K_{max} approaches the fracture toughness) localized fracture events, called static modes, occur at or near the crack-tip [17]. These microscopic fractures may occur at defects or regions of below average fracture toughness. The static modes explanation has been limited to the unstable FCG regime. It is not known if static modes or similar mechanisms occur at FCG threshold. If so, these localized failure modes may be limited to high K_{max} levels, *i.e.* near K_c.

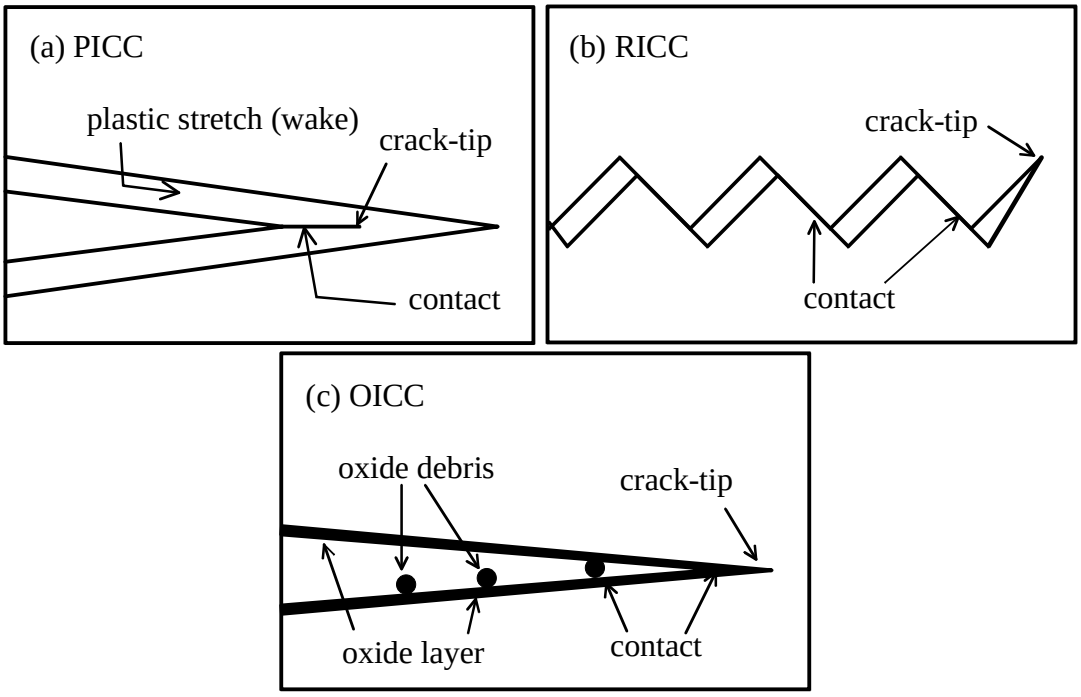

Figure 1.6 – Schematics of the three closure mechanisms most likely at FCG threshold; (a) PICC, (b) RICC, and (c) OICC.

Marci [18] and Lang, *et al*., [19] observed unusual behavior during constant K_{max} threshold tests on low toughness Titanium alloys (K_c = 29 MPa$\sqrt{m}$).[5] While a reduction in ΔK generally leads to decreasing FCG rates, results presented by Marci and Lang suggest this may not always be true. During constant K_{max} threshold testing, FCG rates initially decreased with decreasing ΔK. Below a transition ΔK (ΔK_{trans}), FCG rates increased as ΔK was reduced further. This behavior was only observed at high K_{max}, > 21 MPa$\sqrt{m}$ (approximately 0.7 K_c). A schematic of the unstable FCG behavior presented by Marci and Lang is shown in Figure 1.7 as a solid curve. Arrows indicate the change in FCG response with respect to time. Unstable threshold behavior starts at ΔK_{trans} (between 1 MPa$\sqrt{m}$ and 2 MPa$\sqrt{m}$) where the solid curve deviates from typical FCG threshold behavior (dotted curve). It is not known if unstable threshold behavior could occur in aluminum alloys under similar conditions. If so, this unstable FCG behavior would make ΔK_{th} meaningless as a design parameter, profoundly impacting damage tolerant design. This is especially important for fatigue applications with high mean loads, like bolts and other fasteners.

[5] Constant K_{max} threshold tests are used to achieve FCG threshold without fatigue crack closure effects. See Appendix B for a description of constant K_{max} testing.

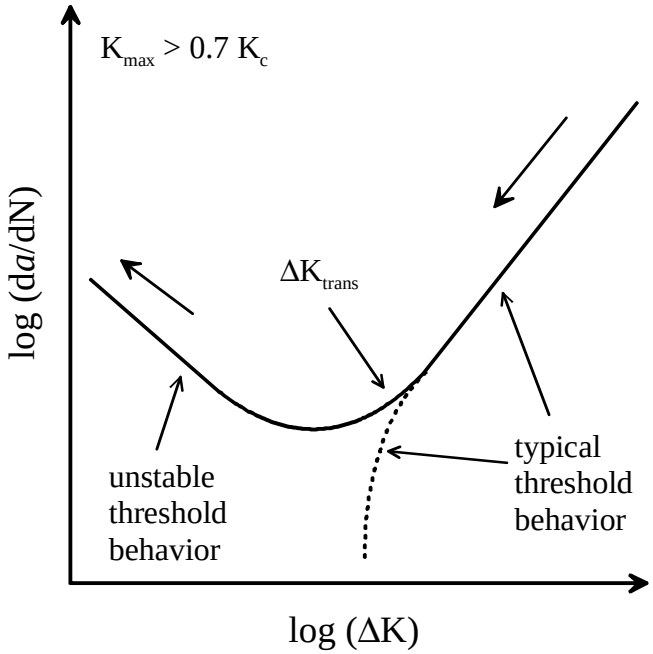

Figure 1.7 – Schematic of unstable FCG threshold behavior during constant K_{max} threshold testing on titanium alloys.

1.6.4 — Short crack issues

Short cracks are known to propagate faster than long cracks subject to the same ΔK and R, an apparent violation of fatigue crack similitude [20-23]. Here, a distinction is made between "short" cracks and "small" cracks [1, 24]. A crack is considered small when all crack dimensions are similar to or less than a characteristic microstructural dimension, likely a typical grain diameter for engineering metals. Therefore, small cracks are generally contained within a limited number of grains, perhaps even a single grain. Because individual grains are highly anisotropic (plastic deformation is restricted to a few slip planes dependent on crystal orientation), the stress intensity factor (assuming isotropic material properties) is not a good descriptor of crack-tip driving force. A crack is considered short if only the crack length is on the order of microstructural features. Because short crack fronts usually occur over many grains, the local anisotropic behavior is averaged so the material appears isotropic and a continuum mechanics description (*i.e.* ΔK) is appropriate. The discussion presented here is limited to short cracks where the stress intensity factor is an appropriate descriptor of crack-tip driving force.

The difference between "short" crack and "long" crack behavior is explained in terms of fatigue crack closure. Both short and long cracks are well described by fracture mechanics and will propagate at the same FCG rate if subjected to the same ΔK_{eff} (considering crack closure). Short cracks have less crack wake for crack closure to occur, in comparison to long cracks. Therefore, closure loads for short cracks are less than for long cracks under similar load conditions. Short cracks propagate faster than long cracks under the same applied ΔK because the effective crack-tip driving force, ΔK_{eff}, is greater for short cracks. A schematic comparing short crack and long crack behavior is shown in

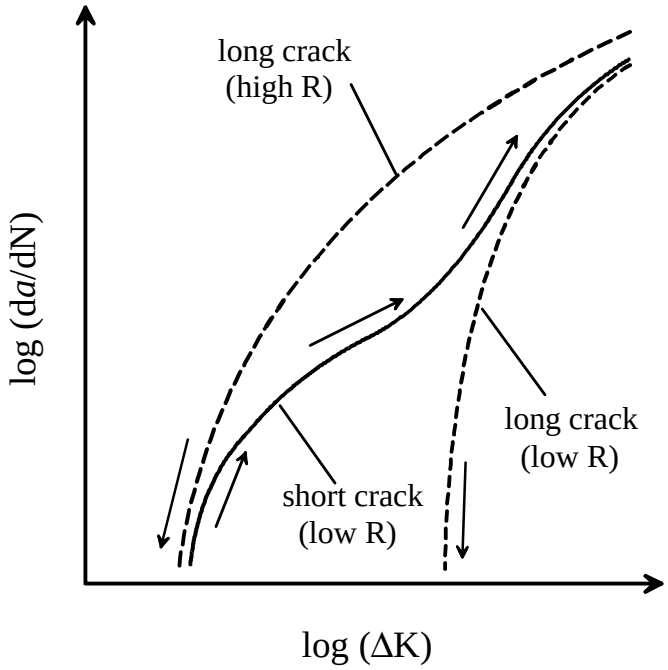

Figure 1.8 – Schematic of typical short fatigue crack data (increasing ΔK) compared with long crack data (decreasing ΔK). (This figure is modified from Tokaji [25].)

Figure 1.8 [25]. Typical short crack behavior, generated at low R, is indicated by the solid curve. For comparison, long crack behavior is presented as dotted curves for cases of high and low R: closure-free and closure-affected behavior, respectively. At threshold conditions, short crack data is in good agreement with long crack data at high R because both are closure-free. As ΔK increases, the (low R) small crack behavior merges with (low R) long crack behavior because a crack wake (of plastic deformation) develops as the short crack grows, *i.e.* fatigue crack closure occurs for both short and long cracks. The arrows parallel to the curves in Figure 1.8 indicate the change in ΔK with respect to time. Short cracks typically propagate under increasing ΔK conditions (constant amplitude cyclic loads). During long crack threshold testing, ΔK is reduced until FCG threshold is reached. Considering crack-tip closure, both long and short cracks should propagate according to the same d*a*/dN versus ΔK_{eff} relation. Recent analyses by Newman [5] and McClung [6] indicate that load history effects influence long crack threshold data. During load shedding FCG tests, more plasticity is generated at the beginning of the test. Residual crack wake plasticity (produced early in a threshold test) may result in crack face contact far from the crack-tip. This remote closure mechanism (which is discussed in greater detail in Section A.2.1) results in artificially high values of ΔK_{th}. Because short crack data does not agree with long crack data at threshold (for the same R), this phenomenon has been called the "short crack anomaly." In light of problems encountered during long crack threshold testing, perhaps it is more accurate to describe this problem as a "long crack anomaly" [26]. Constant K_{max} threshold tests have been used to produce high R (closure-free) threshold conditions for long crack experiments. Both crack-tip closure and remote closure mechanisms are avoided during

constant K_{max} threshold testing. Because closure is eliminated, this technique provides a way to study short crack threshold behavior using long crack data [27].

1.6.5 — Other influences to consider

To study threshold FCG, it is important to identify all influential variables (ΔK, R, environment, microstructure, load history, *etc*.), even if they are not within the scope of the research. Failure to do so may result in inaccurate interpretation of test results [28]. For example, if environmental conditions are allowed to vary while studying load ratio effects, environmental influences may be misinterpreted as load ratio effects. To avoid this pitfall, these alternate influences should be held constant or evaluated to determine their respective influence on threshold behavior.

CHAPTER 2 — RESEARCH MOTIVATION, OBJECTIVES, AND APPROACH

In this chapter, the motivation, objectives, and approach for research on load ratio effects on threshold fatigue crack growth are described. Additional research on threshold FCG is needed to refine damage tolerant analysis. This research focuses on load ratio effects, which are categorized as either extrinsic (closure-affected) or intrinsic (closure-free). Specific objectives and an approach to achieve these objectives are presented. Finally, potential problems likely encountered during threshold FCG are identified.

2.1 — MOTIVATION FOR RESEARCH

Damage tolerant design has evolved as the safest and most cost-effective procedure to prevent fatigue failure of structural components vulnerable to fatigue cracking. However, technological barriers make damage tolerant design impractical for crack sensitive components, where small cracks result in fracture. This limitation is not a fault of the damage tolerant philosophy, but due to problems detecting small cracks and understanding the FCG behavior of these cracks.

Using damage tolerance methods, fatigue lives of load bearing components are calculated in terms of service conditions, known FCG behavior (from laboratory FCG tests), and an initial crack size. The predicted fatigue life is the number of load cycles to propagate the fatigue crack from the initial state to the critical crack size, when failure occurs. Typically, several safety inspections are planned within the predicted fatigue life, so fatigue damage can be monitored and damaged components replaced as needed. Because only small cracks or flaws are initially present in most new structures, it may be difficult or impossible to detect initial damage with current inspection technology. If no crack or defect is detected, fatigue life is calculated using the largest crack that cannot be reliably detected. The assumption that cracks exist when none are detected produces a conservative bias in damage tolerant life prediction, which is needed to ensure safe conditions. Essentially, the portion of fatigue life propagating a crack or flaw from the (actual) initial size to the threshold of detection is neglected. Because this error results in actual fatigue lives longer than predicted, conservative life predictions may be viewed as a type of safety factor instead of a problem. This is an acceptable view if the difference between the smallest detectable flaw and the critical crack length is large, so the majority of fatigue life is spent propagating a detectable crack.

Problems arise when the difference between the detection threshold and the critical crack size is reduced so only a small portion of fatigue life is spent with a detectable crack. In these cases, fatigue life is grossly under-predicted and unnecessarily frequent inspection intervals are prescribed. As an extreme example, consider a scenario where the critical flaw size is too small to detect. Damage tolerant methods cannot be used to predict fatigue life in this case, so “safe life” fatigue analyses (based on S-N data) are used instead. Damage tolerance analyses have not yet replaced safe-life methods for fatigue analyses of helicopter structures because of similar crack detection limitations [29]. Ultimately, technological advances will likely enable damage tolerant analyses and

design for crack sensitive (*i.e.* small critical crack size) helicopter components [30].[6] Two technical problems must be overcome to successfully use damage tolerance on helicopter components. First, fatigue crack detection must be improved to reliably detect smaller cracks. This will reduce the assumed flaw size in undamaged components and increase the portion of fatigue life with a detectable crack. However, resolving the first technical problem produces a second technical problem. Improved crack detection extends the portion of fatigue life where it is possible to monitor fatigue damage. Because ΔK increases with increasing crack size, these smaller cracks are associated with smaller ΔK and threshold FCG. Therefore, improvements in damage tolerant life prediction will require a better understanding of threshold FCG behavior. The objective of this research is to obtain a better understanding of threshold FCG, specifically the effect of load ratio.

2.2 — RESEARCH OBJECTIVES

Before stating specific research objectives, it is useful to divide load ratio effects into two categories, "extrinsic" and "intrinsic." Extrinsic load ratio mechanisms are defined as those acting in the crack wake, while intrinsic mechanisms occur in the crack-tip process zone ahead of the crack.[7] A generic crack-tip region is schematically shown in Figure 2.1 to illustrate the difference between intrinsic and extrinsic load ratio mechanisms. The crack-tip is labeled in the figure (to the right of center) and the direction of FCG is from left to right. The crack wake (left side of figure) is rough with oxide debris in the crack mouth. Crack roughness, oxide debris, and plasticity (not illustrated in the figure) have been identified as fatigue crack closure mechanisms. Because all of these mechanisms

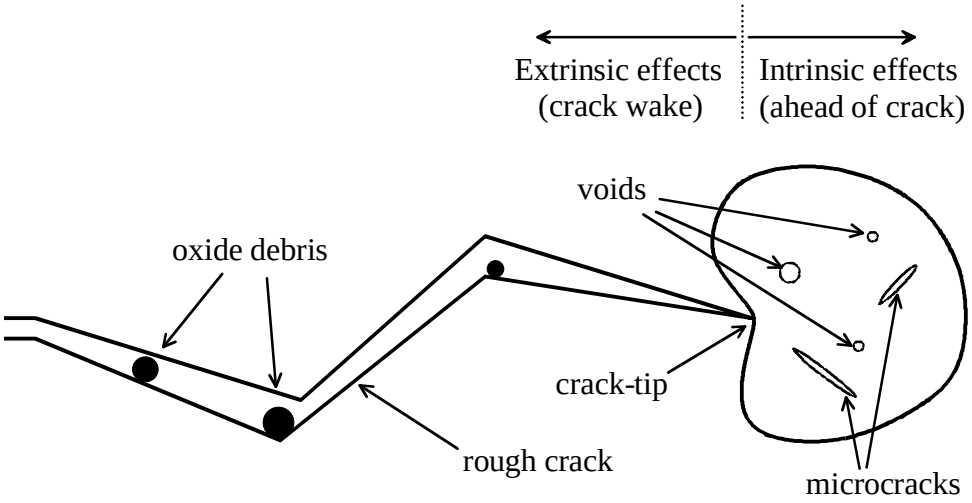

Figure 2.1 – Schematic of a generic crack-tip region used to define extrinsic and intrinsic FCG load ratio effects.

[6] Other applications, currently limited to safe-life fatigue analyses, can also benefit from these improvements in damage tolerant analyses. Helicopters are used here as an example.

[7] Here, process zone is used to describe a zone of plastic deformation at the crack-tip (*i.e.* plastic zone). No distinction between cyclic plasticity and monotonic plasticity is made here.

act in the crack wake, they are extrinsic effects.[8] Voids and microcracks are shown in the crack-tip process zone on the right side of Figure 2.1. This crack-tip damage lowers the lowers the FCG resistance of the material, resulting in accelerated FCG rates. Void and microcrack formation ahead of the crack-tip have been associated with fracture and intrinsic load ratio effects (see Section A.3.1). Because void and microcracks form ahead of the crack-tip they are intrinsic load ratio mechanisms.

It is assumed that extrinsic and intrinsic load ratio mechanisms can be studied and modeled independently because they act in different locations (ahead of and behind the crack-tip, respectively). The most likely load ratio mechanisms considered here are shown as a chart in Figure 2.2. Extrinsic and intrinsic mechanisms are presented (separately) on the left and right sides of Figure 2.2, respectively. Although extrinsic and intrinsic effects are studied separately, an understanding of both will lead to a more complete understanding of threshold FCG (indicated at the bottom of the figure). The extrinsic load ratio mechanisms considered include plasticity-induced crack closure (PICC), roughness-induced crack closure (RICC), and oxide-induced crack closure

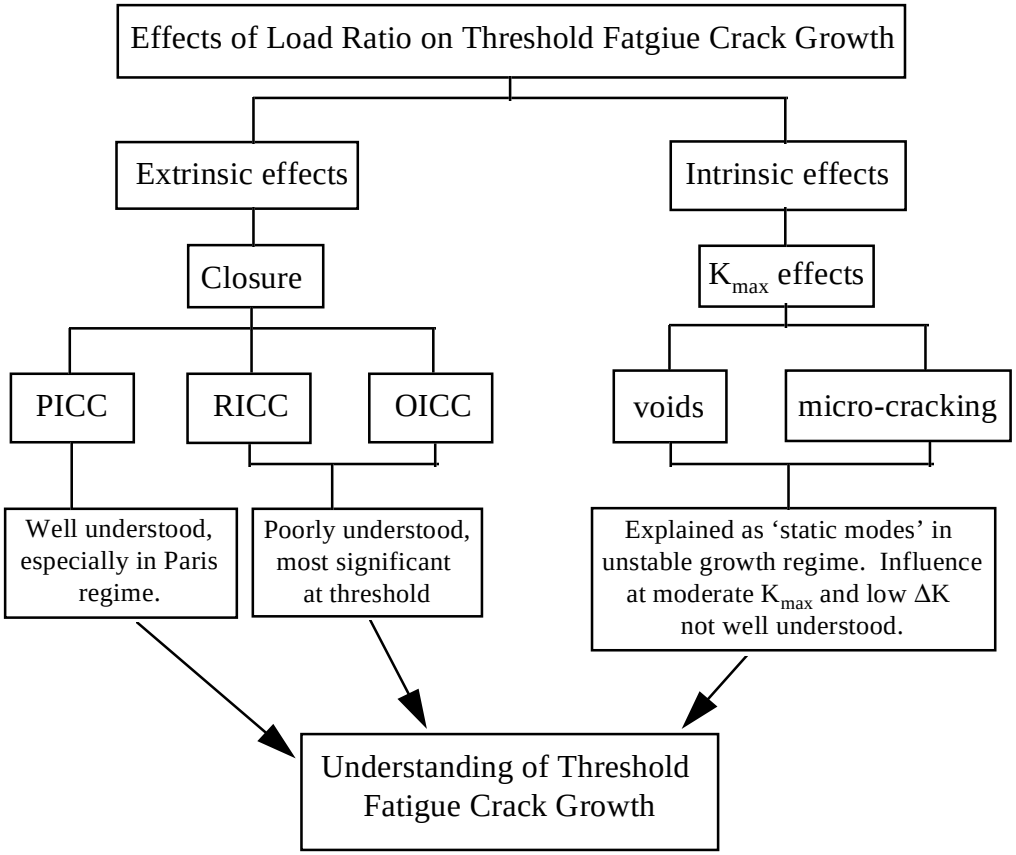

Figure 2.2 – Chart of extrinsic and intrinsic FCG load ratio mechanisms considered most likely to affect FCG threshold.

[8] Because all extrinsic R effects considered here are closure mechanisms, the terms "extrinsic" and "closure-affected" are used interchangeably. Likewise, "intrinsic" and "closure-free" have the same meaning because no intrinsic R effects are associated with closure.

(OICC). PICC, the first known closure mechanism, is dominant (relative to RICC and OICC) for Paris regime FCG. Here, PICC models have successfully predicted crack closure behavior because other closure mechanisms (*e.g*. RICC and OICC) are negligible.

At FCG threshold, RICC and OICC become significant (relative to PICC) and PICC models are less successful. RICC and OICC models that neglect crack-tip and crack wake plasticity have produced unsatisfactory results or relied heavily on empirical parameters to produce reasonable results [14, 31]. At FCG threshold PICC models (that neglect RICC and OICC) and RICC models (that neglect PICC) both produce poor results because PICC, RICC, and OICC are all likely contributors. Including PICC, RICC, and OICC in a single closure model should provide a better description of threshold closure behavior. The primary objective concerning extrinsic R effects is to develop an analytical closure model including PICC, RICC, and OICC. This model (called the PRO closure model, for **P**lasticity, **R**oughness, and **O**xide) is developed in Chapter 3.

The most likely intrinsic R mechanisms are void and microcrack formation in the crack-tip process zone (see left side of Figure 2.2). In the unstable FCG regime (characterized by high ΔK and K_{max} approaching K_c), localized fracture events, called static modes, have been proposed as an intrinsic effect [17]. (Static modes were introduced in Section 1.6.3.) It is not known if static modes, or similar mechanisms, can occur at FCG threshold. If so, these intrinsic mechanisms are believed more likely at K_{max} levels approaching the fracture toughness. Because these intrinsic effects may be limited to high K_{max} levels, they are also called "K_{max} effects." In most engineering alloys, intrinsic R effects are small when compared to the influence of crack closure (extrinsic effects). However, observations by Marci and Lang, *et al*., suggest this may not always be true [18, 19]. Because little is known about intrinsic R effects, the primary objective here is to identify and characterize intrinsic load ratio mechanisms. After specific intrinsic mechanisms have been identified and studied, a model will be developed to describe the influence on closure-free threshold FCG. The results of this study and subsequent crack-tip damage model are presented in Chapter 4.

2.3 — TECHNICAL APPROACH

Existing RICC models have used a two-dimensional sawtooth profile to idealize rough crack surfaces [14, 32]. This configuration provides a reasonable approximation of rough crack geometry and simplifies geometric conditions of crack closure. Most RICC models include plastic mode II crack face displacements to create asperity mismatch upon unloading, but neglect both plastic mode I displacements and crack wake plasticity. These restrictions are not placed on PICC models. Because existing analytical RICC and PICC models consider crack-tip plasticity differently, none works well for both threshold and Paris FCG. To produce a better threshold crack closure model, existing RICC models will be modified to include crack-tip plasticity in a manner consistent with accepted PICC models. A uniform oxide layer along the crack faces will be considered to include OICC. This model, called the PRO closure model (for **P**lasticity, **R**oughness, and **O**xide), will allow closure to be dominated by PICC for Paris FCG, and by RICC for

threshold FCG. The transition between Paris FCG (PICC-dominant) and threshold FCG (RICC-dominant closure behavior) will be handled automatically by the PRO model because the same criteria will be used to describe crack-tip events for all ΔK. If successful, this model will also indicate the nature of interactions between closure mechanisms. Whether these three closure mechanisms (PICC, RICC, and OICC) interact in a linear or non-linear manner, the PRO model should produce a better and more complete description of threshold crack closure.

Not much is known about intrinsic load ratio effects on threshold FCG. In contrast to extrinsic load ratio effects (fatigue crack closure), specific intrinsic mechanisms are not well established. The most likely intrinsic mechanisms are void and microcrack damage ahead of the crack-tip. Thus, the research on intrinsic load ratio effects will focus on identifying intrinsic load ratio mechanisms in aluminum alloys. A model can only be developed after specific mechanisms have been identified and studied. Constant K_{max} threshold tests will be performed on three aluminum alloys to study closure-free threshold FCG. Because fatigue crack closure is eliminated from constant K_{max} tests, intrinsic load ratio effects can be isolated. Evidence of voids, microcracks, or any other type of crack-tip damage should be seen on the fatigue crack surfaces. Identification of intrinsic mechanisms depends on how well crack surface features can be correlated with increasing K_{max} or R. A model will be developed to predict intrinsic load ratio effects on FCG based on these experimental observations. Special consideration will be given to any unusual threshold FCG behavior found in aluminum alloys. Determining a mechanism for any unusual behavior may indicate if the threshold FCG behavior of Marci and Lang is limited to a few alloys with curious material properties, or a more general phenomenon occurring in many alloys.

2.4 — PITFALLS TO AVOID

Many testing variable influence threshold FCG, including load ratio, environment, residual stresses, and load history effects [5, 6, 28]. Although, the scope of this research is limited to load ratio effects on threshold FCG, a more complete understanding of threshold behavior is important to isolate the influence of load ratio from many other variables. The effects of environment (specifically, water vapor or humidity in laboratory air) and load history are considered most likely to affect the FCG data presented in this dissertation. Experiments were designed to avoid, or minimize the effects of, environment and load history effects during FCG testing.

PART II - Research

CHAPTER 3 — FATIGUE CRACK CLOSURE MODEL

An analytical threshold fatigue crack closure model is developed, including three closure mechanisms (PICC, RICC, and OICC), crack meandering, and multi-axial loading. This model is called the "PRO" closure model (for **P**lasticity, **R**oughness, and **O**xide). Rough crack surfaces are modeled as two-dimensional sawtooths that produce mixed-mode crack-tip loads. Continuum mechanics and crack-tip dislocation concepts are used to calculate elastic and plastic crack face displacements. Simple geometric criteria are used to determine closure levels in terms of crack face displacements. Model predictions are verified with finite element results and experimental data.

3.1 — INTRODUCTION

Fatigue crack closure occurs when crack faces contact during cyclic loading. The three closure mechanisms considered most important at threshold are PICC, RICC, and OICC, and were introduced in Section 1.6.2. More detailed descriptions of crack closure mechanisms and models are presented in Section A.2. Descriptions of existing closure models, most significant to the PRO closure model developed here, are given in the following paragraph.

Simple, two-dimensional, geometric, RICC models have been developed by Suresh and Ritchie [14], and Wang, *et al*. [32]. Suresh and Ritchie were among the first to model rough cracks as a two-dimensional sawtooth. The non-planar geometry of rough cracks produces mixed-mode (I and II) crack face displacements. As modeled, a permanent mode II displacement (determined empirically) occurs during loading. As the crack is unloaded, the resulting mismatch of crack face features (asperities) produces RICC. In the Wang model, mode II displacements were calculated by modifying a crack-tip slip model developed for a mode II straight crack [33]. Wang assumed slip was limited to a single slip plane coinciding with the crack-tip direction. This configuration allows only sliding mode plastic displacements, although mixed-mode crack-tip stresses exist. Budiansky and Hutchinson developed an analytical PICC model, where the plastic stretch in the crack wake was related to the crack-tip opening displacement (CTOD) [34]. A value less than the maximum CTOD was used to account for reverse plasticity during unloading. Suresh and Ritchie developed an analytical OICC model, where an oxide layer was considered as a uniform rigid wedge terminating a finite distance behind the crack-tip in an elastic body [31]. Closure levels are determined by comparing elastic crack opening displacements with the oxide thickness. Because only elastic crack face displacements are considered (which is not realistic), predicted closure levels become infinite if even a small oxide layer is considered at the crack-tip.

The objective here is to develop an analytical fatigue crack closure model (the PRO model) including the contributions and interactions of PICC, RICC, and OICC. Because crack face contact is the event of interest, it is necessary to characterize crack face displacements of rough cracks. Although not limited to FCG threshold, special attention is given to threshold applications.

3.2 — MODEL DEVELOPMENT

Step by step development of the PRO closure model is presented here. Consideration of three closure mechanisms (RICC, PICC, and OICC) are discussed separately. Solutions for crack face displacements are developed and used to compute crack closure loads.

3.2.1 — Consideration of RICC and crack meandering

Rough crack surfaces are modeled here as a sawtooth wave (*i.e.* a series of two-dimensional, rigid, triangular asperities, of equal size and shape) similar to the geometry of existing closure models [14, 32, 35-37]. A schematic of this sawtooth crack profile is shown in Figure 3.1a. Characteristic roughness parameters (asperity length, g, and asperity angle, α) should be obtained from real crack surfaces, or related to microstructural features, *e.g.* grain size. The sawtooth geometry is desirable because it is a reasonable approximation for most rough crack surfaces, and simplifies the geometric conditions of crack face contact. This configuration is further modified to consider crack meandering (a macroscopic deviation from global coordinates) as shown in Figure 3.1b.[9] Three coordinate systems are required to describe the crack geometry in Figure 3.1b.

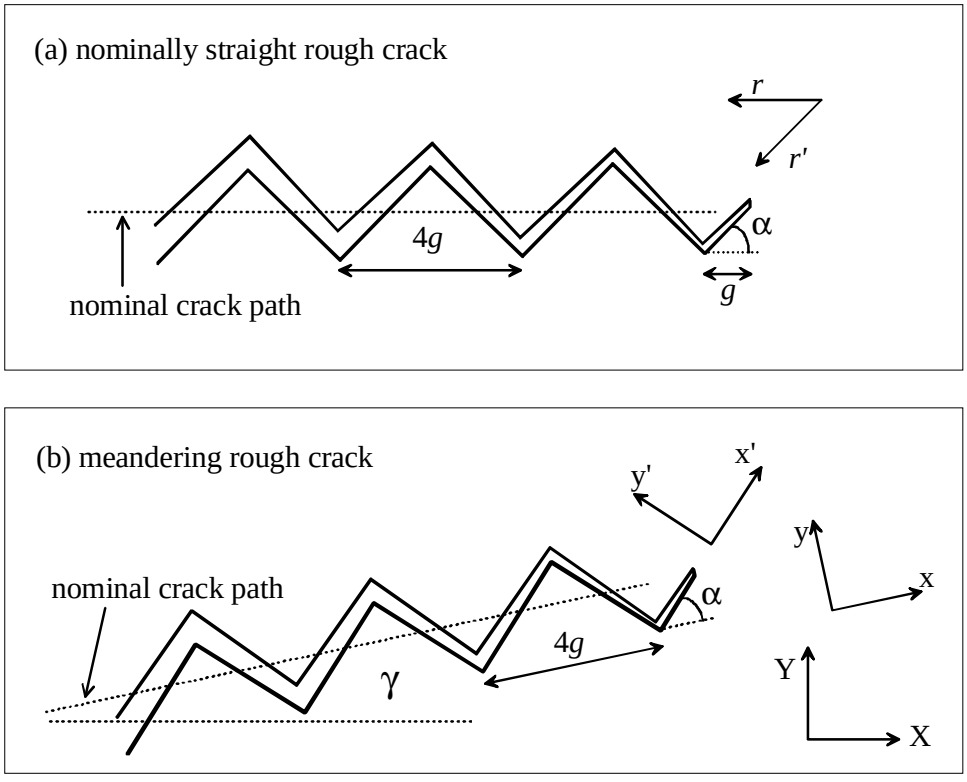

Figure 3.1 – Idealized two-dimensional crack profiles. A schematic of the sawtooth configuration used in previous models is shown in part (a). For this model, the sawtooth is allowed to meander, as shown in part (b).

[9] ASTM standards permit neglecting a meandering angle, γ, less than 10^o, and FCG data for $10^o < \gamma < 20^o$ is considered valid, but crack meandering must be reported [4].

First, a “global” coordinate frame is used to describe loading or specimen geometry, and from which crack meandering is measured. The global coordinate frame is labeled by X and Y in the figure. Next, a “local” coordinate frame is needed. The x-axis of the local coordinate frame coincides with the nominal crack direction (average direction of FCG from a macroscopic point of view). This coordinate frame is labeled in Figure 3.1b by x and y. Finally, a “crack-tip” coordinate frame is needed, whose x-axis coincides with the orientation of the crack-tip on a microscale. As shown in Figure 3.1b, the crack-tip coordinate frame is labeled by x' and y'. When considering crack closure of rough cracks (in Sections 3.3 and 3.4), it will be convenient to describe crack face displacements using both “local” and “crack-tip” coordinates.

3.2.2 — Stress intensity factors

Two crack configurations, for which analytical solutions are considered, are shown in Figure 3.2; (a) an angled straight crack and (b) an angled, infinitesimal kink at the tip of an otherwise straight crack. Both configurations are subject to far-field loading (*i.e.* remote applied stress). These two configurations are the basis for modeling rough meandering cracks. The angled straight crack of Figure 3.2a is used to approximate crack meandering effects on crack-tip stresses. To obtain stress intensity factors for meandering cracks, applied loads (global coordinates) are transformed to local coordinates. The transformed stresses are used to calculate local stress intensity factors in Equations 3.1a and 3.1b, where $K_{Ig} = \sigma_Y\sqrt{\pi a}$, $K_{IIg} = \tau_{XY}\sqrt{\pi a}$, and $K_{Og} = \sigma_X\sqrt{\pi a}$. K_{Og} accounts for non-singular stresses parallel to cracks that contribute to the singularity upon meandering [38]. Note that $2a$ is defined as the crack length projected onto the plane perpendicular to σ_Y. The actual crack length is $2a/\cos(\gamma)$.

$$K_{I\,Local} = K_{Ig}\sqrt{\cos(\gamma)} - 2K_{IIg}\sin(\gamma)\sqrt{\cos(\gamma)} + K_{Og}\left[\frac{\sin^2(\gamma)}{\sqrt{\cos(\gamma)}}\right] \qquad (3.1a)$$

$$K_{II\,Local} = K_{Ig}\sin(\gamma)\sqrt{\cos(\gamma)} - K_{IIg}\left[\frac{\cos^2(\gamma)}{\sqrt{\cos(\gamma)}}\right] - K_{Og}\sin(\gamma)\sqrt{\cos(\gamma)} \qquad (3.1b)$$

The stress intensity factors for a straight crack with an infinitesimal kink (see Figure 3.2b) are used to approximate stress intensity factors for rough (sawtooth) cracks. These relations are given as Equation 3.2, but are valid only if the kink length, δa, is small compared to the K-dominated region at the crack-tip [39]. It will be shown (in Section 3.3) that Equation 3.2 is also valid for sawtooth cracks. Note that local stress intensity factors are used in Equation 3.2. Substitution of Equation 3.1 into Equation 3.2 allows simultaneous consideration of crack roughness and meandering. As schematically shown in Figure 3.2c, the angled straight crack solutions are used first to determine the effect of crack meandering. Then, crack roughness effects are determined from Equation 3.2. The stress intensity factors are expressed in terms of globally applied stress intensity factors because these quantities are normally used to describe FCG tests.

$$K_I = K_{I\,Local}\cos^3\left(\frac{\alpha}{2}\right) - 3K_{II\,Local}\sin\left(\frac{\alpha}{2}\right)\cos^2\left(\frac{\alpha}{2}\right) \qquad (3.2a)$$

$$K_{II} = K_{I\,Local}\sin\left(\frac{\alpha}{2}\right)\cos^2\left(\frac{\alpha}{2}\right) + K_{II\,Local}\cos\left(\frac{\alpha}{2}\right)\left[1 - 3\sin^2\left(\frac{\alpha}{2}\right)\right] \qquad (3.2b)$$

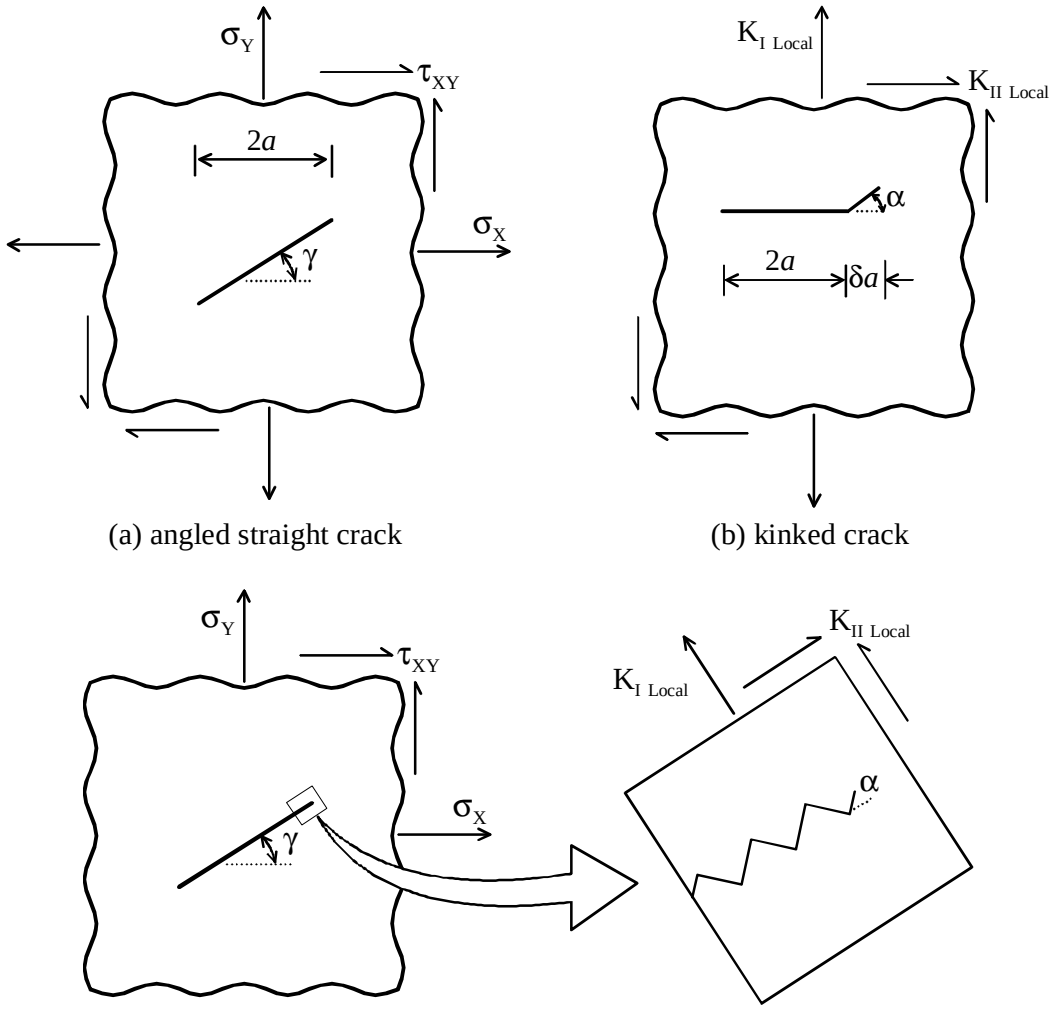

(a) angled straight crack

(b) kinked crack

(c) simultaneous application

Figure 3.2 – Schematics of two crack configurations for which analytical solutions are used; (a) an angled, straight crack and (b) a straight crack with a kinked crack-tip. A schematic illustrating the simultaneous application of these solutions is shown in part (c).

3.2.3 — Elastic crack face displacements

Elastic displacements are functions of the crack-tip stress intensity factors determined in the previous section. Because all rough cracks are subjected to a mixed-mode stress state, both opening and sliding mode crack face displacements are expected. Sliding mode displacements are needed to create misalignment of crack face asperities upon unloading, *i.e.* RICC. Elastic crack face displacements for straight cracks with mixed-mode loading (I and II) are shown in Equation 3.3, where E is the elastic modulus, ν is Poisson's ratio, and r' is the distance behind the crack-tip (see Figure 3.1a) [40]. (Primed quantities indicate use of crack-tip coordinates.) Note that $r' = r / \cos\alpha$ and the total relative displacements between the two crack faces are $2u'$ and $2v'$. For now, this relation is assumed valid in the crack-tip vicinity. It will be shown in Section 3.3 that this assumption is acceptable. The crack face displacements of Equation 3.3 are expressed in crack-tip coordinates, but can be described by local coordinates using the transformations of Equation 3.4. Local coordinates will be convenient when considering crack closure.

$$\begin{Bmatrix} u' \\ v' \end{Bmatrix} = \left[\frac{4\left(1-\nu^2\right)}{E} \sqrt{r'/2\pi} \right] \begin{Bmatrix} K_{II} \\ K_I \end{Bmatrix} \tag{3.3}$$

$$\begin{Bmatrix} u \\ v \end{Bmatrix} = \begin{bmatrix} \cos(\alpha) & -\sin(\alpha) \\ \sin(\alpha) & \cos(\alpha) \end{bmatrix} \begin{Bmatrix} u' \\ v' \end{Bmatrix} \tag{3.4}$$

3.2.4 — Consideration of crack-tip plasticity and PICC

As a cracked body is loaded, a plastic zone forms at the crack-tip [2, 41]. Crack-tip plasticity for mixed-mode loading will produce a crack-tip opening displacement (CTOD) and a crack-tip sliding displacement (CTSD).[10] Existing crack-tip slip models [33, 42] are modified to estimate plastic displacements of a mixed-mode crack-tip. On a microscale, plasticity is the result of dislocation glide originating near the crack-tip [43]. Near the crack-tip, dislocation pairs of opposite sign are created. Dislocations of one sign are attracted to the crack-tip, where they are annihilated, producing plastic strains. Dislocations of the opposite sign are driven away from the crack-tip. Ultimately, these dislocations will either (1) stop at a barrier, such as a particle interface or grain boundary [44-46], or (2) go far from the crack-tip where a reduction in dislocation driving force (stress) occurs [33, 43]. For the model developed herein, slip is assumed to occur by edge dislocations that glide freely along slip paths until reaching the edge of the plastic zone, which acts as a Peierls-Nabarro energy barrier. As in previous crack-tip dislocation emission models, dislocations are assumed to travel along planes originating at the crack-tip.[11] The plane-strain plastic zone radius is shown in Equation 3.5a, as a function of angle from the crack plane, θ [47]. Plane-strain conditions were adopted because the

[10] In general, CTOD and CTSD include both elastic and plastic components. However, Equation 3.3 indicates no elastic displacement exists at the crack-tip. For this model, CTOD and CTSD describe only plastic crack-tip displacements.

[11] Slip is described as occurring on planes whose projection into the two-dimensional model is a line. However, the phrase "slip plane" is used to be consistent with existing literature [48].

PRO model is intended for threshold applications. Equation 3.5a assumes no redistribution of stress due to crack-tip plasticity. Rather, this radius is that of the elastic solution whose vonMises equivalent stress corresponds to yielding. The increase in plastic zone due to stress redistribution was accounted for by increasing the plastic zone of Equation 3.5a by a factor of 1.828 (see Equation 3.5b). This constant was chosen such that the CTOD (which will be calculated using Equation 3.9a) for a straight crack matched the theoretical value (K^2 / E σ_o). This relation is used to determine the monotonic plastic zone (MPZ) associated with K_{max}.[12]

$$r_p^* = \frac{1}{2\pi\sigma_o^2}\left[\begin{array}{c} K_{I\,Local}^2\left\{\cos\left(\frac{\theta}{2}\right)\left[3\sin^2\left(\frac{\theta}{2}\right)+(1-2\nu)^2\right]\right\} \\ +K_{II\,Local}^2\left\{3+\sin^2\left(\frac{\theta}{2}\right)\left[(1-2\nu)^2-9\cos^2\left(\frac{\theta}{2}\right)\right]\right\} \\ +K_{I\,Local}K_{II\,Local}\sin(\theta)\left[3\cos(\theta)-(1-2\nu)^2\right] \end{array}\right] \qquad (3.5a)$$

$$r_p = 1.828\, r_p^* \qquad (3.5b)$$

It is recognized that slip occurs along preferred slip planes that depend on microstructure and local shear stress (acting on these planes). However, it is assumed that slip planes (on average) coincide with planes of extrema in elastic crack-tip shear stress, $\tau_{r\theta}$. This combination of dislocation emission and continuum mechanics is likely valid if crack-tip deformation occurs in multiple grains. This is discussed further in Section 6.1.3. The elastic, singular crack-tip stresses for mixed-mode loading under plane-strain conditions are given in Equation 3.6. The directions of shear extrema, θ_i, satisfy Equation 3.7 (which is obtained by setting the derivative of $\tau_{r\theta}$, with respect to θ, to zero). This equation is transcendental and must be solved numerically, *i.e.* no closed form solution exists for θ_i. Equation 3.7 has three roots, except for straight cracks under pure mode I loading that have only two roots. A plot of the singular shear stress coefficient ($\tau_{r\theta}$ multiplied by $\sqrt{2\pi r}$) versus angle from the crack-tip direction is shown in Figure 3.3a for a crack configuration described by $\alpha = 45^o$, $\gamma = 10^o$, $K_{Ig} = 1$, and $K_{IIg} = 0$. The three local extrema are indicated by vertical dotted lines and labeled in Figure 3.3a. A schematic of the corresponding plastic zone (calculated by Equation 3.5) is shown in Figure 3.3b. Each slip plane indicated in Figure 3.3a is shown in Figure 3.3b as solid lines emanating from the crack-tip. Although the extrema of crack-tip shear do not exactly coincide with extrema in plastic zone radius, the two differ by less than 30^o.

[12] The MPZ is the crack-tip region where plasticity occurs during loading, and is associated with K_{max}. The cyclic plastic zone (CPZ), a subset of the MPZ where reverse plasticity occurs during unloading, is associated with ΔK. The CPZ will be discussed later.

$$\begin{Bmatrix}\sigma_r\\ \sigma_\theta\\ \tau_{r\theta}\end{Bmatrix} = \frac{K_I}{\sqrt{2\pi r}}\cos\left(\frac{\theta}{2}\right)\begin{Bmatrix}1+\sin\left(\frac{\theta}{2}\right)\\ \cos^2\left(\frac{\theta}{2}\right)\\ \sin\left(\frac{\theta}{2}\right)\cos\left(\frac{\theta}{2}\right)\end{Bmatrix} + \frac{K_{II}}{\sqrt{2\pi r}}\begin{Bmatrix}\sin\left(\frac{\theta}{2}\right)\left[1-3\sin^2\left(\frac{\theta}{2}\right)\right]\\ -3\sin\left(\frac{\theta}{2}\right)\cos^2\left(\frac{\theta}{2}\right)\\ \cos\left(\frac{\theta}{2}\right)\left[1-3\sin^2\left(\frac{\theta}{2}\right)\right]\end{Bmatrix} \qquad (3.6)$$

$$K_I\left[1-3\sin^2\left(\frac{\theta_i}{2}\right)\right] = K_{II}\tan\left(\frac{\theta_i}{2}\right)\left[7-9\sin^2\left(\frac{\theta_i}{2}\right)\right] \qquad (3.7)$$

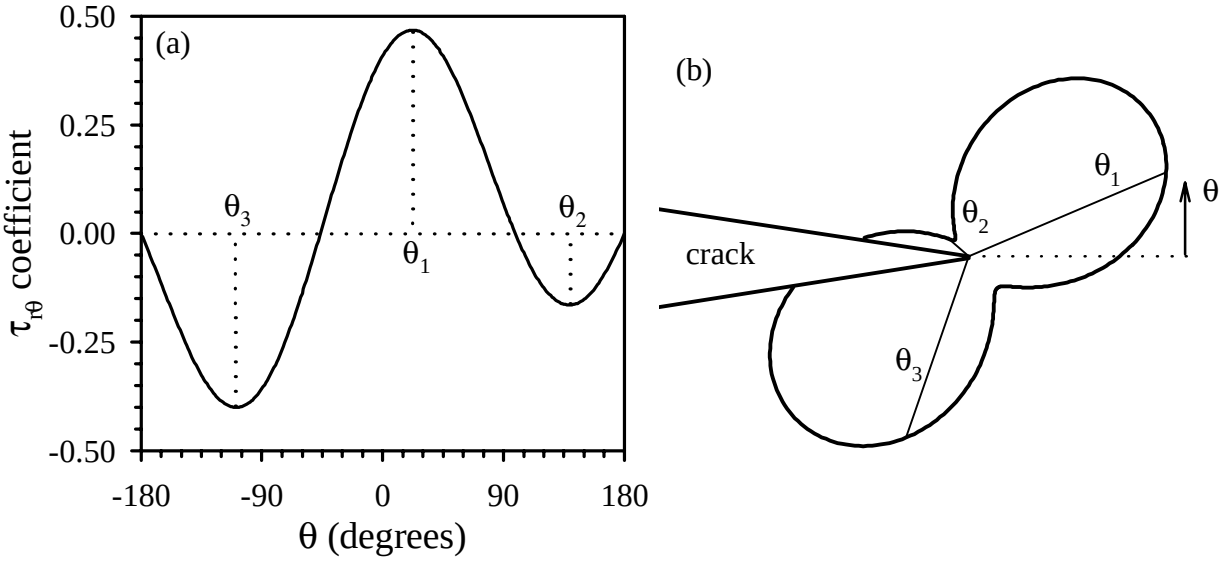

Figure 3.3 – Plot of singular shear stress, $\tau_{r\theta}$, and corresponding plastic zone. In part (a) a plot of the singular shear stress is given, as a function of θ, for $\alpha = 45^o$, $\gamma = 10^o$, $K_{IIg} = 0$. A schematic of the corresponding plastic zone is given in part (b).

The dislocation distribution along individual slip planes has been solved assuming a constant shear stress in the plastic zone (*e.g.* assuming elastic-perfectly plastic behavior at the crack-tip, use $\tau = 0.5\ \sigma_o$) and no interaction between slip planes. The total slip along a slip plane of length B is given by Equation 3.8, where μ is the shear modulus ($\mu = E / 2(1+\nu)$), ν is Poisson's ratio, n is the total number of edge dislocations, and b is the magnitude of the Burger's vector [49].

$$B = nb = \frac{r_p \tau\pi(1-\nu)}{\mu} \qquad (3.8)$$

Using this relation, plastic crack-tip deformations (CTOD′ and CTSD′) are computed by summing the vector components of each slip plane (in crack-tip coordinates) as shown in

Equation 3.9. (Again, primed quantities correspond to crack-tip coordinates.) The symbol Σ indicates summation over the range of the index 'i', which ranges from one to three (the total number of slip planes).[13] Conversion to local coordinates involves the same transformation given in Equation 3.4.

$$CTOD' = \sum B_i \sin\theta_i \tag{3.9a}$$

$$CTSD' = \sum B_i \cos\theta_i \tag{3.9b}$$

The cyclic plastic zone (CPZ) is a subset of the MPZ, where reverse plasticity occurs during unloading. The size of the CPZ is proportional to ΔK^2, and the shape can be calculated using Equation 3.5a, by inserting one-half of the cyclic stress intensity factors in place of the maximum values (*e.g.* $K_{I\,Local}$ is replaced by $\frac{1}{2}\,\Delta K_{I\,Local}$). Reversed plasticity in the CPZ leads to a reduction in residual CTOD and CTSD. For modeling purposes, reversed slip is assumed to occur along the same slip planes as for loading, but using the CPZ boundary as maximum slip length and replacing τ in Equation 3.8 with $-\tau$. Because the MPZ and CPZ radii are proportional to $(K_{max})^2$ and $\frac{1}{2}(\Delta K)^2$, respectively, CTOD and CTSD are also a function of K_{max} and ΔK, as in Equation 3.10. The subscript 'max' corresponds to maximum values of that quantity, which occur at maximum load.

$$\begin{Bmatrix} CTOD \\ CTSD \end{Bmatrix} = \left[1 - \left(\frac{\Delta K}{2K_{max}}\right)^2\right] \begin{Bmatrix} CTOD_{max} \\ CTSD_{max} \end{Bmatrix} \tag{3.10}$$

Although RICC and OICC are most significant at FCG threshold, PICC is still a major contributor and must be considered [50, 51]. Thus, a complete discussion of crack plasticity must include residual crack wake deformation. A PICC model by Budiansky and Hutchinson [34] relates residual plastic deformation to the CTOD. A value less than $CTOD_{max}$ (the CTOD at maximum load) is considered to account for reversed crack-tip plasticity during unloading. For R = 0, the residual wake was calculated as approximately 86% of $CTOD_{max}$, or $\xi = 0.86$. The crack wake compression factor, ξ, is defined in Equation 3.11a, where $CTOD_{wake}$ is the total residual plastic wake (half associated with each crack face). The relation between $CTOD_{max}$ and $CTOD_{wake}$ is shown schematically in Figure 3.4a. Here, a straight crack is shown under load with a blunted crack-tip. The residual crack wake plasticity is indicated by shaded regions along each crack face. Although plastic deformation partially fills the crack mouth in this schematic, the crack is shown open, *i.e.* no contact at the crack-tip. Using results from Budiansky and Hutchinson (open circular symbols), a plot of ξ versus applied R ($R_{applied}$) is shown in Figure 3.4b along with a least squares fitted (4^{th} order) polynomial. This fitted polynomial is expressed symbolically in Equation 3.11b, and is used to estimate ξ as a function of $R_{applied}$. Using Equation 3.11b instead of the entire procedure developed by Budiansky and Hutchinson simplifies evaluation of the PRO closure model.

[13] Recall, only two slip planes exist for a straight crack (*i.e.* $\alpha = 0$), so 'i' ranges from 1 to 2 in this case.

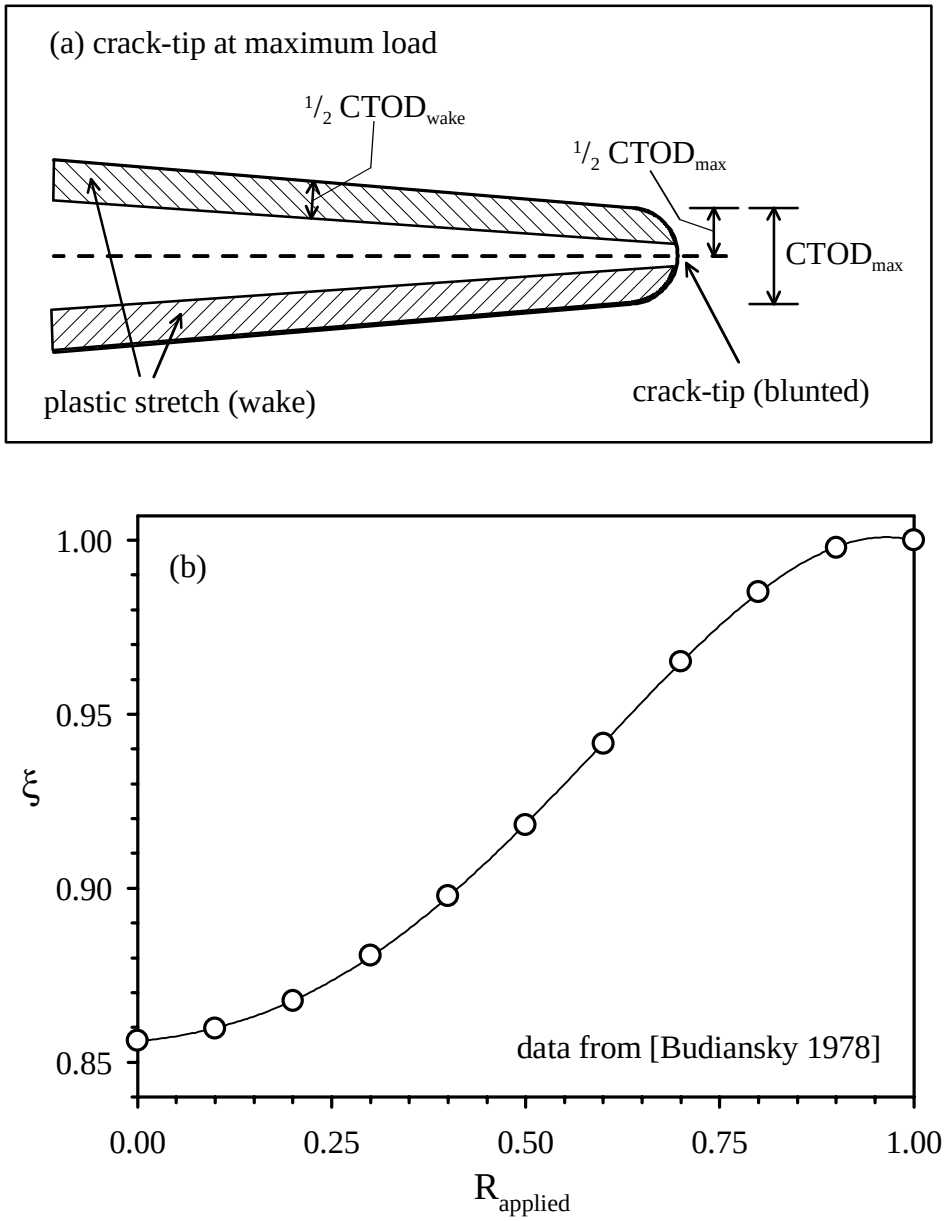

Figure 3.4 – Definition of the crack wake compression factor, ξ. The crack wake compression factor, ξ, is schematically shown in part (a) for a straight crack. A plot of ξ versus $R_{applied}$, obtained from Budiansky and Hutchinson, is shown in part (b).

$$\xi = \frac{CTOD_{wake}}{CTOD_{max}} \tag{3.11a}$$

$$\xi = 0.8561 + 0.0205 \cdot R_{applied} + 0.1438 \cdot R_{applied}^{\,2} + 0.2802 \cdot R_{applied}^{\,3} - 0.3007 \cdot R_{applied}^{\,4} \tag{3.11b}$$

3.2.5 — Consideration of OICC

An oxide layer in the crack mouth was modeled as a rigid wedge of uniform thickness (t) along both crack surfaces. The voluminous oxide layer partially fills the crack mouth, increasing closure levels. Because the available crack opening is small at low values of K_{max}, an oxide layer of finite thickness will produce higher closure levels than at higher values of K_{max}. Consequently, OICC is thought to be most significant near the FCG threshold [52]. Naturally forming oxide layers on fresh aluminum surfaces have been measured as 10 Å thick in dry air [53], and between 50 Å and 150 Å in humid air [31], although considerable variation with environment and temperature was noted. Fretting contact of rough crack surfaces (*i.e*. RICC) can create a large amount of oxide debris, a result of repeated removal and regeneration of crack face oxide [52]. Large amounts of oxide debris may also form in aggressive (oxide producing) environments [9], where the effective oxide thickness can be much larger: up to 1000 Å in moist air for aluminum alloys [52] and 3-5 μm for steels [54]. Although this model assumes a uniform oxide layer on the crack faces, modification can be made to simulate oxide debris (non-uniform). For example, oxide debris generated by fretting asperities may accumulate behind the crack-tip. Oxide debris are normally thicker than the undisturbed oxide layer, expected at the crack-tip. In this case, closure can be determined separately, at the location of the oxide debris and at the crack-tip, using different oxide thicknesses. The location with the largest closure load will contact first and dominate crack-tip behavior.

3.3 — NUMERICAL VERIFICATION OF STRESS INTENSITY FACTORS AND CRACK FACE DISPLACEMENTS

Finite element analyses were performed to validate crack-tip stress intensity and displacement solutions (Equations 3.2 and 3.3) for a sawtooth crack (Figure 3.1a). The projected kink length, g, and the kink angle, α, were varied for the sawtooth configuration. Both mode I and mode II cases were examined, but results are only presented here for the mode I case ($K_{IIg} = 0$).[14] The finite element simulations, described herein, were performed using FRANC2D [55]. Stress intensity factors were extracted from the elastic solutions using the J-integral technique [56]. A typical deformed (grossly exaggerated) mesh used for these analyses is shown under global mode I loading in Figure 3.5, where higher magnification images of the crack-tip region are shown. Taking advantage of symmetry (for mode I loading) only half of a specimen is analyzed, as shown. Symmetry is enforced with appropriate boundary conditions. Arrows point to higher magnification images of the crack-tip region in the figure. The mesh shown in the figure is for $\alpha = 45^o$ and $g/a = 0.05$. A rosette of singular quarter-point elements is inserted around the crack-tip. The rest of the body is meshed with three or four sided quadratic elements. As seen in Figure 3.5, the mesh is refined near the crack-tip. At least four elements were used between the crack-tip and the first asperity behind the crack-tip, regardless of the kink length, g. Further refinement of the crack-tip region did not significantly affect results. The sawtooth wave was extended to form at least 10

[14] Crack face displacements for mode II loading is discussed in Section 6.1.2. Although the PRO model allows some mode II loading, it will be shown later that it is restricted to cases where mode I loading dominates.

complete asperities behind the crack-tip, or to the specimen centerline. The remaining crack profile was modeled as a straight line. Further extension of asperities along the crack surface did not affect results.

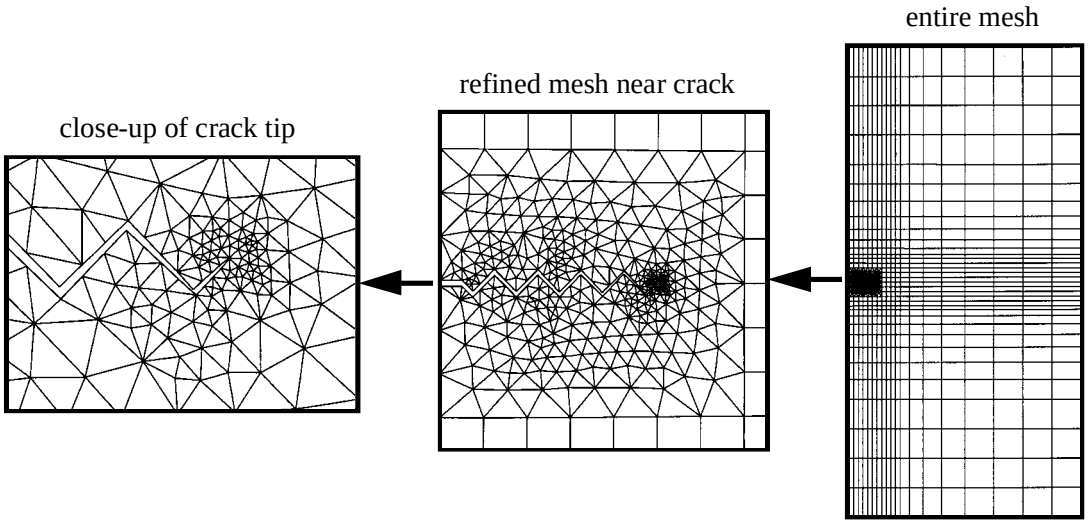

Figure 3.5 – Typical (deformed) mesh used for finite element analyses. Taking advantage of symmetry, for the nominally mode I case, only half of a specimen is analyzed, as shown, and symmetry is enforced with appropriate boundary conditions. Arrows point to higher magnification images of the crack-tip region. For this mesh, $\alpha = 45^o$ and $g/a = 0.05$.

Stress intensity factors obtained from finite element analyses are plotted in Figure 3.6 for asperity angles (α) ranging from 0^o to 45^o, and for normalized asperity length (g/a) ranging from 0.2 to 0.002. K_I results are shown in Figure 3.6a, while K_{II} results are plotted in Figure 3.6b. Finite element results are shown as open symbols, while analytic solutions of angled straight cracks ($g/a = 1$) and kinked crack-tips ($g/a = 0$) are shown as closed symbols. Refer to the legend in the upper left corner of the figure to determine the symbols corresponding to specific values of α. This crack configuration is shown schematically in the upper right corner of the figure. A break in the x-axis is used to show analytical results for straight angled cracks. As normalized asperity length (g/a) approaches zero, the numerical results of a sawtooth crack converge to the kinked crack solutions. This result validates the use of Equations 3.2 for $g/a < 0.05$. Similar agreement between finite element and analytical solutions were obtained for mode II loading, but results are not presented here.

Numerical elastic crack face displacements are plotted against r/g (normalized distance behind the crack-tip) in Figure 3.7 for asperity angles of (a) 30^o and (b) 45^o. Note that all quantities are presented in dimensionless form where appropriate. Dimensionless values for crack face displacements (u^* and v^*) are defined in the upper right corner of the figure. Results for two values of g/a (0.1 and 0.01) are shown as open symbols (circular and square, respectively). Dashed and solid lines correspond to analytical elastic solutions of sliding and opening mode displacements predicted by Equation 3.3

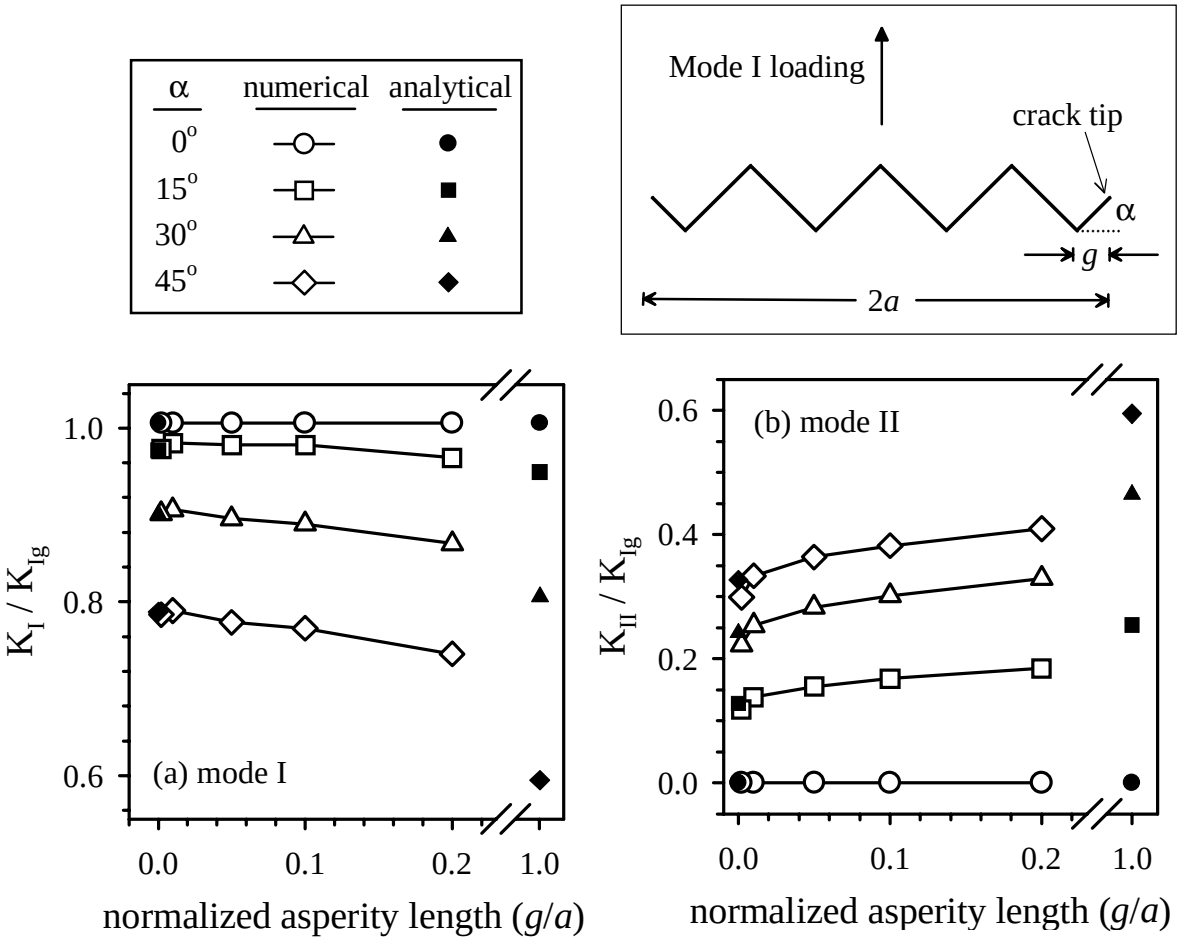

Figure 3.6 – Stress intensity factors for sawtooth cracks under mode I loading (K_{Ig}) for asperity angles $\alpha = 0^o$, 15^o, 30^o, and 45^o.

(transformed to local coordinates), respectively. The dotted line corresponds to the opening displacement expected for a straight crack (*i.e.* $\alpha = 0$) under the same mode I loading. As seen in Figure 3.7, mode II displacements (u^*) match the analytical solution well, but only between the crack-tip and the first asperity behind the crack-tip ($0 < r/g < 1$). Further behind the crack-tip tip ($r/g > 1$), mode II displacements exhibit an oscillatory decay about zero with extreme values corresponding to changes in crack direction, *i.e.* peaks and valleys of the sawtooth. The mode I displacements (v^*) also match the analytical solutions, but far from the crack-tip the numerical solutions approach those expected of a straight crack. The finite element results in Figure 3.7 suggest mode II elastic displacements are greatest, and consequently RICC is most likely to occur, at the asperity nearest the crack-tip. This observation is consistent with finite difference results of Llorca, who reported that the maximum sliding mode displacements occurred at asperity peaks and valleys [35]. However, the significance of the asperity closest to the crack-tip is was not stated by Llorca. This observation implies crack closure is most likely at either the asperity closest to the crack-tip or at the crack-tip. Features further behind the crack-tip are neglected. Similar results for mode II loading, and their implications for sliding mode crack closure, are discussed in Section 5.1.2.

3.4 — EVALUATION OF CLOSURE LEVELS

For rough cracks under applied mode I loading, finite element results reveal that crack face contact might occur at the asperity nearest the crack-tip. However, initial contact is expected at the crack-tip for flat cracks (no roughness) because the elastic displacements are zero. This implies two types of contact are possible for rough cracks; "tip contact" (at the crack-tip) and "asperity contact" (at the asperity nearest the crack-tip). Simple geometric relationships are established here to determine crack closure levels for both types of crack face contact. A schematic of a sawtooth crack with an oxide layer is shown in Figure 3.8, where small boxes enclose the crack-tip and critical asperity (a distance g behind the crack-tip). Open arrows indicate high magnification schematics of these locations at the bottom of the figure. For asperity contact (left side of figure) the total opening and sliding displacements are labeled as ($2v$ + CTOD) and ($2u$ + CTSD), respectively, and oxide layer thickness is indicated (t) as the shaded region. For convenience, local coordinates are used to describe asperity contact. For tip contact (right side of figure), only plastic displacements occur at the crack-tip, so only CTOD′ and t are labeled in the lower right corner of Figure 3.8. (Crack-tip coordinates are used

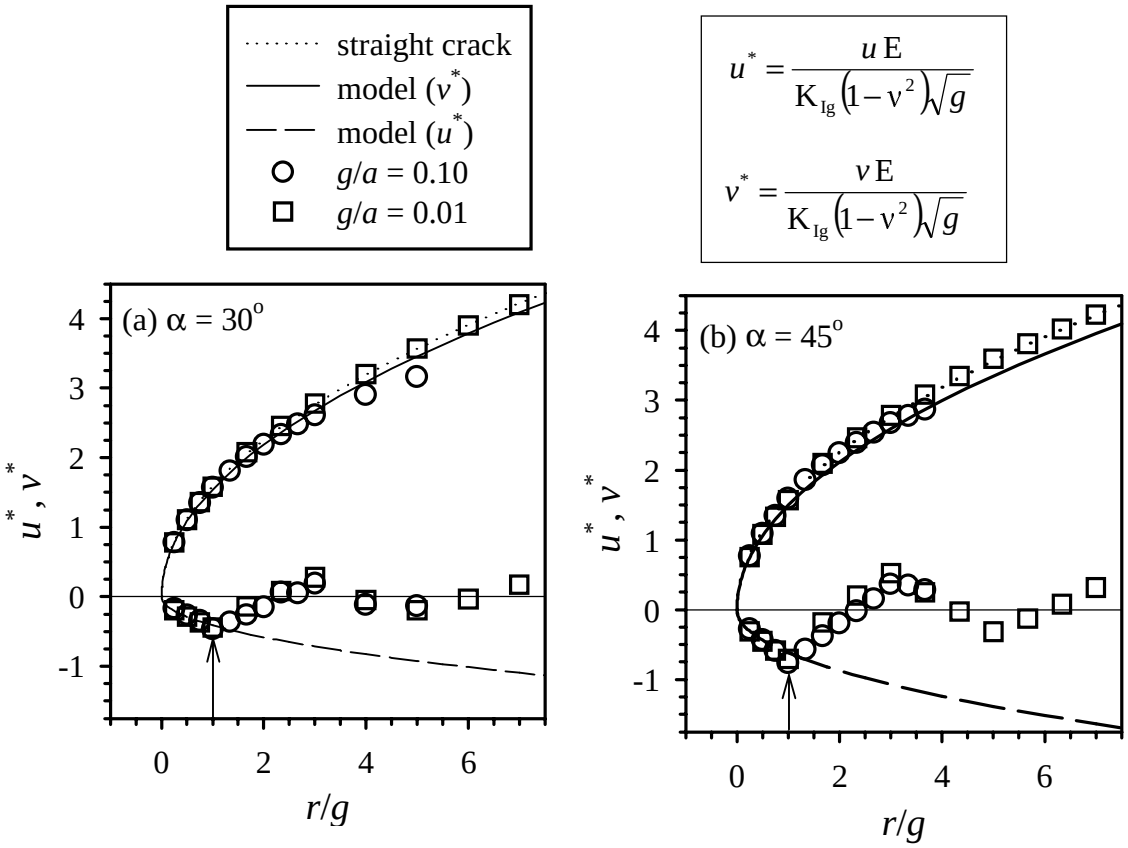

Figure 3.7 – Elastic crack face displacements of sawtooth cracks, plotted against r/g for g/a = 0.10 and 0.01 (indicated by open symbols) for α = (a) 30° and (b) 45°. Solid, dashed, and dotted curves correspond to displacements of Equations 3.4a and 3.4b (model results), and those expected of a straight crack, respectively.

to describe tip contact.) The geometric relations satisfied for asperity contact and tip contact are shown in Equations 3.12a and 3.12b, respectively. The ξ terms in these equations account for residual crack wake plasticity. In Equation 3.12a, the absolute value of the mode II quantity ($2u_{cl}$ + CTSD) is used because sliding mode displacements in either direction promotes closure. Quantities with the subscript 'cl' correspond to values evaluated at crack face contact. Because elastic displacements are proportional to K and plastic displacements depend on K_{max}^2 and ΔK^2 (recall Equations 3.10), all displacements at closure can be expressed in terms of load ratio at closure (R_{cl}) as in Equation 3.13. Substitution of Equation 3.13 into Equation 3.12 allows the closure level, $R_{cl} = K_{cl} / K_{max}$, to be determined at both critical locations.[15] Contact at either location will affect the crack-tip driving force. Therefore, the greater of the two closure levels calculated from Equations 3.12a and 3.12b is used as the R_{cl} affecting crack-tip behavior.

$$\left(2v_{cl} + \mathrm{CTOD}_{cl}\right)\cos(\alpha) - \left|\left(2u_{cl} + \mathrm{CTSD}_{cl}\right)\sin(\alpha)\right| = 2t + \xi\frac{\mathrm{CTOD}_{max}}{\cos(\alpha)} \qquad (3.12a)$$

$$\mathrm{CTOD}_{cl} = 2t + \xi\left(\mathrm{CTOD}_{max}\right)' \qquad (3.12b)$$

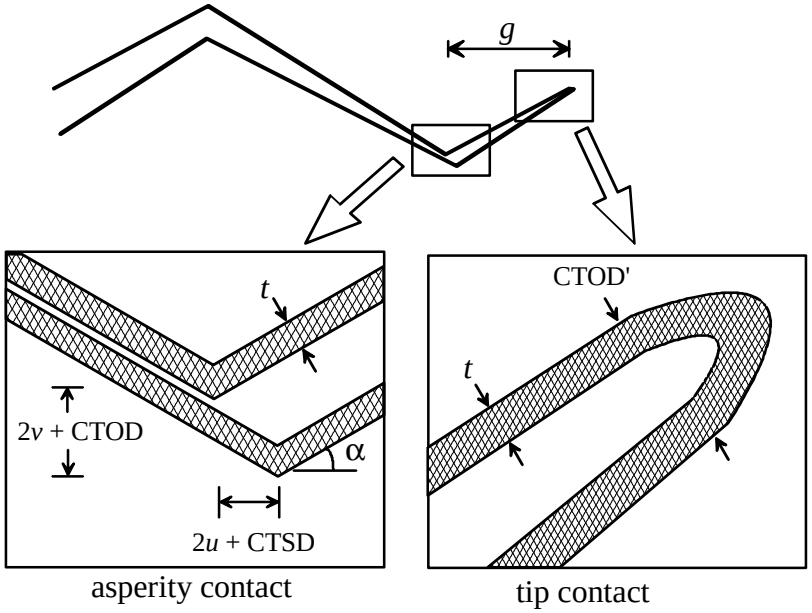

Figure 3.8 – Geometric configuration of crack faces at potential contact points; at the crack-tip and the first asperity behind the crack-tip. A sawtooth crack is schematically shown at the top of the figure. High magnification sketches of the first asperity behind the crack-tip and the crack-tip region are shown at the bottom left and bottom right of the figure, respectively. The shaded region represents an oxide layer.

[15] Throughout this dissertation crack closure is quantified in terms of the value of load ratio at which closure occurs, R_{cl}, (called closure level).

$$\begin{Bmatrix} u_{cl} \\ v_{cl} \end{Bmatrix} = R_{cl} \begin{Bmatrix} u_{max} \\ v_{max} \end{Bmatrix} \tag{3.13a}$$

$$\begin{Bmatrix} CTOD_{cl} \\ CTSD_{cl} \end{Bmatrix} = \left(\tfrac{3}{4} + \tfrac{1}{2} R_{cl} - \tfrac{1}{4} {R_{cl}}^2 \right) \begin{Bmatrix} CTOD_{max} \\ CTSD_{max} \end{Bmatrix} \tag{3.13b}$$

3.5 — MODEL RESULTS

Substitution of Equation 3.13 allows Equations 3.12a and 3.12b to be restated be in terms of R_{cl}. Model results can be obtained (by solving a quadratic equation for R_{cl}) for any set of model parameters. Model parameters (E, σ_o, ν, α, and g) should be tailored to the alloy of interest, and are listed in Table 3.1 for the alloys considered here. For consistency, closure behavior is examined using model parameters for aluminum alloy 2024 unless otherwise indicated. Model predictions for other alloys will be made including several steels. Model results of straight cracks ($\alpha = 0$) and rough cracks ($\alpha \neq 0$) are discussed in separate sections. Where straight crack results are shown, the model parameters α and g are set to zero, instead of the values in Table 3.1. All other parameters are left unchanged. Because threshold FCG is of interest, three low values of K_{max} are used; 2 MPa$\sqrt{m}$, 4 MPa$\sqrt{m}$, and 6 MPa$\sqrt{m}$. Experimental results will be presented in Section 3.6 (to verify model results) which are generated at R = 0.05. Because completely unloading pin-loaded specimens (R = 0) is impractical, model results

Table 3.1 – Model parameters for specific alloys.

Alloy	E (GPa)	σ_o (MPa)	ν	g (μm)	α (degrees)
2024-T3 aluminum	72	350	0.3	10	30
8009 aluminum [1]	88	420	0.3	0	0
Nitinol 50-50 [2]	69	90	0.3	200	22
AISI 1080 steel (CG) [3]	210	410	0.3	74	45
AISI 1080 steel (FG) [3]	210	410	0.3	40.5	45
INCONEL 718 (CG) [4]	200	1410	0.3	9	30
INCONEL 718 (FG) [4]	200	1240	0.3	4	30
Grade E Drill Pipe Steel [5]	210	700	0.3	0	0

[1] Parameters used for both L-T and T-L (from McEvily [57]) orientations.

[2] See Figure D.5a

[3] Data from Gray [58], tested in purified Helium.

[4] Data from Drury [59], tested in laboratory air.

[5] Data from Ruppen [54], in H_2S brine solution.

are presented here for R = 0.05.[16] The computer code used to evaluate model results is listed in Section E.1.

3.5.1 — Straight crack results

Straight cracks (no roughness, $\alpha = 0$) are examined here to evaluate the plasticity and oxide portions of the model before considering roughness. Once the PICC and OICC portions of this model are known to produce good results, additional features (*e.g.* RICC and crack meandering) will be studied. Because straight cracks are examined in this section, only tip contact is considered.

Using results from the PICC model of Budiansky and Hutchinson, the residual plasticity in the crack wake was determined as a function of (applied) load ratio (see Equation 3.11). From this relation closure levels can be determined for straight cracks (without an oxide layer) as a function of ξ. Because no oxide layer is considered, PICC is the only active closure mechanism. A schematic of this crack configuration is shown in the upper left corner of Figure 3.9a. Residual crack wake plasticity is indicated by shaded regions along the crack faces. The crack centerline is shown as a horizontal dashed line. In the schematic the crack is open (no contact at the crack-tip) and under load (the crack-tip is blunted). The closure level is plotted as a function of ξ in Figure 3.9a by the solid curve. Because this discussion is limited to tensile loading, only positive values of R are considered. Although material properties for 2024 aluminum and K_{max} = 5 MPa$\sqrt{m}$ were used, these curves are generic and apply for all straight cracks regardless of material properties or K_{max}. This independence of K_{max} and material properties is evident in Equation 3.12b (for no oxide) because CTOD appears on both sides of the equation (*i.e.* material parameters σ_o and E, and K_{max} cancel out algebraically). As indicated in the upper right corner of the figure, the crack is completely closed (*i.e.* $R_{cl} = 1$) if residual plasticity in the crack wake is equal to $CTOD_{max}$ (*i.e.* $\xi = 1$). As ξ decreases from unity, R_{cl} initially decreases rapidly ($1 > \xi > 0.9$). Although the slope of this curve shallows with decreasing ξ, closure levels continue to decline. At $\xi = 0.75$, closure only occurs when the crack is completely unloaded, *i.e.* $R_{cl} = 0$. Apparently, no closure occurs during tensile loading if $\xi < 0.75$.

Because ξ is related to the applied load ratio, $R_{applied}$, this relation is more meaningful plotted as R_{cl} versus $R_{applied}$, as in Figure 3.9b. The solid curve represents model results. The sloped dotted line corresponds to closure occurring at the minimum load, *i.e.* $R_{cl} = R$. Indicated by labeled arrows in the figure, closure only occurs when the solid curve lies above the dotted line; $R_{applied} < 0.34$. For $R_{applied} > 0.9$, a small degree of closure is predicted, although results shown later (Chapter 4) suggest this does not occur. This high R closure is likely a figment of the polynomial fit in Figure 3.4, and is not considered further.[17] Experimental results for aluminum alloy 8009, tested in laboratory air at ΔK = 6.6 MPa$\sqrt{m}$, are also plotted in Figure 3.9b. Because aluminum alloy 8009 has an ultra-

[16] R = 0.05 is the lowest value of R the computer controlled system used for FCG testing allowed. Model results were generated for this value of R so a direct comparison with experimental results can be made.
[17] The polynomial of Equation 3.11b gives $\xi = 1.0005$ for R = 0.99; an unlikely result.

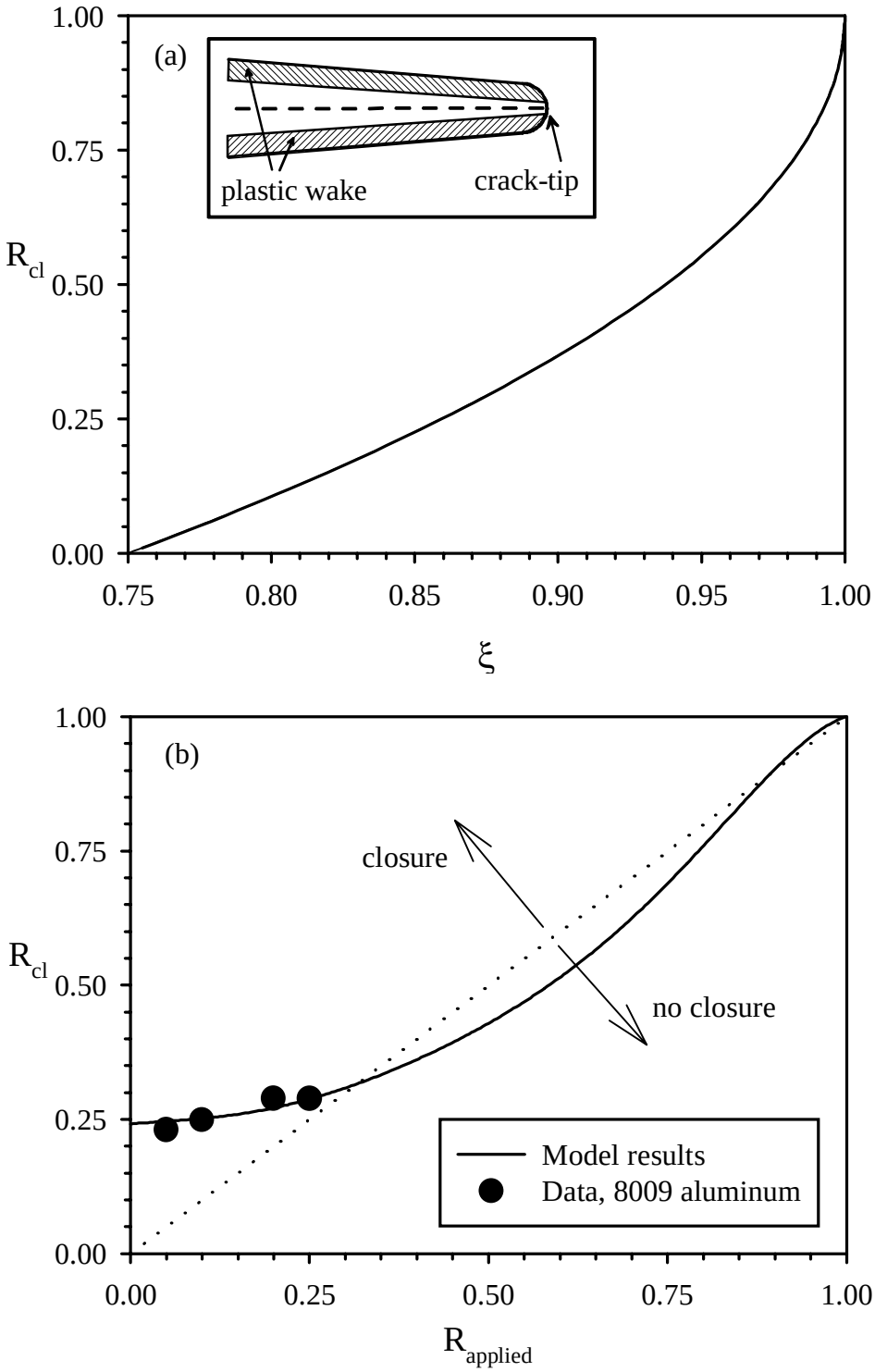

Figure 3.9 – Plots of closure levels for straight cracks. In part (a) R_{cl} is plotted against ξ. Since ξ is related to the applied R, $R_{applied}$ (see Figure 3.4), R_{cl} is related to $R_{applied}$, as shown in part (b). The dotted line corresponds to closure at the minimum load, so that no closure is expected below this line. Experimental results, using compliance data, are shown in part (b) for aluminum alloy 8009 tested at $\Delta K = 6.6$ MPa$\sqrt{m}$ in laboratory air.

fine submicron (0.3 μm - 0.5 μm) grain structure, the resulting fatigue crack surfaces are smooth and nearly featureless [60, 61]. Thus, the influence of crack roughness is minimal and comparison between 8009 aluminum data and straight crack results is reasonable. Although this 8009 aluminum data was generated in laboratory air, it will be shown later that the contribution of a naturally forming oxide layer (OICC) is negligible. As seen in the figure, good agreement exists between model predictions and experimental data. Because model results are compared with R = 0.05 experimental data, it is notable that the corresponding closure level is R_{cl} = 0.252 for a straight crack loaded at R = 0.05, with no crack mouth oxide.

Predicted closure levels are a function only of R, not K_{max}, when PICC is the only active closure mechanism. However, this is no longer true when an oxide layer is considered in the crack mouth. Closure levels are plotted against K_{max} in Figure 3.10a for three oxide layers (t = 0 Å, 100 Å, and 500 Å). A schematic of this crack configuration is shown in the upper right corner of Figure 3.10a, where the crack-tip and oxide layer (t) are indicated. Crack wake plasticity is also considered, but is not indicated in this schematic. Model results are calculated using mechanical properties for 2024 aluminum and R = 0.05. For all K_{max}, the closure level for a straight crack with no oxide layer is constant, indicated by the horizontal dotted line (R_{cl} = 0.252).[18] The presence of an oxide layer in the crack mouth produces an increase in R_{cl} as K_{max} decreases because the oxide layer becomes larger compared with the CTOD. Eventually, a K_{max} will be reached where the oxide layer completely fills the crack-tip opening. For the solid curve in Figure 3.10a (t = 100 Å), the fully closed K_{max} value is labeled (approximately $K_{max\,fc}$ = 1.7 MPa$\sqrt{m}$). For $K_{max} < K_{max\,fc}$ the crack-tip is fully closed, so no FCG occurs here. Although $\Delta K_{eff} = 0$ has not been stated as a criterion for FCG threshold, this is a lower bound for ΔK_{th}. The oxide layer becomes less significant as K_{max} becomes large. Consequently, R_{cl} approaches the value associated with $t = 0$ as K_{max} increases.

As indicated in Figure 3.10a, $K_{max\,fc}$ increases with increasing oxide thickness, t. The relationship between $K_{max\,fc}$ and t is plotted in Figure 3.10b as a solid curve. Conditions above the solid curve correspond to partially open cracks, while those below the curve are fully closed. Because the CTOD is proportional to K_{max}^2, the curve in Figure 3.10b is shaped as a square root function. That is, $K_{max\,fc}$ is proportional to $\sqrt{t}$ for straight cracks.

Instead of allowing an oxide layer at the crack-tip, model results were generated for cases where an oxide layer terminates a finite distance, Δa, behind the crack-tip. Schematics of this crack configuration are shown in the lower right of Figures 3.11 and 3.12. This scenario could occur in practical applications when FCG persists after removal from a corrosive environment. Model results, R_{cl}, are presented against Δa for three different values of K_{max} and three values of oxide layer thickness. Closure levels are computed at the edge of the oxide layer closest to the crack-tip (*i.e.* $g = \Delta a$) using model parameters for 2024 aluminum and R = 0.05. In Figure 3.11, model results are plotted for (a) K_{max} =

[18] Although the PRO model uses concepts from the Budiansky and Hutchensen (BH) model, lower closure levels are predicted. Without an oxide layer, the PRO model predicts R_{cl} = 0.252, while the BH model predicts R_{cl} = 0.55. This is because the current model uses plane-strain conditions (better suited for FCG threshold) while the BH model assumes plane-stress conditions.

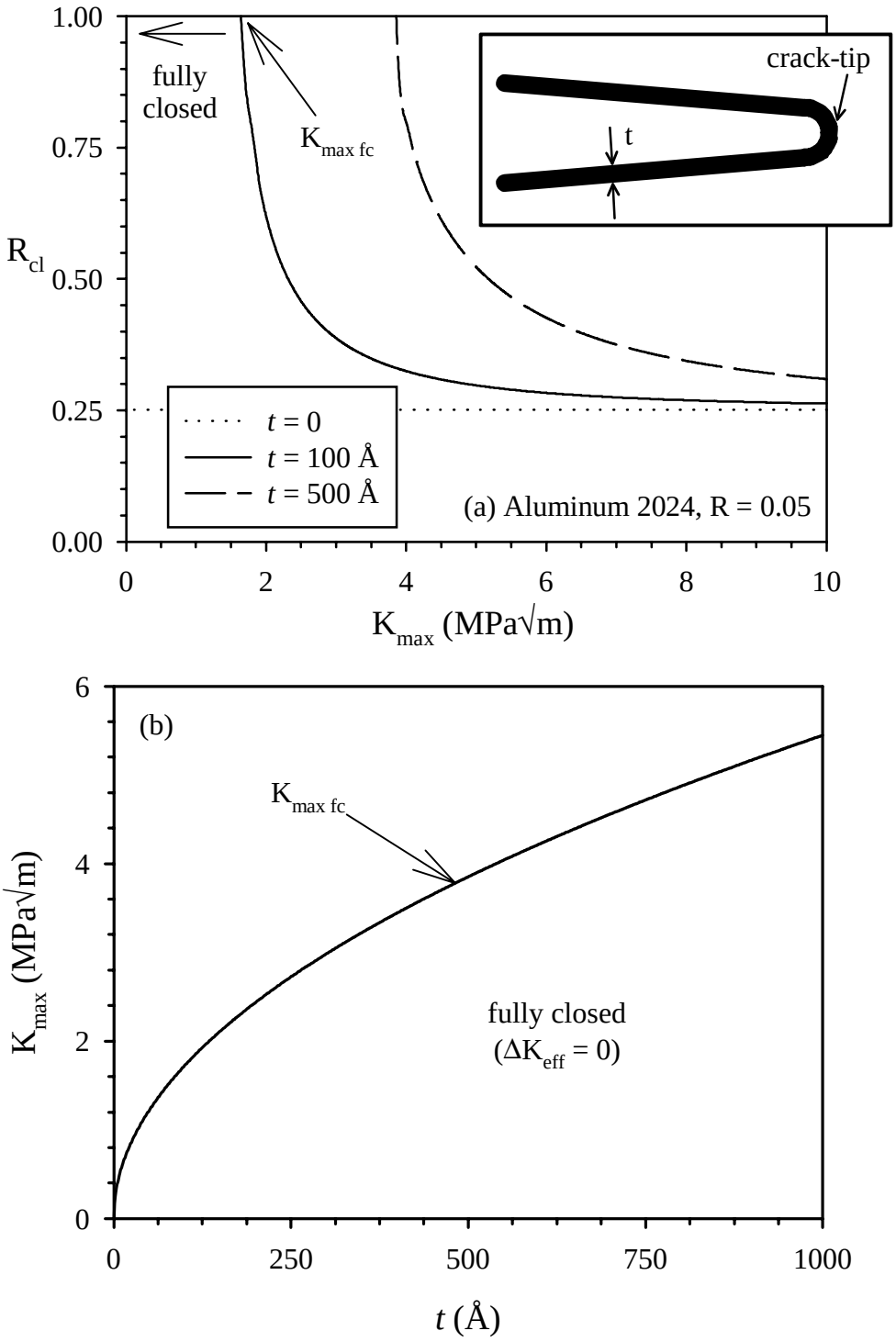

Figure 3.10 – Closure behavior for straight cracks with an oxide layer. In part (a) closure levels, R_{cl}, are plotted against K_{max} for three different values of oxide layers; 0 Å, 100 Å, and 500 Å. In part (b) the fully closed conditions are indicated as a function of K_{max} and t.

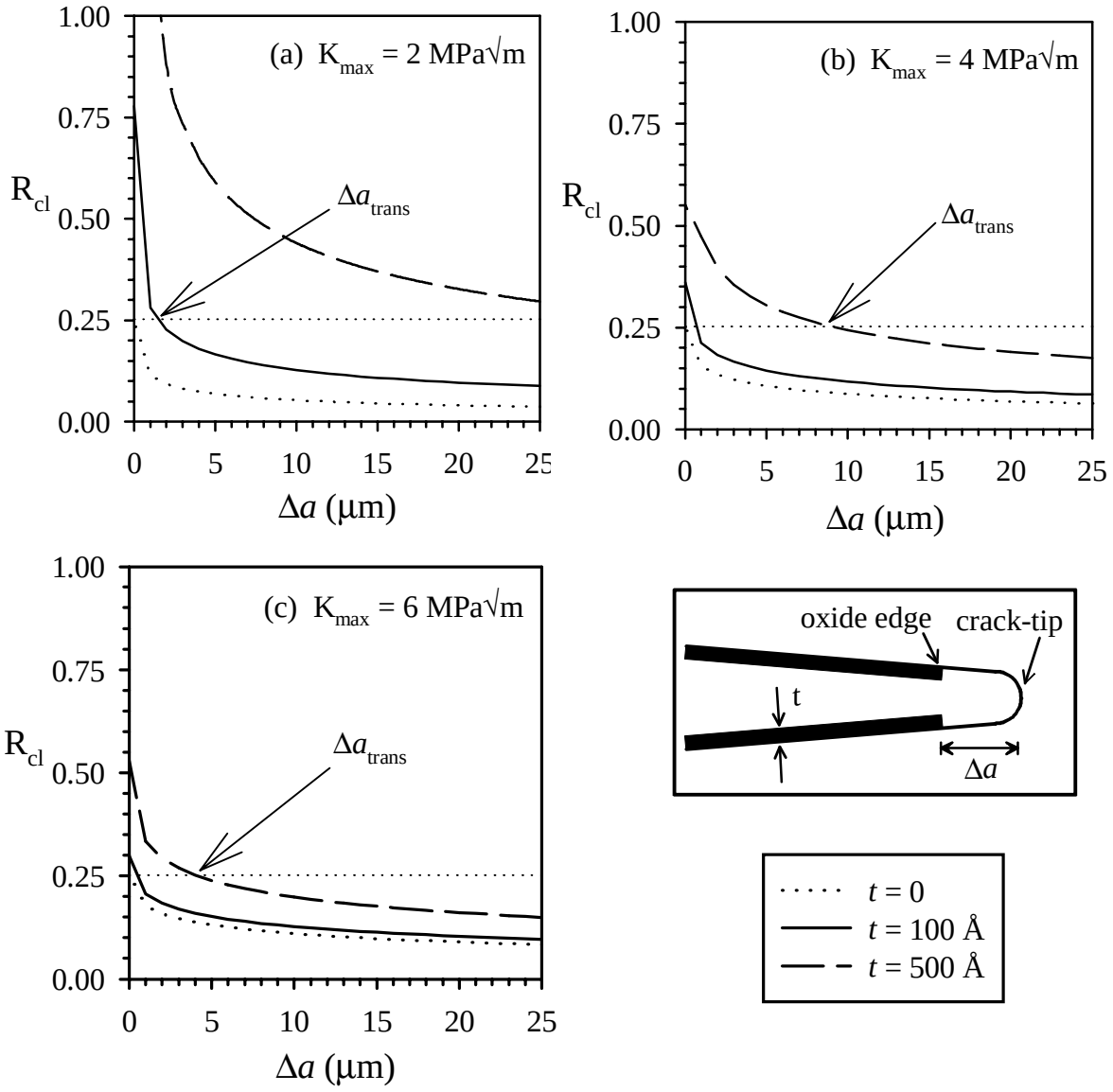

Figure 3.11 – Closure levels, R_{cl}, are plotted against Δa for (a) K_{max} = 2 MPa√m, (b) K_{max} = 4 MPa√m, and (c) K_{max} = 6 MPa√m. Model results for no oxide layer (R_{cl} = 0.252) are indicated by a horizontal dotted line on each plot.

2 MPa√m, (b) K_{max} = 4 MPa√m, and (c) K_{max} = 6 MPa√m. Results for t = 0, 100, and 500 Å are shown as dotted, solid, and dashed curves, respectively. This data is also presented in Figure 3.12 on plots corresponding to (a) t = 0, (b) t = 100 Å, and (c) t = 500 Å. Results for K_{max} = 2 MPa√m, 4 MPa√m, and 6 MPa√m are shown as dotted, solid, and dashed curves, respectively. The horizontal dotted line in each plot corresponds to the closure level predicted for t = 0. When the model results in Figures 3.11 and 3.12 drop below the horizontal dotted line, closure will occur at the crack-tip rather than at the edge of the oxide layer. As Δa increases, crack closure is more likely to occur at the

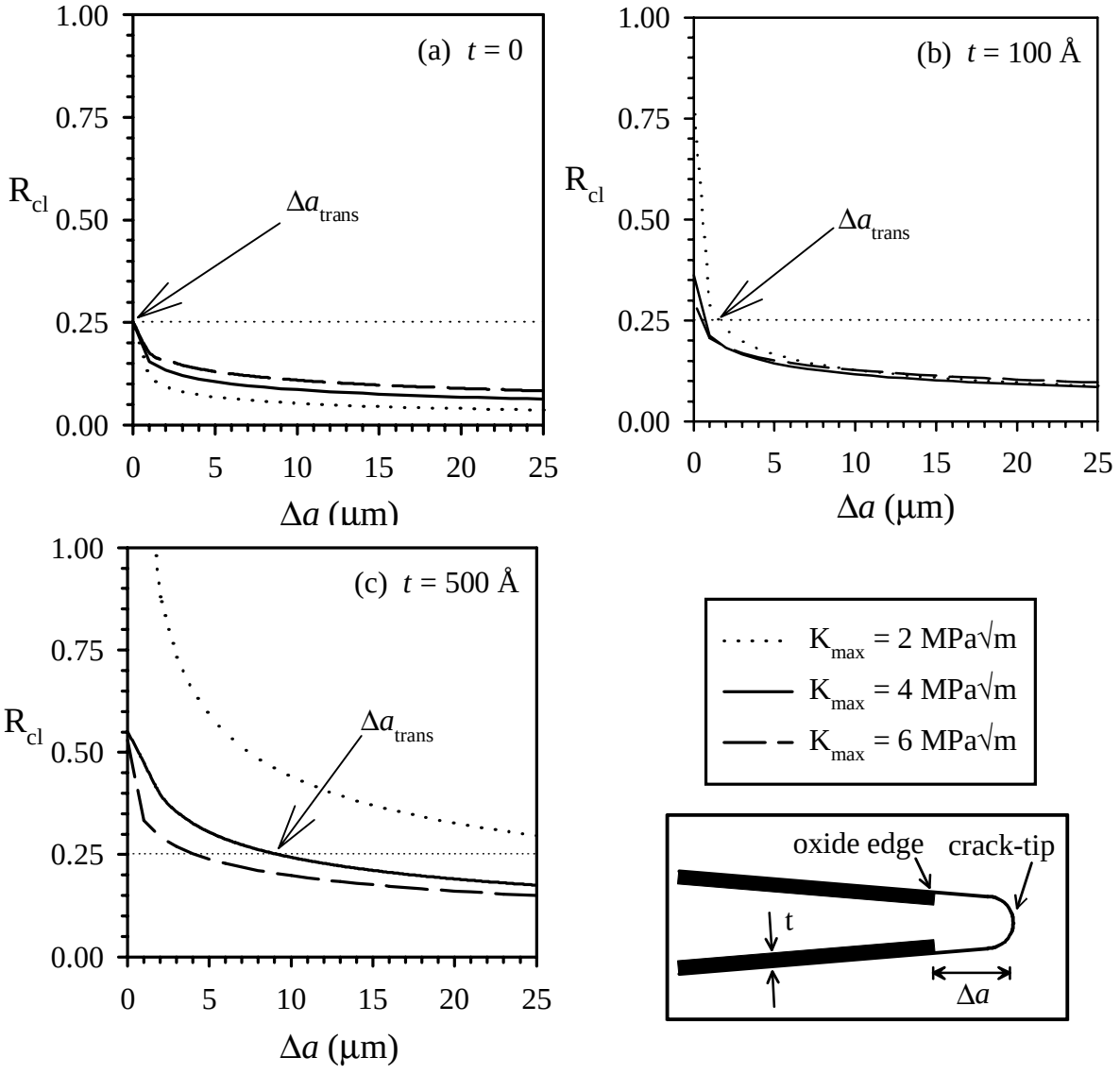

Figure 3.12 – Model results of Figure 3.11 are re-plotted, here for (a) t = 0, (b) t = 100 Å, and (c) t = 500 Å.

crack-tip. A transition from closure at the oxide layer to crack-tip closure occurs when $a = \Delta a_{trans}$ indicated in the figures (by the intersection between the curves and the horizontal dotted line). Model results presented in Figure 3.11 indicate that lower values of K_{max} produce higher values of closure for a given oxide thickness. (This observation is consistent with that of Figure 3.10a.) As a crack grows away from an oxide layer, its effect on closure levels rapidly decreases, especially at higher K_{max}. For instance, closure occurs at the edge of a 500 Å oxide layer after 25 μm of crack growth at K_{max} = 2 MPa√m, but for K_{max} = 6 MPa√m, no closure occurs at a 500 Å oxide layer after only 5 μm of crack growth (see Figure 3.12c). The results presented in Figure 3.12 indicate thicker oxide layers have greater influence on crack growth away from oxide. For no oxide in the crack mouth (t = 0) closure always occurs at the crack-tip (see Figure 3.12a).

As indicated in Figures 3.11 and 3.12, Δa_{trans} varies with K_{max} and t. These relationships are plotted in Figure 3.13. In part (a), Δa_{trans} is plotted against t for K_{max} = 2 MPa√m, 4 MPa√m, and 6 MPa√m (indicated by dotted, solid and dashed curves, respectively.

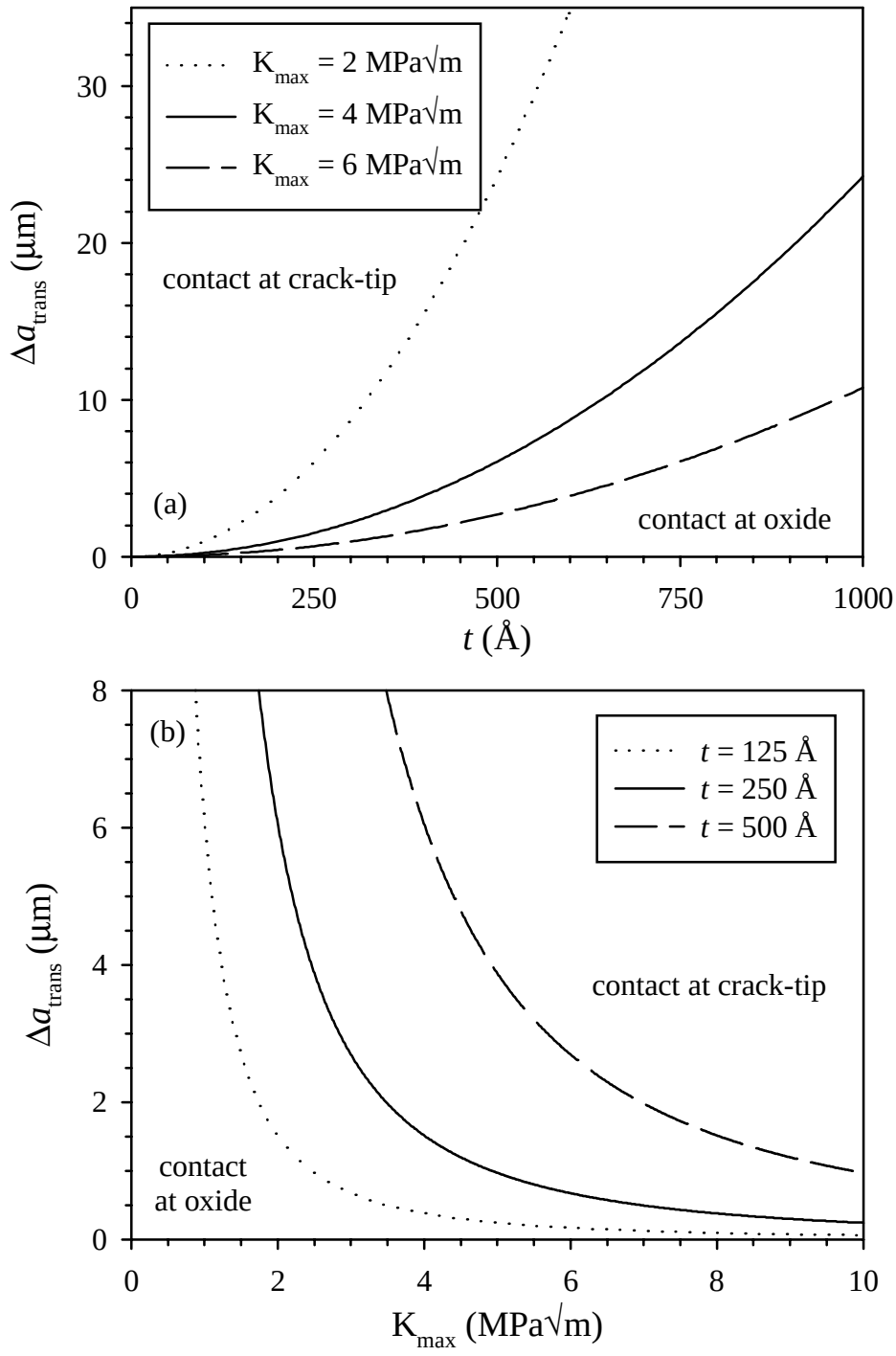

Figure 3.13 – Variation of transition crack length, Δa_{trans}, for a straight crack. In part (a) Δa_{trans} is plotted against oxide layer thickness for three different K_{max} (2,4, and 6 MPa√m). In part (b) Δa_{trans} is plotted against K_{max} for three different oxide thickness (125, 250, and 500 Å).

Above each of these curves crack closure occurs at the crack-tip and below the curves contact occurs at the edge of the oxide layer. As the oxide layer becomes thicker, greater distance from the crack-tip is needed before the oxide layer becomes ineffective. In part (b), Δa_{trans} is plotted against K_{max} for t = 125 Å, 250 Å, and 500 Å (indicated by dotted, solid, and dashed curves, respectively). For crack configurations above each of these curves, contact occurs at the crack-tip, while below the curves contact occurs at the oxide layer edge. As K_{max} increases, Δa_{trans} decreases, along with the closure contribution of the oxide layer.

3.5.2 — Rough crack results

Model results for rough cracks ($\alpha \neq 0$) are presented in Figures 3.14 and 3.15 for three values of K_{max} (2 MPa$\sqrt{m}$, 4 MPa$\sqrt{m}$, and 6 MPa$\sqrt{m}$) and four values of oxide thickness (t = 0 Å, 100 Å, 250 Å, and 500 Å). Model parameters of aluminum alloy 2024 (including α and g) and R = 0.05 are used (see Table 3.1). To evaluate the effects of crack roughness, only asperity contact is considered for now (Equation 3.12a). Closure levels (determined at the asperity closest to the crack-tip without consideration of tip contact) are plotted against asperity angle in Figure 3.14 and 3.15. Later, both tip contact and asperity contact will be considered as closure modes. Plots of closure levels versus α, are presented in Figure 3.14 for (a) t = 0, (b) t = 100 Å, (c) t = 250 Å, and (d) t = 500 Å. (Refer to the legend to determine which curves correspond to specific values of K_{max}.) The same data is re-plotted in Figure 3.15 on plots corresponding to (a) K_{max} = 2 MPa$\sqrt{m}$, (b) K_{max} = 4 MPa$\sqrt{m}$, and (c) K_{max} = 6 MPa$\sqrt{m}$. (Refer to the legend to determine which curves correspond to specific values of t.) A schematic of this crack configuration is shown in Figures 3.14 (upper right corner) and 3.15 (lower right corner). For all cases shown in Figures 3.14 and 3.15, closure levels increase with increasing asperity angle, because sliding mode crack face displacements increase with increasing α. (Recall, RICC is a result of sliding mode displacements causing asperity contact on unloading.) Closure levels increase with increasing α until the crack is fully closed, *i.e.* R_{cl} = 1. For K_{max} = 2 MPa$\sqrt{m}$ in Figure 3.14a, the crack becomes fully closed at the point labeled, α_{fc}. As indicated by the arrow to the right of this point, cracks are fully closed for $\alpha > \alpha_{fc}$. α_{fc} for the remaining curves are not labeled, but occur where the curves intersect the top border of the plot (R_{cl} = 1). The change in α_{fc} with K_{max} is indicated at the top of each plot in Figure 3.14 by $\Delta\alpha_{fc}$. Comparing parts (a) through (d) indicates that $\Delta\alpha_{fc}$ becomes smaller as oxide thickness increases. The change in closure levels at α = 0 are indicated in these plots by ΔR_{cl}. These closure levels correspond to asperity contact without regard to tip contact. Because tip contact is likely to occur (instead of asperity contact) at α = 0, this portion of the model results is not of interest. For no oxide, higher closure levels occur for greater values of K_{max}. As oxide thickness increases, higher closure levels occur, especially at low K_{max} levels. In Figure 3.15, $\Delta\alpha_{fc}$ indicates the change in α_{fc} as oxide thickness increases from 0 to 1000 Å. By comparing the three plots in Figure 3.15, it can be seen that $\Delta\alpha_{fc}$ decreases as K_{max} increases, suggesting that an oxide layer becomes less significant at higher K_{max}. (This is consistent with straight crack results shown in Figure 3.10.) The change in closure levels at α = 0 (ΔR_{cl}) is greater at lower

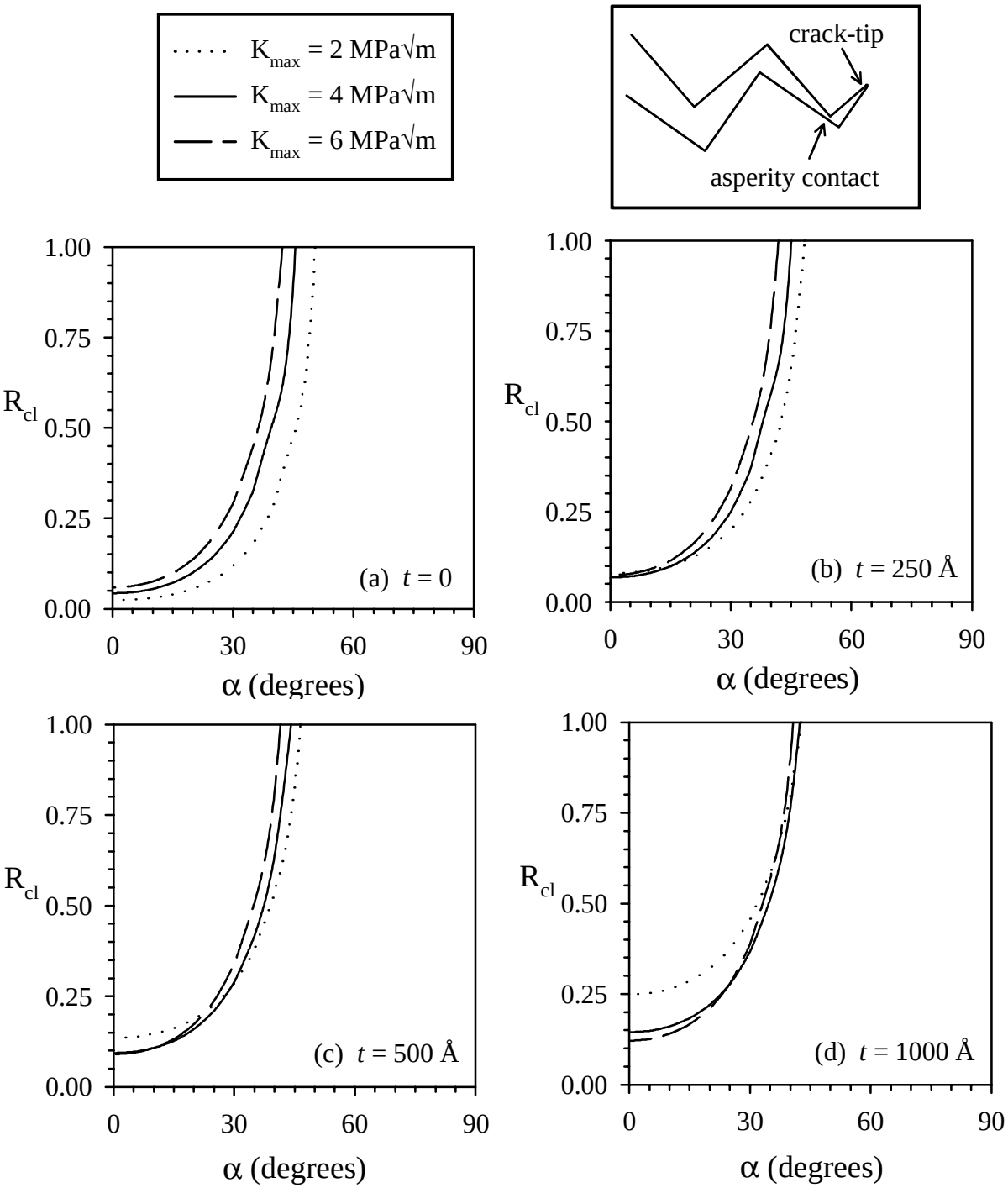

Figure 3.14 – Closure levels, for three different values of K_{max} (2, 4, and 6 MPa√m) plotted against asperity angle, α, for (a) t = 0, (b) t = 100 Å, (c) t = 250 Å, and (d) t = 500 Å.

values of K_{max} because CTOD is smaller. Only results for positive α are presented because symmetry exists about α = 0 (*i.e.* $R_{cl}(\alpha) = R_{cl}(-\alpha)$).

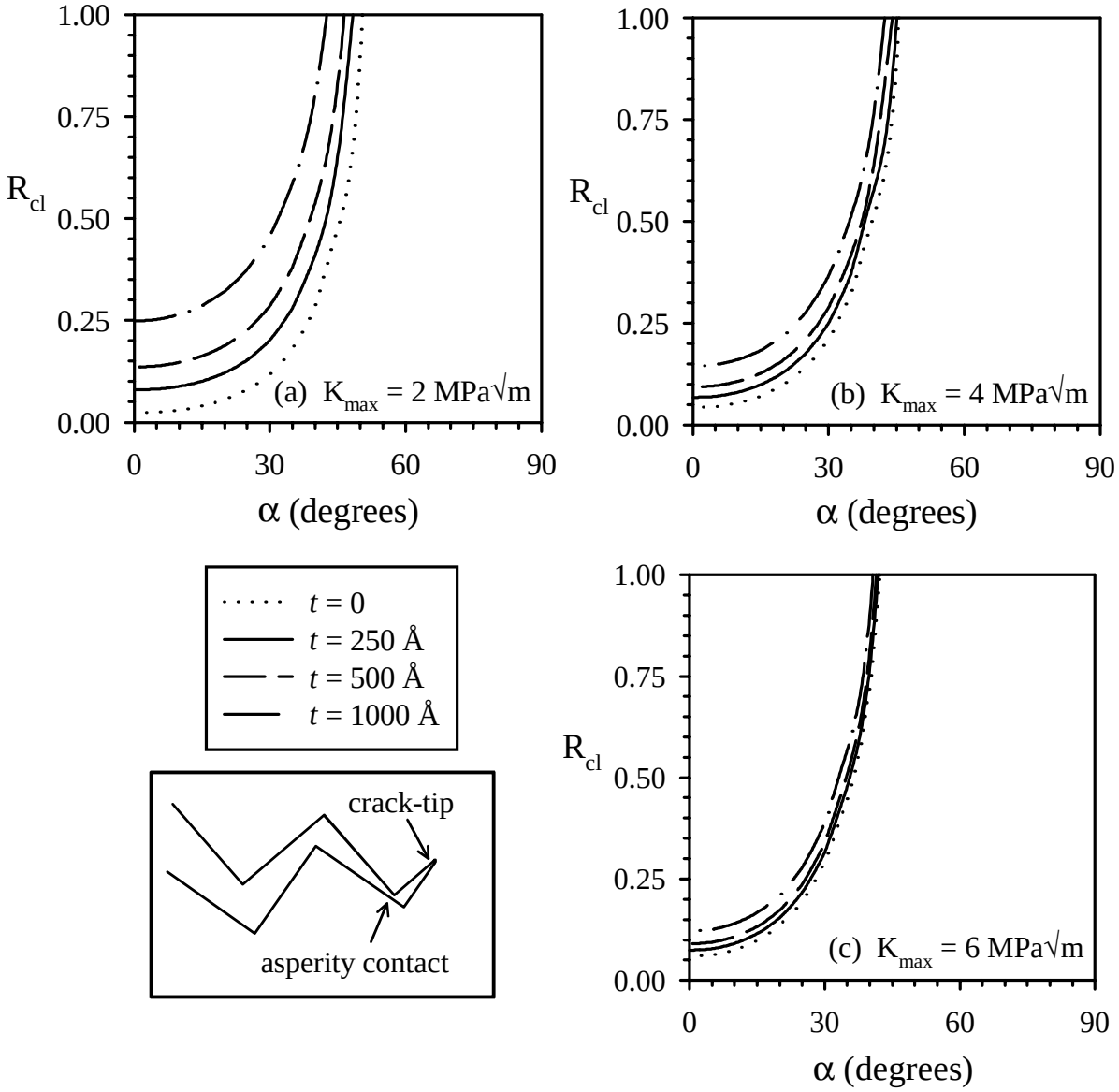

Figure 3.15 – Model results presented in Figure 3.14 are re-plotted for (a) K_{max} = 2 MPa√m, (b) K_{max} = 4 MPa√m, and (c) K_{max} = 6 MPa√m.

The model results of Figure 3.14b are revisited, considering both tip contact and asperity contact. Model results are plotted in Figure 3.16 as R_{cl} versus α, for R = 0.05 and *t* = 100 Å. The crack configuration is shown schematically in the lower right corner of the plot; both tip contact and asperity contact locations are indicated. Curves are presented for K_{max} = 2 MPa√m, 4 MPa√m, and 6 MPa√m, as dotted, solid, and dashed curves, respectively. α_{fc} is indicated for K_{max} = 2 MPa√m. At lower values of α, tip contact occurs. A transition between tip contact and asperity contact is seen as an abrupt slope change in the curves. For K_{max} = 2 MPa√m, this transition point (α_{trans}) is indicated. Where tip contact occurs (low α), the oxide layer produces higher closure levels at low

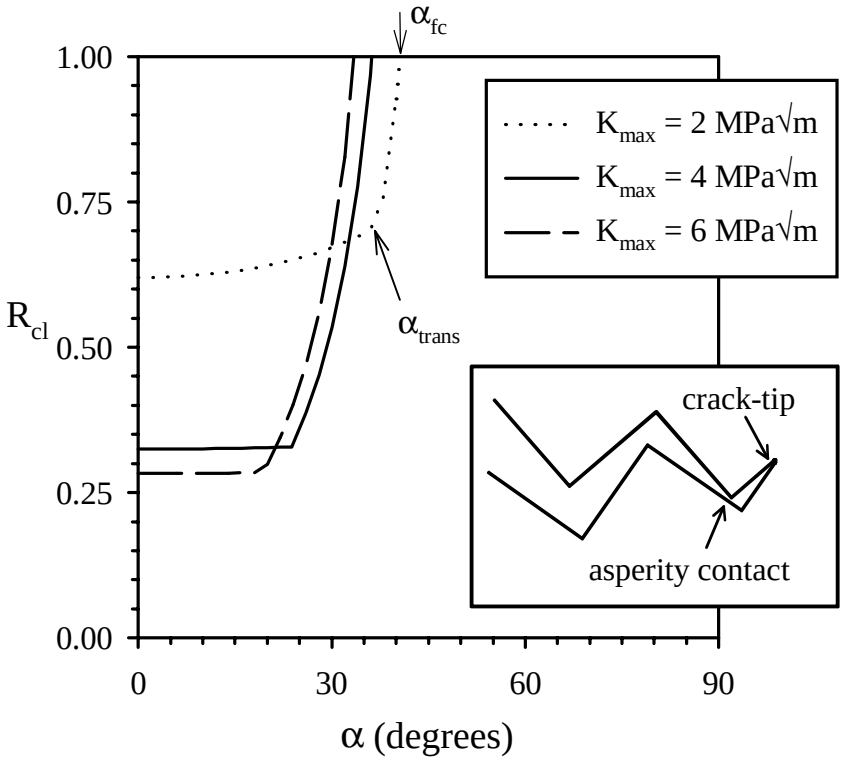

Figure 3.16 – Model results are plotted here for a rough crack (2024 aluminum model parameters) with a 100 Å oxide layer. Both tip contact and asperity contact are considered.

K_{max} (because of lower CTOD). However, this oxide layer is less influential further behind the crack-tip, where asperity contact occurs. Because the importance of oxide changes between tip contact and asperity contact, the curves in Figure 3.16 cross. The fully closed and transition points indicated in Figure 3.16 (α_{fc} and α_{trans}, respectively) vary with oxide thickness and K_{max}. To study this relation, both α_{fc} and α_{trans} are plotted against K_{max} in Figure 3.17 for (a) t = 0, (b) t = 100 Å, and (c) t = 250 Å. In each plot, α_{fc} and α_{trans} are indicated by solid and dashed curves, respectively. Three regions are labeled; fully closed, asperity contact, and tip contact. Above the solid curve, the crack is fully closed. Between the solid and dashed curves, asperity contact occurs. Below the dashed curve, closure occurs at the crack-tip (*i.e*. tip contact). In Figure 3.17a, (t = 0) both curves converge to $\alpha = 60^o$ as K_{max} approaches zero, which is labeled α_o. Because α_o is the maximum value for both α_{fc} and α_{trans}, fatigue cracks will be completely closed for all K_{max} if $\alpha > \alpha_o$. As K_{max} increases, α_{fc} and α_{trans} both decrease. This means crack roughness is more likely to affect crack closure behavior at high K_{max}, but as discussed in Section A.1, rough cracks are more likely at threshold (*i.e*. low K_{max}). As indicated in parts (b) and (c) of Figure 3.17, an oxide layer produces a critical point in the α versus K_{max} plot, where α_{fc} and α_{trans} curves intersect. At K_{max} below these critical points, increasing α results in a transition from tip contact to fully closed, bypassing asperity contact. A comparison of parts (b) and (c) suggests the critical point shifts to higher K_{max} as oxide thickness increases.

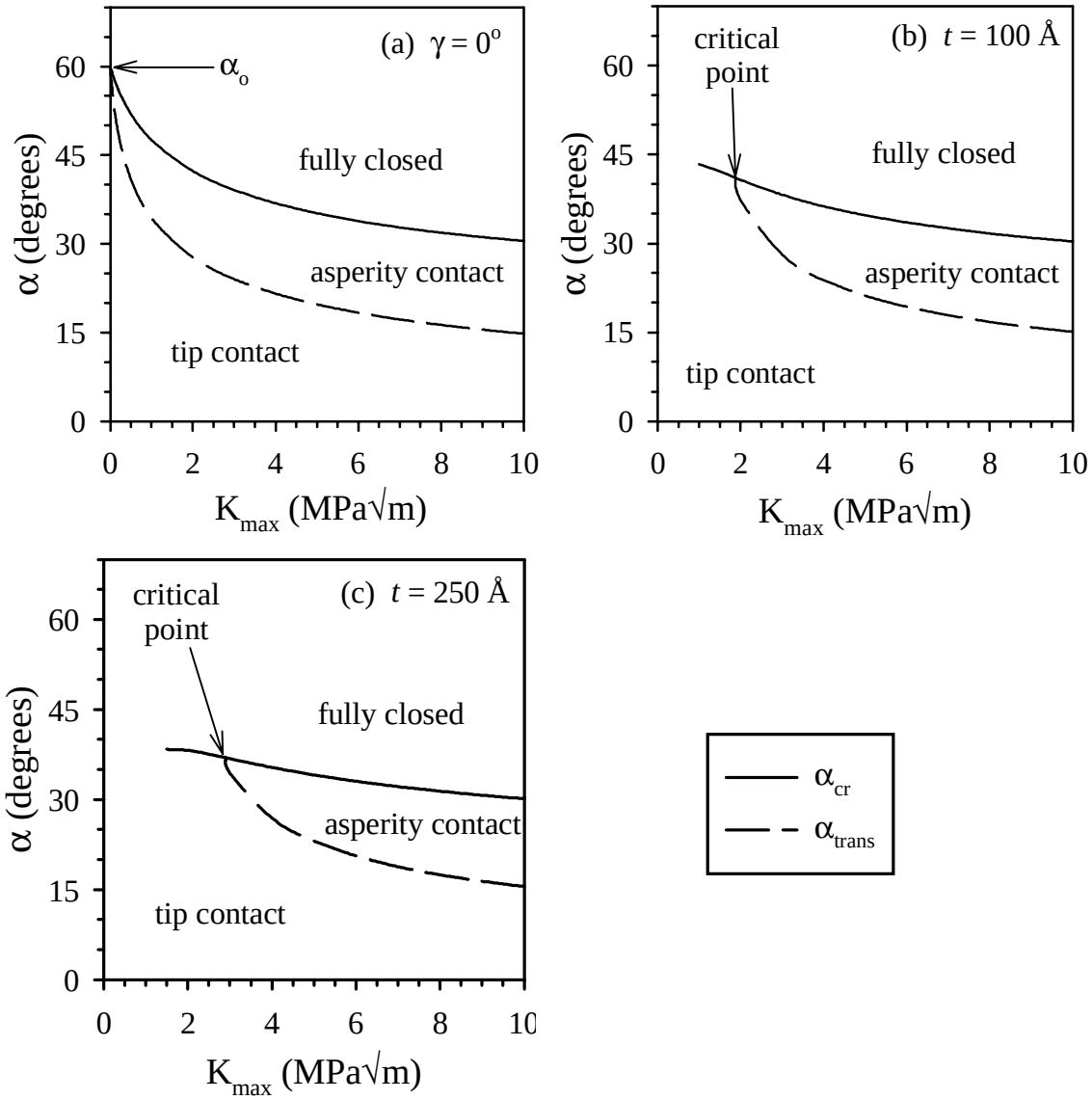

Figure 3.17 – Plots of α_{fc} and α_{trans} versus K_{max} for several oxide layers. These parameters are plotted as solid and dashed curves, respectively, and separate each plot into three regions of crack closure behavior.

The relation between this critical K_{max} ($K_{max\,cr}$) and oxide thickness is plotted as a solid curve in Figure 3.18. (Recall, these results are for aluminum alloy 2024 and R = 0.05.) Above this curve, asperity contact is possible for certain values of α and K_{max}. Closure is limited to the crack-tip for conditions below the solid curve, so asperity contact can be neglected. Asperity contact is most likely eliminated for thick oxide layers and low K_{max} levels, because a small CTOD (associated with low K_{max}) is easily filled with oxide.

Model results for rough meandering cracks ($\alpha \neq 0$ and $\gamma \neq 0$) are presented in Figure 3.19. This crack configuration is shown schematically to the right of Figure 3.19b. Plots for (a) $\gamma = 10^o$, (b) $\gamma = 20^o$, and (c) $\gamma = 30^o$ are presented for K_{max} = 2 MPa√m, 4 MPa√m, and 6 MPa√m (indicated by dotted, solid, and dashed curves, respectively). As before, model

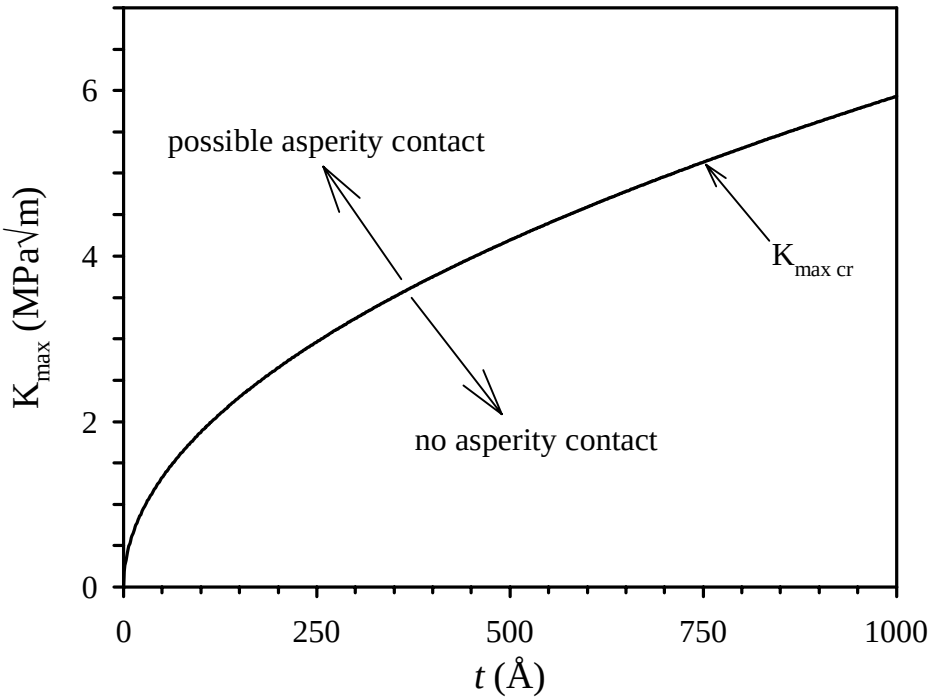

Figure 3.18 – Plot of the relationship between $K_{max\ cr}$ and oxide layer thickness, *t*. Below the curve no asperity contact occurs. Above the curve, asperity contact will occur for some values of α.

parameters for 2024 aluminum, t = 0 Å, and R = 0.05 are used. Closure is only considered at the asperity closest to the crack-tip, neglecting tip contact. Both tip contact and asperity contact will be considered later. Model results are plotted against asperity angle as previously done (see Figures 3.14 and 3.15). Both positive and negative values of α are shown because symmetry about $\alpha = 0$ does not exist for meandering cracks. For each plot, the minimum closure level occurs about $\alpha = 0$, but is not of interest because tip contact is likely to occur here. The changes in α_{fc} for positive and negative α are indicated as $\Delta\alpha_{fc}^{+}$ and $\Delta\alpha_{fc}^{-}$, respectively. As seen by comparison of parts (a) through (c), both α_{fc} and $\Delta\alpha_{fc}$ are larger for positive values of α. Furthermore, as γ increases, the range in α for which the crack is partially open ($\alpha_{fc}^{-} < \alpha < \alpha_{fc}^{+}$) decreases.

The model results of Figure 3.19b are revisited considering both tip contact and asperity contact. Model results are plotted in Figure 3.20, as R_{cl} versus α using parameters for aluminum alloy 2024, R = 0.05, $\gamma = 20^{o}$, and t = 0. The crack configuration is shown schematically above the plot with both tip contact and asperity contact locations indicated. Curves are presented for K_{max} = 2 MPa√m, 4 MPa√m, and 6 MPa√m, as dotted, solid, and dashed curves, respectively. Tip contact occurs in the flat (constant R_{cl}) regions near $\alpha = 0$. For K_{max} = 2 MPa√m, α_{fc}^{+} and α_{fc}^{-} are labeled as the fully closed values of positive and negative α, respectively. Also α_{trans}^{+} and α_{trans}^{-} are indicated as the transition between tip contact and asperity contact for positive and negative values of α, respectively. As K_{max} increases, (the absolute values of) α_{fc}^{+}, α_{fc}^{-}, α_{trans}^{+}, and α_{trans}^{-} decrease. Increased closure levels result from increases in crack roughness (α) and K_{max}.

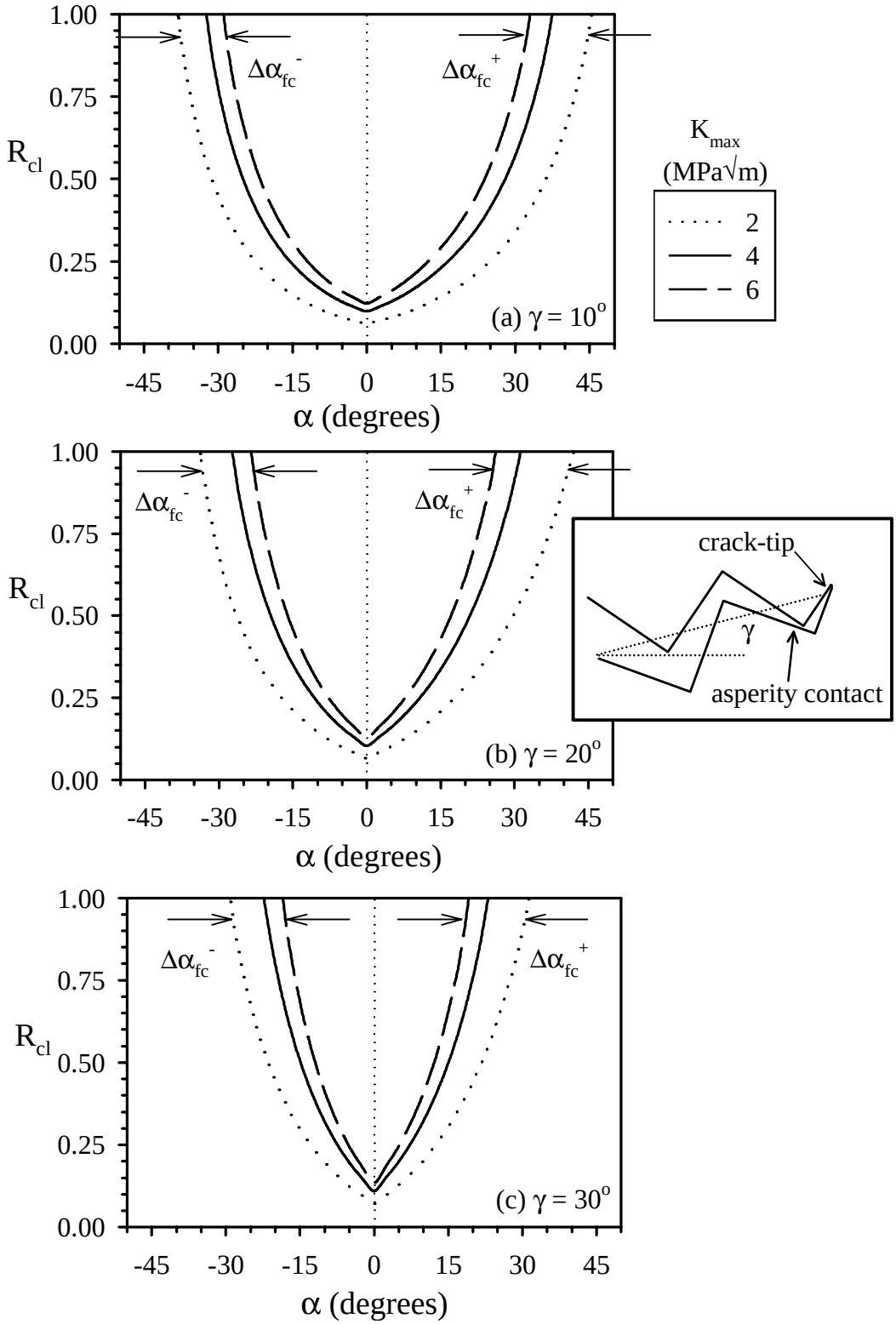

Figure 3.19 – Closure levels versus α, are plotted for three values of K_{max} (2, 4, and 6 MPa√m) and γ (10°, 20°, and 30°) for t = 100 Å. Model parameters for 2024 aluminum were used.

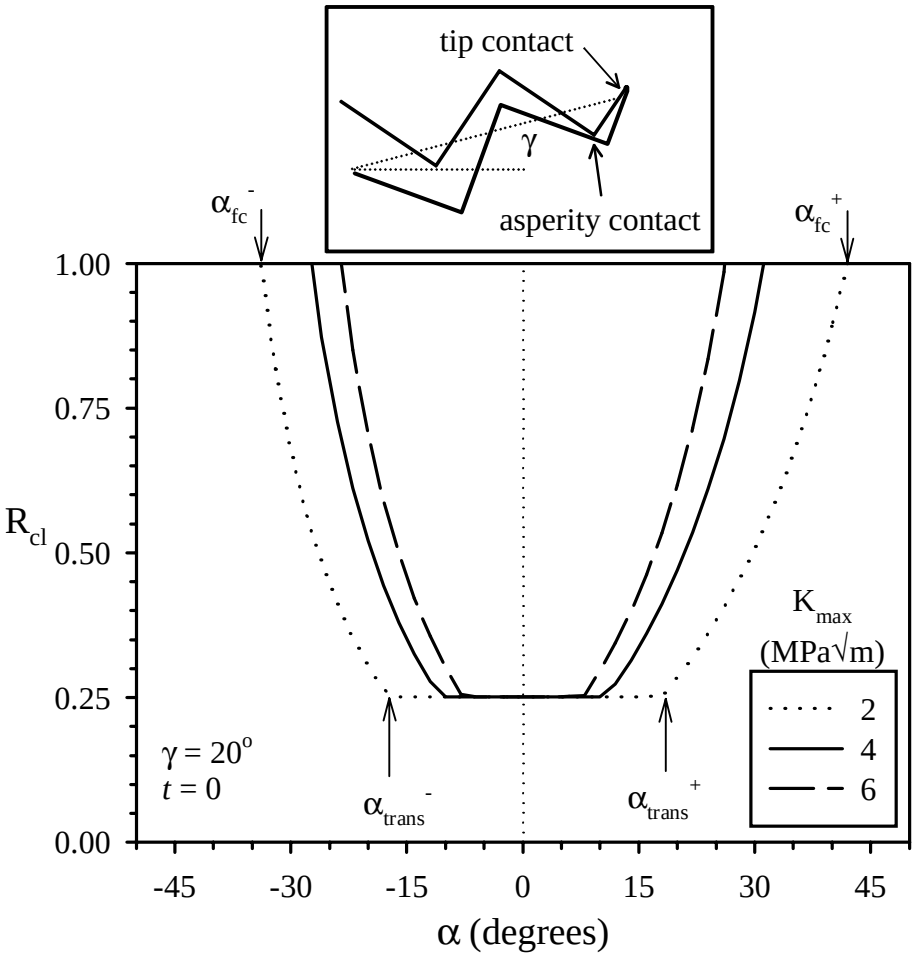

Figure 3.20 – Plot of closure level versus α for a meandering rough crack. Both tip contact and asperity contact are considered for $\gamma = 20^o$ and $t = 0$.

The relationship between α_{fc}, α_{trans}, and K_{max} are plotted in Figure 3.21 for three meandering angles; (a) $\gamma = 0^o$, (b) $\gamma = -10^o$, and (c) $\gamma = +10^o$. In each plot, α_{fc} and α_{trans} are indicated by solid and dashed curves, respectively. Three regions are indicated; fully closed, asperity contact, and tip contact. Above the solid curve, the crack is fully closed. Between the solid and dashed curves asperity contact occurs, and tip contact occurs below the dashed curve. In Figure 3.21a, ($\gamma = 0^o$) both curves converge to $\alpha = 60^o$ as K_{max} approaches zero, which is labeled α_o. (This was also seen in Figure 3.17a.) Because α_o is the maximum value for both α_{fc} and α_{trans}, fatigue cracks will be closed for all K_{max} levels if $\alpha > \alpha_o$. As K_{max} increases, α_{fc} and α_{trans} both decrease. Changes in meandering angle, γ, do not produce a critical point (as shown in Figure 3.17) if no oxide exists in the crack mouth. Instead, both curves converge at $K_{max} = 0$, but the value of α_o varies. The relationship between α_o and γ is plotted as a solid curve in Figure 3.22. As indicated in the figure, α_o increases with increasing γ. Because α_o is the maximum asperity angle for which a crack can open, conditions above the solid curve correspond to a fully closed crack, *i.e.* $R_{cl} = 1$. Below the curve a crack may open, depending on the value of K_{max}. Model results, R_{cl}, for rough cracks have been plotted against asperity

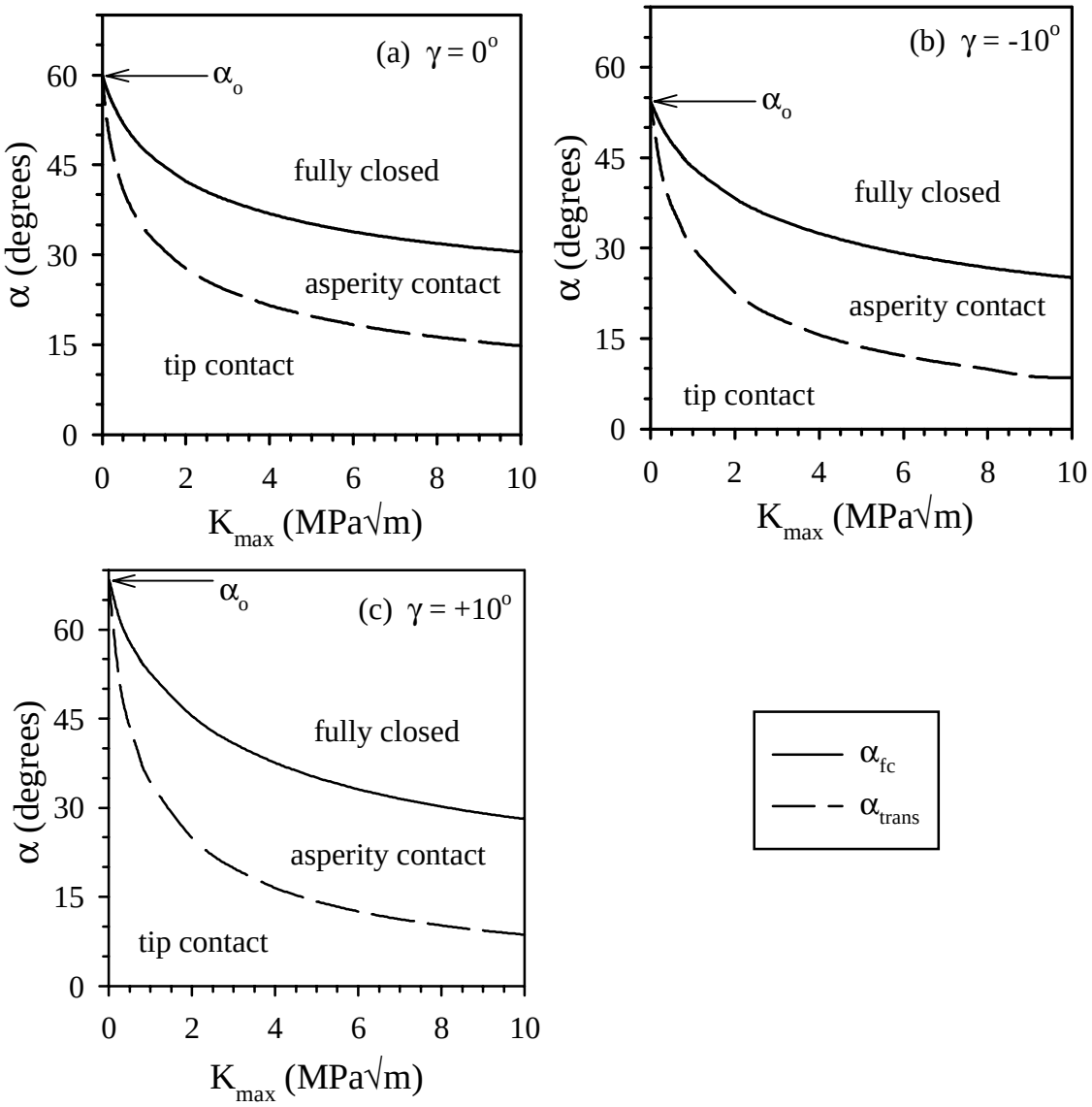

Figure 3.21 – Plots of the relationship between $K_{max\ fc}$ and $K_{max\ trans}$, and α. These parameters are plotted as solid and dashed curves respectively, which divide the plots into three regions of crack closure behavior.

angle, α, to this point. However, it is more natural to compare closure levels against loading parameters, *e.g.* K_{max}. Model results are plotted against K_{max} for rough (but non-meandering) cracks in Figure 3.23. This crack configuration is shown schematically above the plot. Results for two values of oxide thickness (t = 0 and t = 100 Å) are indicated by dashed and solid curves, respectively. Model parameters for 2024 aluminum and R = 0.05 were used and both tip contact and asperity contact are considered. The transition points between tip contact and asperity contact are indicated in the figure. Tip contact occurs at higher values of K_{max} (> 4 MPa√m) and asperity contact occurs at lower values of K_{max} (< 3.5 MPa√m). Dotted lines indicate unrealized model results. For

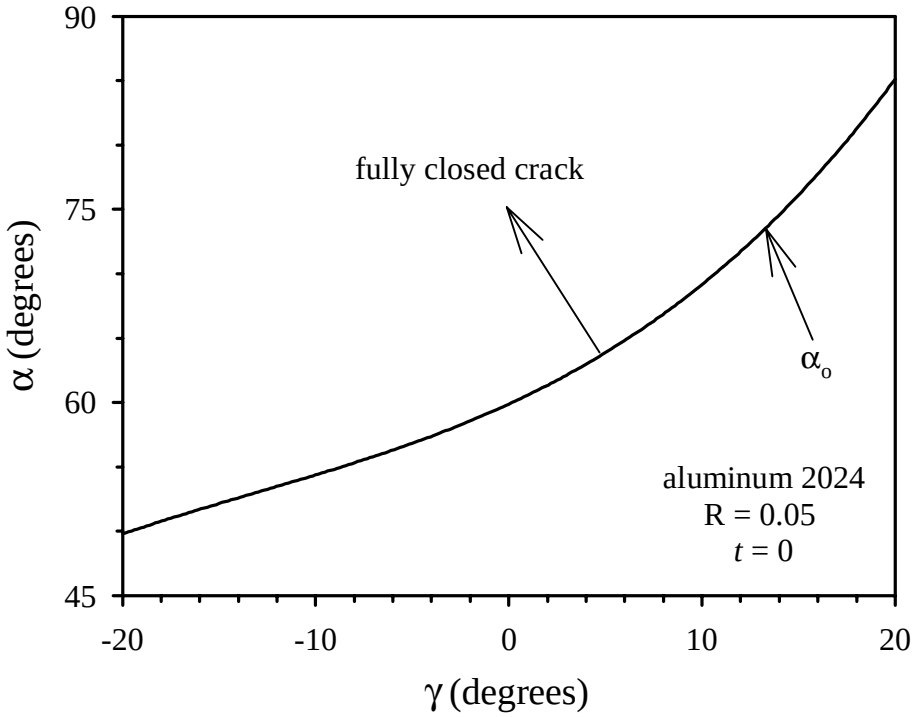

Figure 3.22 – Plot of the relationship between α_o and γ. Above the curve, the crack is always fully closed. Below the curve, the crack may be partially open for some values of K_{max}.

example, the horizontal dotted line at $R_{cl} = 0.252$ for $K_{max} < 3.5$ MPa$\sqrt{m}$ is a mathematical solution to the model (tip contact for $t = 0$), but is not realized because contact occurs at the asperity closest to the crack-tip instead. As seen in the figure, higher closure levels are expected for thicker oxide layers. Also, the rapid increase in R_{cl} with decreasing K_{max} is due to asperity contact. This suggests that RICC causes FCG threshold, as suggested by Suresh and Ritchie [52].[19] This model does not include remote closure (or other load history effects) so care should be taken when comparing this model to threshold test data where K_{max} was reduced during testing.

Changes in closure behavior with asperity angle (α) and oxide thickness (t) have been studied. The influences of yield stress (σ_o), asperity length (g), and meandering angle (γ) on model results are examined here. Model results are generated using parameters for 2024 aluminum, R = 0.05 and $t = 0$ Å, except for the variable to be studied. Closure levels are plotted against K_{max} in Figure 3.24 for variations in (a) σ_o, (b) g, and (c) γ. In Figure 3.24a, model results for $\sigma_o = 175$ MPa, 350 MPa, and 700 MPa are shown as dotted, dashed, and solid curves, respectively. Both crack-tip closure and asperity contact are considered and the contact locations are indicated schematically in the figure (upper right corner). Tip contact is more likely to occur at higher values of K_{max} and is indicated by the horizontal dotted line ($R_{cl} = 0.252$) on the right side of each plot. The transition point for $\sigma_o = 700$ MPa (solid curve) is labeled as $K_{max\ trans}$ in Figure 3.24a (near $K_{max} = 8$ MPa$\sqrt{m}$). In this case, tip contact occurs for $K_{max} > 8$ MPa$\sqrt{m}$ and asperity contact

[19] This implies that threshold occurs when $\Delta K_{eff} = 0$ or $R_{cl} = 1$, and will be discussed in Section 5.1.4.

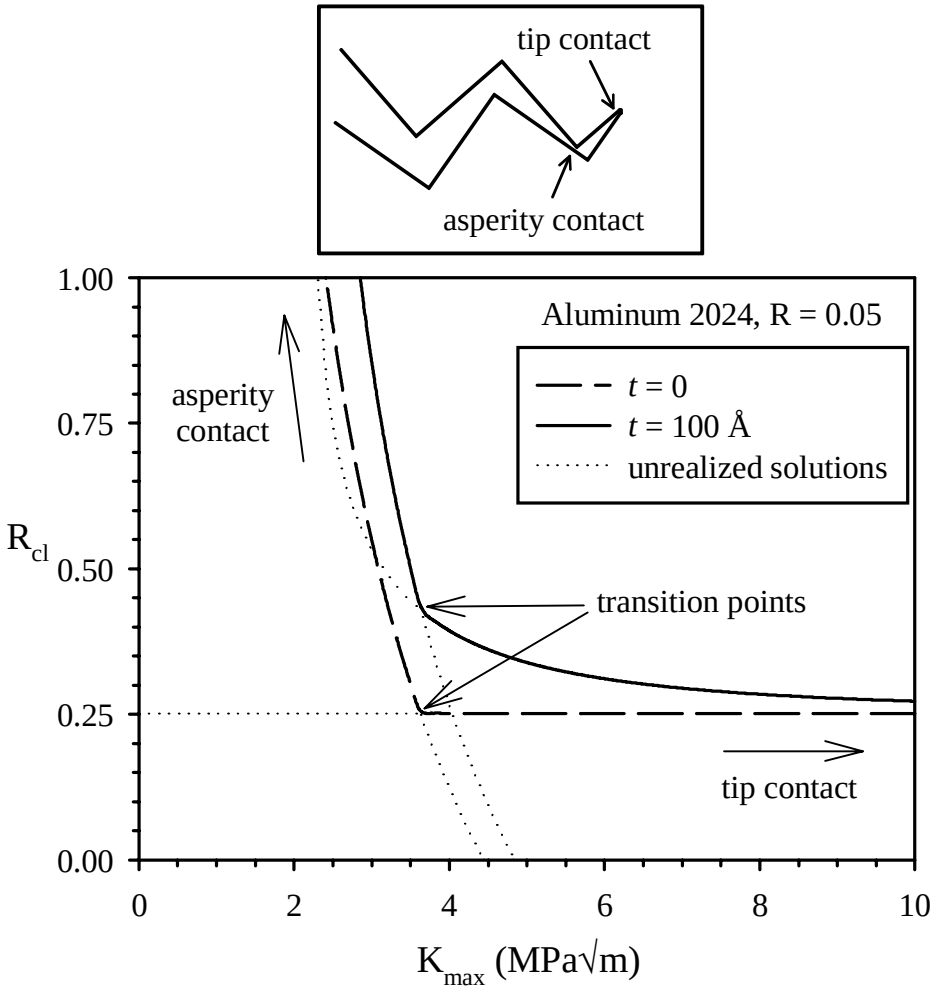

Figure 3.23 – Plot of closure level, R_{cl}, versus K_{max} as typically presented in literature. Results for R = 0.05 and two values of oxide thickness, t = 0 Å and 500 Å, are shown.

occurs if K_{max} < 8 MPa√m. Further K_{max} reduction (below $K_{max\ trans}$) produces rapidly increasing closure levels, until the crack is fully closed, *i.e.* R_{cl} = 1. The fully closed condition occurs near K_{max} = 6 MPa√m for σ_o = 700 MPa, labeled in the figure as $K_{max\ fc}$. Although not labeled for other curves, both $K_{max\ trans}$ and $K_{max\ fc}$ decrease with decreasing σ_o. A greater amount of plasticity is expected with a reduction in σ_o, but this does not increase closure levels because the asperity dimensions are small compared with plastic deformations, *i.e.* CTOD. In other words, crack roughness is more influential when the asperity dimensions are large compared with plastic deformations.

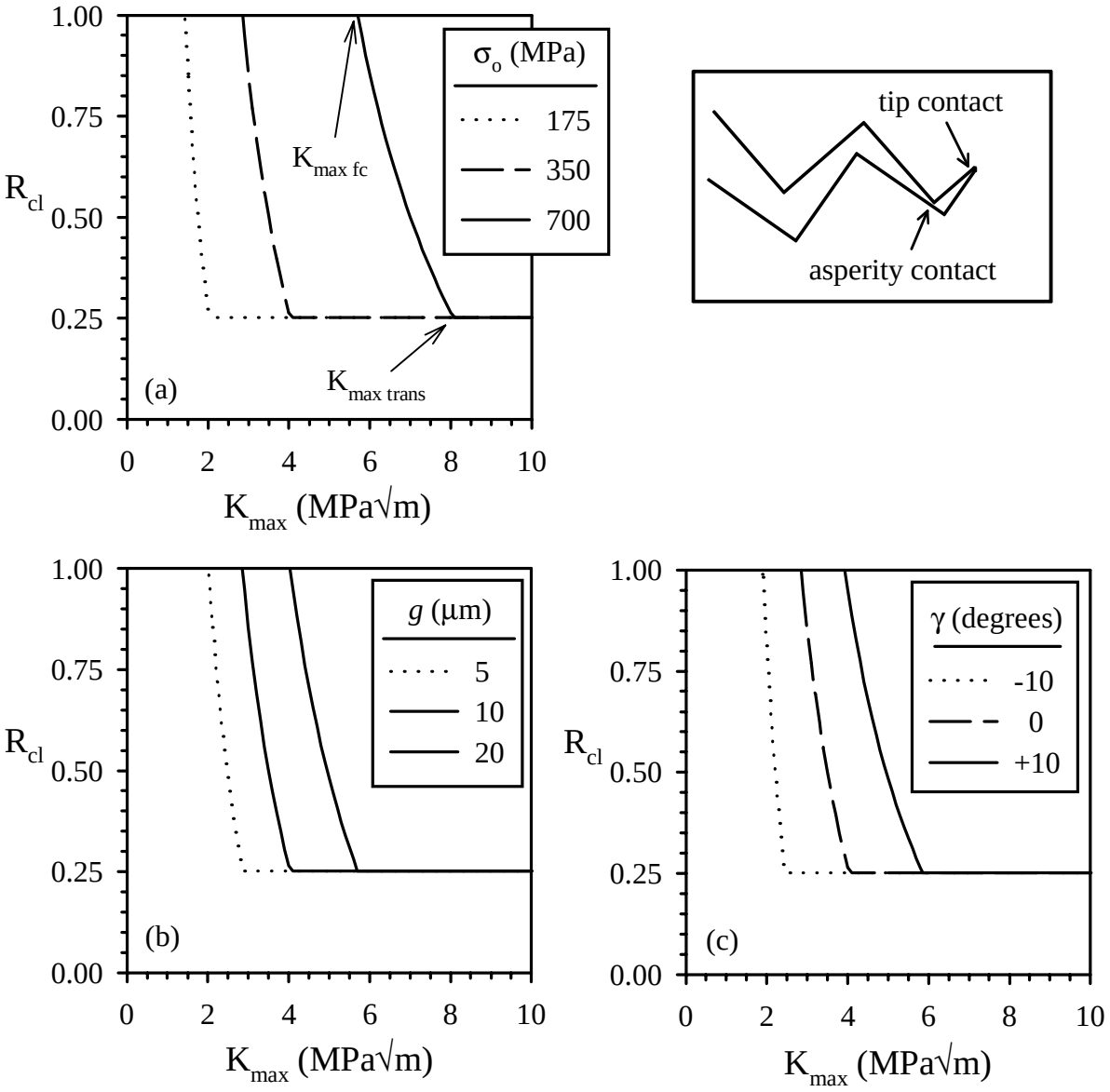

Figure 3.24 – Plots of closure level versus K_{max} for variable (a) yield stress, (b) asperity length, and (c) meandering angle.

In Figure 3.24b, model results are plotted for g = 5 μm, 10 μm, and 20 μm (shown as dotted, dashed, and solid curves, respectively). Although not labeled, the transition and fully closed points can be readily observed as done in part (a). Both $K_{max\ trans}$ and $K_{max\ fc}$ decrease with decreasing g. Consistent with the results of Figure 3.24a, a reduction in the ratio of asperity dimensions (g) to plastic deformations (constant for these curves) reduces the influence of crack roughness (lower R_{cl}).

Model results for three different values of crack meandering angles, $\gamma = -10^o$, 0^o, and 10^o, are shown in Figure 3.24c as dotted, dashed, and solid curves respectively. Negative values here indicate that meandering angle (γ) and asperity angle (α) are of opposite sign.

Although not labeled, both $K_{max\ trans}$ and $K_{max\ fc}$ decrease with decreasing γ. A negative meandering angle reduces the effective asperity angle considered with respect to the (mode I) loading axis, while positive γ increases the angle of the crack tip with respect to the loading axis.

The relationship between $K_{max\ trans}$ and $K_{max\ fc}$ and the model parameters, (a) σ_o, (b) g, and (c) γ, are plotted in Figure 3.25. In Figure 3.25a, $K_{max\ trans}$ and $K_{max\ fc}$ are plotted against σ_o as dashed and solid curves, respectively. As seen in the figure, both $K_{max\ trans}$ and $K_{max\ fc}$ increase linearly with increasing σ_o. Three regions are indicated in this figure; tip contact, asperity contact, and closed. Above the dashed line (high values of K_{max}) tip

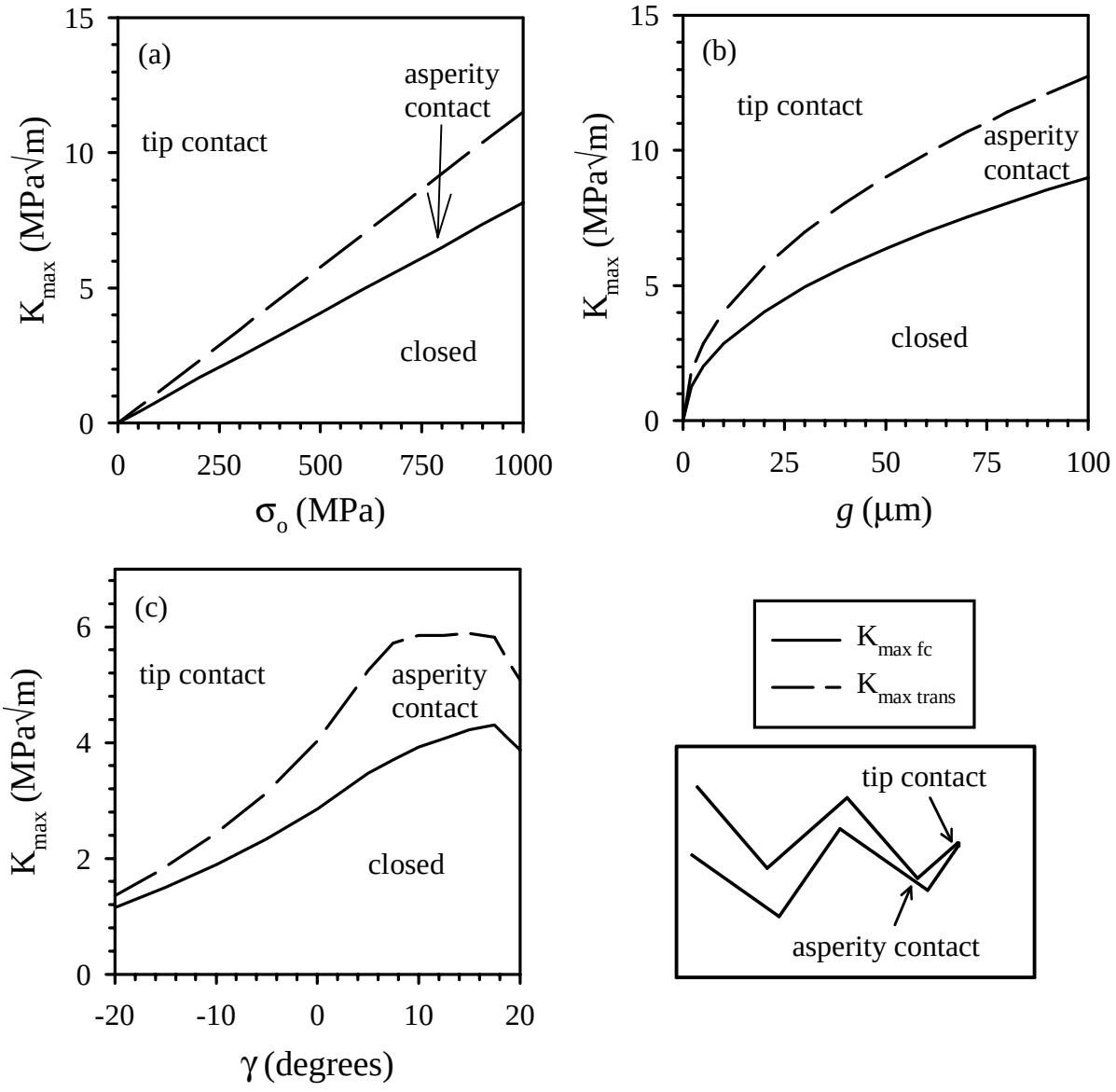

Figure 3.25 – Plots of closure levels against (a) yield stress, (b) asperity length, and (c) meandering angle.

contact occurs. Between the solid and dashed curves, crack face contact first occurs at the asperity closest to the crack-tip. As seen in Figure 3.24, this is the region associated with rapidly increasing closure levels, likely associated with threshold. Below the solid curve the crack is closed. For all other parameters equal, an increase in σ_o leads to an increase in R_{cl}.

In Figure 3.25b, $K_{max\ trans}$ and $K_{max\ fc}$ are plotted against asperity length, *g*, as dashed and solid curves, respectively. Similar to Figure 3.25a, three regions are shown in Figure 3.25b; tip contact (above the dashed curve), asperity contact (between the dashed and solid curves), and closed (below the solid curve). Both $K_{max\ trans}$ and $K_{max\ fc}$ increase with increasing *g*, but the relation is not linear as in part (a). Although only asperity contact was considered in the Ravichandran RICC model [37], similar transitions were observed with increasing yield stress and asperity length [62].[20] For all other parameters equal, an increase in *g* leads to an increase in R_{cl}.

$K_{max\ trans}$ and $K_{max\ fc}$ are plotted against meandering angle, γ, in Figure 3.25c, as dashed and solid curves, respectively. Three regions are also indicated here; tip contact (above the dashed curve), asperity contact (between the dashed and solid curves), and closed (below the solid curve). Both $K_{max\ trans}$ and $K_{max\ fc}$ appear to reach peak values in the range of $10^o < \gamma < 20^o$. At large values of γ, large mode II crack-tip stress intensity factors are expected. As discussed later in Section 6.1.2, sliding mode crack closure is likely here, and is not considered by this model. Consequently, the reduction in $K_{max\ trans}$ and $K_{max\ fc}$ beyond $\gamma = 15^o$ is not of interest and this model should not be used if $\gamma > 15^o$. For $-15^o < \gamma < +15^o$, and all other parameters equal, an increase in γ leads to an increase in R_{cl}.

3.6 — EXPERIMENTAL VERIFICATION

Although the model developed here appears to produce reasonable results, it must be verified with experimental data. First, the model is compared with experimental data where only PICC is an active closure mechanism. Later, OICC and RICC are considered. In this way, simple cases are studied before considering more complicated cases so individual closure mechanisms can be analyzed separately. Model results are compared with experimental data in published literature and data generated here. For data generated here, closure measurement are taken using back-face strain and a novel near-tip measurement technique called Digital Image Displacement System (DIDS)[21] [63]. Additionally, a new (qualitative) technique was developed here to ensure that remote closure (due to load history effects) did not occur for aluminum alloy 8009. These closure measurement techniques are described in Appendix C.

[20] Ravichandran considered the effect of grain size, but related it to asperity length of a sawtooth crack.
[21] DIDS (Digital Image Displacement System) is a technique to determine closure behavior using a series of high-magnification digital images of the crack-tip region. This allows closure behavior to be determined at the crack-tip rather than the "averaged" value produced using compliance techniques. Detailed descriptions of all crack closure measurement techniques are given in Appendix C.

3.6.1 — Plasticity induced crack closure (PICC)

Validation of the plasticity portion of the closure model requires closure measurements to be taken during FCG tests where RICC and OICC are minimal or eliminated. The formation of an oxide layer can be eliminated by performing FCG tests in ultra-high vacuum (UHV, see Appendix B). Elimination of RICC can be done using an alloy that produces a smooth fatigue crack surface. Aluminum alloy 8009 was selected because it has a very fine grain structure (approximate grain diameter of 0.5 μm, see Appendix D) that results in a very flat and featureless crack surface for low R FCG. Thus, FCG tests were performed on aluminum alloy 8009 in UHV at R = 0.05, as described in Appendix B. Constant ΔK tests are performed at several values of K_{max} (and R = 0.05) until steady state FCG was achieved, and fatigue crack closure measurements taken using both DIDS and compliance (back-face strain) techniques. Care is taken to ensure that remote closure is eliminated. (For example, specimens are pre-cracked at low loads and tests performed in order of increasing K_{max}.) UHV closure data is plotted in Figure 3.26 against K_{max}. Compliance and DIDS measurements are indicated by closed circular and triangular symbols, respectively. Model results, using parameters appropriate for 8009 aluminum, are indicated by the horizontal dotted line. (Recall from Figure 3.9b that closure levels for a straight crack with no oxide are R_{cl} = 0.252 for all alloys at R = 0.05.) Data generated in laboratory air is also shown as open symbols (circular and triangular symbols for compliance and DIDS results, respectively). Experimental data is in good agreement (less than 20% deviation) with model results for both UHV and laboratory air environments. Similar closure levels in UHV and laboratory air suggest the naturally forming oxide (in laboratory air) is too thin to significantly affect closure levels for K_{max} > 2 MPa√m. FCG threshold (10^{-10} m/cycle) for 8009 aluminum at R = 0.05 occurred near K_{max} = 2 MPa√m, so results for lower K_{max} were not produced. Furthermore, DIDS measurements (near-tip) were consistently higher (approximately 15%) than far-field compliance measurements. In fact, the DIDS result was greater than the compliance result for every data pair shown in Figure 3.26. This suggests that fatigue crack closure was greatest at the crack-tip and premature contact away from the crack-tip (remote closure) did not occur (see Appendix C). Additionally, closure data for aluminum alloy 8009 (T-L) from McEvily are plotted in Figure 3.26 as cross-hair symbols (+) [57]. The McEvily data was produced in laboratory air, at R = 0.05, and 20 Hz. (See Table D.2 for details of the specimen configuration.) Fatigue crack closure measurements were made using back face strain measurements. These data indicate closure levels increase slightly as K_{max} decreases, which was attributed to RICC. Although McEvily reported an increase in R_{cl}, these data are within 50% of model predictions. However, the RICC explanation seems unlikely because 8009 aluminum produces very smooth fatigue crack surfaces at low R. A more likely explanation for the increased closure level deals with load history effects, *i.e*. remote closure. McEvily reduced ΔK by decreasing the load in steps no greater than 9% of the peak load. As indicated in Appendix C (specifically, Figure C.1), step reductions in load can promote remote closure for 8009 aluminum. Two important observations are made from Figure 3.26; (1) the PRO model is in good agreement with experimental results where PICC is the only closure mechanism and (2) further testing in UHV is not necessary for 8009 aluminum because the OICC contribution in laboratory air is not detectable by DIDS.

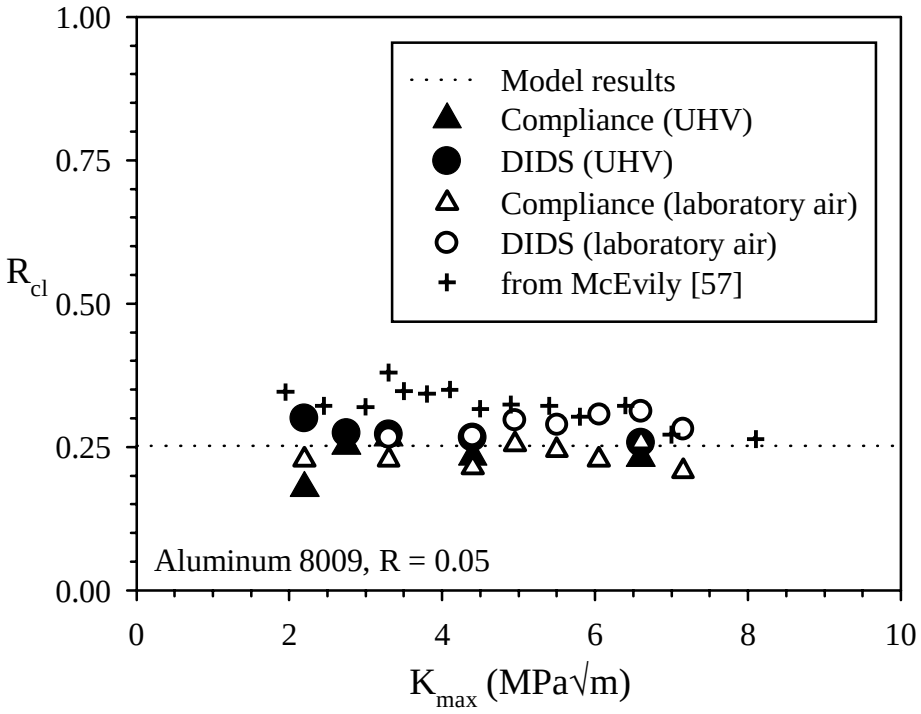

Figure 3.26 – Experimental closure data obtained from aluminum alloy 8009 tested at R = 0.05 in both UHV and laboratory air. Closure measurements using DIDS (near-tip) and back-face strain data are shown. The horizontal dotted line corresponds model results. Additional data for 8009 (T-L) is shown as cross-hair symbols (+) [57].

3.6.2 — Plasticity and oxide induced crack closure (PICC and OICC)

Now that the plasticity portion of the PRO closure model is supported by experimental data, the effect of crack mouth oxide is studied. As suggested from Figure 3.26, naturally forming oxide layers are too small to produce detectable closure levels. Furthermore, it was determined that testing in pure oxygen at room temperature (23 ^{o}C) and elevated temperature (121 ^{o}C) also failed to produce an oxide layer thick enough to be detected by DIDS. Thus, an artificial oxide layer is needed and was accomplished by injecting small particles into the crack. Alumina powder (Al_2O_3), commonly used to polish metal surfaces, is readily available in a variety of fine uniform particle sizes. Two grades of alumina powder were obtained with average particle diameters of 0.05 and 0.30 μm (500 and 3000 Å). (Recall that naturally forming oxide layers on aluminum surfaces are typically 10 Å [53].)

The alumina powder (Al_2O_3) was mixed with alcohol to produce a liquid solution (called slurry) to help permeate all regions of the crack surface. Alumina slurry was injected into the crack after steady state FCG was achieved. The specimen was loaded to (approximately) 95% of the maximum load to ensure an open crack-tip, without risking an accidental overload. As the powder concentration in the solution increased gradually,

increased closure levels were monitored. Further increases in powder concentration did not increase closure levels once a critical alumina powder concentration was reached. The powder concentration was increased above this critical value by 50% to ensure enough powder was present to produce consistent results. The final mixture for both powder sizes was 3 mL of alumina powder mixed with enough alcohol to increase the total volume to 10 mL. Based on SEM examination of fatigue crack surfaces, agglomeration of particles was a concern, although no particle agglomeration was observed in the crack-tip region. (Some agglomeration did occur far from the crack-tip, producing an artificial remote closure effect. This will be discussed in Section 3.7.) Injection of the slurry was done from both sides of the specimen using a syringe. The slurry washed through the open crack mouth and out of the opposite side of the specimen. The alcohol evaporated quickly, leaving the particles distributed along the crack surfaces. (The distribution of particles along the crack surfaces will be examined in Section 3.7.) After injecting the slurry into the crack, the specimen was returned to mean load, and the test restarted moments later. Because the presence of alcohol at the crack-tip may affect FCG rates, this technique was used only as a tool to study the contribution of crack mouth oxide to fatigue crack closure levels.

Closure levels using both near-tip (DIDS) and compliance techniques, were obtained after injection of slurry into the crack mouth, but before significant crack growth occurred. Again, aluminum alloy 8009 was used to eliminate RICC and testing was performed (as described in Appendix B) at R = 0.05 in laboratory air. Here, only PICC and OICC are active closure mechanisms. Experimental data and model predictions are plotted against K_{max} in Figure 3.27a after 0.05 μm slurry was injected into the crack mouth. DIDS and compliance data are indicated by closed and open symbols, respectively. Model results (using a total oxide thickness of 500 Å, parameters for 8009 aluminum in Table 3.1, and R = 0.05) are plotted as a solid curve. Model results agree well with the DIDS data for $K_{max} > 5$ MPa√m. Here, the compliance measurements were consistently lower than the corresponding DIDS measurements. For $K_{max} < 5$ MPa√m, closure measurements deviated from model results. It will be shown in Section 3.7 that this is due to alumina particles not reaching the crack-tip. (As indicated in Figures 3.11 and 3.12, closure levels decrease significantly if an oxide layer in the crack mouth fails to reach the crack-tip.) At $K_{max} < 4$ MPa√m (labeled A in the figure), the crack opening at maximum load (14% of $CTOD_{max}$ considering crack wake plasticity at R = 0.05) was less than the average particle diameter, so oxide at the crack-tip is not expected.

The same experimental procedure was repeated with 0.30 μm alumina particles. Results are presented in Figure 3.27b, as done for 0.05 μm particles. DIDS and compliance data are indicated by closed and open symbols, respectively. Model results for a total oxide thickness of 3000 Å are shown as a solid curve, using parameters for 8009 aluminum. The model results agreed well with DIDS data for $K_{max} > 13$ MPa√m. Compliance measurements were generally less than DIDS values. For $K_{max} < 13$ MPa√m the experimental data is significantly less than model predictions, probably because alumina particles did not reach the crack-tip. For $K_{max} < 12$ MPa√m (indicated as point B in the figure), the crack opening at maximum load (14% of CTOD considering crack wake plasticity) equaled the average particle size, so no particles are expected at the crack-tip.

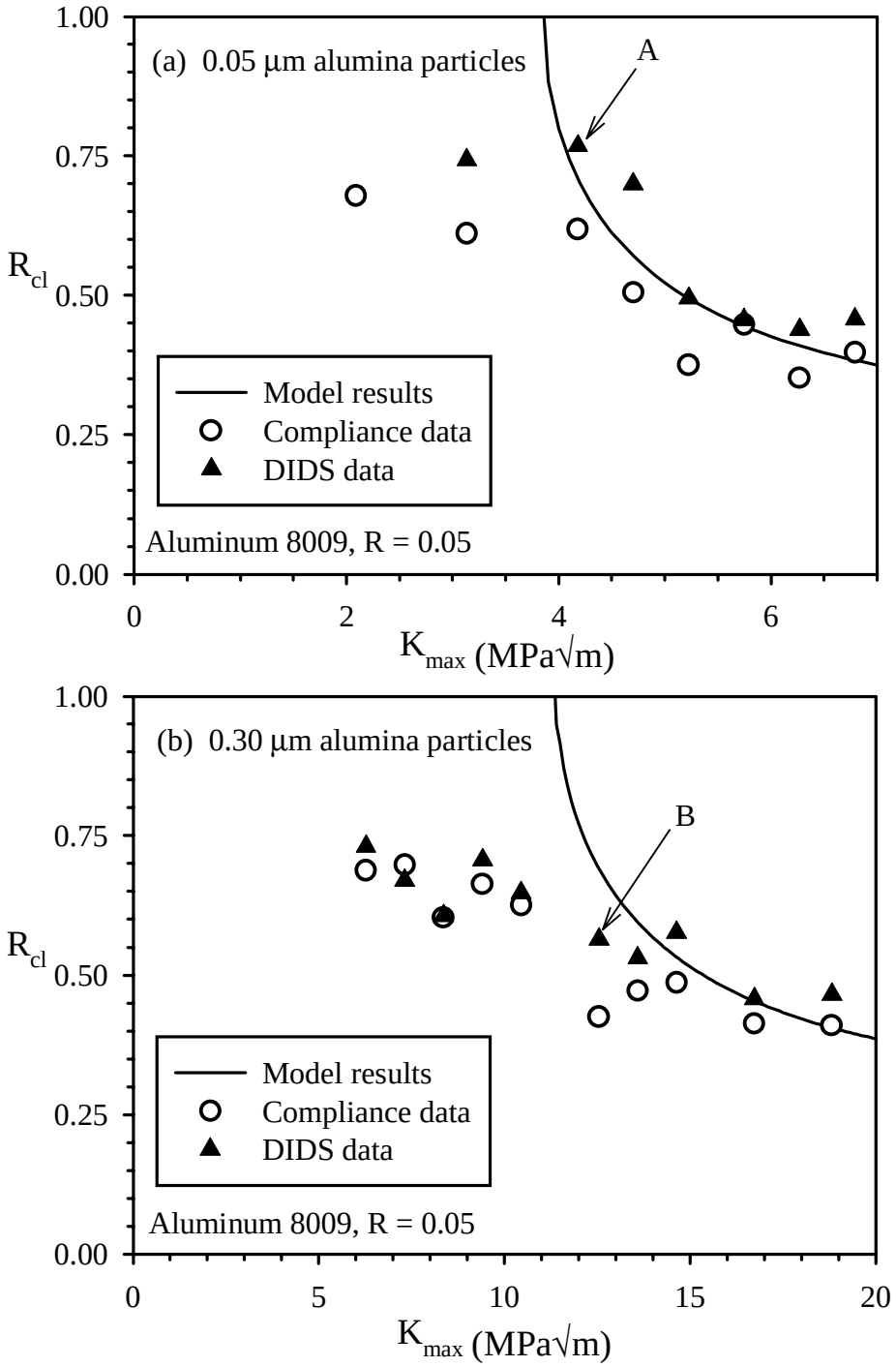

Figure 3.27 – Experimental closure data obtained from aluminum alloy 8009 tested at R = 0.05 in laboratory air, after (a) 0.05 μm and (b) 0.30 μm alumina particles were inserted into the crack mouth. Model results are indicated by the solid curve.

Fatigue crack closure data has been presented by Ruppen for a drill pipe steel tested in a (H_2S) brine solution [54]. Testing was done at R = 0.1 and 4 Hz for both increasing and decreasing ΔK (or K_{max}). Closure levels from Ruppen are plotted against K_{max} in Figure

3.28. Increasing and decreasing K_{max} data are shown as open circular and closed triangular symbols, respectively. Values of K_{max} for fully closed cracks ($K_{max\ fc}$) are indicated as A and B for decreasing and increasing K_{max}, respectively. Point A occurred at K_{max} = 7.7 MPa√m, and point B occurred at K_{max} = 10.9 MPa√m. According to model results (for a straight crack configuration) the oxide layers corresponding to these points are approximately 360 Å and 700 Å, respectively. Because testing occurred in a brine solution, a thick layer of black oxide was seen in the crack mouth. Little quantitative information was given regarding the oxide thickness. For increasing K_{max} conditions, Ruppen measured the oxide layer as approximately 1 μm (1000 Å) thick at the surface [54]. It is not clear if the oxide debris seen at the surface was in the crack or squeezed out of the crack mouth. Because little quantitative information about the oxide layer was available model results are presented for four different oxide layers, t = 0, 250 Å, 500 Å, and 1000 Å (plotted in the figure as dotted, dashed, solid, and dash-dot curves, respectively). The model parameters used here are listed in Table 3.1. Although no roughness information is presented, the presence of a thick oxide layer is expected to enhance tip contact and reduce the influence of crack roughness (see Figure 3.18). Model results for t = 1000 Å is considered to be an upper bound and results for t = 0 (straight crack with no oxide) are shown for reference. As K_{max} increases above 30 MPa√m, model results approach the straight crack result. Model results for t = 1000 Å slightly

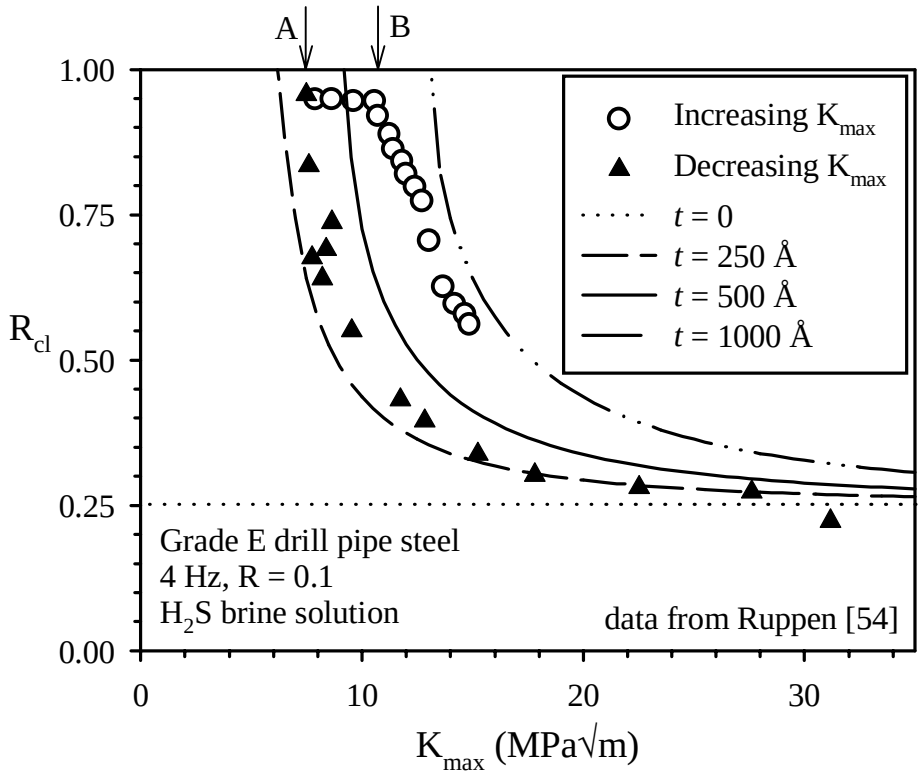

Figure 3.28 – Plot of closure level versus K_{max} for steel specimens tested in brine solution. Results for increasing and decreasing K_{max} are shown as open and closed symbols, respectively. Model results are indicated for several oxide layers as line curves.

over-predict closure levels for the increasing K_{max} data. The decreasing K_{max} data appeared to follow model results for t = 250 Å, a plausible value for oxide thickness. Model results for t = 500 Å lie between the two sets of data. Because specific values of oxide layer thickness are difficult to determine from the available information, the differences between model results and data are considered less important than trends, *e.g.* shape of the curves. In Figure 3.28, the data and model results have the same shape, which suggests that the model is accurately describing the relationship between PICC and OICC.

To further test the model, closure behavior of a fatigue crack growing away from alumina particles (inserted into the crack) was also studied. Model results presented in Figures 3.12 and 3.13 suggest that the influence of oxide rapidly diminishes as distance between the crack-tip and oxide (Δa) increases. Experimental data was generated for fatigue cracks growing away from 0.05 μm alumina particles at two K_{max} levels (4.4 and 4.95 MPa$\sqrt{m}$ at R = 0.05). This load range was chosen because it produced the greatest (initial) closure levels still in good agreement with model predictions (refer to Figure 3.29a).

Steady state FCG conditions were achieved for K_{max} = 4.4 MPa$\sqrt{m}$ (R = 0.05) before injecting 0.05 μm slurry into the crack. DIDS and compliance techniques were used to measure closure levels periodically as the crack grew away from the oxide particles. The experimental data, R_{cl}, plotted against the increase in crack length, Δa, are presented along with the model predictions in Figure 3.29a. DIDS and compliance data are indicated by triangular and circular symbols, respectively. Model results are shown as a solid curve, which predicts the oxide layer becomes ineffective at $\Delta a_{trans} \approx 10$ μm (indicated in the figure as "model Δa_{trans}"). After slurry was injected into the crack, the visual crack length (surface measurement), a_{vis}, diverged from the compliance value, a_{comp}. According to compliance data, FCG resumed immediately after cyclic loading was restarted. However, visual crack measurements indicated no FCG occurred until a_{comp} increased nearly 100 μm. During further crack growth, a_{vis} increased but lagged approximately 100 μm behind a_{comp}. Because model predictions agreed best with experimental data plotted against a_{vis}, visual crack measurements were used in Figure 3.29. The DIDS data presented in the figure are slightly higher than the predicted values, but otherwise follows model results. (Recall, from Figure 3.26 that DIDS measurements were consistently higher than compliance measurements.) The DIDS data indicate that the oxide layer becomes ineffective near $\Delta a_{trans} \approx 17$ μm (indicated in the figure as "data Δa_{trans}"). Compliance-based closure levels decrease slower than predicted, and are in poor agreement with model results for the first 100 μm of (visual) crack growth. Elevated compliance closure levels are likely due to remote closure at agglomerated particles. In light of results presented in Chapter 4, differences in a_{vis} and a_{comp} during this test may result from crack tunneling at high R (for 8009 aluminum). Although $R_{applied}$ = 0.05, the effective value, R_{cl}, was approximately 0.75 after particles were inserted into the crack.

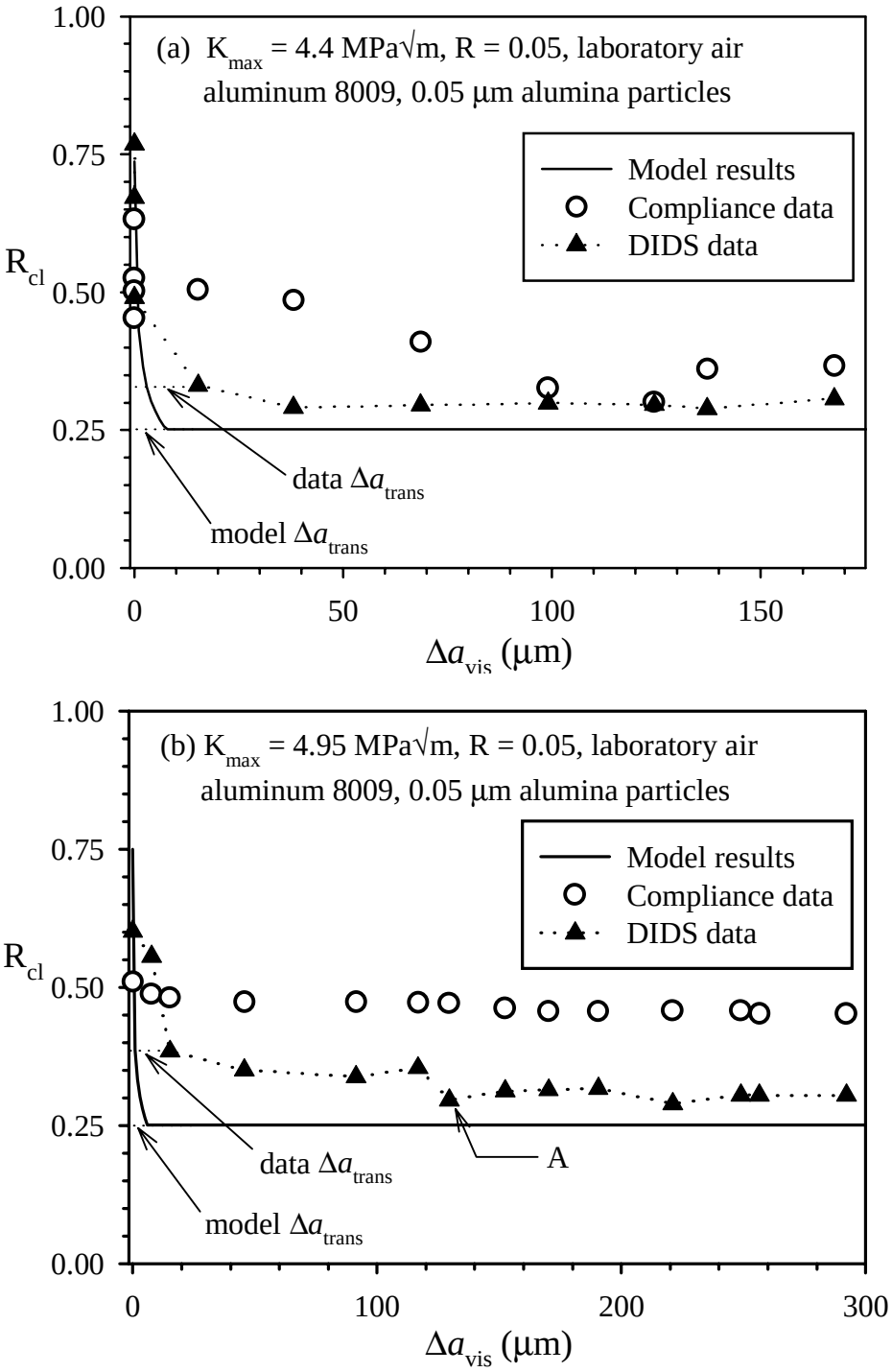

Figure 3.29 – Closure levels, R_{cl}, plotted against the change in crack length after the addition of oxide into the crack, are shown here. Results correspond to aluminum alloy 8009 FCG (away from 0.05 μm alumina particles) at R = 0.05, (a) K_{max} = 4.4 MPa√m and (b) K_{max} = 4.95 MPa√m, and in laboratory air.

The test results of Figure 3.29a were repeated, expect the value of K_{max} was increased to 4.95 MPa√m. The values of a_{vis} and a_{comp} agreed well during this test. (The initial effective R in this case was reduced to 0.60 decreasing the likelihood of crack tunneling.) Data for this test are plotted against Δa_{vis} in Figure 3.29b. Similar to part (a), the DIDS data in part (b) follows the trend suggested by the model results, although actual closure levels are greater than predicted. The values of Δa_{trans} for model and data are approximately 7 μm and 17 μm, respectively, and indicated in the figure as "model Δa_{trans}" and "data Δa_{trans}." Compliance closure measurements decrease much slower than crack-tip measurements (DIDS), possibly due to remote agglomeration of particles.

The DIDS data presented in Figure 3.29 correspond to contact at or just behind (within 20 μm) the crack-tip. Because of the difference in compliance and near-tip values, DIDS measurements were taken, well behind the crack-tip. This was done for only one case (after 130 μm of visual crack growth from 0.05 μm particles at K_{max} = 4.95 MPa√m), indicated by point A in Figure 3.29b. Point A was chosen because the difference between the DIDS and compliance results were large and no crack tunneling was suspected. DIDS results are plotted as a function of distance behind the crack-tip in Figure 3.30. The compliance value is indicated by a solid line at $R_{contact}$ = 0.506. A line is used for the compliance datum because closure is reduced to single "average" value. $R_{contact}$ is used instead of R_{cl} to indicate that this was not a crack-tip measurement. The

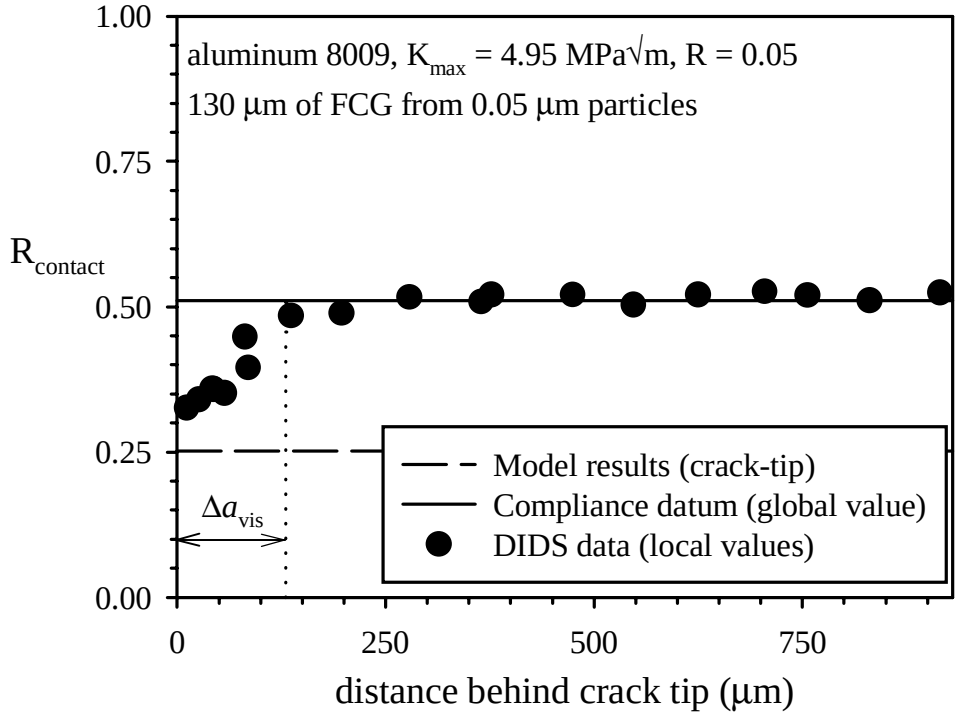

Figure 3.30 – Crack face contact data, $R_{contact}$, plotted against distance behind the crack-tip is shown here. The conditions for this data correspond to that of point A in Figure 3.30b. The model prediction is indicated by the horizontal dotted line (R_{cl} = 0.252), while the compliance datum is shown as a horizontal dashed line (R_{cl} = 0.506).

model prediction is indicated by the horizontal dashed line at $R_{cl} = 0.252$. (Recall, that this corresponds to crack-tip closure.) The DIDS data in Figure 3.30 just behind the crack-tip are slightly higher (about 20%) than the model prediction. (Recall from Figures 3.26 through 3.29 that DIDS values are generally slightly higher than model predictions, possibly due to a small plane-stress bias at the specimen surface.) Further behind the crack-tip, $R_{contact}$ increases until Δa_{vis} is approximately 130 μm (where alumina particles are expected). Further behind the crack-tip, contact loads ($R_{contact}$) are in good agreement with the compliance measurement. The observations made from data in Figure 3.30 are, (1) remote closure probably occurs if compliance closure measurements are greater than DIDS results, and (2) compliance closure measurements are biased towards remote closure, and are not always a good indicator of crack-tip events.

3.6.3 — Roughness induced crack closure (RICC)

Results have shown that the closure model developed in this chapter is accurate for straight cracks (smooth crack surfaces) where PICC and OICC are closure mechanisms. Now crack roughness effects must be examined and is best done if other closure mechanisms can be eliminated. However, the nature of FCG makes elimination of PICC all but impossible. Regardless of crack-tip loads (K), an intense region of plasticity about the crack-tip (*i.e.* plastic zone) will always exist. Without applied loads, crack propagation will not occur. Crack wake plasticity will be recovered, using a shape memory alloy called Nitinol, composed of equal parts nickel and titanium (50% each, by molar content). For this composition, the alloy will be called Nitinol 50-50. Details of Nitinol 50-50 important to FCG are given in Appendix D. Shape memory alloys are capable of recovering plastic deformations by heating (above 93 ^{o}C) and cooling (a process called annealing) to cycle the material through a martinsite/austenite hysterysis loop. However, recent studies indicate that extremely intense deformations, or cyclic deformations, may not be completely recoverable [64]. In other words, the shape memory effect may be destroyed by deformations in the crack-tip process zone. It will be determined if crack-tip deformations are severe enough to damage the shape memory effect. A schematic of the (ideal) annealing process is shown in Figure 3.31. In part (a), an open crack is shown with residual plasticity in the crack wake prior to annealing. Plastic deformation in the crack wake is indicated as shaded regions. If the shape memory effect is not destroyed, crack wake plastic deformations will be recovered by annealing. This is indicated by the absence of hatched regions in part (b). Because $\xi \approx 0.86$ for $R = 0.05$, and no closure will occur for tensile loading if $\xi < 0.75$, only a 13% reduction in crack wake plasticity is needed for this technique to successfully eliminate PICC. During FCG after annealing, a crack wake will develop and steady state crack closure will be re-established (see Figure 3.31c).

FCG experiments were performed to evaluate the amount of crack wake plasticity recovered by annealing. Details of specimen configuration are given in Table D.2. Testing was performed in a UHV environment to eliminate oxide along the crack faces, *i.e.* no OICC. After steady state FCG was achieved, the specimen was heated to 121 ^{o}C

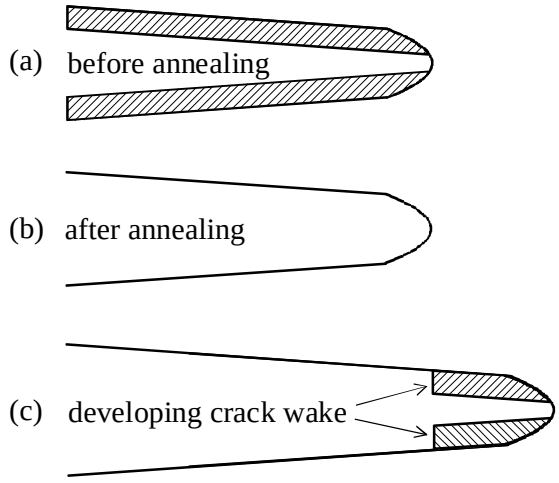

Figure 3.31 – Schematic illustrating (possible) recovery of crack wake plasticity (shown as hatched regions) before and after annealing a shape memory alloy specimen.

for 1 hour to recover the plasticity in the crack wake and at the crack-tip.[22] The applied load was held at 15 N (about 2% of the maximum load) to ensure that high temperature deformation mechanisms (*e.g.* creep) would not occur. After the specimen was cooled, the fatigue loading was restarted and compliance closure measurements were periodically taken. (DIDS measurements were difficult because the vacuum chamber limited visual access to the specimen.)

Steady state FCG was achieved at K_{max} = 8.8 MPa$\sqrt{m}$ and R = 0.05. The steady state (compliance) closure level for these loads (R_{cl} = 0.190) was slightly less than for 8009 aluminum (R_{cl} = 0.240). The steady state FCG rate for these conditions was 1.07 x 10^{-9} m/cycle. After annealing, closure was not detected (using back face strain) for R < 0.05, indicating the recovery of plastic wake is at least partially successful. FCG was resumed until a steady state was re-established, and then annealed again. Crack length versus cycle data is presented in Figure 3.32 for this test. The specimen was annealed twice, indicated by vertical dashed lines. Steady state data is shown as closed circular symbols, while closure-free data after annealing is indicated as open square symbols. As the crack grew after annealing, a crack wake quickly began to form. The resultant transient data is plotted as open triangular symbols. Compliance closure measurements, R_{cl}, are plotted as closed square symbols at the bottom of Figure 3.32, using the vertical axis on the right hand side of the figure. The steady state closure value is shown as a horizontal dash-dot line. Immediately after annealing, closure levels were undetectable and FCG rates increased by a factor of 2 or 3. Here, the effective ΔK increased from 7.1 MPa$\sqrt{m}$ to 8.4 MPa$\sqrt{m}$. Similar changes in ΔK for existing FCG data on Nitinol 50-50 indicate that fatigue crack growth rates also increase by a factor of 2 or 3 [65, 66]. Three important observations made from Figure 3.32 are: (1) some crack wake plasticity can be recovered using a shape memory alloy and (2) the increase in fatigue

[22] Annealing at 121 ^{o}C was done to ensure that the austenite finish transition temperature (A_f) was exceeded (see Appendix D for details).

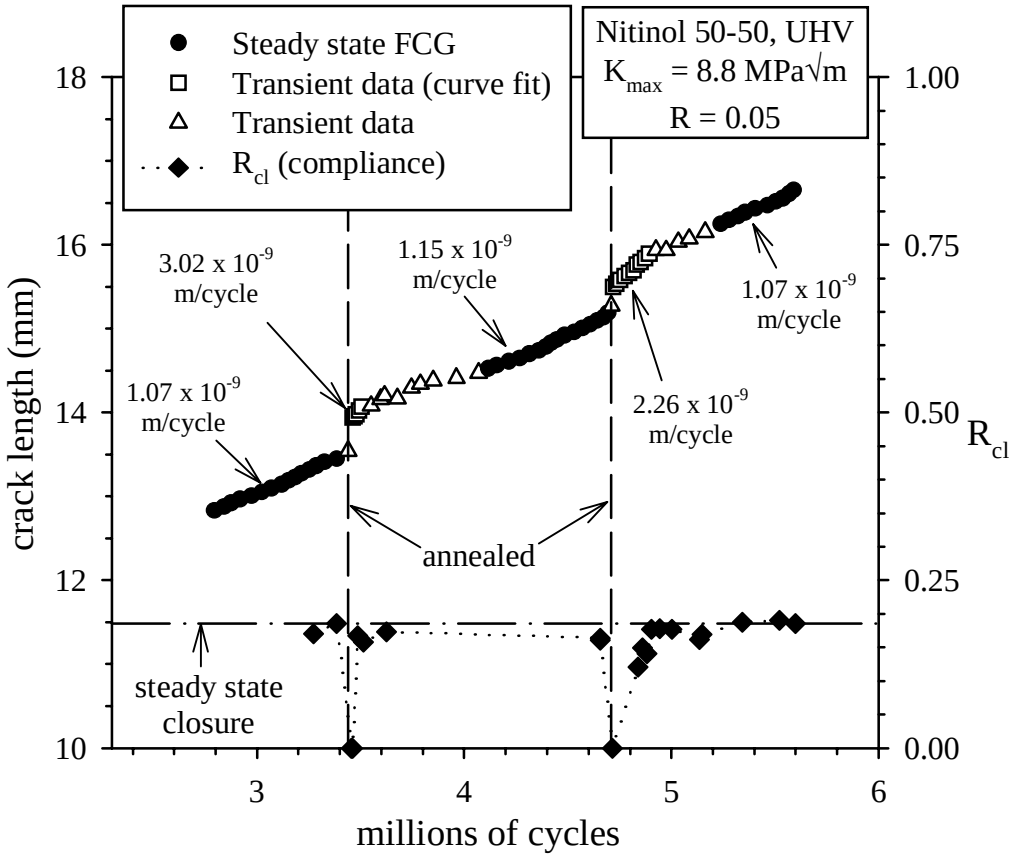

Figure 3.32 – Experimental data for Nitinol 50-50 before and after the specimen was annealed to recover crack wake plasticity. Cyclic loading was applied at K_{max} = 8.8 MPa√m, R = 0.05, and 11 Hz in UHV.

crack growth rate after annealing coincided with the decrease in measured closure levels, consistent with existing data considering the increase in ΔK_{eff}, and (3) steady state closure levels and FCG rates are quickly re-established with further crack propagation.

The results shown in Figure 3.32 only suggest that closure levels are less than K_{min}. To determine the amount of residual crack wake plasticity (after annealing), closure was monitored as a fatigue crack grew following an overload (*i.e.* larger MPZ). Steady state crack growth was established at K_{max} = 8.8 MPa√m, and R = 0.05, before an overload of K_{ol} = 15.4 MPa√m (R_{ol} = 1.75) was applied. As fatigue loading resumed, approximately 180 μm of FCG occurred prior to crack arrest. (Presumably crack arrest was a result of increased plasticity and crack closure). The specimen was then annealed to recover plastic deformation. After annealing, closure levels decreased and FCG resumed. Compliance closure measurements (R_{cl}) obtained during this procedure are plotted in Figure 3.33 against Δa_{vis}, the increase in (visual) crack length following the overload. The overload was applied at Δa_{vis} = 0, so negative and positive values of Δa_{vis} correspond to events before and after the overload, respectively. The crack lengths corresponding to

the overload and annealing are indicated in the figure by horizontal dotted lines. The change in crack length is normalized by the plane-strain overload MPZ, r_p^*, assuming σ_o = 90 MPa (see Figure D.5a), and is shown along the upper horizontal axis. Closure measurements before the overload (steady state) are indicated by closed circular symbols. The average value of steady state closure is R_{cl} = 0.190, indicated by the horizontal dashed line. The steady state data deviate less than 10% from the average value. Closure measurements taken after the overload, but before annealing, are plotted as open circular symbols. Immediately after the overload, no closure was detected. (Although this point is indicated in the figure at R_{cl} = 0, it can only be stated that R_{cl} < 0.05.) However, closure levels were above R_{cl} = 0.35 after approximately 100 μm of FCG. After annealing, closure levels were nearly R_{cl} = 0.25. These data are shown in the figure as open triangular symbols. As the crack grew through the overloaded region ($0 < \Delta a_{vis} / r_p^* < 1$), closure levels gradually decreased and approached the steady state value.

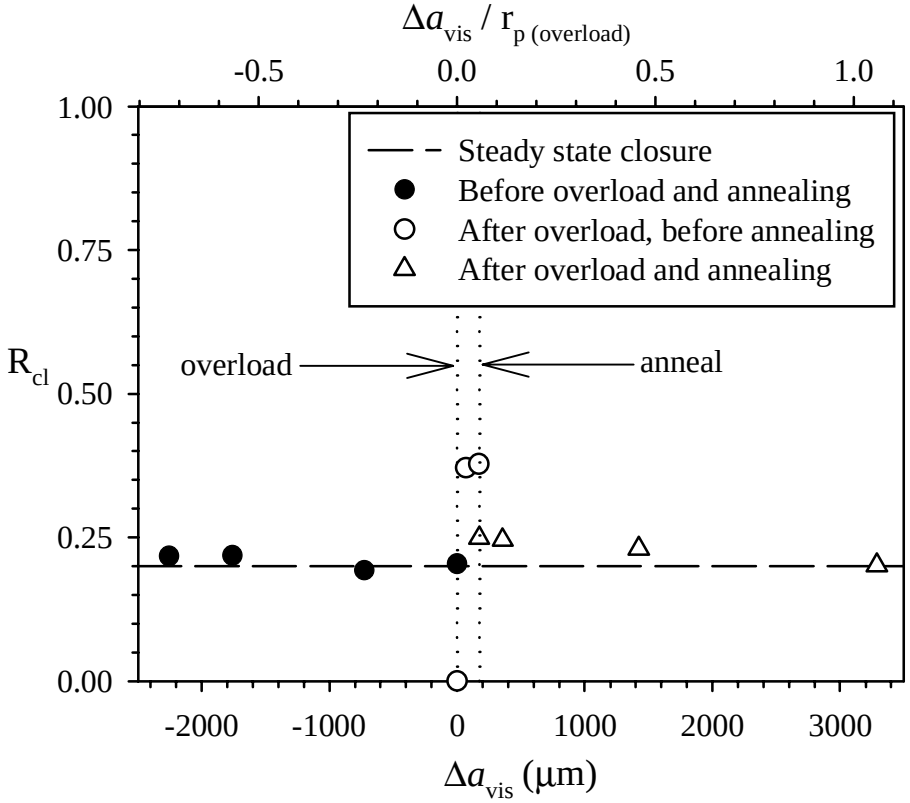

Figure 3.33 – Measured closure levels before and after application of an overload, and before and after subsequent annealing, of Nitinol 50-50.

In the overloaded region, closure levels after annealing were approximately R_{cl} = 0.25. Assuming residual plastic deformation is proportional to K_{max}^2 (recall Equation 3.5), the closure level after annealing a steady state MPZ (see Figure 3.32) should have been R_{cl} = 0.07. Two points are implied from this analysis; (1) after annealing a steady state crack wake (recall Figure 3.32), the minimum load was likely very near the closure load, and (2) recovery of the plastic wake is only partly successful, but enough to (nearly) eliminate PICC for tensile loading. (Figure 3.4a suggests only 13 % of plastic strain is recovered.)

The closure characteristics of Nitinol 50-50 were studied before and after annealing. Initially steady state FCG was established at K_{max} = 8.8 MPa√m and R = 0.05 (also in UHV at 11 Hz) where closure measurements were taken using DIDS. (Because DIDS measurements were complicated by limited visual access to the specimen, compliance measurements were used for data in Figures 3.32 and 3.33. DIDS measurements are used here so a distinction can be made between tip contact and asperity contact.) The crack was then loaded at K_{max} = 6.6 MPa√m and R = 0.05 for a few cycles to take closure measurements. Because no measurable FCG occurred, the crack wake and crack-tip plasticity were associated with K_{max} = 8.8 MPa√m, so the closure load (K_{cl}) should remain unchanged (but R_{cl} is should increase due to the reduction in K_{max}). In this way, closure measurements are also taken for K_{max} = 4.4 MPa√m and 2.2 MPa√m, both at R = 0.05. These data (before annealing) are plotted in Figure 3.34 as open circular symbols. The dashed curve corresponds to the closure load measured at K_{max} = 8.8 MPa√m, which fits the data (open circular symbols) well. This indicates that closure loads were constant and the increase in R_{cl} with decreasing K_{max} is not due to a change in closure mode (*i.e.* change from tip contact to asperity contact). The order of testing is indicated by arrows parallel to the curve. Tests were performed in order of decreasing K_{max} before annealing. After these four closure measurements, the specimen was annealed (as previously described) indicated in the upper left corner of Figure 3.34. Fatigue loading was restarted at R = 0.05 and closure measurements were taken at a variety of K_{max}. Since annealing is expected to partially recover both crack-tip and crack wake plasticity, closure

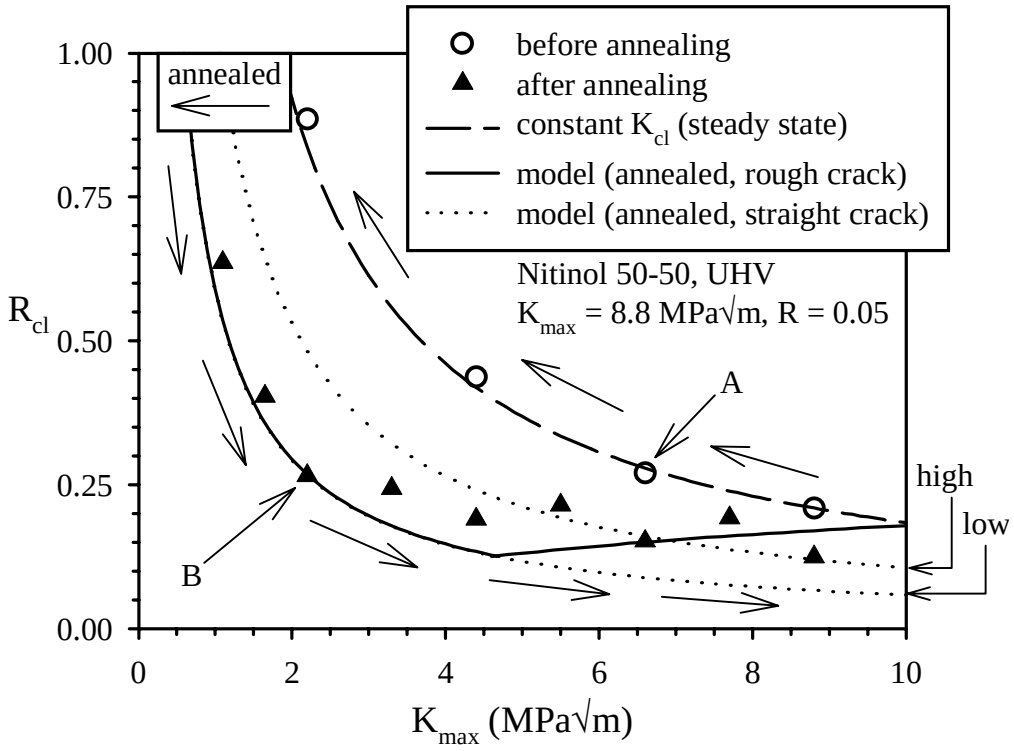

Figure 3.34 – Fatigue crack closure results for Nitinol, before and after annealing. Data after annealing suggest that closure mode changes from asperity contact to tip contact as K_{max} increases.

measurements were taken in order of increasing K_{max}. By doing this, the crack-tip plasticity increased, while the crack wake plasticity remained constant. (Recall, no measurable FCG occurred during this process.) Closure data taken after annealing are plotted as closed triangular symbols in the figure. The arrows parallel to the data indicate the order closure measurements were taken (in order of increasing K_{max}). Closure loads measured after annealing are not expected to be constant because crack-tip plasticity increases with increasing K_{max}, while the crack wake plasticity was constant. Two dotted curves are plotted in the figure, which correspond to constant closure loads at high K_{max} (6.6 MPa$\sqrt{}$m through 8.8 MPa$\sqrt{}$m) and low K_{max} (2.2 MPa$\sqrt{}$m through 1.1 MPa$\sqrt{}$m). These curves are indicated in the lower right corner of the figure by "high" and "low," respectively. Neither curve fits the data (closed triangular symbols) well over the entire range of data . This suggests a change in closure mode occurs. Model results, using parameters for Nitinol 50-50 (see Table 3.1), are plotted as a solid curve in the figure. Because testing occurred in UHV no oxide layer is expected (t = 0). The model results provide a good fit over the entire range of data. For K_{max} < 4.6 MPa$\sqrt{}$m, asperity contact is predicted, while tip contact is expected for K_{max} > 4.6 MPa$\sqrt{}$m. The transition between these closure modes can be seen in the figure as an abrupt change in slope near K_{max} = 4.6 MPa$\sqrt{}$m. The portion of the curve where tip contact occurs is not a straight line because the model was modified for constant *(i.e.* not steady state) crack wake plasticity (associated with K_{max} = 8.8 MPa$\sqrt{}$m after annealing).

Because a change in closure mode is predicted in Figure 3.34, two DIDS analyses were performed along the crack wake where tip contact and asperity contact are expected. These cases are indicated as points A and B in Figure 3.34, respectively. Tip contact is expected to occur at point A. The corresponding DIDS data are plotted, as a function of distance behind the crack-tip, in Figure 3.35a (open circular symbols). The corresponding compliance measurement is indicated as a horizontal dotted line. The first asperity behind the crack-tip was observed (at the surface) approximately 200 μm from the crack-tip, as indicated in the figure. The DIDS measurements indicate closure levels greater than compliance measurements at the crack-tip. The local contact levels ($R_{contact}$) approach the compliance value with increasing distance behind the crack-tip. Because $R_{contact}$ was greatest at the crack-tip and no increase in contact level was seen at the critical asperity, tip contact does indeed occur here. Recall from Section 3.4 that the location of first contact between crack faces determines the type of closure (*i.e.* "tip contact" or "asperity contact"). Similar data for point B (in Figure 3.34) are shown in Figure 3.35b, but asperity contact is expected in this case. As indicated in the figure, the maximum $R_{contact}$ occurs at the asperity nearest the crack-tip (200 μm), indicating asperity contact occurs. Elimination of crack wake plasticity produces a change in closure mode. Recall from Figures 3.17 and 3.18, that thicker oxide layers tend to eliminate asperity contact. Results in Figure 3.34 suggest that a decrease in crack wake plasticity (similar to a decrease in oxide thickness) tends to promote asperity contact. The observation that increased oxide eliminates RICC is now expanded to include any mechanism, including crack wake plasticity, that partially (but uniformly) fills the crack.

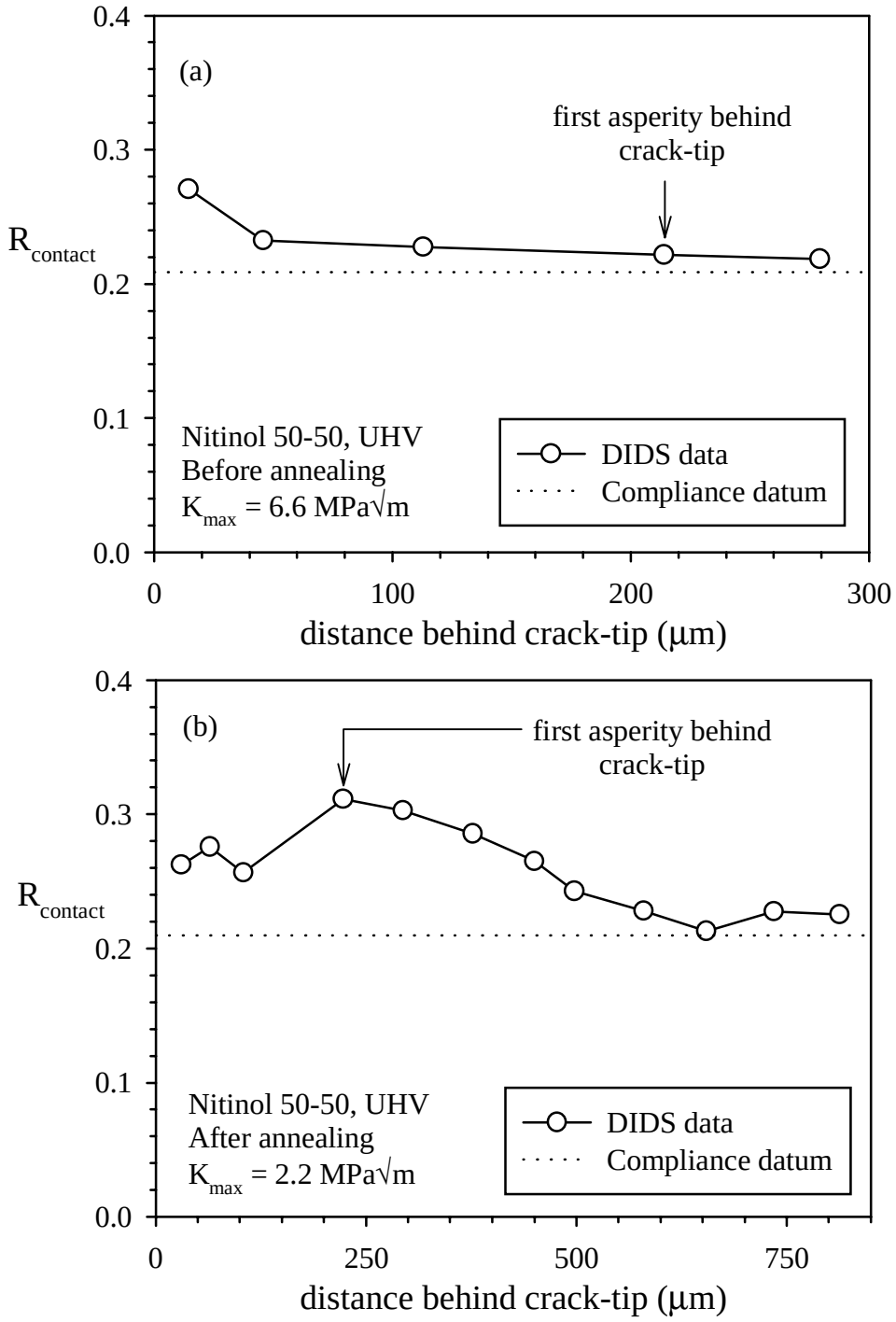

Figure 3.35 – Crack contact levels ($R_{contact}$) as a function of distance behind the crack-tip. Tip contact and asperity contact are expected in part (a) and part (b), respectively, at points A and B, respectively.

Two studies have been published that study RICC by comparing closure behavior for two different heat treatments of the same alloy. The difference in heat treatments primarily changes the texture of the microstructure without significantly altering mechanical

behavior, *e.g*. crack-tip plasticity. Fatigue crack closure data from Gray, *et al*., is presented for course grained (CG) and fine grained (FG) versions of AISI 1080 steel [58]. Testing was performed at R = 0.1, 30 Hz, and in a purified Helium environment. Model parameters were selected using details presented by Gray (see Table 3.1). Because Helium is inert, it is assumed that no oxide layer existed in the crack mouth. The CG and FG data are plotted in Figure 3.36a as closed triangular and open circular symbols, respectively. Corresponding model results for CG and FG configurations are indicated by dotted and solid curves. Tip contact is indicated by the horizontal portion of the curves at high values of K_{max} (> 14 MPa$\sqrt{m}$). Asperity contact for both cases is indicated by a rapid increase in R_{cl} with decreasing K_{max}. All data presented by Gray appears to correspond with asperity contact. No closure data is presented for higher K_{max} where tip contact is expected. As seen in the figure, the Gray data and model results are in good agreement.

A similar study was done on INCONEL 718 (a nickel-based alloy) by Drury, *et al.* [59]. Closure data for course grained (CG) and fine grained (FG) heat treatments of INCONEL 718 are plotted in Figure 3.36b. CG and FG data are indicated as closed triangular and open circular symbols, respectively. Model results using CG and FG parameters (see Table 3.1) are shown as dotted and solid curves, respectively. Testing was performed in laboratory air at R = 0.1 and 40 Hz. An oxide layer 10 Å thick (a value measured in reference [53] for aluminum) was assumed to exist because of the laboratory air environment. No information regarding oxide was provided by Drury. The transition from tip contact (at higher K_{max}) to asperity contact (at lower K_{max}) is seen as an abrupt slope change for both curves. Crack closure appears to occur at the crack-tip for all FG data shown in Figure 3.36b, although the data point at K_{max} = 11.7 MPa$\sqrt{m}$ appears to be near the transition to asperity contact. Although the FG data is slightly lower than predicted, they agree well with model predictions. Two of three CG data points agree well with model results. The point that disagrees with model results is labeled P. For this point, the model predicts the crack should be fully closed (*i.e*. threshold), but a result of R_{cl} = 0.55 is indicated. Otherwise, model predictions are in good agreement with data in Figure 3.36b.

The model results are compared with closure data for aluminum alloy 2024 tested in laboratory air at R = 0.1. Data for both constant R threshold tests (reducing ΔK and K_{max}) and constant ΔK tests are plotted in Figure 3.37 as circular and triangular symbols, respectively. Both compliance (back-face strain) and DIDS measurements are shown, indicated as open and closed symbols, respectively. Testing was performed in accordance with ASTM standards (see Appendix B). All three closure mechanisms considered here (PICC, RICC, and OICC) are likely to contribute. Model results corresponding to this data are indicated by the solid curve. Because testing was performed in laboratory air, an oxide layer 10 Å thick was assumed. (Recall, an oxide layer on an undisturbed aluminum surface is expected to be approximately 10 Å thick [53].) For K_{max} > 4.0 MPa$\sqrt{m}$, tip contact is predicted, with closure levels of (approximately) R_{cl} = 0.25. Here (K_{max} > 4.0 MPa$\sqrt{m}$), experimental results are slightly greater than model predictions. Asperity contact is predicted for 4.0 MPa$\sqrt{m}$ > K_{max} > 2.9 MPa$\sqrt{m}$, and closure levels increase from R_{cl} = 0.27 to R_{cl} = 1, as K_{max} decreases in

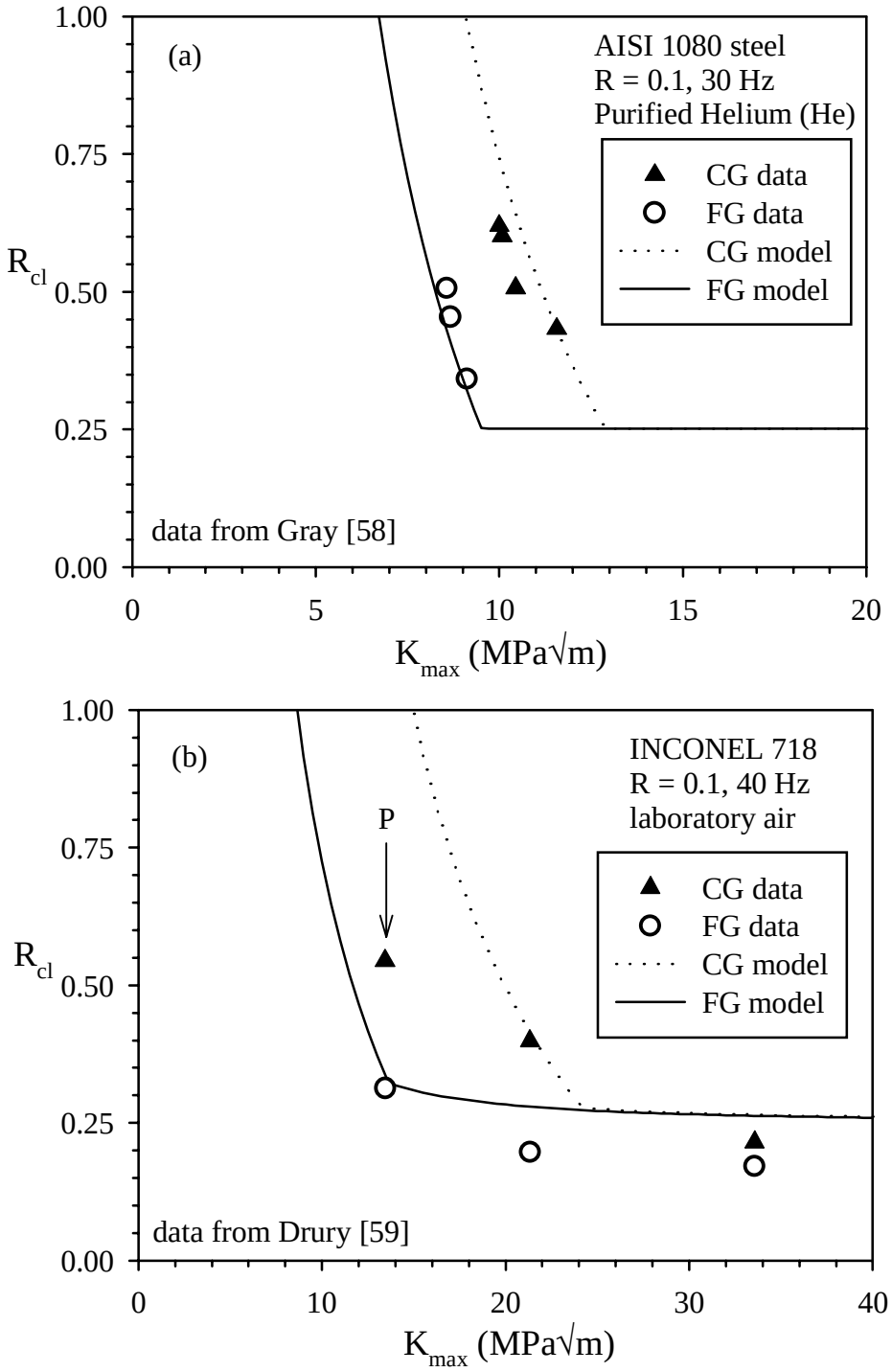

Figure 3.36 – Closure data for course and fine grained microstructures of (a) AISI 1080 steel and (b) INCONEL 718.

this range. Where asperity contact is expected, experimental data are slightly lower than model predictions. Model results agree well with the data in Figure 3.37, suggesting the PRO model works for all three closure mechanisms (PICC, RICC, and OICC).

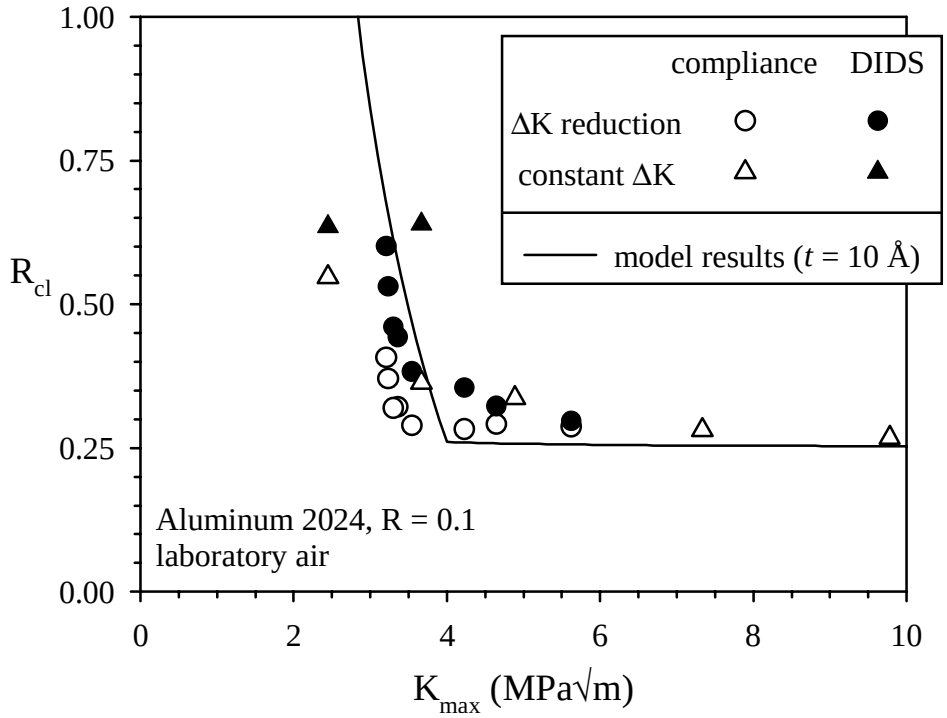

Figure 3.37 – Aluminum alloy 2024 closure data for constant R threshold tests and constant ΔK tests, at R = 0.1.

3.7 — FRACTOGRAPHY

To verify the OICC portion of this crack closure model, alumina particles were injected into 8009 aluminum fatigue cracks to simulate a thick oxide layer (see Section 3.6.2). This was done because naturally forming oxide layers were to thin for the OICC contribution to be detected. Although this technique successfully increased closure levels, three hypotheses were made to explain deviations between experimental data and model predictions. Fractographic evidence is given to support these hypotheses as described in the following paragraphs.

Crack closure levels were measured after inserting alumina particles into the crack mouth. The data are plotted in Figure 3.27 for (a) 0.05 μm particles and (b) 0.30 μm particles. Good agreement between experimental data and model results occurred for K_{max} greater than the transition points, labeled A and B in parts (a) and (b), respectively. Data deviated from model results for K_{max} values less than these transition points. Model predictions indicated that the crack configurations of Figure 3.27 would be fully closed for (a) $K_{max} < 3.9$ MPa√m and (b) $K_{max} < 11.6$ MPa√m. Because the crack opening is less than a particle diameter, it was hypothesized that the alumina particles did not reach the crack-tip. Model results presented in Figures 3.11 and 3.12 indicate that this may explain experimental results were less than predicted. To verify this hypothesis, fatigue crack growth specimens were broken after inserting alumina particles in the crack. Values of K_{max} were chosen on either side of the transition points (A and B) in Figure 3.27; K_{max} = 3.3 and 7.7 MPa√m for 0.05 μm particles, and K_{max} = 7.7 and 15.4 MPa√m

for 0.30 μm particles. Fractographs for each surface are presented in Figures 3.38 and 3.39, for 0.05 μm and 0.30 μm particles, respectively. In both figures, four images are presented. Low magnification and high magnification images are shown on the top and bottom rows, respectively. Columns correspond to a specific value of K_{max}, indicated at the top of each column. Images are shown in the left column where particles are not expected to reach the crack-tip (lower K_{max}). The right columns in Figures 3.38 and 3.39 are associated with higher K_{max} where particles are expected to reach the crack-tip. The crack front at fracture is labeled A in each figure. Near the specimen edge, the fatigue

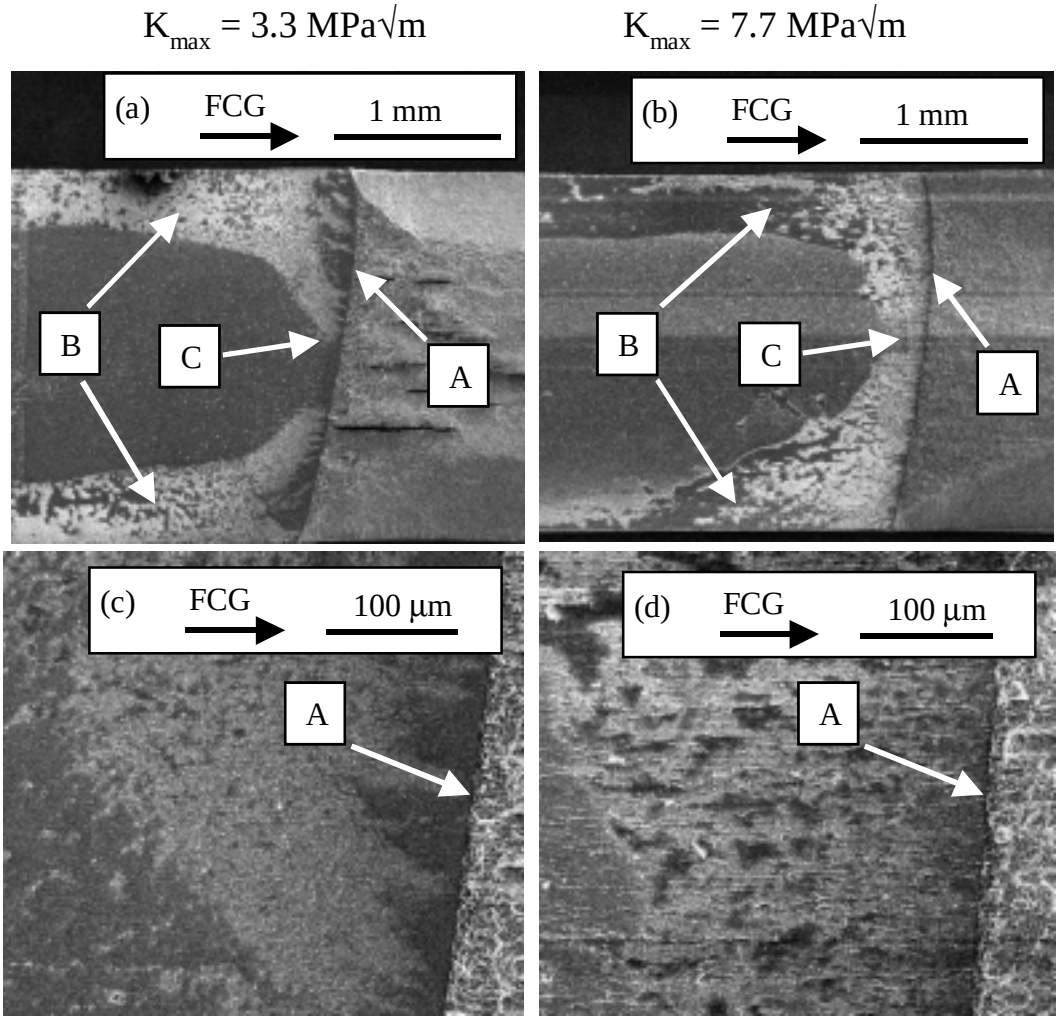

Figure 3.38 – Micrographs of crack surfaces after 0.05 μm particles were injected into the crack mouth. Conditions where particles are not expected to reach the crack-tip (K_{max} = 3.3 MPa√m) are shown on the left. Particles are expected to reach the crack-tip for K_{max} = 7.7 MPa√m (right column). In the top row, specimen surfaces can be seen along the top and bottom of both micrographs. The crack front at fracture (A) and dense regions of particles near the specimen surface (B) are indicated. High magnification images of regions labeled C are shown in the bottom row.

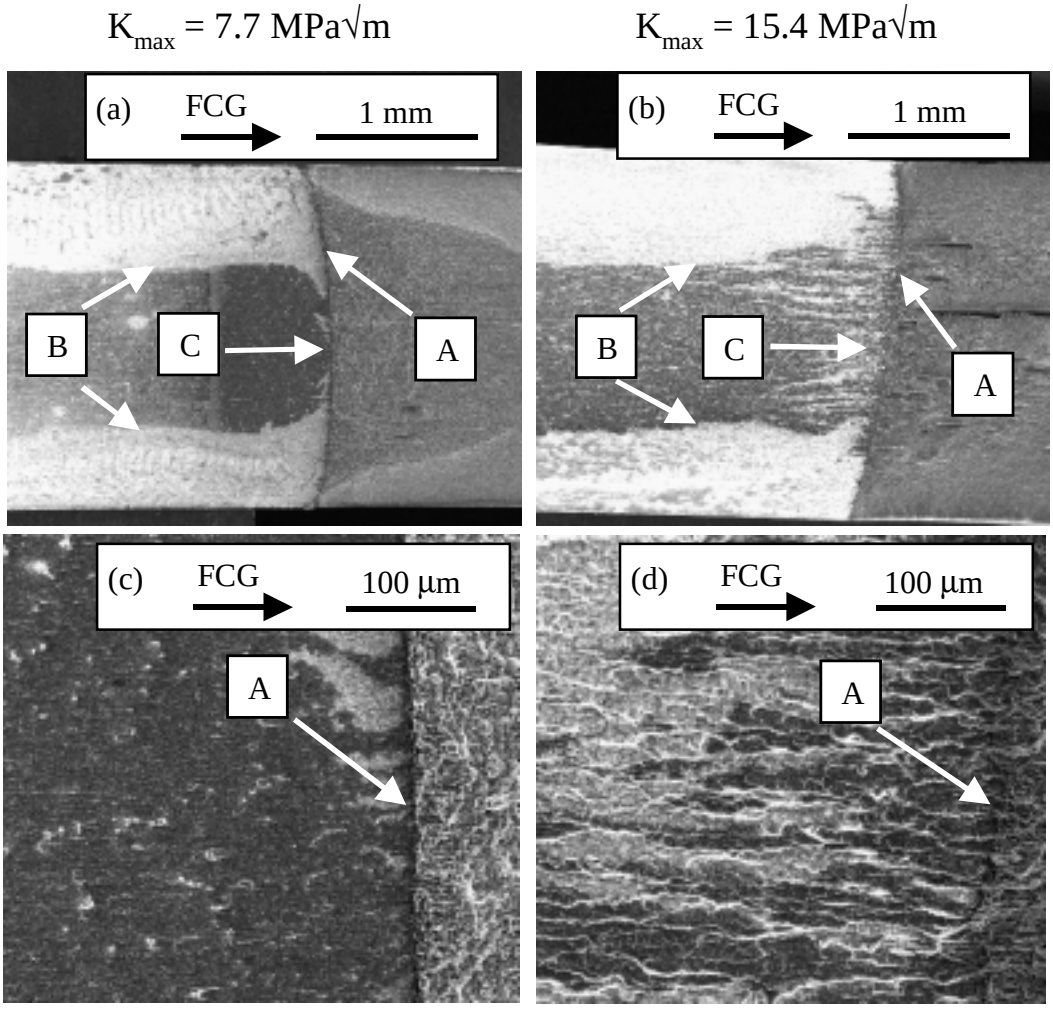

Figure 3.39 – Micrographs of crack surfaces after 0.30 μm particles were injected into the crack mouth. Conditions where particles are not expected to reach the crack-tip (K_{max} = 7.7 MPa√m) are shown in the left column. Particles are expected to reach the crack-tip for K_{max} = 15.4 MPa√m (right column). In the top row, both specimen surfaces can be seen along the top and bottom of both micrographs. The crack front at fracture (A) and dense regions of particles near the specimen surface (B) are indicated. High magnification images of regions labeled C are shown in the bottom row.

crack surface appeared white because of high alumina particle density. These regions of high particle density are labeled B. Although the particle density was higher at the specimen surface, alumina particles were observed throughout the specimen interior. It is believed that the particle density in the specimen interior was enough to produce crack closure, so no though-thickness effects were considered. High magnification images of the regions labeled C in Figures 3.38a,b and 3.39a,b (the top rows) are shown in Figures 3.38c,d and 3.39c,d (the bottom rows), respectively. As hypothesized, alumina particles did not reach the entire crack front at low values of K_{max} (left side of the figures), but did at higher K_{max} levels. Based on the correlation between fractography and FCG behavior,

the absence of particles at the crack-tip is a likely explanation for the low K_{max} behavior noted in Figure 3.27.

It was believed that remote agglomeration of alumina particles produced remote closure and resulted in compliance closure levels greater than near-tip values (see Figures 3.29a and 3.30). In Figure 3.40, micrographs are shown of the crack surface generated at K_{max} = 7.7 MPa$\sqrt{m}$ and R = 0.05, after 0.30 μm particles were injected into the crack mouth. Images both near the crack-tip, and approximately 1.6 mm behind the crack-tip, are shown, at the specimen centerline and specimen surface. Figure 3.40 consists of four images arranged as a table. Right and left columns correspond to images at the specimen interior and specimen surface, respectively. Top and bottom rows correspond to the crack surface near the crack-tip (within 60 μm), and approximately 1.6 mm behind the crack-tip, respectively. In all images, FCG proceeded left to right, as indicated in the legend. Individual particles (labeled A) are indicated by arrows in parts (a), (b), and (d). In the specimen interior, far from the crack-tip, clumps of agglomerated particles were observed and labeled B in Figure 3.40c. These clusters of particles are as large as 3 μm in diameter (approximately 10 individual particle diameters).

For fatigue loading of K_{max} = 5.5 MPa$\sqrt{m}$ and R = 0.05, remote agglomeration of 0.05 μm particles is shown approximately 5 mm behind the crack-tip in Figure 3.41. As shown in the legend, FCG proceeded from left to right. Agglomerated particles are labeled A, while a few individual particles are labeled B. From Figures 3.40 and 3.41, remote agglomeration occurs well behind the crack-tip (> 1 mm), likely producing remote closure and compliance closure greater than corresponding DIDS values. Agglomerated particles behave as a thicker oxide layer (perhaps 10 times thicker) that terminates a finite distance from the crack-tip. Remote closure is expected to affect the closure behavior at the crack-tip and may explain why near tip DIDS measurements in Figure 3.30 were (approximately 20%) greater than expected.

Differences between a_{vis} and a_{comp} occurred after 0.05 μm particles were injected into a fatigue crack loaded by K_{max} = 4.4 MPa$\sqrt{m}$ and R = 0.05 (see Figure 3.29a). It was suggested that crack tunneling (typical of high R loading for 8009 aluminum) might explain this behavior. The identical test procedure used to generate the data in Figure 3.29a were repeated. After the addition of 0.05 μm particles (the second time), a_{vis} began to increase after a_{comp} reached 80 μm. Fatigue loading was stopped when a_{comp} increased 100 μm after the particles were injected into the crack (a_{vis} increased by 20 μm). The specimen was then fractured, marking the final fatigue crack front. A micrograph of this crack surface is shown in Figure 3.42. FCG progressed from left to right, as indicated by an arrow (FCG). The crack front that existed when the alumina particles were injected into the crack mouth is indicated as the near vertical feature labeled A. The oxide in the crack wake is especially thick near the specimen surface (labeled B). No particles exist

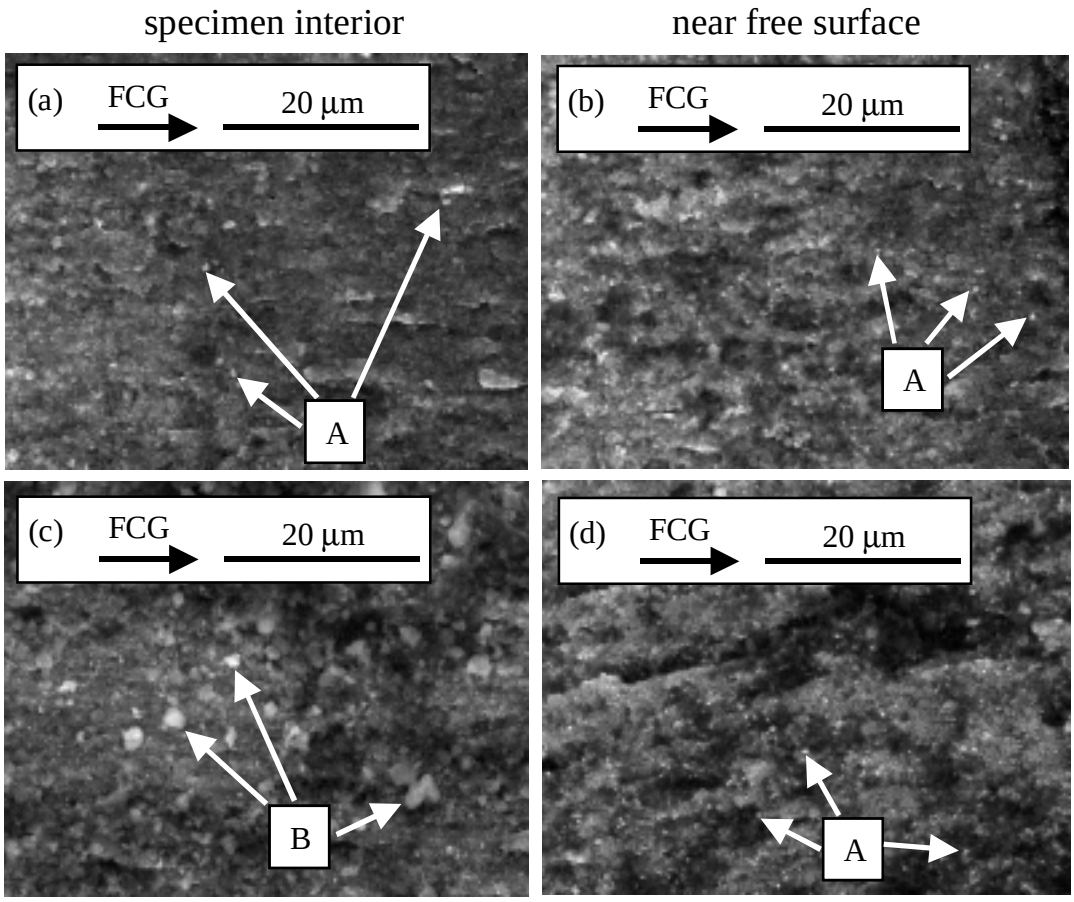

Figure 3.40 – Micrographs of a fatigue crack surface (K_{max} = 7.7 MPa√m and R = 0.05) after 0.30 μm particles were injected into the crack mouth. Images of the specimen interior and near the specimen edge are indicated in the left and right columns, respectively. Top and bottom rows correspond to images near the crack-tip (within 60 μm) and approximately 1.6 mm behind the crack-tip, respectively. Individual and agglomerated particles are labeled A and B, respectively.

within 7 μm of the crack-tip, and particles density is lower in the specimen interior (compared with the specimen surface). As hypothesized, a tunneled crack front is observed at the FCG/fracture interface (labeled C). The change in compliance and visual crack lengths between the addition of particles and fracture are indicated by near vertical dashed lines, labeled Δa_{comp} and Δa_{vis}, respectively. Although not shown, the fatigue crack surface produced as crack tunneling occurred (*e.g.* under the label C) is marked by voids, similar to crack surfaces shown later in Chapter 4.

3.8 — SUMMARY

In this chapter, an analytical fatigue crack closure model was developed that included three closure mechanisms (PICC, RICC, and OICC), crack meandering, and (limited) mixed-mode loading. Because no existing models include all of these mechanisms

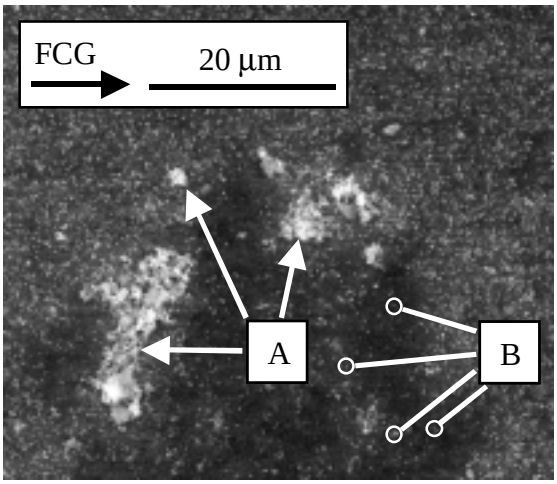

Figure 3.41 – Micrograph of agglomerated (0.05 μm) alumina particles approximately 5 mm behind the crack-tip (labeled A). Fatigue loads are K_{max} = 5.5 MPa√m (R = 0.05). A few individual particles are labeled (B).

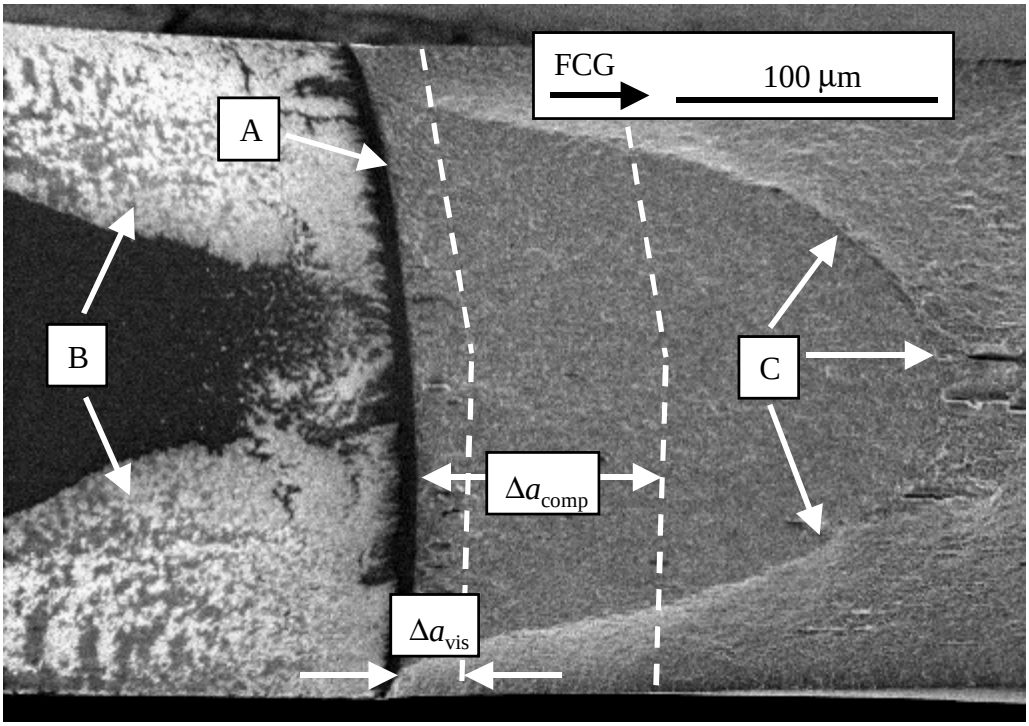

Figure 3.42 – Fatigue crack surface produced before and after 0.05 μm particles were injected into the crack mouth. Applied fatigue loads were K_{max} = 4.4 MPa√m and R = 0.05. The divergence of a_{vis} and a_{comp} are a result of crack tunneling.

simultaneously, and these mechanisms are likely important at threshold, this model is uniquely suited for threshold applications. Two modes of crack face contact are considered: (1) tip contact and (2) asperity contact. This model accounts for both closure modes. The transition from tip contact to asperity contact as K_{max} decreases (similar to constant R threshold testing), leads to an abrupt increase in closure levels, eventually arresting the crack (*i.e.* FCG threshold). Model results are well supported by the experimental data presented in Section 3.6.

CHAPTER 4 — INTRINSIC LOAD RATIO EFFECTS

Closure free load ratio effects on aluminum alloys are studied here using constant K_{max} threshold tests to eliminate fatigue crack closure at threshold. Accelerated fatigue crack growth rates are correlated with increases in crack-tip void production (damage) occurring at higher K_{max} values. Finally, an analytical model is developed to describe the relationship between crack-tip damage and accelerated fatigue crack growth rates.

4.1 — INTRODUCTION

Some load ratio effects are not explained by closure arguments, especially at FCG threshold [15, 16]. Because closure-free R effects are small (in comparison with closure) for many engineering materials, they have received little research attention. However, intrinisic load ratio effects should be studied for two reasons. First, even small changes in threshold FCG behavior can have a large impact on the total fatigue life (as discussed in Section 1.2). Second, the unstable threshold behavior presented by Marci and Lang, *et al.*, indicate closure-free load ratio effects are not always small (recall Section 1.6.3) [18, 19]. Although unstable threshold FCG has only been found in a few alloys, similar behavior may occur for many alloys. If structural components currently in service are designed (unintentionally) to operate on the verge of FCG instability, premature fatigue failure may result.

Intrinsic threshold FCG load ratio (or K_{max}) effects are studied for three aluminum alloys (2024, 7050, and 8009). Alloy 7050-T6 (S-L orientation, plate), and powder metallurgy (PM) 8009 (L-T orientation, sheet) were selected because accelerated threshold FCG rates are observed at high R [60, 67]. This behavior is not explained satisfactorily by plasticity-induced crack closure models suggesting closure-free R mechanisms exist. Aluminum alloy 2024-T3 (L-T orientation, sheet) was selected because its FCG behavior is well characterized and crack closure models successfully describe threshold behavior over a wide range of R. Relevant material properties and description of physical metallurgy are presented in Appendix D for all three alloys. Special attention will be given to atypical threshold FCG behavior at high K_{max} levels (near the fracture toughness, K_c), if found.

4.2 — TEST PROCEDURE AND RESULTS

Constant K_{max} FCG threshold tests are used to eliminate crack closure at threshold [27]. By maintaining constant K_{max} as ΔK is reduced, R increases as the test progresses. Recall, that closure is less likely at high R. (See Appendix B for details of mechanical testing procedures.) Unless otherwise stated, FCG tests were performed in laboratory air at a loading frequency of 11 Hz. A K-gradient of $C = -0.8\ mm^{-1}$ was used for constant K_{max} threshold tests in this study. ASTM standards recommend using $C = -0.08\ mm^{-1}$ for constant R threshold tests [4]. However, a steeper K-gradient can be used for constant K_{max} testing because the crack-tip monotonic plastic zone (MPZ) does not change as the crack grows, and interfering crack wake effects are not produced (*i.e.* no remote closure). For test results described herein, maximum applied loads were no less than 40% of the

load capacity, and the load range was within 1% of the maximum allowed. Use of a 16-bit data acquisition board ensured sufficient resolution of load under all test conditions. Fatigue crack closure measurements were made during the constant K_{max} threshold tests using back-face strain and DIDS techniques, as described in Appendix C. Due to the complexities involved in using DIDS, only a few tests in which crack closure was deemed most likely were analyzed this way. Constant K_{max} = 5.5 MPa√m tests were deemed most likely to exhibit closure, because R at threshold (≈0.8) was lower than the other cases. No closure was detected using compliance or DIDS measurements for FCG data presented in this chapter.

4.2.1 – Aluminum alloy 2024

FCG data from constant K_{max} threshold tests on aluminum alloy 2024 are plotted in Figure 4.1 for the longitudinal-transverse (L-T) orientation. Results are shown for K_{max} = 5.5, 11.0, 16.5, 22.0, 27.5, 33.0, and 38.5 MPa√m, by symbols indicated in the legend (lower right). FCG rate is plotted against ΔK, on logarithmic axes, scaled to focus on the threshold region (1 MPa√m < ΔK < 3 MPa√m). Closure affected data would lie within the hatched region (lower right corner), but no fatigue crack closure occurred. As seen in the figure, increasing K_{max} produces accelerated FCG rates. Consider the vertical dotted line about ΔK = 1.5 MPa√m. The constant K_{max} = 5.5 MPa√m data intersects this line at approximately 10^{-10} m/cycle. The FCG rate at the same ΔK, but for K_{max} = 38.5 MPa√m, is 1.4 x 10^{-9} m/cycle, shown by a horizontal dotted line. In this example, increasing K_{max} by a factor of 7 (from 5.5 to 38.5 MPa√m) increased FCG rates by a factor of 14 (from 10^{-10} to 1.4 x 10^{-9} m/cycle), indicated by 'Δ'(d*a*/dN) in the figure. K_{max} effects are less pronounced at higher ΔK. The range in FCG rate at ΔK = 3 MPa√m is indicated by Δ on the right side of the figure. Here, FCG rates increase from 3.7 x 10^{-9} m/cycle to 5.3 x 10^{-9} m/cycle (factor of 1.4) as K_{max} increases from 5.5 MPa√m to 38.5 MPa√m (factor of 7).

During FCG threshold testing, ΔK is reduced as the crack propagates. FCG threshold is ideally the ΔK for which no FCG occurs. Because crack propagation is required to decrease ΔK, no ideal threshold is reached so that FCG completely stops. A working definition for FCG threshold (ΔK_{th}) is provided in ASTM standards. By this procedure, a line is fit through at least five data points between FCG rates of 10^{-9} m/cycle and 10^{-10} m/cycle. FCG threshold, ΔK_{th}, is defined as the value of ΔK at the intersection of this fitted line with 10^{-10} m/cycle. For typical threshold behavior, ΔK_{th}, is approximately the ΔK corresponding to a FCG rate of 10^{-10} m/cycle. The ASTM threshold rate is shown as a horizontal dotted line, labeled (with an arrow) on the right side of Figure 4.1. As K_{max} increases the ΔK corresponding to the ASTM threshold rate decreases, indicated by $\Delta(\Delta K_{th})$. The data for K_{max} levels of 11.0, 22.0, and 33.0 MPa√m are plotted between 10^{-9} m/cycle and 10^{-10} m/cycle in Figure 4.2a (log-log plot) as circular, square, and triangular symbols, respectively. A straight line is fit through each set of data as prescribed by ASTM standards, and ΔK at the intersection of the fitted lines with 10^{-10} m/cycle is defined as ΔK_{th}. For the K_{max} = 11.0 MPa√m threshold test data, ΔK_{th} is indicated in the figure at 1.42 MPa√m. Also, the slope of the fitted line, m^*, is indicated in the figure. The slope of the threshold data is represented by m^* to avoid confusion

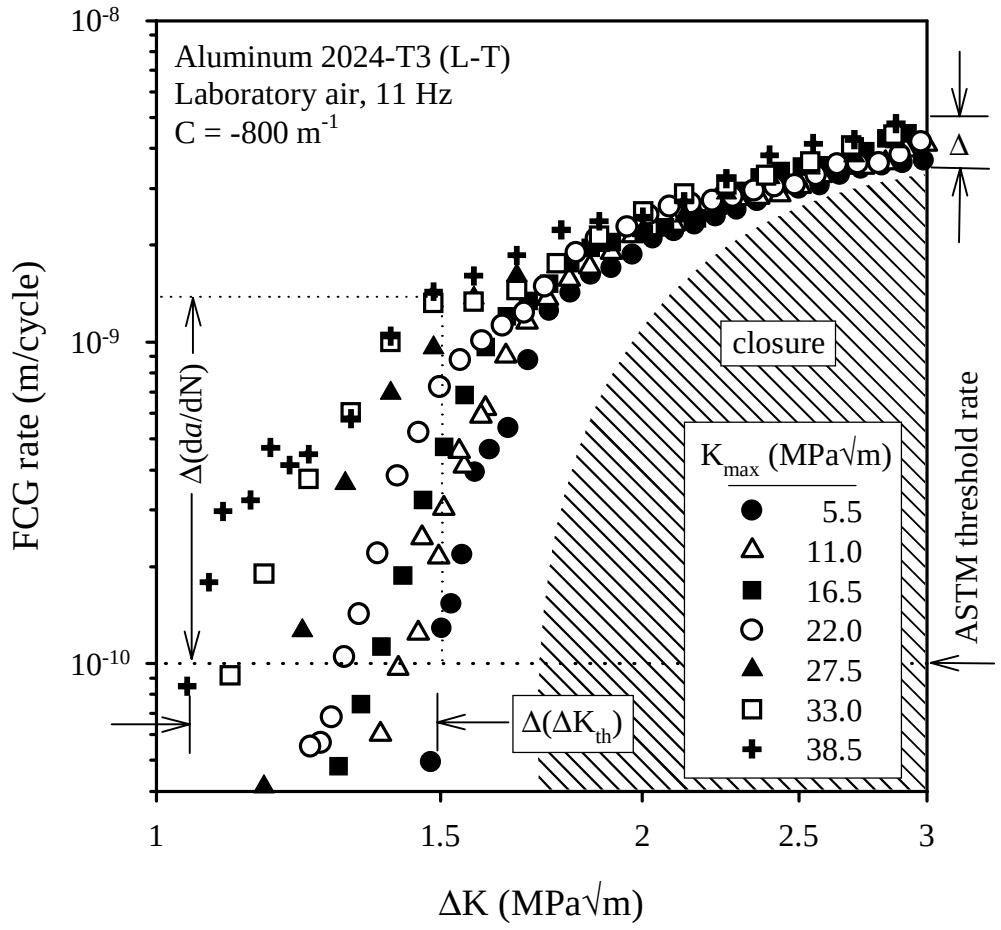

Figure 4.1 – FCG data for constant-K_{max} threshold tests of aluminum alloy 2024-T3. Testing was performed in laboratory air at 11 Hz. Closure affected data would lie within the hatched region. The ASTM suggested threshold rate (10^{-10} m/cycle) is indicated by the horizontal dotted line.

with the slope of FCG data in the Paris regime, m (recall Equation 1.1). ΔK_{th} and m^* (for each constant K_{max} test in Figure 4.1) are plotted in Figure 4.2b, as closed and open symbols, respectively. ΔK_{th} and m^* are plotted against K_{max} using the left and right vertical axes, respectively. Along the top axis of this plot, the value of K_{max} is scaled by the fracture toughness for this specimen configuration (see Table D.2), K_c = 42 MPa√m. (Note that K_{Ic} = 35 MPa√m for this material. See Table D.1.) Solid and dashed lines are fit to the ΔK_{th} and m^* data, respectively. For engineering metals in the Paris regime, the slope of the FCG data typically ranges from 2 to 4, indicated by the horizontal dotted lines in Figure 4.2b. This slope is expected to increase and theoretically approach infinity as a true FCG threshold is achieved. As seen in the figure, both ΔK_{th} and m^* decrease with increasing K_{max}. The value of ΔK_{th} decreases from 1.42 MPa√m to 1.00 MPa√m (a 30% reduction) as K_{max} increases from 5.5 MPa√m to 38.5 MPa√m. The relationship between ΔK_{th} and K_{max} is nearly linear, as indicated by the close fit of the solid line. The slope of the data near threshold, m^*, decreases with increasing K_{max}. For example, as

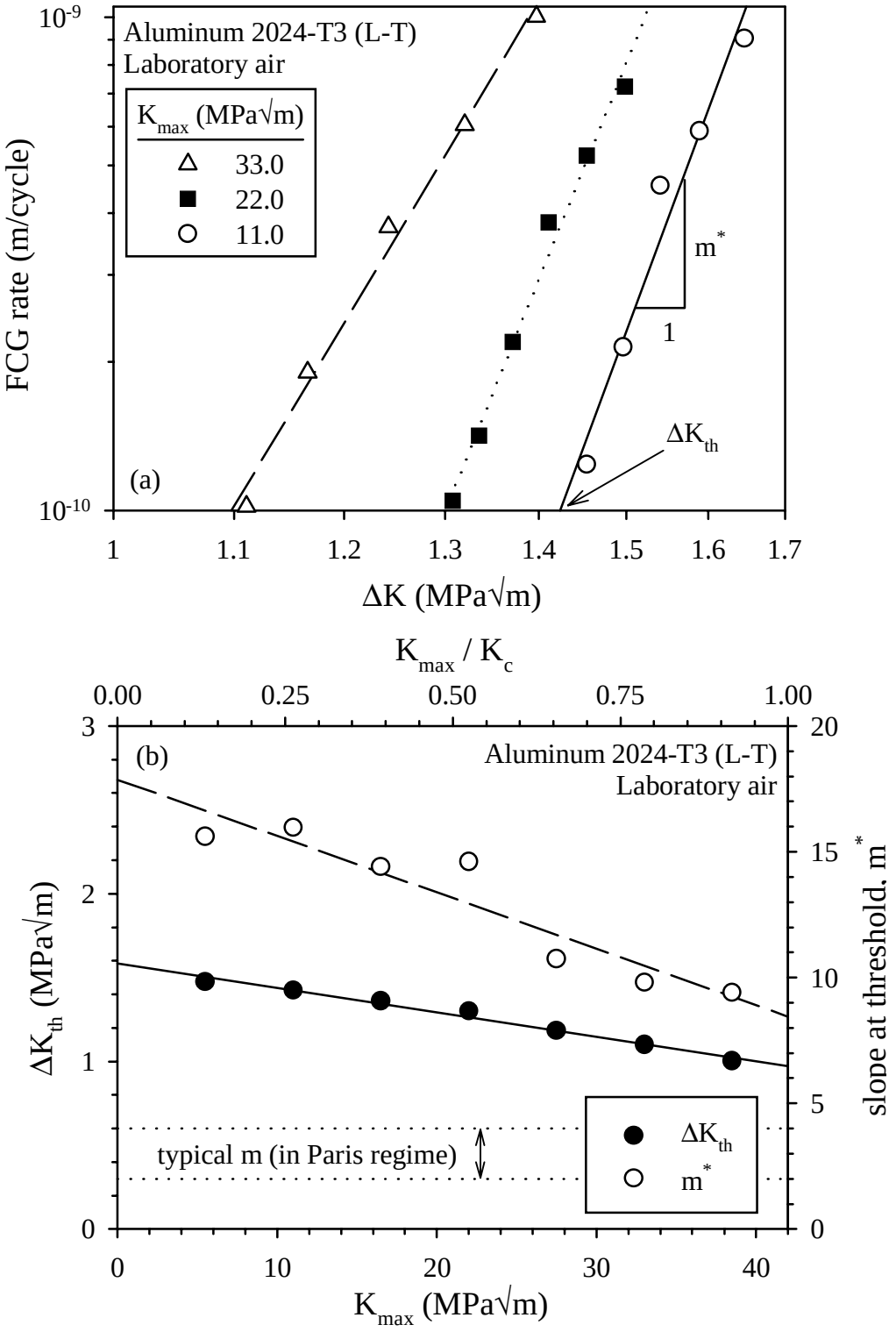

Figure 4.2 – Plots of threshold FCG parameters m^* and ΔK_{th} for 2024 aluminum. Threshold data shown in part (a) is used to determine m^* and ΔK_{th}, which are plotted in part (b).

K_{max} increases from 5.5 MPa√m to 38.5 MPa√m, m^* decreases from (approximately) 16 to 10 (a 38% reduction). Because a finite slope is shown to exist at threshold, the ASTM procedure likely produces non-conservative values of ΔK_{th}. It is believed that ΔK_{th} is overestimated more at lower values of threshold slope, m^*. This implies that the true threshold (ΔK below which no FCG occurs) would decrease with increasing K_{max} to a greater degree than ΔK_{th} in Figure 4.2b. From the data plotted in Figures 4.1 and 4.2, three observations are made. Increasing K_{max} results in:

(1) accelerated FCG rates, especially at low ΔK.
(2) a reduction of ΔK_{th} (ASTM definition).
(3) a reduction of the threshold FCG data slope, m^*.

4.2.2 – Aluminum alloy 7050

FCG data from constant K_{max} threshold tests on aluminum alloy 7050 are plotted in Figure 4.3 for the short-longitudinal (S-L) orientation. Results are shown for K_{max} = 5.5, 11.0, 16.5, and 22.0 MPa√m as indicated in the legend. FCG rate is plotted against ΔK using logarithmic axes scaled for threshold (0.6 MPa√m < ΔK < 3 MPa√m). Closure affected data would lie within the hatched region in the lower right corner of the figure, but no fatigue crack closure was detected. The ASTM suggested threshold rate is indicated as a horizontal dotted line. As seen in the figure, increasing K_{max} leads to increasing FCG rate. Consider the vertical dotted line about ΔK = 1.15 MPa√m. The constant K_{max} = 5.5 MPa√m data intersects this line at approximately 1.5 x 10^{-10} m/cycle. The corresponding FCG rate for K_{max} = 22.0 MPa√m (at the same ΔK) is approximately 2.0 x 10^{-9} m/cycle, shown by a horizontal dotted line. For this example, increasing K_{max} by a factor of 4 (from 5.5 to 22.0 MPa√m) produced a factor of 17 increase in FCG rate (from 1.15 x 10^{-10} to 2.0 x 10^{-9} m/cycle), indicated by $\Delta(da/dN)$ in the figure. However, K_{max} effects are less pronounced at higher ΔK (*i.e.* further from threshold). The range in FCG rate at ΔK = 3 MPa√m is indicated by Δ on the right side of the figure. Here, FCG rates increase from 10^{-8} m/cycle to 2.2 x 10^{-8} m/cycle (factor of 2.2) as K_{max} increases from 5.5 MPa√m to 22.0 MPa√m (factor of 4). Although increasing K_{max} tends to produce increased FCG rates, little or no difference between K_{max} levels of 16.5 MPa√m and 22.0 MPa√m is seen. Because these threshold tests were performed in laboratory air and required two to three weeks of test time, it is believed that changes in humidity levels are responsible for this scatter. The effects of humidity on threshold FCG have been studied, and results are presented in Appendix E.

The parameters ΔK_{th} and m^* are obtained for aluminum alloy 7050 as done previously for 2024 aluminum. ΔK_{th} and m^* for aluminum alloy 7050 are plotted against K_{max} in Figure 4.4, as closed and open symbols, using the left and right vertical axes, respectively. Along the top axis of this plot, the value of K_{max} is scaled by the fracture toughness for this specimen configuration (see Table D.2), K_c = 35 MPa√m. (Note that K_{Ic} = 30 MPa√m for this material. See Table D.1.) Solid and dashed lines are fit to the ΔK_{th} and m^* data, respectively. For engineering metals in the Paris regime, the slope of the FCG data typically ranges from 2 to 4, as indicated by horizontal dotted lines in Figure 4.4. As seen in the figure, both ΔK_{th} and m^* decrease with increasing K_{max}. The value of ΔK_{th}

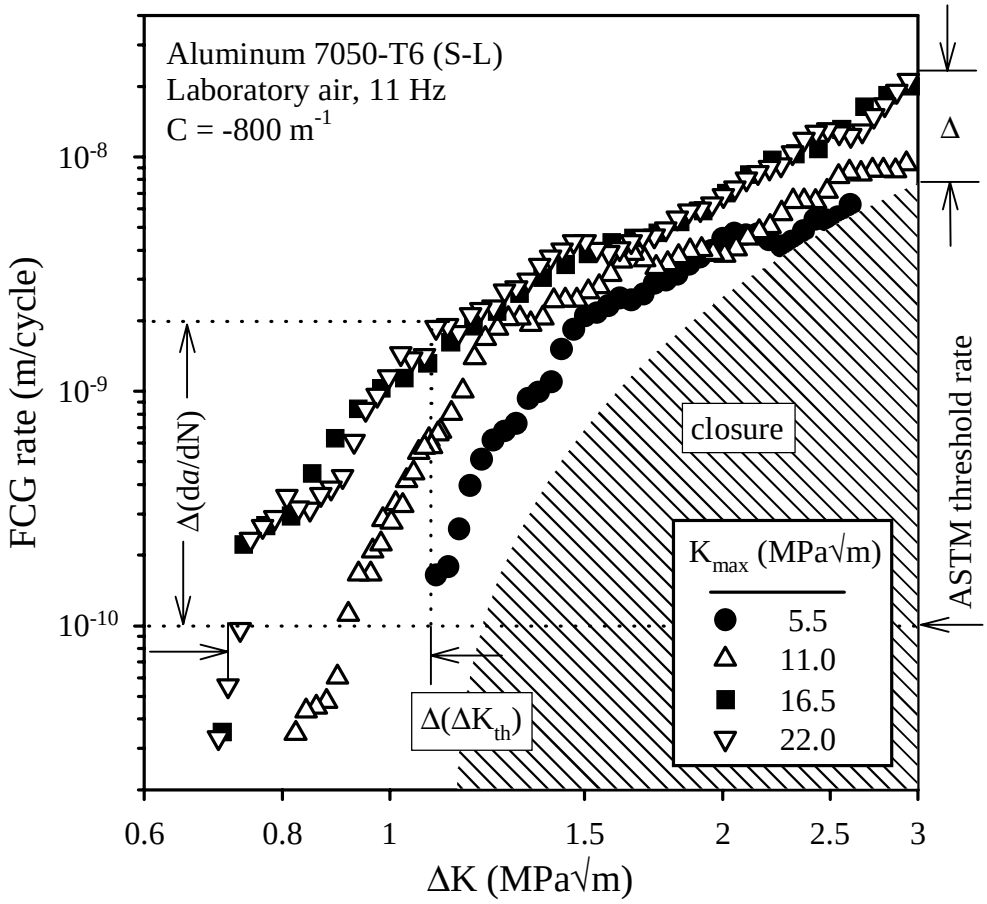

Figure 4.3 – FCG rate versus ΔK data of alloy 7050-T6 for constant-K_{max} threshold tests. Closure-affected FCG data (not shown) would have occurred in the shaded region. The ASTM suggested threshold rate (10^{-10} m/cycle) is indicated by the horizontal dotted line. Testing was performed in laboratory air, at 11 Hz.

decreases from 1.03 MPa√m to 0.63 MPa√m (a 39% reduction) as K_{max} increases from 5.5 MPa√m to 22.0 MPa√m. The relationship between ΔK_{th} and K_{max} is nearly linear, as indicated by the close fit of the solid line. The slope of the data near threshold, m^*, also decreases with increasing K_{max}. For example, as K_{max} increases from 5.5 MPa√m to 22.0 MPa√m, m^* decreases from (approximately) 9 to 5 (a 45 % reduction). At K_{max} > 22.0 MPa√m, the threshold slope, m^*, is expected to become as shallow as typical Paris regime data. As a true threshold is approached (*i.e.* a ΔK below which no FCG occurs), the slope of the FCG curve is expected to become infinite. Such low values of m^* suggest that a true threshold may be significantly less than the ΔK_{th} determined here, especially at high K_{max}.

From the data plotted in Figures 4.3 and 4.4, threshold FCG behavior of aluminum alloy 7050 is more sensitive to K_{max} than 2024 aluminum. This K_{max} sensitivity is observed over the entire range of ΔK, as shown in Figures 4.1 and 4.3. However, similar trends

were observed for both alloys. For aluminum alloy 7050, an increase in K_{max} resulted in:

(1) increased FCG rates, especially pronounced at low ΔK.

(2) a reduction of ΔK_{th} (ASTM definition).

(3) an increase in FCG data slope at threshold, m^*.

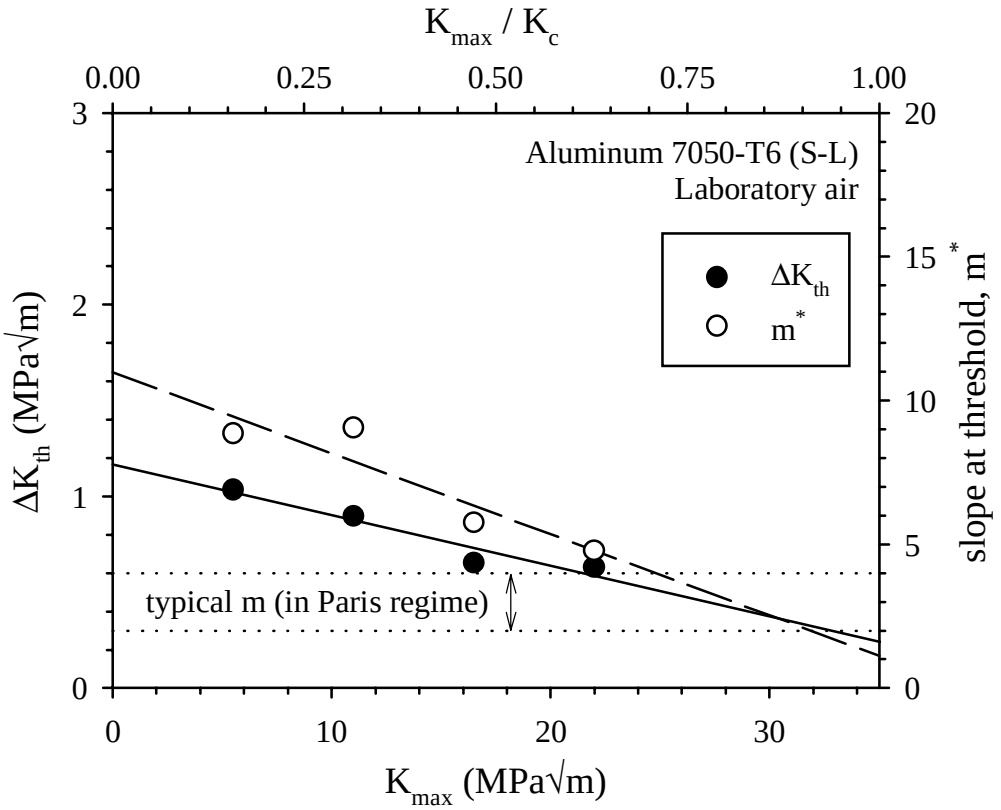

Figure 4.4 – Plots of threshold FCG parameters m^* and ΔK_{th} for 7050 aluminum.

4.2.3 – Aluminum alloy 8009

Constant K_{max} threshold test data for 8009 aluminum, in the longitudinal-transverse (L-T) orientation, is shown in Figure 4.5 for K_{max} levels of 2.75, 4.4, 5.5, 7.7, 11.0, 16.5, and 22.0 MPa√m. Testing was performed in laboratory air at 11 Hz. FCG rate is plotted against ΔK on logarithmic axes. Closure affected data would lie within the hatched region in the lower right corner, but crack closure was not detected. The ASTM suggested threshold rate of 10^{-10} m/cycle is indicated as a horizontal dotted line. For aluminum alloys 2024 and 7050, the values of FCG rate and ΔK_{th} changed with K_{max}, but the shape of the data curves (*i.e.* the character of threshold behavior) remained the same. For aluminum alloy 8009, both the magnitude and character of the FCG threshold response varied with K_{max}. Three types of behavior are observed in Figure 4.5. First, consider the data for K_{max} = 2.75 MPa√m, where FCG rate smoothly decreased with ΔK reduction until reaching 3 x 10^{-11} m/cycle. Although the slope of the FCG curve at threshold is finite, this data behaves in a manner similar to aluminum alloys 2024 and

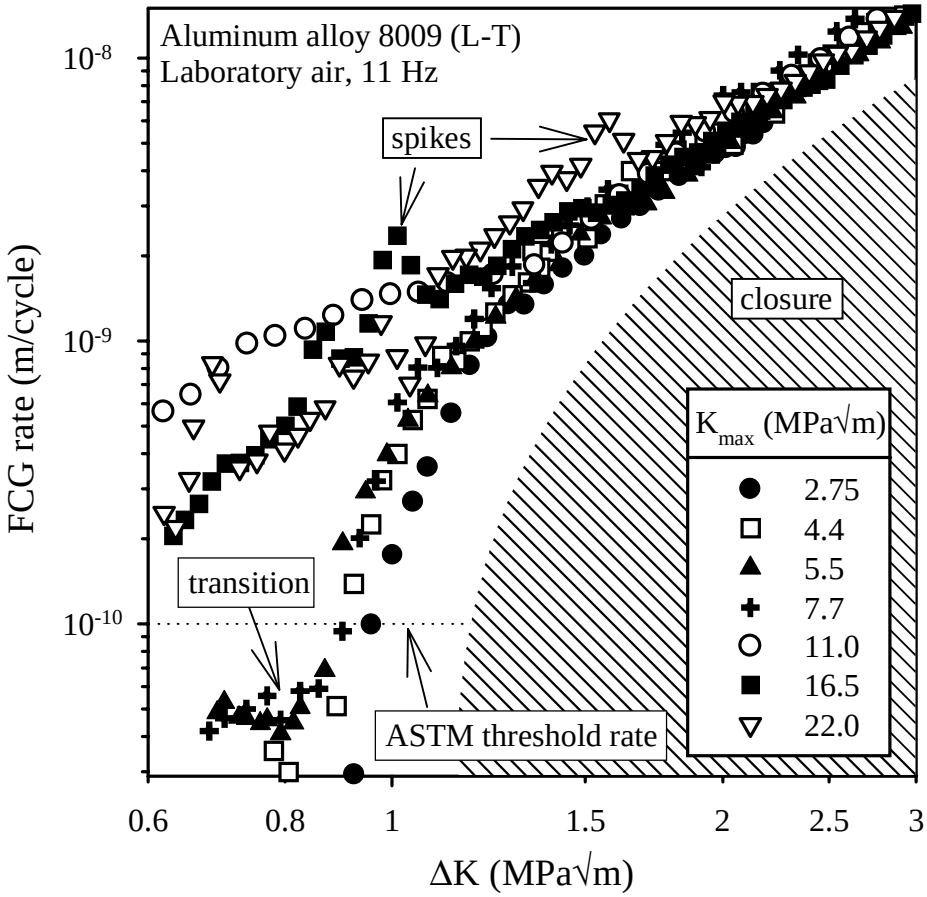

Figure 4.5 – FCG rate versus ΔK data of alloy 8009 for constant-K_{max} threshold tests. Closure-affected FCG data (not shown) would have occurred in the shaded region. The ASTM suggested threshold rate (10^{-10} m/cycle) is indicated by the horizontal dotted line. Testing was performed in laboratory air, at 11 Hz.

7050. Second, consider the threshold behavior for K_{max} levels of 4.4, 5.5, and 7.7 MPa√m. These data also exhibit a smooth decrease in FCG rate with ΔK reduction until a FCG rate of approximately 4 x 10^{-11} m/cycle is reached. At this point, further reduction in ΔK does not result in decreasing FCG rate. Rather, FCG rates appear nearly independent of ΔK for 0.7 MPa√m < ΔK < 0.8 MPa√m at these K_{max} levels. These transitions, indicated in Figure 4.5, occur at nearly the same FCG rate and ΔK for all three K_{max} levels. If a threshold test were stopped at 10^{-10} m/cycle, the ASTM threshold procedure would estimate ΔK_{th} without knowledge of the accelerated FCG behavior at ΔK < 0.8 MPa√m. Use of that ΔK_{th} as a (safe) damage tolerant design parameter would lead to non-conservative fatigue life prediction and likely premature failure if service loading corresponded to accelerated FCG behavior. The third type of threshold behavior occurs at $K_{max} \geq 11.0$ MPa√m, where accelerated FCG occurs above 10^{-10} m/cycle. The data shown in Figure 4.5 indicate that reduction in ΔK decreases FCG rates (for $K_{max} \geq$ 11.0 MPa√m), although no intersection with 10^{-10} m/cycle occurs for ΔK > 0.6 MPa√m. Spikes in FCG data are observed for K_{max} levels of 16.5 and 22.0 MPa√m. Two of these spikes are indicated in the figure.

Threshold data for K_{max} levels of 5.5 MPa√m and 11.0 MPa√m are re-plotted in Figure 4.6 as open and closed symbols, respectively. This plot is similar to Figure 4.5, but only two sets of data are shown for clarity. The respective transitions to accelerated FCG are labeled A and B in the figure. Although the transition at point B occurs at a FCG rate 50 times greater than point A, both sets of data are smooth without erratic spikes. It will be shown in Section 4.3 that these transitions are similar with regard to crack-tip damage production.

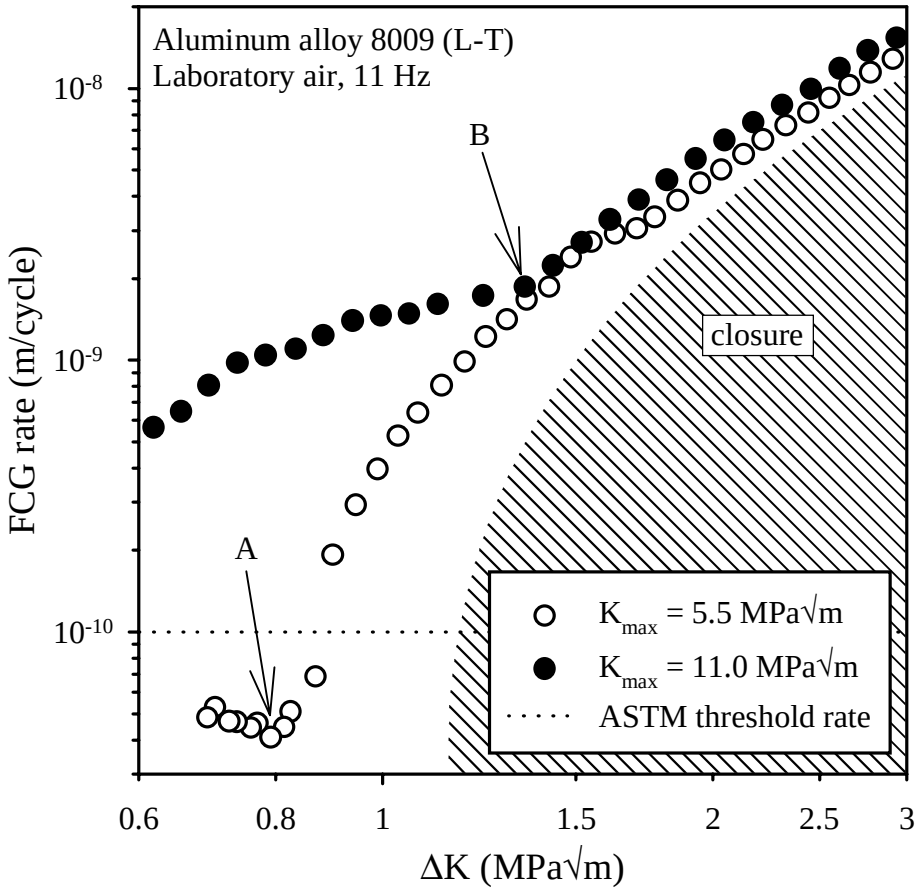

Figure 4.6 – Plot of constant K_{max} threshold data for K_{max} levels of 5.5 MPa√m and 11.0 MPa√m. Transitions to accelerated FCG are indicated.

Threshold data for K_{max} levels of 11.0 MPa√m and 22.0 MPa√m are plotted in Figure 4.7 as open and closed symbols, respectively. Data is presented here for ΔK as low as 0.4 MPa√m. The shaded region indicating closure conditions and the ASTM threshold rate are not shown in this figure. For ΔK > 2.2 MPa√m, (upper right corner of plot) both sets of data are smooth and typical of engineering alloys (*i.e.* small K_{max} effect). Transitions to accelerated FCG occur at points B and C, for K_{max} levels of 11.0 MPa√m and 22.0 MPa√m, respectively. For ΔK < 1.3 MPa√m (point B in Figure 4.7), a smooth reduction in FCG rate with decreasing ΔK occurred for K_{max} = 11.0 MPa√m. In contrast, erratic FCG behavior occurs during K_{max} = 22.0 MPa√m threshold testing for ΔK < 2 MPa√m (point C in Figure 4.7). Two spikes are indicated in Figure 4.7, where FCG rates increase

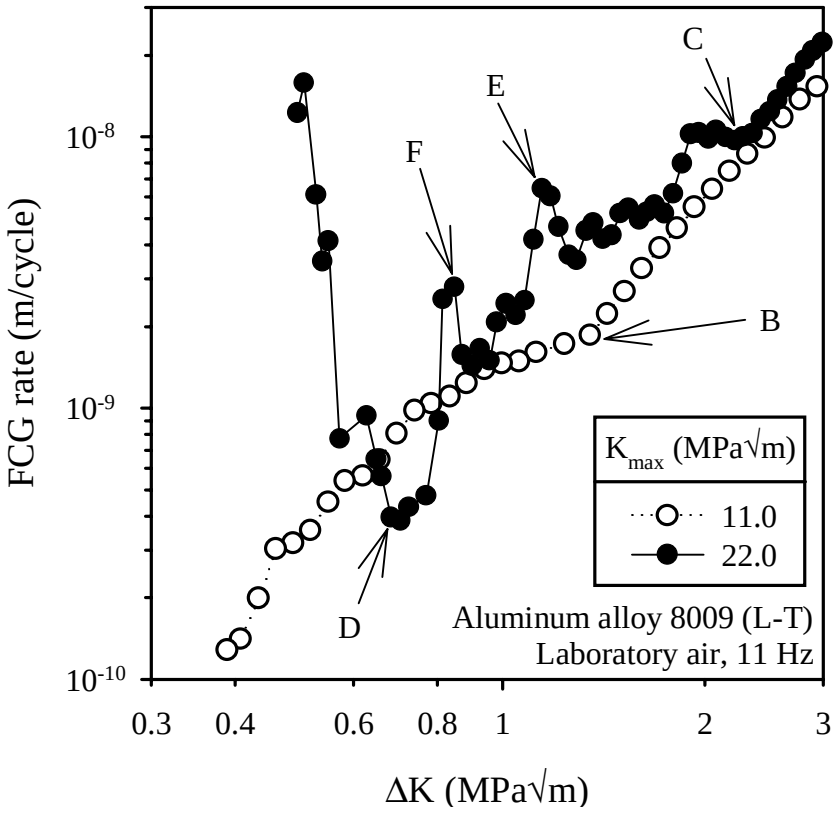

Figure 4.7 – Plot of constant K_{max} threshold data for K_{max} levels of 11.0 and 22.0 MPa√m. Transitions to accelerated FCG and unstable threshold behavior for K_{max} = 22.0 MPa√m are indicated.

sharply during testing. No sharp increases are expected because ΔK is reduced smoothly (C = -0.8 mm^{-1}). For ΔK < 0.65 MPa√m, further reduction in ΔK appears to produce a rapid increase in FCG rate. This unstable threshold behavior coincides with a transition to slant cracking. In Figure 4.8, schematics are shown for (a) flat crack growth and (b) slant crack growth, as viewed from the back face with the loading direction vertical. The specimen surfaces are seen as vertical parallel lines separated by the specimen thickness. As shown, the upper and lower parts of the specimen are separated in two pieces by the crack. Although small slanted surfaces (shear lips) may exist near the specimen surfaces, a flat crack propagates normal to the specimen surface (90^o), as shown in part (a). Crack growth along a 45^o slant, with respect to the free surface, is shown in part (b). Fatigue crack surfaces of 8009 aluminum were typically flat with no shear lips.

Cracks may grow on a 45^o slant if plane-stress conditions dominate, *i.e.* the MPZ is not small compared with the specimen thickness [1]. It will be shown in Section 5.2.3 that plane-stress conditions are important at K_{max} = 22.0 MPa√m, but not at K_{max} = 11.0 MPa√m. Recall a similar unstable FCG threshold response was reported by Marci and Lang *et al.*, but no mechanistic explanation for this behavior was presented (*e.g.* slant cracking, plane-stress conditions, *etc.*). Using similar analysis and fractographic observations presented in Section 4.3, a mechanism for the unstable threshold FCG of

8009 aluminum is proposed in Section 5.2.2.[23] Furthermore, this unstable behavior (second transition, point D in Figure 4.7) will be related to the transition to (stable) accelerated behavior (first transition, point C in Figure 4.7).

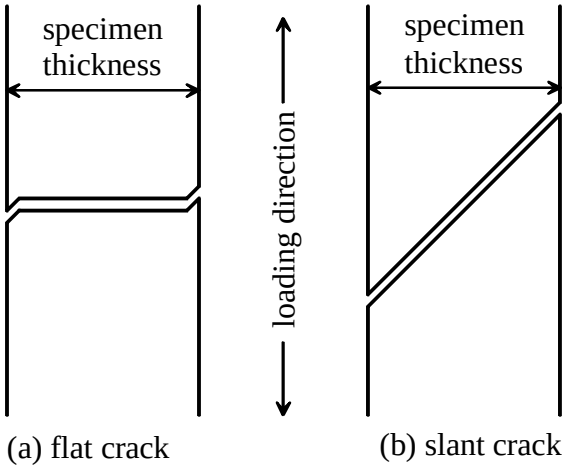

Figure 4.8 – Schematic comparing (a) flat crack and (b) slant crack geometries.

The threshold parameters ΔK_{th} and m^*, for 8009 aluminum, are plotted in Figure 4.9 as closed and open symbols, respectively. As done previously for alloys 2024 and 7050, a line was fit through FCG data between 10^{-9} and 10^{-10} m/cycle. Accelerated FCG data was considered in the linear fits, but the unstable threshold FCG of K_{max} = 22.0 MPa√m was omitted. Although the ASTM procedure allows these parameters to be determined for all K_{max} levels, only the data for low K_{max} levels (< 10 MPa√m) actually achieve a FCG rate of 10^{-10} m/cycle. Circular and triangular symbols indicate conditions where FCG rates below 10^{-10} m/cycle were, and were not, achieved, respectively. A vertical line is shown in the figure at 10 MPa√m to distinguish these regions. For K_{max} < 10 MPa√m, solid and dashed lines are fit through the ΔK_{th} and m^* data, respectively. Values of ΔK_{th} and m^* are lower for 8009 aluminum than for aluminum alloys 2024 and 7050. The slope of the FCG data at threshold, m^*, is very shallow for K_{max} < 10 MPa√m because of accelerated FCG data.

Additional tests were conducted to investigate the pronounced acceleration of threshold FCG rates of 8009 aluminum noted in Figure 4.6. Specifically, the transition observed in the K_{max} = 5.5 MPa√m data is of interest because the FCG rates appear to be independent of ΔK between 0.7 MPa√m and 0.8 MPa√m. An explanation for this behavior is an alternative crack growth mechanism operating in this regime, *e.g.* creep crack growth (CCG) or stress corrosion cracking (SCC). If CCG or SCC contribute to this accelerated FCG, the FCG response would be time (or frequency) dependent. To explore this possibility, a constant ΔK test was conducted at K_{max} = 5.5 MPa√m and ΔK = 0.77 MPa√m for loading frequencies of 11, 5, and 1 Hz. Test results are plotted as crack

[23] Although the mechanism presented in Section 5.2.2 explains unstable threshold behavior for 8009 aluminum, it does not explain the threshold behavior presented by Marci and Lang.

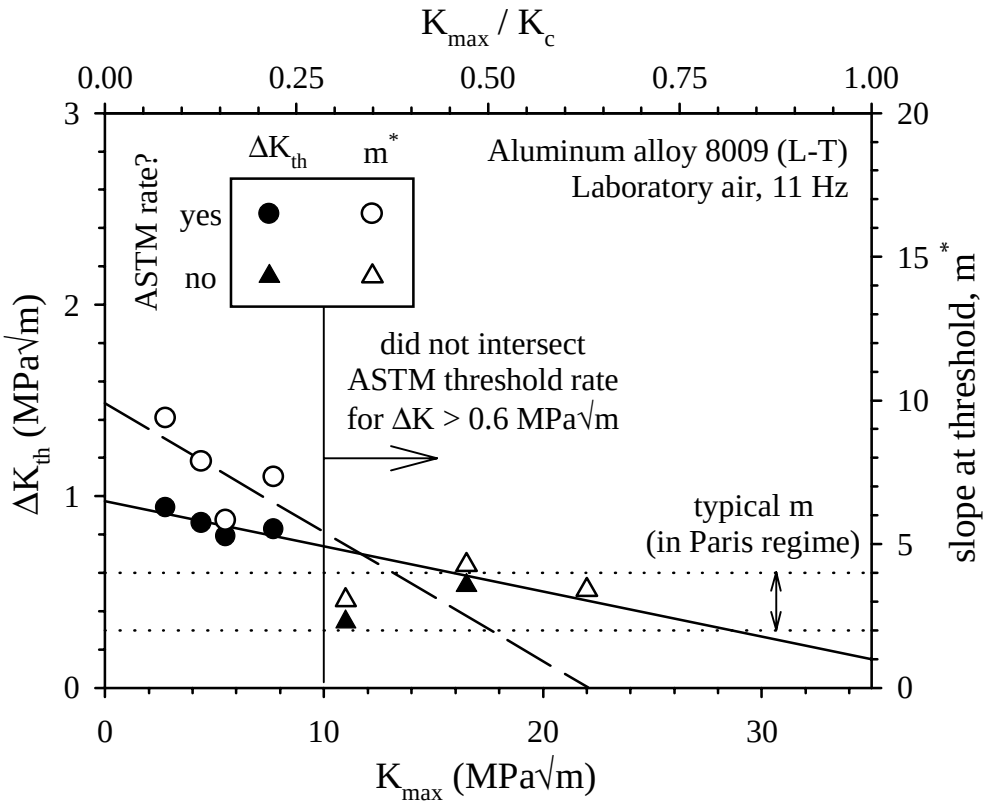

Figure 4.9 – Plots of threshold FCG parameters m^* and ΔK_{th} for 8009 aluminum.

length versus cycle count in Figure 4.10a. Data generated at 11, 5, and 1 Hz are indicated by circular, triangular, and square symbols, respectively. The slope of a linear fit through each set of data is used to determine the FCG rate (d*a*/dN), shown in the figure. For loading frequencies of 11 Hz and 1 Hz (factor of 11 difference), the corresponding FCG rates are 5.0×10^{-11} m/cycle and 5.9×10^{-10} m/cycle (factor of 12 difference). Because these data indicate that a time dependence does exist under these conditions, the data in Figure 4.10a is re-plotted as crack length versus time in Figure 4.10b. Similar to part (a), test results are plotted in part (b) as crack length versus time. Data generated at 11, 5, and 1 Hz are indicated by circular, triangular, and square symbols, respectively. The slope of a linear fit through each set of data is used to determine the FCG rate (d*a*/dt), shown in the figure. As seen in Figure 4.10b, the slope of all three curves are nearly identical. This suggests that FCG rates are time dependent rather than cycle dependent.

CCG and SCC are considered the most likely time dependent mechanisms. If either mechanism is responsible for the accelerated FCG behavior of 8009 aluminum, crack growth should persist under a constant (static) load. A constant load of K = 5.5 MPa√m (equivalent to the K_{max} applied in Figure 4.10) was held in laboratory air immediately following the 1 Hz test. No crack growth was detected after 1 week (168 hours) at this load. Had the time-dependent crack growth rate (d*a*/d*t*) of Figure 4.10b persisted, approximately 0.3 mm of crack growth would have occurred during the allotted time.

This may suggest that the accelerated FCG behavior of 8009 aluminum is not purely time or cycle dependent.

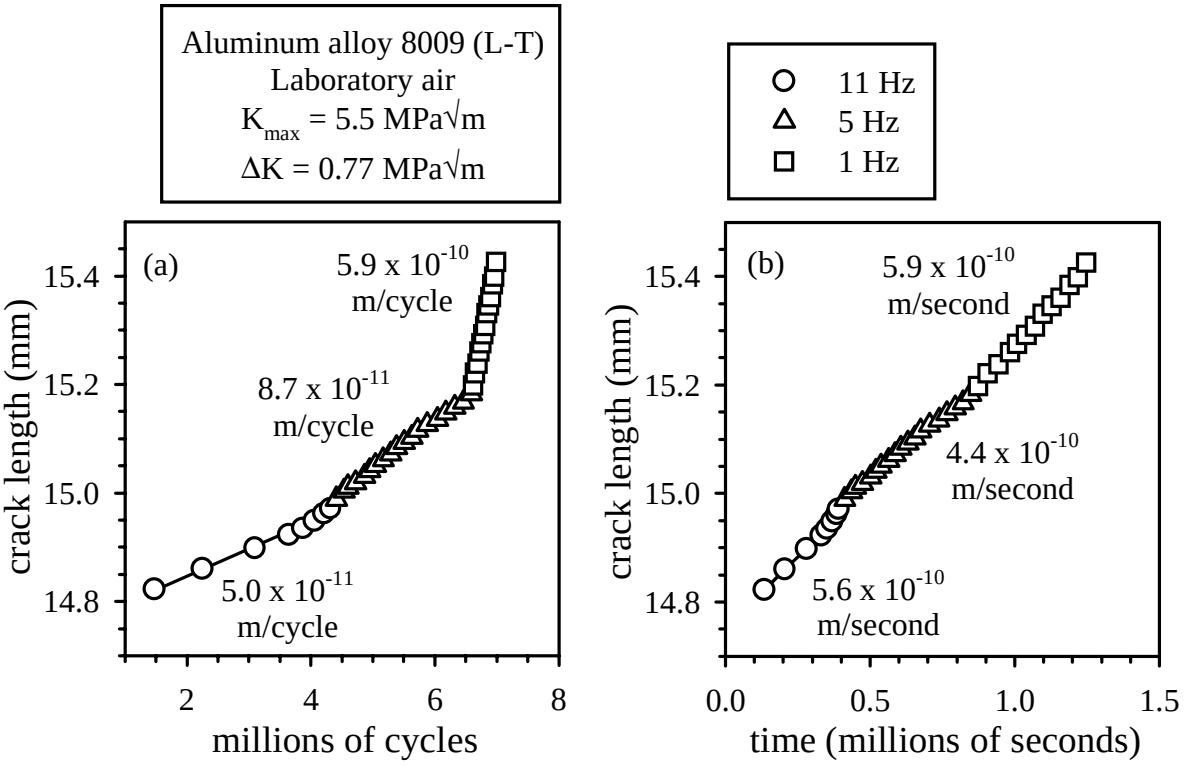

Figure 4.10 – Crack length plotted as a function of (a) cycles and (b) time, for alloy 8009 subject to constant K_{max} = 5.5 and ΔK = 0.77 MPa√m loading in lab air at 11, 5, and 1 Hz. FCG rates for each frequency are indicated.

To determine if the time dependent behavior noted in laboratory air was a result of environment, similar tests were conducted in UHV (see Appendix B). Comparison of constant K_{max} (5.5 and 11.0 MPa√m) threshold test data, conducted in air and vacuum under identical mechanical loading, are shown in Figure 4.11. In general, FCG rates in air are faster than in vacuum, a likely result of damaging water vapor. Both vacuum and air data exhibit transitions in FCG behavior at A_{vac} and A_{air}, respectively, for K_{max} = 5.5 MPa√m, and at B_{vac} and B_{air}, respectively, for K_{max} = 11.0 MPa√m. Constant ΔK tests at 11, 5, and 1 Hz were performed at K_{max} = 5.5 MPa√m and ΔK = 1.21 MPa√m in UHV to determine if accelerated FCG rates observed in vacuum are dependent on loading frequency. This loading condition is near the point A_{vac} in Figure 4.11. The constant ΔK test data in UHV is plotted in Figure 4.12 against (a) applied cycles and (b) time, similar to the plots presented in Figure 4.10. Data generated at 11, 5, and 1 Hz are indicated by circular, triangular, and square symbols, respectively. The slope of a linear fit through each set of data is used to determine the FCG rate (d*a*/dN or d*a*/dt), shown in the figure. As seen in part (a) of the figure, FCG rate increases with decreasing frequency. When plotted against time, these data indicate a time dependence on FCG rate, similar to that observed in laboratory air (recall Figure 4.10).

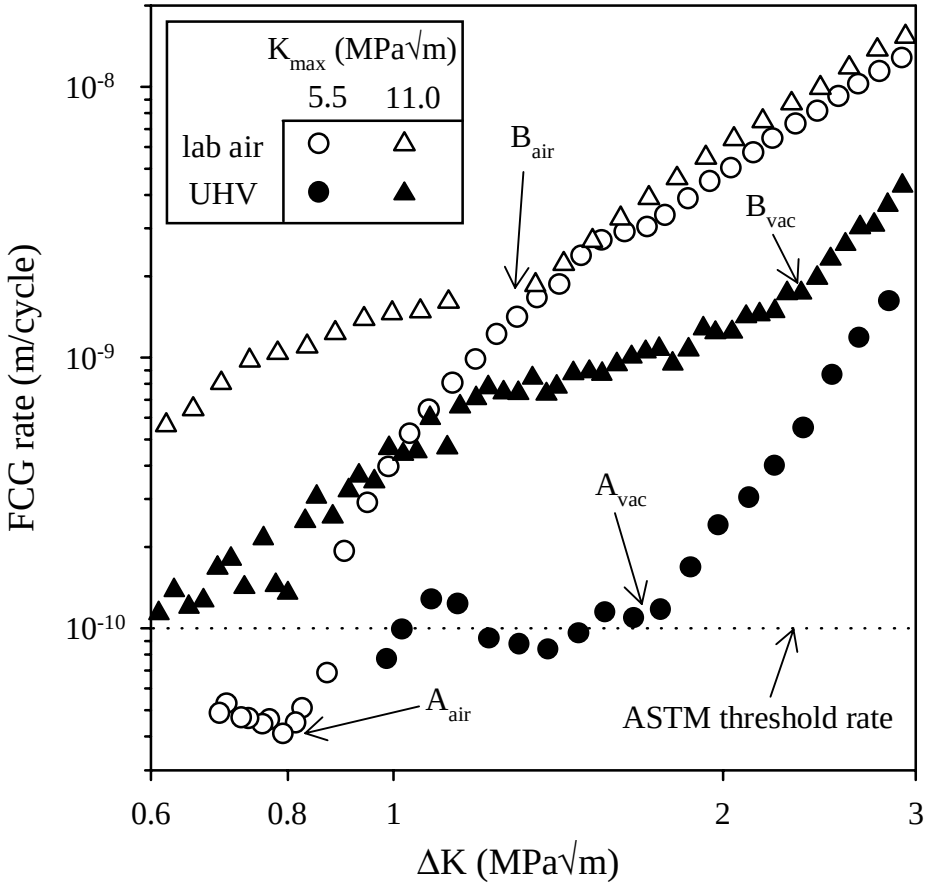

Figure 4.11 – FCG rate versus ΔK data for constant-K_{max} = 5.5 and 11.0 MPa√m threshold tests on 8009 aluminum, in both lab air (open symbols) and UHV (<$5x10^{-7}$ Pa, as closed symbols). The ASTM suggested threshold rate (10^{-10} m/cycle) is indicated by the horizontal dotted line. Testing was performed at 11 Hz, using C = -0.8 mm^{-1}. Transitions in FCG behavior are indicated as appropriate.

Near-threshold accelerated (fatigue) crack growth behavior of 8009 has been shown to be time dependent during cyclic loading in laboratory air and UHV environments. Because crack growth does not occur under a static load, this crack growth is not purely time dependent. It is believed that accelerated threshold FCG occurs by interactions between creep and fatigue mechanisms, as discussed in Section 5.2.2.

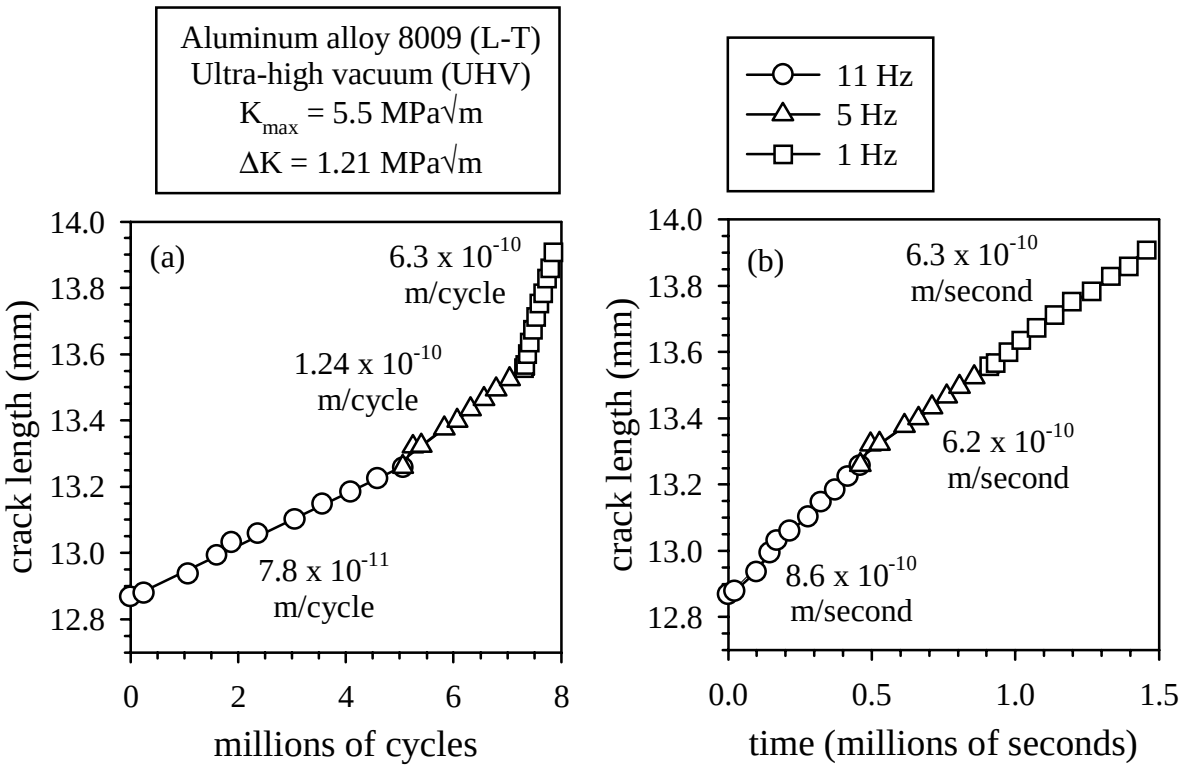

Figure 4.12 – Crack length as a function of (a) cycles and (b) time for alloy 8009 subject to constant K_{max} = 5.5 and ΔK = 1.21 MPa√m loading in UHV (<5x10^{-7} Pa) at 11, 5, and 1 Hz. FCG rates for each frequency are indicated.

4.3 — FRACTOGRAPHY

Increasing FCG rates with increasing K_{max} suggest additional crack-tip damage occurs at higher K_{max}. Examination of crack surfaces produced during constant K_{max} testing was done to identify and characterize possible K_{max} enhanced damage. Alloy 2024 fatigue crack surface micrographs are shown in Figures 4.13a and 4.13b for tests conducted at constant K_{max} = 5.5 and 22.0 MPa√m, respectively. The figures correspond to the crack surface generated at minimum ΔK (FCG rate = 5 x 10^{-11} m/cycle), as shown in Figure 4.1. The direction of FCG is from left to right, indicated by an arrow. Crack surfaces typical of transgranular FCG (flat regions) are observed in Figures 4.13a and 4.13b with widely dispersed voids (a few are labeled A). On the right side of the figures, voids are marked by white circles and the left side is unmarked. A detailed comparison of Figures 4.13a and 4.13b shows the microvoids density (voids per unit area) increased nearly 25% as K_{max} increased from 5.5 to 22.0 MPa√m. Void formation is the dominant mechanism of quasi-static fracture, as shown in Figure 4.13c (K_c = 42 MPa√m). Voids (labeled A in Figure 4.13c) are larger and more numerous than those observed on fatigue surfaces (Figures 4.13a and 4.13b). Figure 4.13d is a micrograph at high magnification showing a typical microvoid on the fatigue surface shown in Figure 4.13b. At high magnification,

particles (labeled B) are seen at the bottom of the voids. Energy dispersive X-ray (EDX) analysis identified these particles as an undissolved phase, Al_2CuMg. Although not shown here for fracture, both FCG and fracture produce void nucleation about second phase particles. Presumably, voids are produced within the MPZ because void density at threshold increases with increasing K_{max} and MPZ.

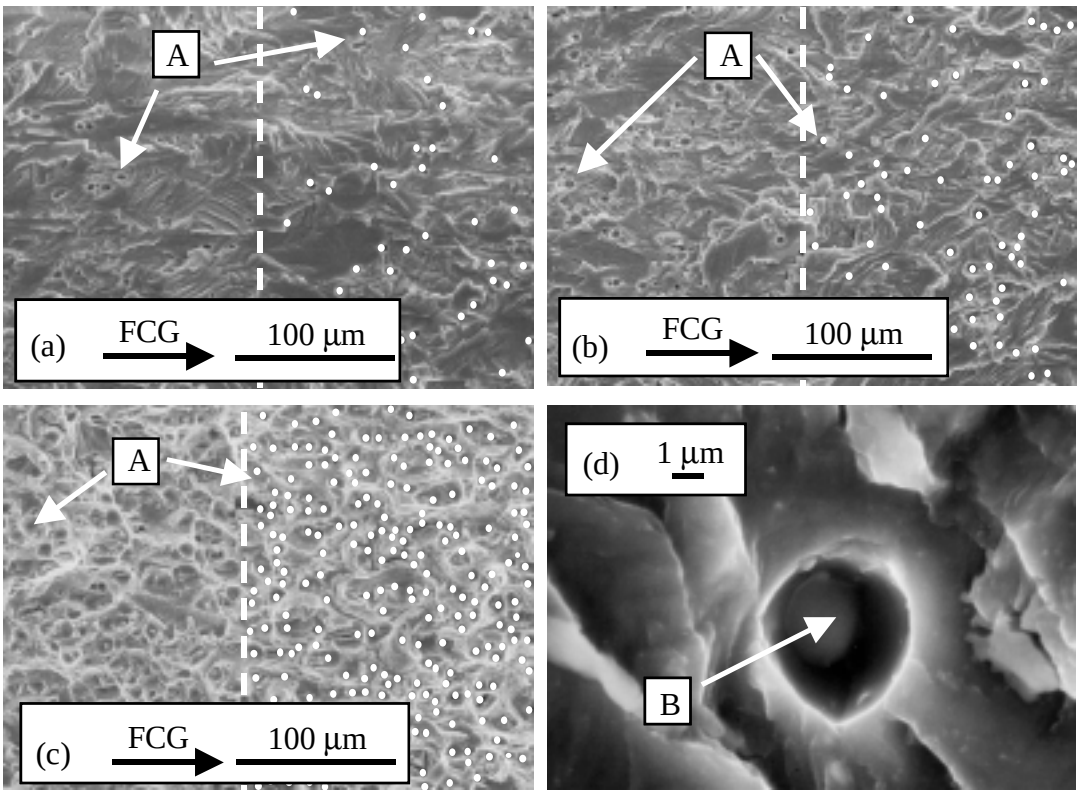

Figure 4.13 – SEM fractographs of alloy 2024-T3 fatigue crack surfaces produced by constant-K_{max} = (a) 5.5 and (b) 22.0 MPa√m threshold tests, (c) quasi-static fracture (K_c = 42 MPa√m), and (d) a high magnification fractograph of a typical microvoid produced on the fatigue crack surface of Figure 4.13b. For Figures 4.13a-c, microvoids are marked by white circle (or ovals) on the right, but unmarked on the left.

Figures 4.14a and 4.14b are micrographs showing the fatigue crack surface of alloy 7050 generated at constant K_{max} = 5.5 MPa√m (ΔK = 1.1 MPa√m and FCG rate = 1.5 x 10^{-10} m/cycle) and constant K_{max} = 22.0 MPa√m (ΔK = 0.7 MPa√m and FCG rate = 3 x 10^{-11} m/cycle), respectively (refer to Figure 4.3). These micrographs show crack surfaces typical of transgranular crack growth (flat regions labeled B) interrupted by rough regions (outlined in white and labeled A). As K_{max} increases, the percent of crack surface covered by rough regions increases. At monotonic fracture (K_c = 35 MPa√m), nearly the entire crack surface is consumed with these rough regions, as shown in Figure 4.14c. Figure 4.14d is a high magnification micrograph showing a typical rough region observed on the fatigue crack surface in Figure 4.14b. Closer examination of the rough regions

revealed clusters of microvoids, each containing a small particle, labeled C in Figure 4.14d. EDX analyses identified these particles as Al_7Cu_2Fe, second phase constituent particles. Further study of Figure 4.14d reveals faint white lines surround most of particles, which is evidence of ductile lips marking the outer regions of microvoids. A comparison of fatigue crack surfaces produced at K_{max} levels of 5.5, 11.0, 16.5, and 22.0 MPa√m revealed an increase in (constituent particle) microvoid density as K_{max} increased. Voids seen on the crack surface occur about second phase particles during FCG and fracture.

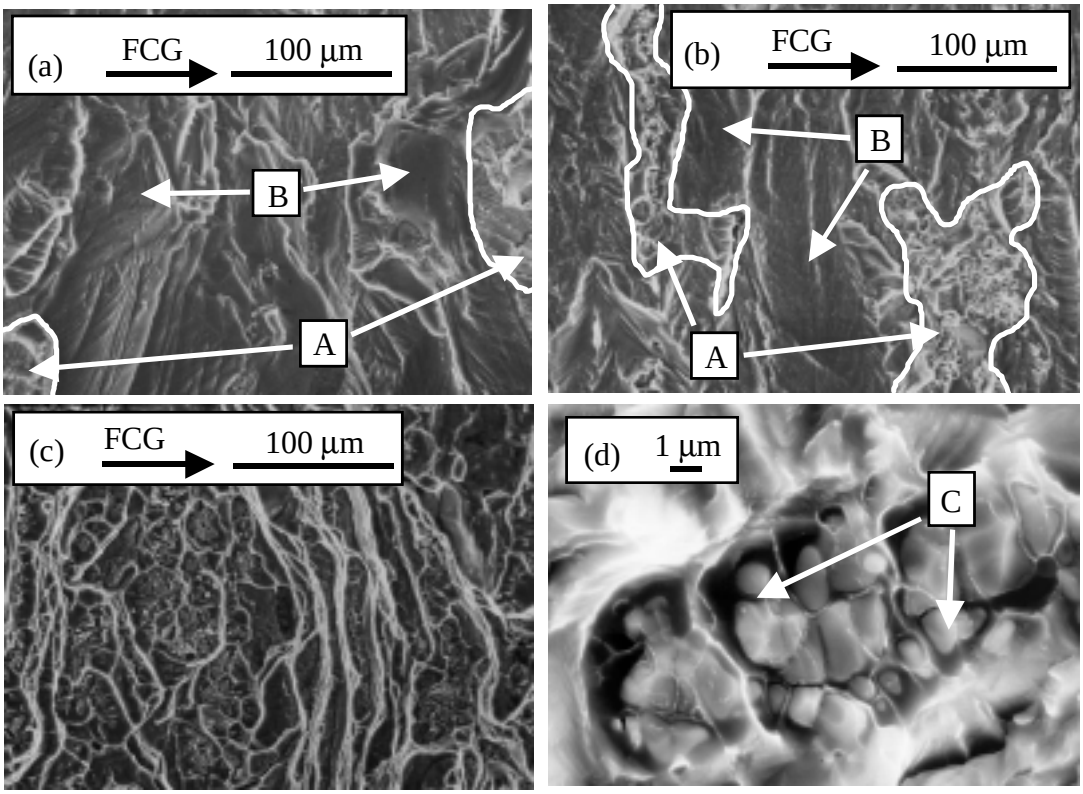

Figure 4.14 – SEM fractographs of alloy 7050-T6 fatigue crack surfaces produced by constant-K_{max} = (a) 5.5 and (b) 22.0 MPa√m threshold tests, (c) quasi-static fracture (K_c = 35 MPa√m), and (d) a high magnification fractograph of a typical region labeled A on the fatigue crack surface shown in part (b). Regions labeled A in parts (a) and (b) are outlined in white, while regions B in the figures remain unmarked. Figure 4.14c is almost completely consumed with regions previously denoted as A.

Figure 4.15a is a micrograph showing the through-the-thickness fatigue crack surface of an alloy 8009 specimen tested at constant K_{max} = 5.5 MPa√m. A transition in crack surface appearance, labeled A (in the center of the micrograph), separates dark regions on the left (labeled B) from light regions on the right (labeled C). This change in fatigue crack morphology coincides with the transition to accelerated FCG (point A in Figure 4.6). The final crack front at the end of the test is labeled D on the right side of the

micrograph. A delamination crack parallel to the direction of FCG and normal to the fatigue crack surface is labeled E in Figure 4.15a. During fatigue cracking, delamination occurred along oxide boundaries produced during manufacture of the sheet [68]. Figures 4.15b and 4.15c are micrographs showing regions A and B in Figure 4.15a,

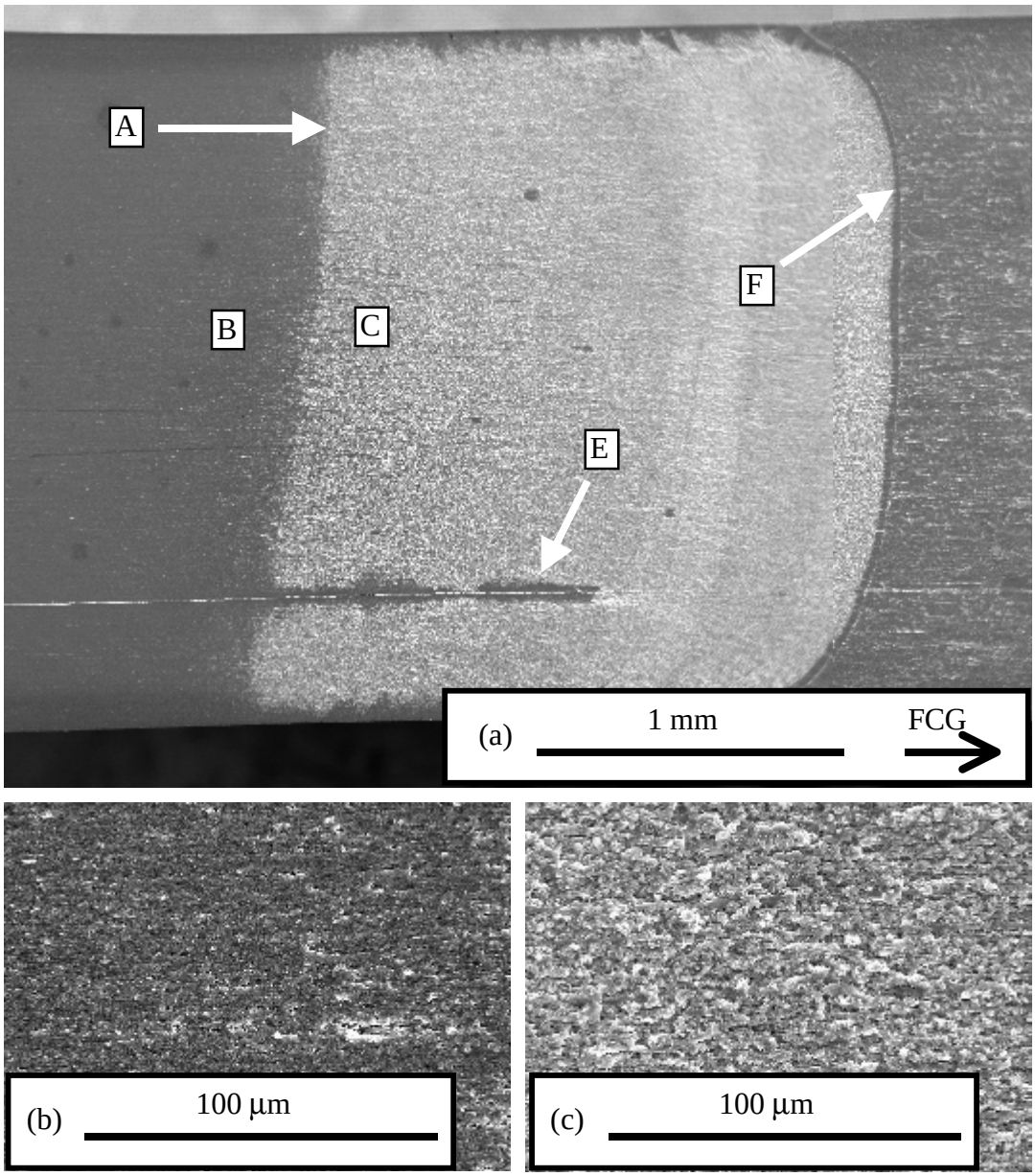

Figure 4.15 – SEM fractographs of alloy 8009 fatigue crack surfaces produced by a constant-K_{max} = 5.5 MPa√m threshold test; (a) the entire fatigue crack surface, (b) high magnification fractograph of region A in part (a), and (c) high magnification fractograph of region B in Figure 4.9a. Figures 4.15b and 4.15c correspond to FCG rates just before and just after point A in Figure 4.7. (Recall threshold tests performed with decreasing ΔK.)

respectively, at higher magnification. High magnification images are shown to highlight differences between dark and light regions of the fatigue crack surface shown in part (a). Prior to the transition (Figure 4.15b), the crack surface is somewhat featureless with widely space voids. The crack surface becomes rough due to a sudden increase in void density after the transition.

Figure 4.16a is a micrograph showing the through-the-thickness fatigue crack surface of an alloy 8009 specimen tested at constant K_{max} = 11.0 MPa√m. The crack surface transition, labeled A, separates dark crack surface on the left (labeled B) from light crack

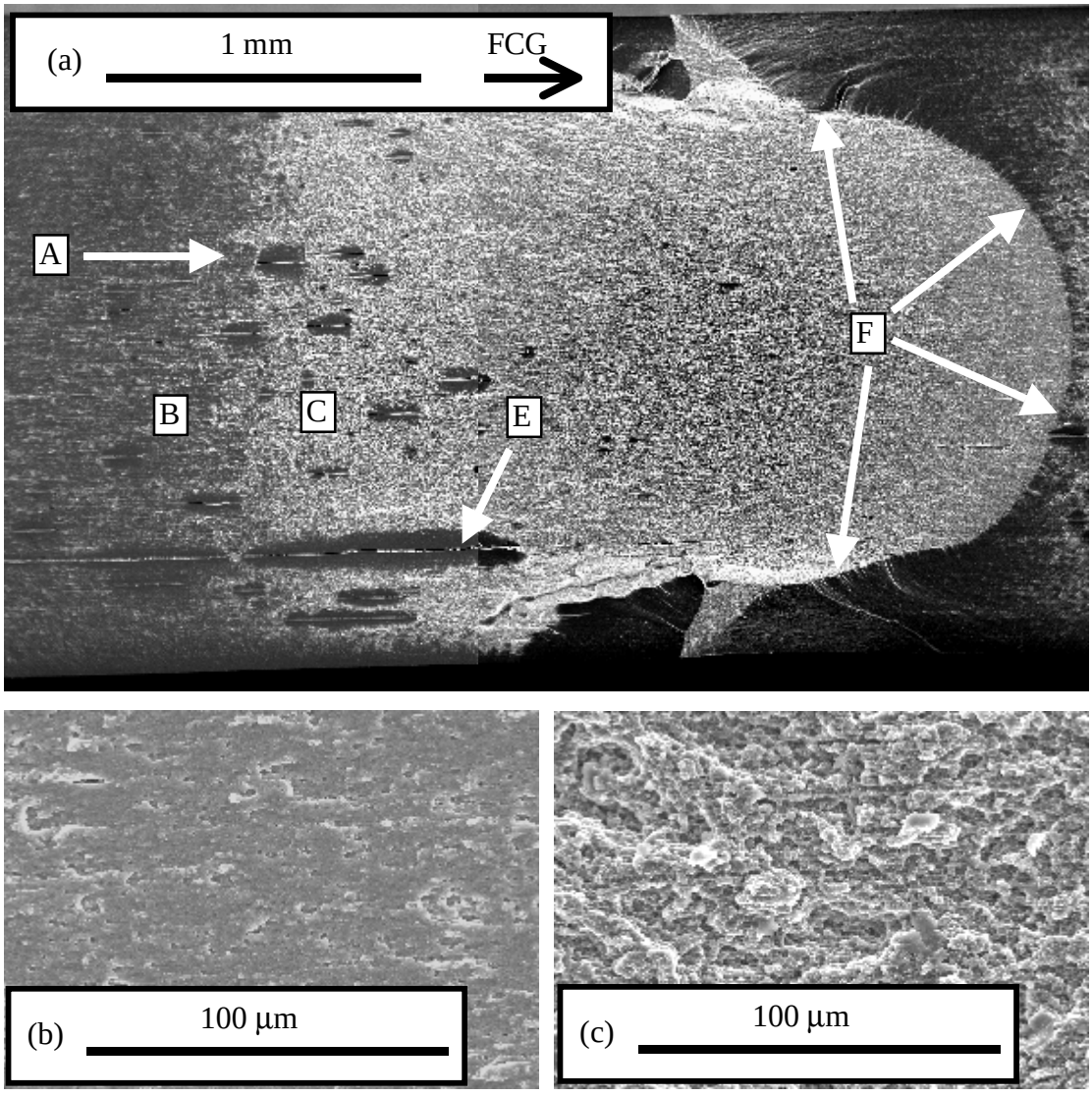

Figure 4.16 – SEM fractographs of alloy 8009 fatigue crack surfaces produced by a constant-K_{max} = 11.0 MPa√m threshold test; (a) the entire fatigue crack surface, (b) high magnification fractograph of region A in part (a), and (c) high magnification fractograph of region B in part (a). Figures 4.16b and 4.16c correspond to FCG just before and just after point B in Figure 4.6.

surfaces on the right (labeled C). This change in fatigue crack morphology coincides with the transition to accelerated FCG rates (point B in Figure 4.6). The crack front at the end of the test is labeled D. A delamination crack parallel to the direction of FCG and normal to the fatigue crack surface is labeled E. In contrast to the final crack front in Figure 4.15a, the crack front in Figure 4.16a indicates a great deal of tunneling (labeled D) occurred after the transition in FCG. Figures 4.16b and 4.16c are high magnification micrographs of regions labeled A and B, respectively, in Figure 4.16a. Figure 4.16b shows the fatigue crack surface just prior to accelerated FCG (to the right of point B in Figure 4.6) and Figure 4.16a shows the accelerated FCG surface morphology (to the left of point B in Figure 4.6). Here, accelerated FCG rates are correlated with a distinct increase in void size and density on the crack surfaces.

Examination of 8009 aluminum FCG surfaces (similar to Figure 4.16c) indicate only microvoids, with no mating convex surfaces, exist. An alternative explanation for crack surface voids is cracking along boundaries (grain or particle boundaries). If cracking occurred along boundaries, individual grains or particles would separate from one crack surface and remain attached to the conjugate surface producing convex and concave features. The difference between void production and boundary cracking are shown schematically in Figure 4.17. A void is shown after coalescence with the main crack in Figure 4.17a. Convex surfaces are produced on both crack surfaces. If boundary cracking were responsible for these holes, concave and convex surfaces would be produced in pairs, as shown in Figure 4.17b. Because no convex/concave mating features were observed on the crack surfaces, a void coalescence damage mechanism is likely. Similar microvoid nucleation processes have been observed by other researchers [68, 69]. No EDX analysis was performed on alloy 8009 due to the extremely fine microstructure. However, void formation about small dispersoids (400-800 Å in diameter) of $Al_{13}(Fe,V)_3Si$ has been observed [69]. Note that the voids seen on the crack surfaces are approximately 5 μm in diameter and are much larger than the typical grain diameter and dispersoid diameter (0.5 μm and 0.05 μm, respectively).

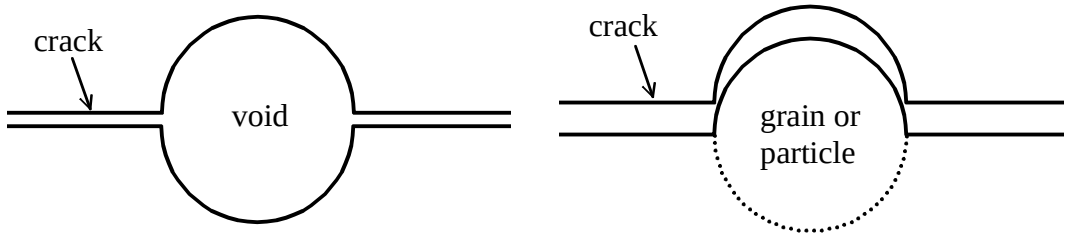

(a) void coalescence (b) boundary cracking

Figure 4.17 – Schematic illustrating the difference between concave surfaces produced by void coalescence and boundary cracking mechanisms.

The fractography presented in Figures 4.13 through 4.16 indicate that voids density on the fatigue crack surfaces increase with increasing K_{max}. It was assumed that this damage was produced ahead of the crack-tip, likely within the MPZ since it is the crack-tip

feature that increases with increasing K_{max}. To verify this assumption, similar voids seen on the crack surface must be found within the crack-tip MPZ or along the crack wake within material that formerly was within the MPZ. Because the void density and MPZ increase with increasing K_{max}, locating crack-tip damage sites in the MPZ should be easier at higher K_{max} levels. Damage sites (*e.g.* voids or microcracks) may be closed and undetectable at zero load so fatigue cracks will be wedged open at maximum load before looking for voids in the MPZ. Because void formation may occur more readily for plane-strain conditions (which was shown for 8009 aluminum), crack-tip damage may be easier to detect in the specimen interior. Therefore, FCG specimens were milled down (after FCG testing) to search for crack-tip damage in the specimen interior.

Of the three aluminum alloys studied here, evidence of crack-tip damage is likely easier to locate for 7050 aluminum for two reasons. First, voids formed at flat particle clusters along the crack plane and perpendicular to the specimen free surface. This geometry increased the likelihood of damage intersecting the free surface (after milling). Also, large clusters of voids should be easier to find than individual voids. Second, 7050 aluminum has the lowest yield stress of the three aluminum alloys. Decreasing the yield stress increases the MPZ (for a given K_{max}), so more surface area exists where damage may be found. Considering these factors, crack-tip damage is most likely detected in 7050 aluminum, at high K_{max} FCG threshold. A constant $\Delta K = 0.77$ MPa$\sqrt{m}$ at $K_{max} =$ 22.0 MPa$\sqrt{m}$ was considered. As seen in Figure 4.3, the FCG rate for these conditions is about 10^{-10} m/cycle. For $K_{max} = 22.0$ MPa$\sqrt{m}$ and $\Delta K = 0.77$ MPa$\sqrt{m}$, the plane-strain MPZ and CPZ are calculated as 0.82 mm and 0.25 μm, respectively (recall Equation 3.5a). Approximately 10 mm of steady state FCG occurred to ensure that a large area existed where crack-tip damage is expected. The specimen was then held at the maximum load ($K_{max} = 22.0$ MPa$\sqrt{m}$) and the crack was filled with epoxy to wedge the crack open. As the specimen was unloaded (after the epoxy cured), the back-face strain was monitored. Less than 5% of the back face strain was recovered, indicating the crack-tip stress intensity factor remained near the maximum value. One side of the specimen was milled down by approximately 0.85 mm (or $^1/_3$ of the specimen thickness) and polished to examine the specimen interior. This surface was not etched because (potential) pitting about microstructural features (resulting from the etchant) may be interpreted as fatigue damage. No significant damage sites were observed ahead of the crack-tip, in the MPZ. Because the CPZ is smaller than the void damage on the crack surface (0.25 μm and 3 μm, respectively) no damage is expected to exist here. However, numerous voids and microcracks were observed along the crack wake within the MPZ radius. During the constant ΔK test, this material was within the MPZ. Far from the crack, no such damage was observed. Six micrographs of the crack wake are shown in Figure 4.18. The direction of FCG was from left to right. Particles, voids, the main crack, microcracks, and fractured particles are labeled in each figure as indicated in the legend above the figures.

In Figure 4.18a, a high magnification image is shown of a particle cluster within the main crack. If viewed normal to the crack surface this feature would appear similar to the regions labeled 'A' in Figure 4.14. Damage about Al_7Cu_2Fe particles is shown to exist

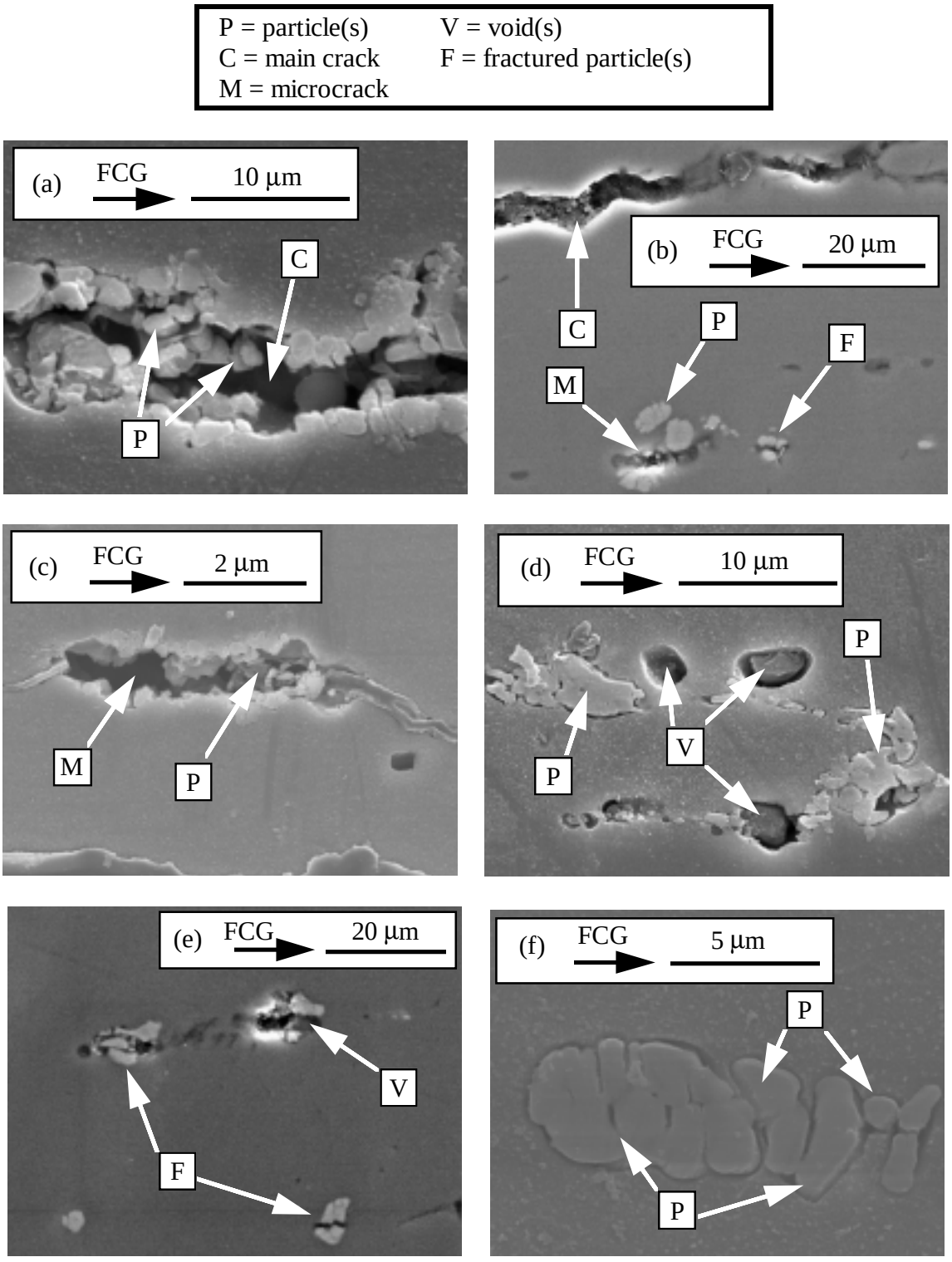

Figure 4.18 – Photographs of crack-tip damage along the plastic crack wake (MPZ) generated at K_{max} = 22.0 MPa√m, and ΔK = 0.77 MPa√m for aluminum alloy 7050. Surfaces are shown unetched and the FCG direction is indicated by an arrow.

away from the main crack in Figure 4.18b[24]. The main crack (labeled C) is seen at the top of this figure. Several clusters of particles are seen the lower portion of this figure, approximately 40 μm from the main crack. These features are well within the MPZ, but are approximately 300 CPZ radii from the main crack. Particles about which no damage is seen are labeled P. A particle cluster that appears to be fractured is labeled F. A microcrack that appears to have nucleated about similar particles is labeled M. Another example of voiding around particle clusters is shown in Figure 4.18c, approximately 170 μm from the main crack. In this figure, voids about individual particles have coalesced and a microcrack appears to be developing (labeled M). Large voids are seen within 40 μm of the crack face in Figure 4.18d. Although some particles in this figure are surrounded by large voids (labeled V), other particles are shown with little or no delamination from the matrix (labeled P). Additional voiding and particle fractures are indicated approximately 100 μm from the crack face in Figure 4.18e. As seen in Figures 4.18b through 4.18e, microcracks that initiated at particles grew normal to the applied load and parallel to the main crack.

For comparison a particle cluster far from the crack (approximately 6 mm) is shown in Figure 4.18f. A few individual particles are labeled P. Because these particles are approximately 7 MPZ radii from the main crack, no fatigue damage is expected here. Although a shallow groove exists between the particles and the surrounding matrix, no voiding or microcracks are observed. It is believed that this groove at the particle interface is a result of exposure to liquid water as the specimen was polished and does not represent fatigue damage. The damage noted at particle interfaces in the MPZ (Figures 4.18a through 4.18e) is much greater than that far from the crack (Figure 4.18f). These observations suggest that (1) crack-tip damage forms outside the CPZ, but inside the MPZ, and (2) although the crack-tip damage may initially exist as voids around second phase particles, microcracks also form about these features.

4.4 — CRACK-TIP DAMAGE MODEL

In Sections 4.2 and 4.3 it was shown that (1) FCG rates increase with increasing K_{max} (for a given ΔK) and (2) these accelerated FCG rates were correlated with an increase in void size and density along the crack surfaces. In this section a quantitative model will be developed and compared with experimental results for aluminum alloys 2024 and 7050. The threshold FCG behavior of 8009 aluminum is not modeled quantitatively here. (See Section 5.22 for a qualitative description of 8009 FCG threshold behavior.)

4.4.1 — Model development

In Section 4.3 microvoid damage was shown to occur about constituent particles at high K_{max}. For aluminum 7050, microvoids were shown to occur at these constituent particles within the MPZ; some of which developed into microcracks. Presumably, similar crack-tip damage occurs in other particle strengthened aluminum alloys (*e.g.* 2024 aluminum) at high K_{max}. Voids and microcracks are a result of strain concentration at constituent

[24] The chemical composition of these particles was identified by EDX analysis.

particles. Accelerated FCG is believed caused by interactions between the (main) crack-tip and localized damage sites ahead of the crack-tip. For convenience, crack-tip damage is modeled as microcracks. The interaction of a microcrack near the tip of a large crack has been modeled for general crack-tip loading (*i.e.* K_I, K_{II}, and K_{III} are non-zero, in general) by Meguid, *et al.*, [70]. A schematic of the Meguid model geometry is shown in Figure 4.19a. As shown in the figure, a single microcrack (of length 2*c*) exists near the tip of the main crack. The distance between the tip of the main crack and the center of the microcrack is defined as *d*. Although, the microcrack is allowed to rotate by the two angles shown in the figure (θ and ϕ). Here, both of these angles are assumed to be zero for convenience. The resulting stress intensity factor at the main crack-tip is given as K_{Imc} in Equation 4.1, where $K_{Iapplied}$ is the stress intensity factor

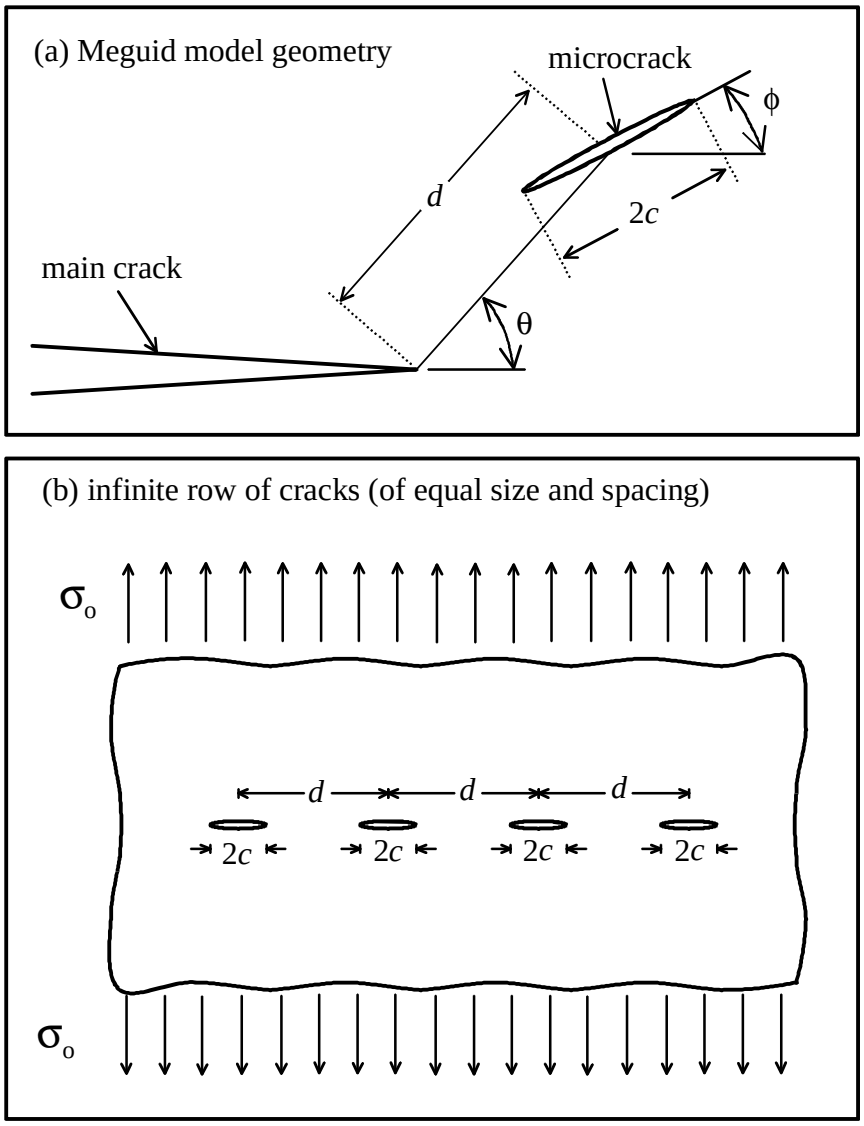

Figure 4.19 – Schematics of crack configurations used to develop the crack-tip damage model. In part (a) a simplified form of the Meguid model is shown. An infinite row of microcracks are shown in part (b).

associated with the main crack without considering the microcrack. The variable *r* is used to describe the distance from the main crack-tip to the center of the microcrack as the crack grows. The parameter *d* is used instead as a characteristic length related to microstructural spacing of voids. Although crack-tip damage occurs at many locations, Equation 4.1 only describes the influence of a single microcrack. To include the influence of multiple microcracks, the crack-tip damage ahead of the main crack is modeled as a series of microcracks of equal size and spacing, co-linear with the main crack. This crack configuration is schematically shown in Figure 4.20. The simplified Meguid model is shown on the left side of the figure. An infinite row of microcracks is considered ahead of the main crack, as shown on the right side of the figure.

The contributions of additional microcracks are estimated by considering a series of co-linear cracks of equal size and spacing in an infinite body. Only mode I loading is considered here. A schematic of this crack configuration is shown schematically in Figure 4.19b, where 2*c* is the microcrack length, *d* is the spacing between crack centers, and σ_y is the applied stress normal to the cracks. The stress intensity factor at the individual crack tips is given as $K_{Iseries}$ in Equation 4.2 [39]. The stress intensity factor for a single crack in an infinite body is given as $K_{Isingle}$ in Equation 4.3. The ratio of $K_{Iseries}$ and $K_{Isingle}$ is expressed in Equation 4.4. This factor represents the increase in crack tip stress intensity factor caused by the presence of additional microcracks in an infinite body. It is assumed that the crack-tip stress intensity factor of Equation 4.1 also increases by factor when an infinite row of microcracks are considered ahead of the main crack, as shown in Figure 4.20. The resulting crack-tip stress intensity factor (at the tip of the main crack) is given as K_{Imodel} in Equation 4.5, where *d* is the spacing between microcracks of length 2*c*, and *r* is the distance between the main crack-tip and the center of the closest microcrack. Because the parameters *d* and *c* are treated as constants, which are obtained empirically from crack surfaces, the growth of microcracks in the MPZ is neglected.

$$K_{I\,mc} = K_{I\,applied}\left[1+\left(\frac{c}{2r}\right)^2\right] \tag{4.1}$$

$$K_{I\,series} = \sigma_Y \sqrt{d \cdot \tan\left(\frac{\pi c}{d}\right)} \tag{4.2}$$

$$K_{I\,single} = \sigma_Y \sqrt{\pi c} \tag{4.3}$$

$$\frac{K_{I\,series}}{K_{I\,single}} = \sqrt{\left(\frac{d}{\pi c}\right)\cdot \tan\left(\frac{\pi c}{d}\right)} \tag{4.4}$$

$$K_{I\,model} = K_{I\,applied}\sqrt{\left(\frac{d}{\pi c}\right)\cdot \tan\left(\frac{\pi c}{d}\right)}\cdot\left[1+\left(\frac{c}{2r}\right)^2\right] \tag{4.5}$$

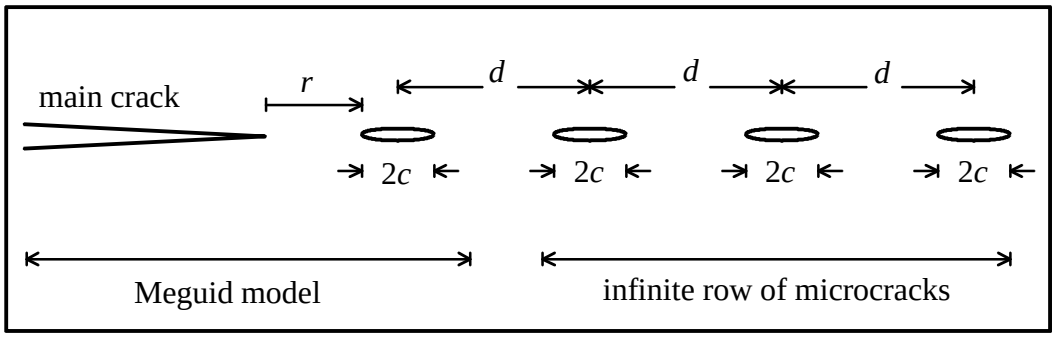

Figure 4.20 – Geometry of the crack-tip damage model developed here. An infinite row of microcracks is added to the (simplified) Meguid model.

4.4.2 — Evaluation of fatigue crack growth rates

Once the main crack stress intensity factor is determined from Equation 4.5, the corresponding FCG rate must be evaluated. A baseline FCG curve (FCG rate versus ΔK), not affected by closure or (high K_{max}) crack-tip damage, is needed. Constant K_{max} threshold test data is closure-free, but is subject to K_{max} effects, especially at high K_{max}. Constant K_{max} = 5.5 MPa$\sqrt{m}$ data is used as baseline FCG data because it is closure-free, and only slightly influenced by K_{max} effects. The baseline curves (constant K_{max} = 5.5 MPa$\sqrt{m}$ data) for aluminum alloys 2024 and 7050 are plotted in Figure 4.21. Constant K_{max} FCG data are plotted for K_{max} levels of 5.5 MPa$\sqrt{m}$ and 22.0 MPa$\sqrt{m}$ in Figure 4.21a, by closed and open circular symbols, respectively. Threshold FCG behavior of 2024 aluminum is characterized by a region of accelerated FCG below ΔK = 5 MPa$\sqrt{m}$ [71]. Because constant K_{max} = 5.5 MPa$\sqrt{m}$ threshold data falls within this region, constant K_{max} = 22.0 MPa$\sqrt{m}$ data are reduced (shifted lower) to match FCG rates at ΔK = 3 MPa$\sqrt{m}$ and K_{max} = 5.5 MPa$\sqrt{m}$. The modified K_{max} = 22.0 MPa$\sqrt{m}$ data is shown in Figure 4.21a as closed triangular symbols. Two fitted curves comprise the baseline FCG curve (fitted to closed symbols in Figure 4.21a). For ΔK > 2.1 MPa$\sqrt{m}$, a fifth order polynomial is fit through the data, and a linear curve is fit through data at ΔK < 2.1 MPa$\sqrt{m}$. These fitted curves are given by Equations 4.6a and 4.6b, and are plotted in Figure 4.21a as solid and dashed curves, respectively.

$$\log\left(\mathrm{d}a/\mathrm{dN}\right) = -10.37 + 3.69 * \log(\Delta K) \tag{4.6a}$$

$$\log\left(\mathrm{d}a/\mathrm{dN}\right) = -33.62 + 317.4 * \log(\Delta K) - 1617 * \log(\Delta K)^2 + 4099 * \log(\Delta K)^3 - 5136 * \log(\Delta K)^4 + 2541 * \log(\Delta K)^5 \tag{4.6b}$$

Constant K_{max} = 5.5 MPa$\sqrt{m}$ data for 7050 aluminum was used (as baseline data) without modification, as plotted in Figure 4.21b. For ΔK < 1.7 MPa$\sqrt{m}$ a fifth order polynomial was fit to the data (solid curve) and a linear curve was fit through the data for ΔK > 1.7 MPa$\sqrt{m}$ (dashed line). These two curves comprise the baseline FCG curve of 7050 aluminum, and are expressed symbolically in Equations 4.7a and 4.7b.

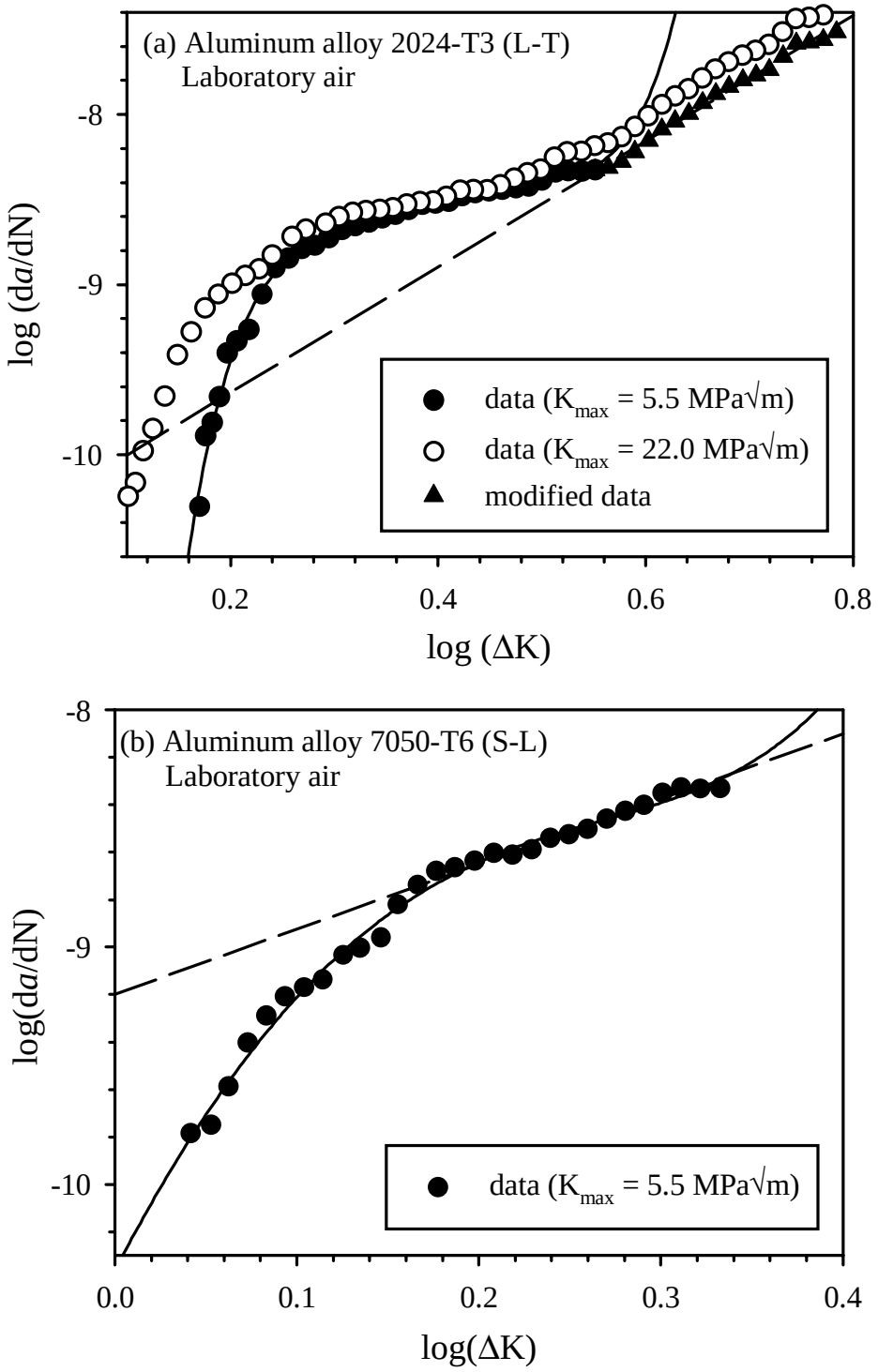

Figure 4.21 – Plot of baseline data used for the crack-tip damage model. Results are presented for (a) 2024 aluminum and (b) 7050 aluminum.

$$\log\left(da/dN\right) = -9.20 + 2.74 * \log\left(\Delta K\right) \tag{4.7a}$$

$$\log\left(da/dN\right) = -10.36 + 14.78 * \log\left(\Delta K\right) - 33.02 * \log\left(\Delta K\right)^2 + 0.014 * \log\left(\Delta K\right)^3 + 33.80 * \log\left(\Delta K\right)^4 + 96.48 * \log\left(\Delta K\right)^5 \tag{4.7b}$$

As the main crack grows closer to the microcrack, the stress intensity factor and, thus, FCG rate increases. A simple numerical procedure is used to evaluate this crack-tip damage model and determine the resultant (average) FCG rate, considering high K_{max} crack-tip damage. Model evaluation is described by the following eight-step procedure. (A computer program was written to evaluate the model and is listed in Section F.2.)

(1) Start at $r = d - c$, just after the main crack has coalesced with a microcrack.
(2) Evaluate the main crack stress intensity factor due to the damage ahead of the crack (Equation 4.5).
(3) Determine the corresponding FCG rate (Equations 4.6 or 4.7).
(4) Divide the distance between the two crack-tips ($r - c$) into many small increments. Allow the main crack to grow by a small increment at the FCG rate calculated in step 3. Determine the number of cycles for a small increment of crack growth (n_i) using Equation 4.8.
(5) Add the number of cycles for the small increment of crack growth to the total count using Equation 4.9. (Note that $N_{total} = 0$ at step 1.)
(6) Re-evaluate steps 2-5 after reducing r by the small increment of crack growth.
(7) Repeat steps 2-6 until $K_{max} = K_c$. At this point, the main crack fractures the ligament between the crack-tips and immediately coalesces with the microcrack.
(8) The predicted FCG rate is calculated by Equation 4.10.

$$n_i = \frac{\Delta a_{increment}}{\left(da/dN\right)_{step\ 3}} \tag{4.8}$$

$$N_{total} = \sum n_i \tag{4.9}$$

$$\left(da/dN\right)_{resultant} = \frac{d}{N_{total}} \tag{4.10}$$

4.4.3 — Model results

The crack-tip damage model (developed in the previous section) is used to predict accelerated FCG rates as K_{max} increases from 5.5 MPa√m to 22.0 MPa√m for both aluminum alloys 2024 and 7050. FCG data for these K_{max} levels (5.5 MPa√m to 22.0 MPa√m) are plotted in Figures 4.22 and 4.23 (as circular and triangular symbols) for aluminum alloys 2024 and 7050, respectively. The baseline FCG curve in each plot is shown as a solid curve. From micrographs of crack surfaces produced at K_{max} = 22.0

MPa√m, the microvoids for both aluminum alloys (2024 and 7050) are approximately 5 μm in diameter (2*c*) and spaced approximately 10 to 25 μm apart (*d*).[25]

In Figure 4.22, model results for aluminum alloy 2024 are plotted using *d* = 20 μm, 15 μm, and 10 μm, as dashed, dotted, and dash-dotted lines, respectively. Model results for *d* = 10 μm fit the K_{max} = 22.0 MPa√m well at FCG threshold (*i.e.* ΔK = 1.4 MPa√m), but overpredict FCG rates at higher ΔK. For model results to match experimental data, the model parameter *d* (damage spacing) must decrease, or *c* (damage size) must increase, as FCG threshold is approached.

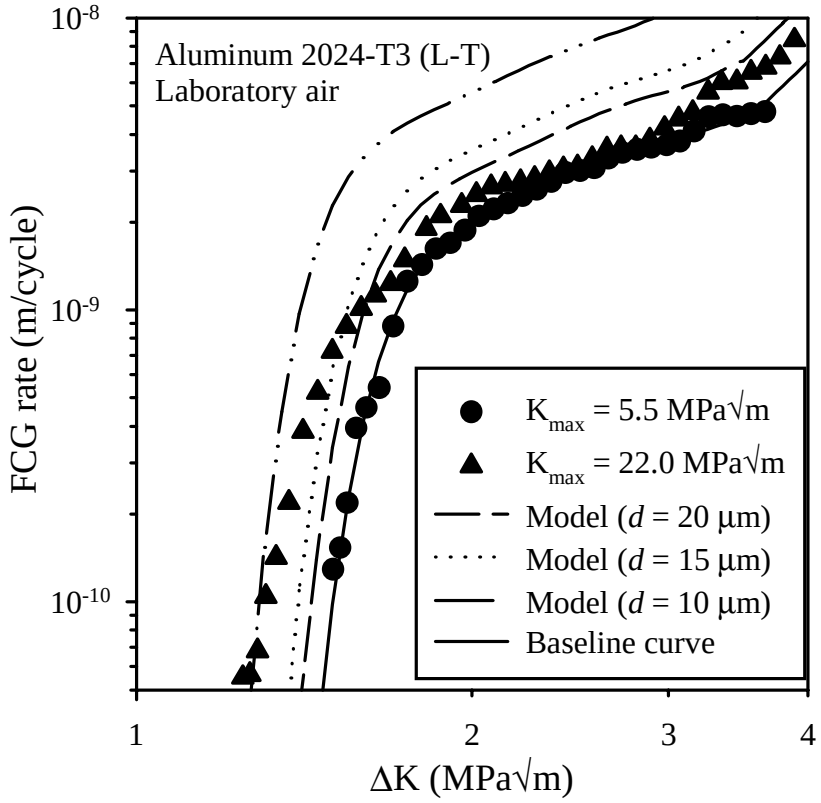

Figure 4.22 – Comparison of experimental data and crack-tip damage model results for aluminum alloy 2024.

Similar trends between model results and test data are seen in Figure 4.23, for 7050 aluminum. Model results are plotted in the figure for using *d* = 25 μm, 12 μm, and 10 μm, as dashed, dotted, and dash-dotted lines, respectively. Model results for *d* = 10 μm fit the K_{max} = 22.0 MPa√m well at FCG threshold (*i.e.* ΔK = 0.8 MPa√m), but over-predict FCG rates at higher ΔK. For ΔK > 1.2 MPa√m, FCG data agrees well with model results for *d* = 20 μm. For aluminum alloy 7050, the model parameter *d* must decrease,

[25] These values were used for 7050 aluminum although voids formed in clusters instead of a more uniform spacing. These values for *c* and *d* are considered to be average for 7050 aluminum.

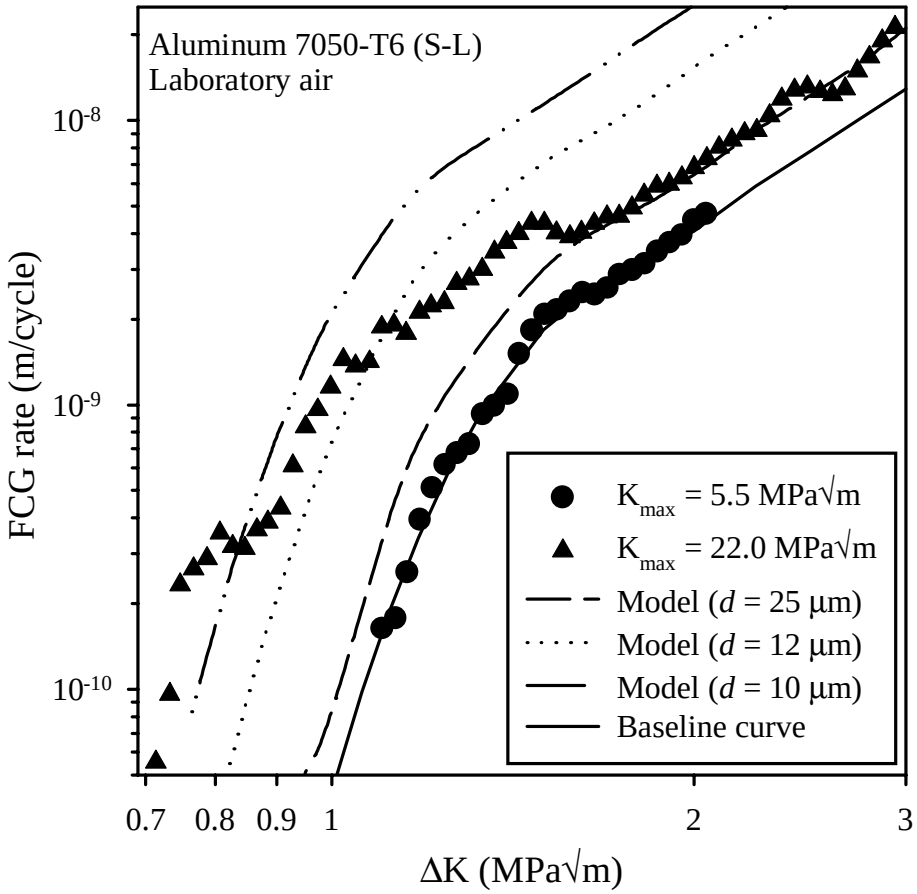

Figure 4.23 – Comparison of experimental data and model results for aluminum alloy 7050.

or *c* must increase, as FCG threshold is approached for model results to match experimental data. (The same trend was noted for 2024 aluminum model results in Figure 4.22.)

The crack-tip damage model, developed in Sections 4.4.1 and 4.4.2, predicted accelerated FCG rates at high K_{max}. Model results were in good agreement with experimental data at FCG threshold for aluminum alloys 2024 and 7050 ($\Delta K < 1.8$ MPa√m and 1.2 MPa√m, respectively). However, the model overpredicted FCG rates at higher ΔK (> 2.0 MPa√m and 1.2 MPa√m, respectively) by factors of 2.5 and 3.5, respectively. Likely explanations for high ΔK model problems are poorly chosen model parameters and neglected microcrack FCG. First, the model parameters used for results in Figures 4.22 and 4.23 were chosen from fractographs shown in Figures 4.13 and 4.14. Because these fractographs corresponded to threshold FCG, the model parameters were tailored to low ΔK conditions and the model performance was optimized at FCG threshold. Use of variable model parameters (*c* and *d* vary with ΔK and K_{max}) was not considered here. Second, neglecting FCG of microcracks could also explain the model performance noted in Figures 4.22 and 4.23. As an example, consider two cracked specimens loaded at K_{max} = 22.0 MPa√m, one at ΔK = 1.8 MPa√m and the other at ΔK = 4.0 MPa√m. For both

specimens the MPZ are of equal size. (For this discussion neglect the CPZ because they are small compared with the MPZ.) Because the FCG rates are different, the specimen at higher ΔK consumes an MPZ faster than the low ΔK specimen. A potential damage site in the MPZ (*e.g.* constituent particle) would be exposed to more load cycles in the low ΔK specimen, and would have more opportunity to grow before coalescing with the main crack. Therefore, crack-tip damage is expected to be greater as ΔK is reduced. Including microcrack FCG, and other possible model improvements are discussed in Section 5.2.4.

4.5 — SUMMARY

Results show that (1) closure-free near-threshold FCG rates depend on both ΔK and K_{max} and (2) no single value of closure-free ΔK_{th} exists. For well-behaved alloys, such as alloy 2024, this K_{max} effect is relatively small and corresponding changes in ΔK_{th} are minimal. However, some alloys (*e.g.* aluminum 7050, S-L orientation) can exhibit significant variations in ΔK_{th} for K_{max} sensitive orientations. Results also show that fine-grained microstructures (*e.g.* alloy 8009) can be greatly influenced by K_{max}, resulting in profound changes in threshold FCG characteristics.

Accelerated near-threshold FCG rates are correlated with increasing levels of crack-tip process zone damage. The increase in damage is related to microvoid nucleation at dispersoid or precipitate particles. It is speculated that the increase in K_{max} driving force promotes void growth by forcing additional dislocations (or vacancies) to accumulate at microstructural barriers (*e.g.* incoherent particle-matrix interface). This is discussed in greater detail in Section 5.2.

An analytical crack-tip damage model was developed, based on the observation that accelerated FCG rates at high K_{max} were correlated with increased crack-tip damage. This model was based on the assumption that accelerated FCG rates were a result of crack-tip damage (modeled as microcracks) elevating the main crack stress intensity factor. Model results, presented in Figures 4.22 and 4.23, were in good agreement with experimental data at FCG threshold, but overpredicted FCG rates at higher ΔK. Agreement between model results and test data would likely improve (for all ΔK) if FCG of the microcracks were considered.

PART III – Analysis of Results and Conclusions

CHAPTER 5 — DISCUSSION OF RESULTS

Fatigue crack closure, intrinsic load ratio (K_{max}) effects, and threshold humidity effects are discussed in separate sections. The most significant results are summarized and discussed in terms of practical applications and new understanding of threshold behavior. Finally, the contributions of this research are discussed in terms of a comprehensive threshold model that will include both extrinsic and intrinsic load ratio effects. Because this comprehensive model is only partially complete, the relationship between current models and future needs are outlined.

5.1 — DISCUSSION OF CLOSURE MODEL RESULTS

The PRO closure model was developed in Chapter 3 and included the three most likely threshold closure mechanisms (PICC, RICC, and OICC), crack meandering, and multi-axial loading. A sawtooth was used to model a rough crack wake. Residual crack wake plasticity was included by modifying an existing plasticity model [34]. A uniform layer along the crack faces was considered to model OICC. Due to the non-planar geometry of rough cracks, a mixed-mode crack-tip stress state exists. The stress intensity factors for rough meandering cracks were approximated with analytical solutions of angled straight cracks and kinked cracks. The resulting crack face displacements were used to determine closure loads.

Two key finite element results aided development of the PRO closure model. First, it was shown that stress intensity factors of sawtooth cracks approached the analytical solutions of a kinked crack-tip as asperity length, g, became small ($g/a < 0.05$). Second, elastic crack face displacements agreed with analytical solutions, but only between the crack-tip and the asperity nearest the crack-tip. Beyond the first asperity, crack-tip sliding mode displacements exhibited an oscillatory decay about zero, while opening mode displacements approached the straight crack solution. This observation suggests crack face contact may occur at this critical asperity. Therefore, crack closure must be considered at two locations, (1) the crack-tip and (2) the asperity nearest the crack-tip.

The RICC models of Suresh and Ritchie [14] and Wang, *et al.* [32], and the OICC model of Suresh [31] are special cases of the PRO closure model. The PRO closure model is more general and requires less empirical input. Some of the limitations, or peculiar behavior, of existing closure models are eliminated in the PRO model. To activate RICC, the Suresh and Ritchie model used an empirical value for CTSD. Analysis of crack face displacements was limited to linear-elastic stress-strain behavior so no CTOD or residual plastic deformation was considered. Wang calculated CTSD by considering crack-tip dislocation emission along a single slip plane that coincided with the crack-tip direction. In the PRO model, no plastic displacements occurred normal to slip plane, *i.e.* CTOD′ = 0. Because multiple slip planes and general crack-tip plasticity (*i.e.* both CTSD and CTOD) are considered, the PRO model is more general than previous RICC models. The OICC model developed by Suresh considers a cracked (straight mode I crack) linear-elastic body with an oxide layer along the crack faces. Because crack-tip plasticity is neglected (*i.e.* CTOD = 0), and elastic crack face displacements are always zero at the

crack-tip, there is no room for an oxide layer of finite thickness at the crack-tip (as modeled). In the Suresh OICC model, the oxide layer must terminate a finite distance behind the crack-tip to produce finite closure loads. This difficulty is overcome by including crack-tip plasticity, as done for the PRO model.

5.1.1 — Interaction of closure mechanisms

A synergetic relationship exists between closure mechanisms such that the closure resulting from multiple mechanisms is greater than the sum of individual mechanisms acting alone. If superposition were valid, the total closure, $R_{cl(TOTAL)}$, would be the sum of contributions from PICC, OICC, and RICC ($R_{cl(PICC)}$, $R_{cl(OICC)}$, and $R_{cl(RICC)}$, respectively), as shown in Equation 5.1. Although it will be disproved, assume for now that Equation 5.1 (superposition) is valid. The following example will show that interactions between closure mechanisms exist, and are predicted by the PRO model. Consider the four crack configurations schematically shown in Figure 5.1, subjected to cyclic loads of K_{max} = 3.5 MPa$\sqrt{m}$ and R = 0.05. Straight crack configurations are shown in cases (a) and (b), for no oxide layer and a 500 Å oxide layer, respectively. Two rough crack configurations ($\alpha = 30^o$ and g = 10 μm) are shown in cases (c) and (d), for t = 0 and 500 Å, respectively. Each of the four cases discussed here are summarized as a table in Figure 5.1. The active closure mechanisms for each case and the model results (R_{cl}) are shown to the right of the corresponding schematic. Model results were determined using mechanical properties of 2024 aluminum (E = 72 GPa, σ_o = 350 MPa, ν = 0.3). For consistency, crack contact is only considered 10 μm behind the crack-tip. In cases (c) and (d), 10 μm is the critical location for asperity contact, and must be considered to analyze the contribution of RICC. Two vertical dashed lines in Figure 5.1 indicate the distance from the crack-tip (line on the right) to the point where contact is considered (left line, g = 10 μm). Because crack-tip plasticity is always present, PICC is an active closure mechanism in each case. RICC and OICC are either active ($\alpha = 30^o$ and t = 500 Å) or are inactive (α = 0 and t = 0). The contribution of each closure mechanism is assumed to be a specific value where active, or zero where inactive. For example, (1) the PICC contribution, $R_{cl(PICC)}$, is identical for all four cases and (2) the RICC contribution in cases (c) and (d) are identical, but $R_{cl(RICC)} = 0$ for cases (a) and (b).

As indicated in Figure 5.1, case (a) includes only PICC and has a corresponding closure level of $R_{cl(TOTAL)} = 0.066$.[26] In terms of Equation 5.1, this is the plasticity contribution to closure (for all four cases), as expressed in Equation 5.2.

$$R_{cl(TOTAL)} = R_{cl(PICC)} + R_{cl(RICC)} + R_{cl(OICC)} \tag{5.1}$$

$$R_{cl(PICC)} = \mathbf{0.066} \tag{5.2}$$

[26] Recall that results in Figure 3.10 predict crack-tip closure levels of R_{cl} = 0.252 for straight cracks with no oxide. These results are not inconsistent because contact is considered 10 μm behind the crack-tip here.

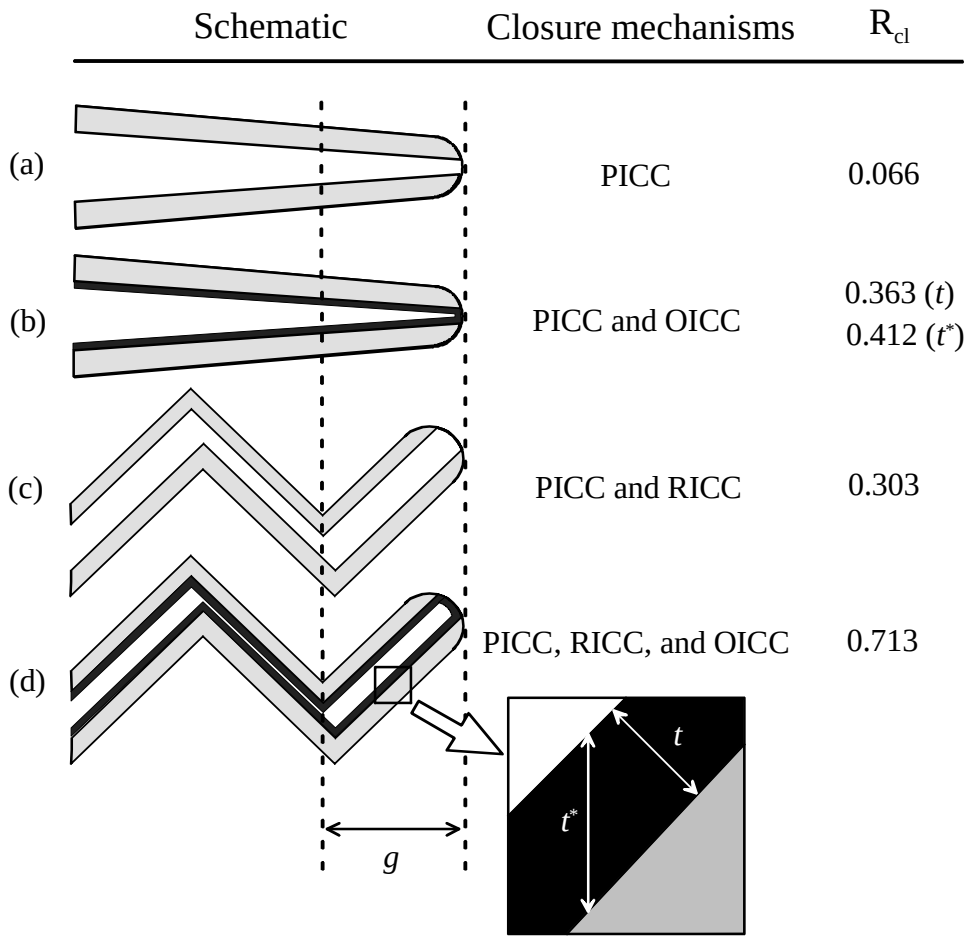

Figure 5.1 – Table of schematics, active closure mechanisms, and closure levels for four crack configurations, used to show interactions between closure mechanisms for FCG at K_{max} = 3.5 MPa√m and R = 0.05.

Both PICC and OICC are active closure mechanisms in case (b). For a 500 Å oxide layer the PRO model predicts $R_{cl(TOTAL)} = 0.363$.[27] Using $R_{cl(PICC)}$ from Equation 5.2, the contribution of OICC is calculated and shown in Equation 5.3.

$$R_{cl(OICC)} = R_{cl(TOTAL)} - R_{cl(PICC)} = 0.363 - 0.066 = \mathbf{0.297} \qquad (5.3)$$

The active closure mechanisms for case (c) are PICC and RICC and the resultant closure is $R_{cl(TOTAL)} = 0.303$. Using the PICC contribution from case (a), the RICC contribution is calculated in Equation 5.4. For this example, the contributions of RICC and OICC appear to be nearly equal (20% difference), and the contribution of PICC small by comparison (smaller by a factor of 4).

$$R_{cl(RICC)} = R_{cl(TOTAL)} - R_{cl(PICC)} = 0.303 - 0.066 = \mathbf{0.237} \qquad (5.4)$$

[27] A variation of case (b) will be examined later using a thicker oxide layer, t^* = 577 Å.

For case (d), all three closure mechanisms (PICC, OICC, and RICC) are active, and model results indicate $R_{cl(TOTAL)} = 0.713$. For superposition of crack closure to be valid, the closure level must be the sum of bold quantities in Equations 5.2 through 5.4. As shown in Equation 5.5, superposition predicts a closure level of $R_{cl(TOTAL)} = 0.600$, which is less than the model result. From this example, it is shown that (1) superposition is not valid for crack closure and (2) the total closure is greater than the sum of individual contributions. Although not proved in general, it seems the total closure is generally greater than superposition would predict.

$$R_{cl(TOTAL)} = 0.066 + 0.297 + 0.237 = \mathbf{0.600} < \mathbf{0.713} \tag{5.5}$$

An argument can be made that the effect of oxide is greater along the rough crack wake of case (d) than for the flat crack wake of case (b), and consideration of this may resolve the difference between superimposed and model results. Therefore, a variation of the previous example is analyzed using a thicker oxide layer. An effective oxide layer is defined as $t^* = t / \cos(\alpha) = 577$Å, and shown schematically in Figure 5.1. The crack face region indicated by a small box in case (d) is shown at higher magnification (indicated by open arrow). The oxide layer, t, is measured normal to the crack asperity, while t^* is measured normal to the nominal crack direction. This geometric effect is automatically considered (by the model) for rough cracks, so only case (b) needs re-evaluation. For case (b) with a 577 Å oxide layer, the model result is $R_{cl(TOTAL)} = 0.412$. Similar to Equation 5.3, the OICC contribution is calculated in Equation 5.6. Assuming the contributions of PICC and RICC are independent of OICC (*i.e.* superposition), their contributions are unchanged by the increase in oxide layer. By considering the thicker oxide layer in case (b), superposition still underestimates closure levels, as shown in Equation 5.7. Essentially, using the effective oxide layer for case (b) considered interactions between RICC and OICC. The inequality in Equation 5.7 exists because interactions with plasticity were not included.

$$R_{cl(OICC)} = R_{cl(TOTAL)} - R_{cl(PICC)} = 0.412 - 0.066 = \mathbf{0.346} \tag{5.6}$$

$$R_{cl(TOTAL)} = 0.066 + 0.346 + 0.237 = \mathbf{0.649} < \mathbf{0.713} \tag{5.7}$$

Only by considering all closure mechanisms simultaneously can threshold fatigue crack closure be understood. The contributions of individual mechanisms are often not easy to determine or even define because of synergetic interactions between closure mechanisms. For example, consider a rough sawtooth crack in an elastic body, where no plasticity occurs at the crack-tip, or in the crack wake, and no oxide layer exists in the crack mouth. Closure occurs at exactly zero load (*i.e.* $R_{cl} = 0$), both at the crack-tip and at the asperity closest to the crack-tip. If superposition were valid, this would imply crack roughness does not contribute to closure and RICC is not a closure mechanism.

As a special case of the PRO model, consider the OICC model developed by Suresh [14]. Here, a straight crack exists in an elastic body with a uniform oxide layer in the crack mouth. Because plastic displacements are neglected, no CTOD exists, and linear-elastic

analysis predicts no crack face displacement at the crack-tip. Thus, the Suresh OICC model allows no room at the crack-tip for an oxide layer of finite thickness. An oxide layer must terminate a finite distance behind the crack-tip for the Suresh model to predict finite closure loads. As the oxide layer approaches the crack-tip, closure levels become infinite. An infinite (or very large) value added to a finite (or relatively small) value results in an infinite (or very large) sum. Therefore, if superposition were valid any crack with an oxide layer at (or near) the crack-tip would produce infinite (or very large) closure levels. This would imply (if superposition were valid) that OICC is the most significant closure mechanism, regardless of oxide thickness or crack-tip loads (K_{max} and ΔK). Experimental observation and PRO model results indicate that superposition, stated symbolically in Equation 5.1, is not valid.

5.1.2 — Sliding mode crack closure (SMCC)

During mode II loading, sliding mode crack face displacements might cause contact between rough crack asperities. This crack face contact mechanism, called sliding mode crack closure (SMCC), reduces the crack-tip driving force. Similar to RICC, the portion of the load cycle when crack faces are contacting is ineffective (or less effective) in terms of crack-tip damage accumulation. However, two fundamental differences exist between SMCC and RICC. First, RICC reduces the crack-tip driving force (ΔK_I) by increasing the effective K_{min}, but SMCC reduces the (mode II) driving force (ΔK_{II}) by decreasing the effective (mode II) K_{max}. Second, applied loads are considered ineffective while crack faces are in contact for RICC, but not necessarily for SMCC. After sliding mode contact, increases in mode II loading tend to force contacting asperities past each other. As the asperities slide past each other, the crack is wedged open, producing an opening mode load on the crack-tip. This opening load is a result of asperity contact, not the mixed-mode stress state at a rough crack-tip. Although SMCC reduces ΔK_{II}, the potential addition of ΔK_I may increase crack-tip damage [72]. A schematic of SMCC for a sawtooth crack is shown in Figure 5.2. Initially sliding mode crack face displacements are dominant, indicated by horizontal arrows in part (a). As asperities slide past each other, the crack faces are wedged open (an opening mode displacement), as indicated by arrows (with both horizontal and vertical components) in part (b). Detailed descriptions of SMCC and SMCC models are given in Appendix A.

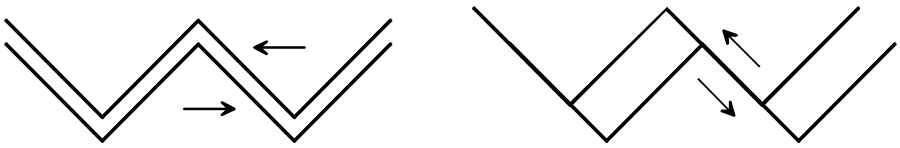

(a) initial displacments (b) displacments after contact

Figure 5.2 – Schematic illustrating sliding mode crack closure (SMCC). Under mode II loading, crack faces (a) initially move perpendicular to each other. When asperities touch (b), the rough crack features tend to slide past each other producing opening mode displacements of the crack surfaces. Arrows indicate direction of crack face movement.

Although the PRO closure model allows both mode I and mode II loading, it was not developed to describe SMCC. Typically mode II (or mode III) loading is dominant where SMCC occurs. The observation that crack face contact is likely to occur at the asperity nearest the crack-tip was based on finite element results for mode I loading. Crack face displacement behavior needs to be re-examined for mode II loading before modeling SMCC.

Finite element analyses were performed for (non-meandering) sawtooth cracks, similar to that of Figure 3.7, but for mode II loading. Non-dimensional quantities for opening and sliding mode crack face displacements (u^{**} and v^{**}, respectively) are plotted against r/g. These results are plotted in Figure 5.3 for $\alpha = 45^o$. Results for $g/a = 0.10$ and $g/a = 0.01$ are shown as circular and square symbols, respectively. No contact conditions are placed on the crack faces so asperity contact loads are neglected. Analytical solutions used by the PRO model are indicated as solid and dashed curves for u^{**} and v^{**}, respectively. (Definitions of u^{**} and v^{**} are given in the lower right corner of Figure 5.3.) The analytical solution (u^{**}) for a mode II straight crack is shown as the dotted curve. For mode II loading, the opening load displacements reach their maximum value at the asperity nearest the crack-tip, indicated by the vertical down arrow (at $r/g = 1$). Further behind the crack-tip, opening mode displacements exhibit an oscillatory decay about zero, while (the absolute value of) sliding mode displacements increase steadily with increasing r/g. Because the crack opening is greatest at the asperity nearest the crack-tip, crack face contact is least likely to occur there, and most likely far from the crack-tip. Because every point along a short crack is close to the crack-tip, the effects of SMCC are probably dependent on crack length. Longer cracks are likely more affected by SMCC than short cracks, especially if crack roughness is a factor. An increase in crack length is likely to produce little change in SMCC behavior for long cracks (well-developed rough

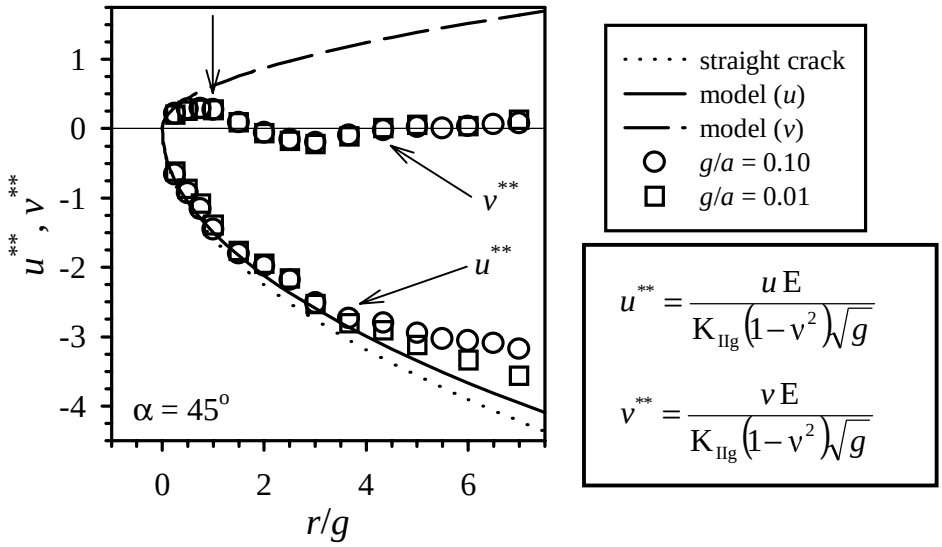

Figure 5.3 – Crack face displacement data from finite element analyses are shown for $\alpha = 45^o$, plotted against r/g.

wake), when compared with short cracks. These crack face displacements are important for modeling SMCC. Yu and Abel have presented SMCC data for two different long crack lengths (6.8 mm and 8.8 mm) [73, 74], but no change in SMCC behavior occurs from this (30%) increase in crack length. However, this crack-length-independence may not apply to short cracks (> 1 mm). Modifying the PRO model for SMCC is difficult because closure behavior likely depends on crack length. The PRO closure model was developed for traditional closure (primarily mode I), and the asperity nearest the crack-tip is a likely location for closure. Because the PRO model was not developed for SMCC, it is limited to scenarios where crack opening dominates (*i.e.* $K_{Ig} > K_{IIg}$).

5.1.3 — Crack-tip plasticity (slip)

As modeled, crack-tip plastic deformations (*i.e.* CTOD and CTSD) are a result of crack-tip dislocation emission. Pairs of dislocations are created near the crack-tip and driven apart. Dislocations of one sign are attracted to the crack-tip where they are annihilated, producing plastic strains. The dislocations of the opposite sign are driven away from the crack-tip until they pile-up at the elasto-plastic boundary (*i.e.* edge of plastic zone). The PRO closure model considered three slip planes coinciding with extreme values of crack-tip shear stress. In the RICC model developed by Wang *et al.*, only one slip plane is considered, coinciding with the crack-tip direction. Wang considered a single slip plane because cracks at FCG threshold tend to grow along slip paths [75]. Although the description of crack-tip deformation used by the PRO model is different, this does not imply the Wang model is invalid. Rather, it is believed the Wang model provides a better description of crack-tip slip for a crack front contained within a single grain, and the PRO model is better for crack fronts affected by multiple grains. The deformations of individual grains are averaged and a continuum mechanics description becomes valid when multiple grains affect the crack front [1, 76]. Because FCG specimens used here are at least 30 grains thick, the PRO model is believed superior.

Plastic crack-tip displacements were determined using a combination of dislocation and continuum mechanics concepts. Deformation was a result of dislocations produced at the crack-tip, but the slip paths were determined using the singular (continuum mechanics) crack-tip stress field. Because reversed slip is assumed to occur on the same slip paths as slip during loading, the PRO model is limited to cases of proportional crack-tip loading. Here, proportional crack-tip loading occurs when the ratio K_{Ig} / K_{IIg} is constant during the load cycle. An example of non-proportional loading is a static shear stress (mode II) superimposed on cyclic normal stress (mode I). Here, dislocation structures and deformation produced by the mode II static load likely affects mode I cyclic deformation. In terms of plasticity theory, crack-tip deformation is described here by the deformation theory of plasticity. Modification for non-proportional loading would require use of the more complicated incremental theory of plasticity.[28]

[28] Non-proportional crack-tip loads occur during SMCC wedge loading. This is another limitation of the PRO model that must be overcome to model SMCC. (Other problems related to SMCC modeling were discussed in Section 5.1.2.

The assumption that loading and unloading deformation are similar, and occur along the same slip planes, may not be valid when an oxide layer exists at the crack-tip. Fatigue crack growth tests, performed in air and vacuum, indicate that crack-tip slip is affected by (laboratory air) environment [52, 71]. These environmental effects on slip could be modeled as a change in residual crack wake plasticity (*i.e.* change in ξ), but is not done here. (Threshold FCG behavior is affected by environment in many ways. Additional environmental effects are discussed in Section A.1.2. However, the scope of this dissertation is limited to FCG load ratio effects. For details of environmental effects interested readers should refer to the references listed in this section, or in Section A.1.2.)

For mode I loading, mode II crack face displacements are a result of rough crack geometry. However, microstructural considerations can be made to allow mode II deformation, even for straight cracks. The slip system is considered to be symmetric about the crack plane for a straight crack in an isotropic medium (*i.e.* a continuum). Mixed-mode displacements can occur if microstructural barriers alter the slip system and destroy symmetry. If a slip plane intersects an obstacle, such as a grain boundary or an included particle, the crack-tip slip system will become unsymmetric, as schematically shown in Figure 5.4a. These barriers may eventually be overcome (see Appendix A), but the symmetry of the slip system is destroyed. Slip locally occurs along preferential planes, whose orientation varies from grain to grain. It is highly unlikely that slip planes will be oriented symmetrically about the crack plane in all grains. Also, the angles of slip relative to the crack direction may be unequal (not symmetric), as shown schematically in Figure 5.4b. Because these (potential) effects occur over multiple grains for FCG tests performed here, the average result is expected to be negligible.

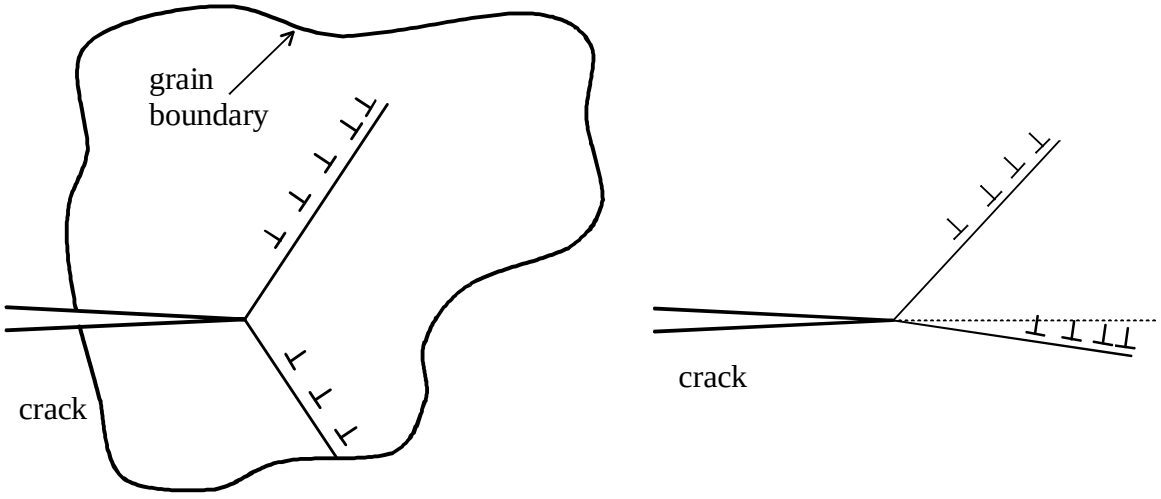

(a) unequal slip lengths (b) unequal slip angles

Figure 5.4 – Possible sources of mixed-mode displacements for a straight crack due to asymmetry of the slip system; (a) unequal slip lengths due to barrier in dislocation motion and (b) unequal angles of slip planes due to geometry of microstructure dependent preferred slip planes.

5.1.4 — Closure model limitations

The PRO closure model successfully describes contributions and interactions of PICC, RICC, and OICC, for both threshold and Paris FCG, in a variety of engineering metals. Because the PRO model is analytical, computation requirements are less than finite element models. However, some assumptions were made as the model was developed (see Sections 3.2 and 3.4), as listed below.

(a) Closure occurs at either the crack-tip or the asperity nearest the crack-tip. Remote closure and load history effects are not considered.

(b) The continuum/dislocation description of crack-tip deformation (described in Section 3.2.4) is valid and the crack front is affected by multiple grains.

(c) Reversed crack-tip slip is uninhibited.

(d) Crack-tip loading is proportional.

(e) No sliding mode crack closure (SMCC) occurs. Although a limited amount of mode II loading is allowed, opening mode crack face displacements dominate.

(f) Deformation of contacting crack asperities is neglected. No crack-tip damage occurs when crack faces are in contact.

(g) Plane-strain conditions dominate.

Because the PRO model was only used to determine closure levels and not FCG rates, the assumption that FCG threshold occurred when $\Delta K_{eff} = 0$ was not specifically stated. Experimental evidence indicates that threshold occurs when the effective crack-tip driving force is reduced to (nearly) zero [14, 31], implying that no ΔK_{th} exists in the absence of closure. Threshold models were developed using dislocation concepts, that indicate a finite ΔK_{eff} is tolerated without FCG [42, 77, 78]. For model results presented in Chapter 3, it was stated that FCG threshold occurred when $R_{cl} = 1$ (*i.e.* $\Delta K_{eff} = 0$). Although this statement implies $\Delta K_{eff} = 0$ at FCG threshold, it is approximately true even if an small intrinsic ΔK_{th} is tolerated because of the rapid rise in closure levels at threshold.

5.2 — DISCUSSION OF INTRINSIC LOAD RATIO (K_{max}) EFFECTS

Results in Chapter 4 show threshold FCG is dependent on both ΔK and K_{max}. Accelerated FCG rates are correlated with increasing levels of crack-tip process zone damage as K_{max} increases. The increase in damage (manifested as voids and microcracks) is related to microvoid nucleation at constituent particles (Al_2CuMg particles in alloy 2024, Al_7Cu_2Fe particles in alloy 7050, and probably $Al_{13}(Fe,V)_3Si$ dispersoid particles in 8009 [68]). The effect of increasing K_{max} on ΔK_{th} is summarized in Table 5.1. The table lists the decrease in ΔK_{th} (ASTM method) for corresponding increases of K_{max}. For example, ΔK_{th} for alloy 7050 decreased from 1.3 MPa$\sqrt{m}$ to 0.73 MPa$\sqrt{m}$ as K_{max} increased from 5.5 MPa$\sqrt{m}$ to 22.0 MPa$\sqrt{m}$. To relate FCG test results to a meaningful fracture parameter, K_{max} is normalized with K_{Ic}, the linear-elastic (plane-strain) fracture toughness. Table 5.1 shows that the K_{max} levels compared here are well below the plane-strain fracture toughness: $K_{max} / K_{Ic} \leq 0.65$ for 2024, ≤ 0.57 for 7050,

and ≤ 0.37 for 8009. Use of the plane-strain fracture toughness is conservative because the "as tested" fracture toughness is greater (*i.e.* $K_{Ic} < K_c$). A discussion of the likely crack-tip damage mechanisms is presented here for aluminum alloys 2024 and 7050. The ultra-fine microstructure and unusual threshold FCG behavior of 8009 aluminum requires special consideration and is discussed separately. Plane-strain / plane-stress constraint issues are discussed because they appear to be important for the threshold FCG behavior of 8009 aluminum.

Table 5.1 – Changes in threshold FCG behavior with K_{max}.

	Alloy (orientation)		
	2024-T3 (L-T)	7050-T6 (S-L)	8009 (L-T)
Change in K_{max} (MPa√m)	$5.5 \rightarrow 22.0$	$5.5 \rightarrow 22.0$	$5.5 \rightarrow 11.0$
Change in ΔK_{th} (MPa√m)	$1.5 \rightarrow 1.3$	$1.3 \rightarrow 0.73$	$1.15 \rightarrow < 0.6$
K_{max} / K_{IC}	$0.16 \rightarrow 0.65$	$0.19 \rightarrow 0.57$	$0.18 \rightarrow 0.37$
Void initiation sites (particles)	Al_2CuMg	Al_7Cu_2Fe	$Al_{13}(Fe,V)_3Si$ *
Particle size (μm)	2 to 3	1 to 3	0.04 to 0.08

* not determined by EDX; from references [68, 69]

5.2.1 — High K_{max} crack-tip damage in aluminum alloys 2024 and 7050

Results indicate at moderate levels of K_{max} ($K_{max} / K_{Ic} \leq 0.65$) threshold FCG in alloys 2024 and 7050 exhibited increased void production with increased K_{max}. Similar to voids produced at fracture, the voids produced during FCG nucleate at constituent particles. At high K_{max}, this voiding might be explained as "static modes," where isolated regions of the microstructure exhibit low toughness properties and fail during a single loading cycle (monotonic loading) [17]. Because void production is most active at FCG threshold, and can occur at relatively low K_{max} levels, a more subtle but important alternative rationalization, in terms of process zone fatigue damage, might be needed to explain this behavior. The preexisting state of damage (dislocation cell structure) contained in a cyclic process zone is greater than that contained in a monotonic process zone. An increase in K_{max} driving force promotes further dislocation motion, essentially expanding the region of intense damage at the crack-tip. Additional dislocations accumulate at microstructural barriers where voids nucleate and grow. Potential barriers about which voids might form include particle/matrix interfaces and dispersoids. The presence and growth of crack-tip damage (voids, microcracks, *etc*.) is correlated with accelerated FCG rates.

5.2.2 — Unusual threshold behavior of 8009 aluminum

Two transitions were observed during constant K_{max} threshold testing of 8009 aluminum. The first transition was associated with crack-tip void production at $K_{max} > 4.4$ MPa√m (see Figure 4.6). At $K_{max} = 22.0$ MPa√m, a second transition occurred when the crack

started to propagate on a 45° slant (at point D in Figure 4.7). No slant crack transition was observed at lower K_{max} levels. After the first transition (crack-tip void production), accelerated FCG rates were observed, but FCG rates did not increase with decreasing ΔK. Dramatic (apparent) increases in FCG rate occurred after the slant crack transition (see Figure 4.7). The first transition (void production) is discussed in the following paragraph. The slant crack transition will be discussed in Section 5.2.3.

Much like aluminum alloys 2024 and 7050, an increase in crack-tip void production was observed with increasing K_{max} for 8009 aluminum. However, the ultra-fine microstructure of powder metallurgy (PM) alloy 8009 requires further mechanistic considerations. Because 8009 contains a submicron grain size, it is unlikely that crack-tip process zone dislocation cell structures are developed [79, 80]. From previous research, the fracture properties of alloy 8009 are apparently governed by microvoid damage produced from dislocation interactions with dispersoids [69]. The microvoid morphology of 8009 aluminum fatigue crack surfaces in this study was similar to room temperature fracture surfaces produced by previous researchers [69]. This suggests the first transition (during constant K_{max} threshold testing of 8009) is related to a "dispersoid-type" microvoid damage mechanism. This transition is only observed for $K_{max} > 4.4$ MPa$\sqrt{m}$ suggesting void formation is K_{max} dependent. Because void growth is especially active near FCG threshold, an apparent ΔK dependence exists as well. Perhaps, slow FCG at threshold allows more time for void growth to occur. Increased FCG rates with decreased loading frequency suggest a time dependent process occurs. Creep crack growth (CCG) and stress corrosion cracking (SCC) are the most likely time dependent crack growth mechanisms, but accelerated FCG rates in UHV eliminates SCC. Because no crack growth occurred under a constant (static) load pure CCG does not occur. It is believed that accelerated threshold FCG by void growth is promoted by a room-temperature creep/fatigue interaction process. Here, fatigue loading is required to generate an abundance of mobile dislocations that are driven by K_{max} to dislocation sinks (dispersoids). The accelerated threshold FCG rate characteristics shown in Section 4.2.3 are consistent with a creep/fatigue mechanism. Figure 5.5 is a linear plot of the FCG parameters associated with this (void) transition (ΔK_{trans}, da/dN_{trans}, and K_{max}). ΔK_{trans} and da/dN_{trans} are plotted against K_{max} and indicated by open circular and closed triangular symbols, respectively. For K_{max} = 5.5 and 11.0 MPa$\sqrt{m}$, these transition points were shown in Figure 4.6 (points A and B). Transition points for K_{max} = 4.4, 7.7, 16.5, and 22.0 MPa$\sqrt{m}$ threshold tests are also plotted in Figure 5.5. For $K_{max} < 7.7$ MPa$\sqrt{m}$, the transition points are nearly constant ($\Delta K_{trans} \approx 0.8$ MPa$\sqrt{m}$ and $da/dN_{trans} \approx 6 \times 10^{-11}$ m/cycle). For this range of K_{max}, the MPZ is approximately equal to the void size produced at higher K_{max} levels. The smaller MPZ associated with low K_{max} would be unable to accommodate production of large voids, and is likely the reason why ΔK_{trans} and da/dN_{trans} are nearly constant for $K_{max} < 7.7$ MPa$\sqrt{m}$ in Figure 5.5. For $K_{max} > 10$ MPa$\sqrt{m}$, both ΔK_{trans} and da/dN_{trans} increase with increasing K_{max}. This suggests that increases in FCG rate require additional K_{max} driving force to support microvoid crack propagation.

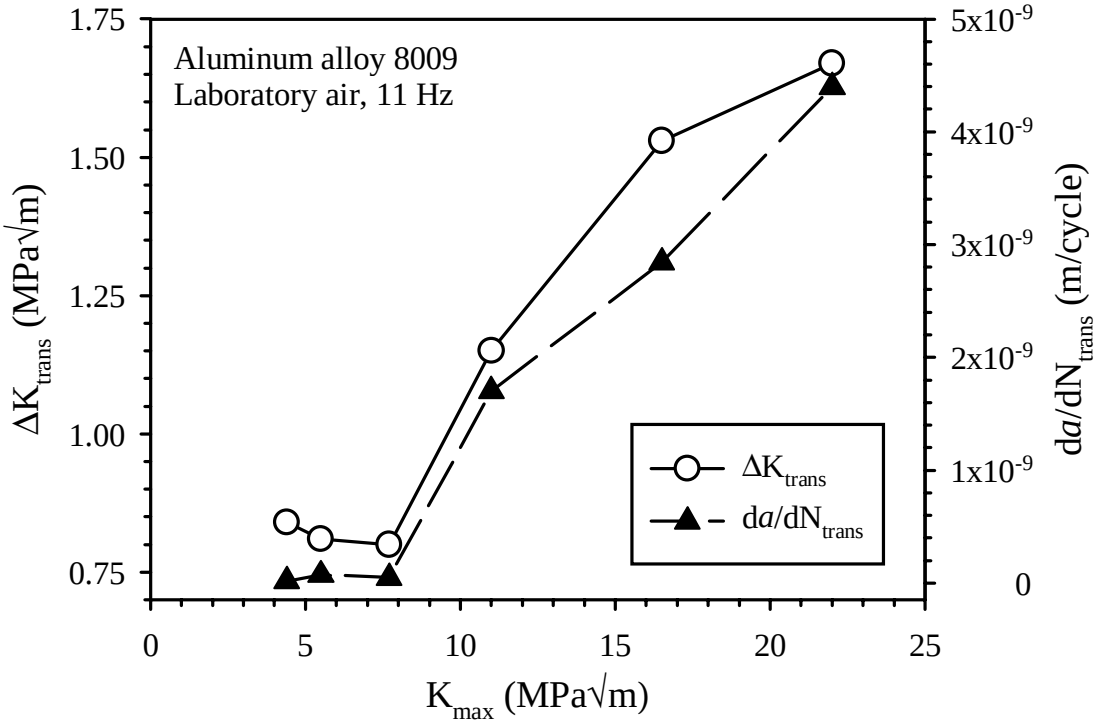

Figure 5.5 – Linear plot of FCG conditions for the first transition in 8009 aluminum. ΔK_{trans} (open symbols, left vertical axis), and da/dN_{trans} (closed symbols, right vertical axis), are plotted against K_{max}.

5.2.3 — Plane-strain dominance

Because unusual FCG threshold behavior of 8009 aluminum was associated with plane-strain conditions, crack-tip constraint is examined here. Crack-tip constraint is not uniform through the specimen thickness. At the surface of the specimen plane-stress conditions exist. In the specimen interior (far from any surfaces) the surrounding material inhibits lateral contraction and creates (near) plane-strain conditions. In reality, FCG specimens must have a finite thickness so a combination of plane-stress and plane-strain conditions exist. However, plane-strain conditions are dominant if Equation 5.8 is satisfied [1]. This relation insures that the plane-stress MPZ (at the surface) is much smaller (approximately a factor of 8 smaller) than the specimen thickness. The MPZ radius for plane-stress and plane-strain conditions are shown as Equations 5.9a and 5.9b, respectively. Plane-stress conditions are more likely to dominate at high K_{max} where a large MPZ exists. For aluminum alloys 8009, 2024, and 7050, the largest values of K_{max} to satisfy Equation 5.8 are $K_{\varepsilon\,max}$ = 12.74, 10.62, and 7.91 MPa√m, respectively, as summarized in Table 5.2. These values do not represent an abrupt transition where conditions suddenly change from plane-strain to plane-stress. Instead, the transition from plane-strain to plane-stress is gradual (with increasing K_{max}). Equation 5.8 is used here to provide qualitative information about crack-tip constraint. For example, from results in Table 5.2, it is apparent for all three alloys that plane-stress conditions are significant when K_{max} >15 MPa√m.

$$t \geq 2.5\left(\frac{K_{max}}{\sigma_o}\right)^2 \tag{5.8}$$

$$r_{p\sigma} = \frac{1}{\pi}\left(\frac{K_{max}}{\sigma_o}\right)^2 \tag{5.9a}$$

$$r_{p\sigma} = \frac{1}{3\pi}\left(\frac{K_{max}}{\sigma_o}\right)^2 \tag{5.9b}$$

Table 5.2 – Limits of plane-strain dominance, $K_{\varepsilon\,max}$, for each alloy.

Alloy	thickness (mm)	σ_o (MPa)	$K_{\varepsilon\,max}$ (MPa√m)
8009 aluminum	2.3	420	12.74
2024 aluminum	2.3	350	10.62
7050 aluminum	2.5	250	7.91

Fractography presented in Chapter 4 suggest that void production after with the first transition is limited to the specimen interior, where plane-strain conditions dominate. At K_{max} = 5.5 MPa√m plane strain conditions were dominant and the crack front remained nearly straight (see Figure 4.15). At K_{max} = 11.0 MPa√m, the plane-stress regions at the specimen surfaces were larger and had a greater influence on FCG behavior. FCG was accelerated in the specimen interior, but not at the surfaces. This resulted in crack tunneling as shown in Figure 4.16. The plane-stress ligaments at the surface lagged behind the plane-strain crack front. This curved crack front increased the stress state in the plane-stress ligaments until fracture occurred, typically at a 45° angle. Fatigue cracks may grow in a (45° angle) shear mode if plane-stress conditions dominate [1]. Consider a tunneled crack subject to a K_{max} slightly smaller than would normally facilitate slant crack growth. Although FCG initially occurs on flat planes normal to the specimen surface, fracture of plane-stress ligaments on a 45° slant might disturb the flat crack stability and initiate slant cracking. Because stress intensity factors are calculated assuming a flat crack configuration, ΔK is a poor descriptor of slant crack driving force.[29] The unstable slant crack behavior is probably an artifact of using ΔK where it is not appropriate. This "tunneling/slant-crack" mechanism is believed responsible for the unstable threshold behavior observed during constant K_{max} = 22.0 MPa√m threshold testing (see Figure 4.7). As shown in Table 5.2, plane-strain conditions dominate for the 8009 specimens if K_{max} > 12.74 MPa√m. Therefore, it is not surprising that slant cracking was not observed during constant K_{max} = 11.0 MPa√m threshold testing (see Figure 4.7).

[29] Also, ΔK is a poor descriptor of crack-tip driving force if the small scale yielding assumption is violated.

Although the first transition was related to plane-strain conditions, the second transition was associated with plane-stress. If the mechanism proposed for the slant crack transition is valid, only the first transition (associated with void production) would occur when Equation 5.8 is satisfied for $K_{max} \geq K_{Ic}$. For example, 8009 aluminum specimens should be at least 12.75 mm thick to avoid slant cracking (*i.e.* $K_{\varepsilon\,max} = K_{Ic}$). Although this "tunneling/slant-crack" mechanism presumably explains the unusual threshold behavior of 8009 aluminum, it apparently does not explain the behavior shown by Marci and Lang, *et al*. The titanium specimens tested by Lang are 10 mm thick, but only need to be 1.57 mm thick for plane-strain dominance at fracture.[30] Therefore, another unstable threshold mechanism must occur for titanium alloys.

The first threshold transition of 8009 aluminum is a product of the material and represents the intrinsic plane-strain behavior. The same transition points plotted in Figure 5.5 would likely occur if thicker specimens were used. However, the second transition (associated with slant cracking) is related to crack tunneling and does not represent intrinsic material behavior. Slant cracking at threshold is probably dependent on specimen thickness, and K_{max}. Like fracture toughness, K_c, the slant crack transition is a function of specimen thickness. However, use of plane-strain fracture toughness (K_{Ic}) provides a conservative estimate for fracture. In contrast, dangerously non-conservative threshold FCG rates result if plane-strain behavior is assumed, but slant cracking (*i.e.* plane-strain behavior) occurs. Because this behavior was only observed in 8009 aluminum, it is not known if similar behavior exists in other engineering alloys.

5.2.4 — Crack-tip damage model

Assuming crack-tip damage produces stress fields similar to microcracks, a fracture mechanics based model was developed (in Section 4.4) to predict accelerated FCG rates at high K_{max}. An existing crack/microcrack interaction model was modified to model crack-tip damage as an array of microcracks of equal size and spacing. The presence of crack-tip damage increased the stress intensity factor at the main crack-tip. Using a baseline FCG curve, accelerated FCG rates were calculated for aluminum alloys 2024 and 7050. Although the model results predicted an appropriate increase in FCG rates at threshold, FCG rates were over-predicted at higher ΔK. FCG of microcracks in the process zone of the main crack was neglected. Including microcrack FCG might resolve the overestimation of FCG rates at higher ΔK, and perhaps model the unusual threshold behavior (void growth mechanism) of 8009 aluminum.

5.3 — HUMIDITY EFFECTS AT THRESHOLD

Threshold FCG rates tend to increase with increasing humidity (see Appendix E). For aluminum alloy 7050-T6 tested in the S-L orientation, FCG rates at threshold increased by a factor of 7 as humidity increased from 0% to 100% relative humidity. However, in the ambient range of humidity (30% to 70% relative humidity) FCG rates were nearly

[30] For the titanium alloy tested by Lang, $K_{Ic} = 29\ MPa\sqrt{m}$ and $\sigma_o = 1158$ MPa.

independent of humidity. In this case, the ambient humidity range was bounded by two transition regions where FCG rate increased rapidly with increasing humidity.

As humidity decreased from the ambient range to dry air, accelerated FCG rates of humid air persisted until the crack grew through the MPZ developed in humid air. No such transition was observed as the crack went from dry to humid air. This suggests that a product of the environment, likely hydrogen from water vapor, permeates the MPZ producing accelerated FCG rates. Previous studies of water vapor (humidity) effects on FCG rate indicate that absorbed hydrogen in the crack-tip process zone causes accelerated FCG rates [81, 82]. Presumably, this is also true for the data presented in Appendix E. Where variable humidity is an issue, the peak value of humidity is likely more significant than an average value. As an example, consider a cracked structural member, subjected to fatigue loading in an outdoor environment 24 hours per day. Typically, daytime humidity is low (< 50% relative humidity), but during the night dew may form (100% humidity). If the cumulative FCG during a 24-hour period is less than the MPZ, the FCG rate will correspond to that associated with nighttime humidity. Exposure to humid air (even for a short period of time) may affect FCG rates for many cycles.

5.4 — COMPREHENSIVE THRESHOLD MODEL

Presumably, intrinsic and extrinsic load ratio effects can occur simultaneously. Because intrinsic damage occurs ahead of the crack-tip and fatigue crack closure (extrinsic effects) occurs in the crack wake, it was assumed that these effects are not interacting and were considered separately. A methodology is presented here to include both extrinsic and intrinsic load ratio effects simultaneously. The PRO closure model (Chapter 3) and the crack-tip damage model (Chapter 4) are put into the context of this comprehensive threshold model, as shown in Figure 5.6. The comprehensive threshold model is comprised of three individual models indicated by boxes stacked vertically in the center of the figure. The models developed here are shown in solid boxes. A third model, which has not been developed, is shown in a dashed box. The needed input is shown to the left of the corresponding model (box) and the output is shown on the right. The models must be evaluated from top to bottom, indicated in the figure by open arrows. For a given FCG scenario, the crack closure behavior should be evaluated first. The model developed here needs material properties, crack geometry, loading conditions, and deformation behavior as input. Effective crack-tip loads, K_{max} and ΔK_{eff}, are output. Using effective crack-tip loads, deformation behavior, and description of the microstructure at the crack-tip. The development of crack-tip damage must be determined next. Although this model has not been developed here, it is believed that this model should describe interactions between dislocations and microstructural features (*i.e*. grain boundaries, constituent particles, *etc*.). A description of damage accumulation from microstructural defects through development of small cracks is needed. Because of microstructural variation, this model will likely be stochastic in nature (at least with regard to the description of microstructure). This model will output a description of the crack-tip damage state (*e.g*. microvoid or microcrack density). Finally, the interaction of crack-tip fatigue damage with the primary fatigue crack will be modeled as done in

Chapter 4. Once the crack-tip damage can be described by fracture mechanics (*i.e.* ΔK), this model should include the growth of microcracks in the crack-tip process zone. (Recall that microcrack FCG was neglected by the crack-tip damage model developed in Chapter 4.) From the crack-tip damage state, K_{max}, ΔK_{eff}, and a baseline FCG curve (FCG rate versus ΔK data) this model will determine the resulting FCG rate.

Because inclusion of all influences will likely produce a better description of threshold FCG, environmental effects should eventually be included in this scheme. Also, the possibility of interactions between these models should be examined. For example, the crack-tip slip behavior (considered in the closure model) might be affected by crack-tip damage.

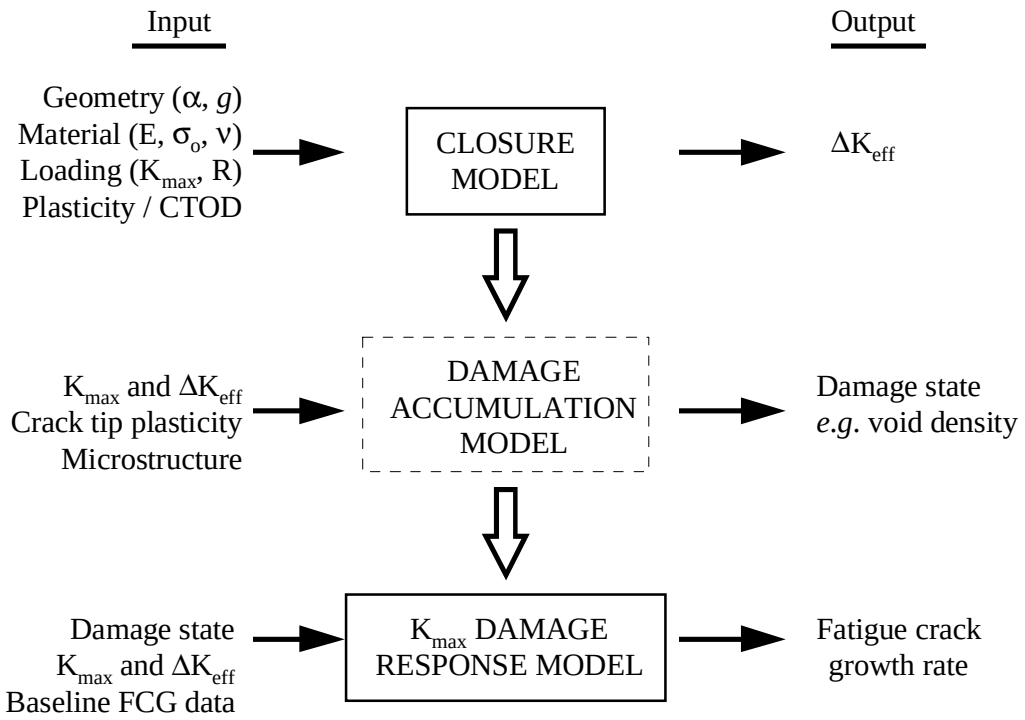

Figure 5.6 – Chart illustrating how current models fit in with a comprehensive threshold FCG model.

CHAPTER 6 — CONCLUDING REMARKS

Research results, their practical implications, and advances made to further current understanding of threshold FCG are outlined. This research effort was discussed in terms of a comprehensive threshold model in Section 5.4. Because this comprehensive model is only partially complete, additional research needs are listed.

6.1 — SUMMARY OF RESEARCH RESULTS

A summary of the most significant research results, and their significance, are presented here. Consistent with the organization of this dissertation, results for fatigue crack closure and intrinsic load ratio effects are presented in separate sections. Significant observations of humidity effects on threshold FCG behavior (see Appendix E) are also presented.

6.1.1 — Fatigue crack closure

By including PICC, RICC, and OICC, the PRO closure model (developed in Chapter 3) is uniquely suited for, but not limited to, threshold FCG. Comparison with experimental data indicates that model results are valid over a wide range of crack-tip loads for both aluminum alloys and steels. Two key findings have resulted from this crack closure study as described below.

(1) Closure is most likely at the crack-tip or at the asperity closest to the crack-tip for rough fatigue cracks. These types of crack face contact are described as "tip contact" and "asperity contact" respectively. Both locations must be considered to understand closure of rough fatigue cracks. Tip contact is more likely as oxide layer thickness increases, asperity angle (α) decreases, and K_{max} increases. Asperity contact becomes more likely as oxide layer thickness decreases, asperity angle increases, and K_{max} decreases. Consistent with experimental results, the PRO model indicates crack roughness is most important at FCG threshold. As ΔK is reduced, asperity contact (RICC) dominates over tip contact. When the closure mode changes from tip contact to asperity contact, the closure level (R_{cl}) increases rapidly with further ΔK reduction. Model results suggest crack roughness contributes to FCG threshold.

(2) When multiple closure mechanisms act simultaneously, the resulting closure level is greater than the sum of individual contributions. This synergistic behavior requires consideration of all significant closure mechanisms to determine the resulting closure loads. Superimposing the contributions of individual closure mechanisms is inadequate where PICC, RICC, and OICC are important, *i.e.* threshold FCG regime.

Two additional comments of significance to fatigue crack closure are presented below.

(3) Fatigue crack closure measurements using far-field compliance are poor indicators of crack-tip events. Changes in compliance are sensitive to remote closure or when a large portion of the crack closes. Because FCG behavior is determined by crack-tip events, near-tip measurement techniques (*e.g.* DIDS) are better suited to describe fatigue crack behavior.

(4) Two model alloys have been successfully used here. A shape memory alloy was used to partially recover plastic deformation in the crack wake and eliminate PICC. Aluminum alloy 8009 was studied because fatigue cracks were smooth, eliminating RICC. Although structural applications may be limited for these alloys, their special features make them attractive for fatigue crack closure studies.

6.1.2 — Intrinsic load ratio effects

Constant K_{max} threshold tests were conducted to study intrinsic FCG load ratio effects of aluminum alloys. Accelerated FCG rates and decreased ΔK_{th} result from increases in K_{max}. The mechanism for K_{max}-affected behavior was identified and modeled. The significant results related to intrinsic load ratio effects are discussed as follows.

(1) Accelerated FCG rates at high K_{max} are correlated with increases in crack-tip damage. This damage is seen as voids on the crack surfaces and in the plastic wake. Because this damage seems to accumulate within the MPZ, more damage is expected within a larger MPZ, *i.e.* high K_{max}.

(2) No true threshold is reached during FCG threshold testing. Although ASTM standard procedures provide a working definition for threshold, this always provides a non-conservative value (*i.e.* ΔK_{th} too large). Because the slope of the FCG data at threshold, m^*, decreases with increasing K_{max}, the underestimation of ΔK_{th} is probably greater at higher K_{max}. Furthermore, m^* was smaller for alloys that exhibited pronounced closure-free load ratio effects (*e.g.* aluminum alloys 7050 and 8009). Using constant K_{max} threshold tests to simulate short crack behavior (by eliminating closure) may affect test results due to intrinsic effects at high K_{max}.

(3) Two types of unusual FCG threshold behavior were observed during constant K_{max} threshold tests of aluminum alloy 8009. One transition was related to plane-strain conditions followed by another related to plane-stress conditions. A transition to a void coalescence mechanism at threshold is associated with plane-strain conditions. Although this transition does not lead to unstable threshold behavior (*i.e.* increasing FCG rates with decreasing ΔK) it does produce accelerated FCG rates. Crack tunneling occurs at $K_{max} \geq 11.0$ MPa$\sqrt{m}$. The plane-stress ligaments, which lag behind as the crack grows faster in the specimen interior, tend to fracture producing sudden increases in FCG rates. These bursts of crack growth are indicated as spikes in FCG data (see Figure 4.7). At $K_{max} = 22.0$ MPa$\sqrt{m}$, the fracture of plane-stress ligaments occurs on a 45^o slant, leading to a slant crack occurring through the specimen thickness. This transition to slant crack growth is accompanied by increasing FCG rates, apparently as ΔK decreases. However, the solution for ΔK assumes a flat crack through the specimen thickness and this unstable FCG is likely a result of a poorly defined stress intensity factor for slant cracking.

6.1.3 — Effects of humidity on threshold behavior

The effects of humidity on intrinsic threshold FCG were explored for aluminum alloy 7050. This was done to ensure environmental influences on threshold FCG were not interpreted as load ratio effects. Two key results from this study are described as follows.

(1) As relative humidity increases from 0% to 100%, the FCG rate at threshold increased

by a factor of 7 for aluminum alloy 7050. However, over the range of ambient humidity (30% - 70%) FCG rates were nearly constant. Therefore, environmental influences are small for FCG tests conducted in laboratory air at ambient conditions.

(2) Accelerated FCG rates observed in high humidity (> 30% relative humidity) continued in dry air until the crack propagated through the MPZ generated at high humidity. In contrast, increases in humidity produced immediate increases in FCG rate. This suggests that a component of water vapor, probably hydrogen, rapidly affects the MPZ lowering the resistance to fatigue cracking.

6.2 — FUTURE RESEARCH TOPICS

Although the research presented here has improved the current understanding of threshold FCG load ratio effects, more work is needed. In Section 5.4 the current research was described in the context of a comprehensive threshold FCG model, including both intrinsic and extrinsic load ratio effects. Ultimately, other influences such as environment should also be included. Future research topics presented here are divided into three parts: (1) further development of a comprehensive threshold model, (2) improvements to models developed here, and (3) applications of models developed here.

Further development of a comprehensive threshold model

(1) Crack-tip damage needs to be related to crack-tip deformation, microstructural features, and the effective crack-tip loads, K_{max} and ΔK_{eff}. A quantitative model needs to be developed to connect the PRO closure model (Chapter 3) and the crack-tip damage model (Chapter 4). This damage accumulation model would fill the gap in the comprehensive threshold model indicated by the dashed box in the center of Figure 5.6. If the unusual behavior of 8009 aluminum can be described in this model, bounds on unstable threshold behavior can be established and avoided.

(2) Damage accumulation will likely affect the slip character at the crack-tip. Although shown in Figure 5.6 to be independent, this would link the closure model to the damage accumulation model. Furthermore, accumulation of damage is highly likely to be cycle dependent. In terms of Figure 5.6, this would link the K_{max} damage response model to the damage accumulation model. In general, all three of these models may be coupled (but under certain conditions interactions may be negligible).

(3) Ultimately, environmental effects should be included in the comprehensive threshold model. The study of humid air in Appendix E was done only to ensure environmental effects were not perceived as a product of load ratio. Modeling environmental effects would require more detailed study to identify specific mechanisms (*e.g.* hydrogen entering the MPZ, hydrogen weakening the fatigue resistance of the material, *etc.*) and include them in existing models.

Incremental improvements to current models

(4) Use of the fatigue crack closure model developed here requires rough crack surfaces to be characterized as a two-dimensional saw tooth wave. In other words, a crack surface is described by two parameters, α and g. Further research is needed to determine what crack surface features (on irregular crack surfaces) are most significant from a closure standpoint.

(5) This closure model is only used to predict the initial contact between crack faces. Deformation along the crack faces due to contact stress is neglecting. In cases where asperity contact is predicted, further unloading may result in additional crack-tip damage. Similar to remote closure (due to plastic strain history), contact at the closest asperity to the crack-tip may not be a good indicator of crack-tip events. However, as the distance between the first asperity and the crack-tip (g) becomes small, this is expected to be less important.

(6) Two modes of unstable threshold behavior were observed for aluminum alloy 8009, one associated with plane-strain conditions and the other with plane-stress. Conditions associated with these undesirable and potentially dangerous behaviors need to be determined, evaluated for all alloys, and considered in the design process.

(7) The crack-tip damage model presented in Chapter 4 would be improved by including FCG of microcracks (as discussed in Sections 4.4.3 and 5.2.4).

(8) It was observed that accelerated FCG rates (associated with high humidity) persisted in low humidity until the crack grew through the MPZ generated at high humidity. As humidity varies (*e.g.* low humidity during the day followed by dew at night), this implies that the peak humidity has the greatest influence on FCG behavior. It is not known if cyclic loading at peak humidity is required to produce environmentally affected FCG. Consider three cracked specimens under cyclic loading during the day (dry environment). At night (humid conditions), the first specimen is cyclically loaded, the second is held under a static load, and the third is completely unloaded. If fatigue loading is needed to drive hydrogen into the MPZ, only the first specimen would exhibit accelerated FCG rates. If static loading is sufficient, both the first and second specimens would exhibit accelerated FCG rates.

Applications of current models and techniques

(9) This closure model may explain why some small cracks initiate but fail to propagate. Because small cracks are contained within a limited number of grains, the direction of crack growth normally coincides with preferential slip planes. As a small crack grows from one grain into a neighboring grain, a change in crack direction occurs. The resulting crack is faceted (rough), likely producing a dramatic increase in crack closure level possibly leading to crack arrest.

(10) The fatigue crack closure model developed here was partially verified by injecting debris (alumina particles) into 8009 aluminum fatigue cracks to simulate a thick oxide layer. Injecting debris into existing fatigue cracks may be a practical method to enhance fatigue crack closure and inhibit further FCG. Although not a likely tool for design engineers, this technique may provide a temporary solution for fatigue crack damage until proper repair can be made.

(11) Use of shape memory alloys may allow short crack behavior to be studied using long cracks. By annealing a cracked specimen, residual deformation in the crack wake is (at least partially) recovered. As FCG resumes, a crack wake is developed and closure levels increase. This results in decreasing FCG rates (and possibly crack arrest), similar to short crack behavior.

PART IV – Appendices

APPENDIX A — LITERATURE REVIEW

A comprehensive literature review was performed to outline previous research efforts of interest to this research. Topics include threshold fatigue crack growth (FCG), fatigue crack closure, and intrinsic crack-tip damage (associated with K_{max}). Although mechanical load ratio effects are of interest here, other variables (*e.g.* environment and microstructure) are discussed because their influence at threshold may be misinterpreted as load ratio effects. This literature review is divided into three sections. First, a general description of threshold FCG is given, including the influences considered most important. The other two sections discuss research results and models of extrinsic (fatigue crack closure) and intrinsic (closure-free) load ratio effects.

A.1 — THRESHOLD FATIGUE CRACK GROWTH

In contrast to the Paris regime, threshold FCG is significantly affected by many variables. The most significant differences between threshold and Paris FCG, important to the proposed research, are listed in Table A.1. Threshold FCG is influenced by load ratio, environment, and microstructure to a greater degree than Paris FCG. Also associated with threshold FCG are higher closure levels than PICC models anticipate and rough (faceted) crack paths. Paris FCG is relatively insensitive to R, microstructure, and environment, and is associated with smoother striated crack surfaces. The subjects listed in Table A.1 are discussed in detail in the following paragraphs. However, load ratio effects and fatigue crack closure are discussed in separate sections because of their importance to this research.

Table A.1 – Comparison of threshold and Paris FCG. (Modified from Suresh [83].)

	Threshold	Paris regime
Load ratio effects	High	Low
Crack closure levels	High	Low
Microstructural effects	High	Low
Environmental effects	High	Low
Crack path description	Stage I (faceted)	Stage II (striated)
PICC model performance	Poor	Good

A.1.1 — Microstructure

As a short crack grows under constant loads, the crack-tip stress intensity factor increases leading to a change in crack propagation mode. At low stress intensities, fatigue cracks propagate along slip bands emanating from the crack-tip. This mode of crack growth is called “Stage I” and is characterized by rough and faceted crack surfaces [75]. Higher closure levels associated with rough crack paths have been suggested as the cause of FCG threshold [16]. As ΔK increases, the number of active slip planes increase leading to smoother crack surfaces. This crack propagation mode, characterized by relatively smooth but striated crack surfaces, is called “Stage II” crack growth. Short fatigue cracks

subject to increasing ΔK generally graduate from Stage I to Stage II FCG when the crack-tip plastic zone becomes larger than a typical grain. During long crack threshold, this transition occurs in reverse (from Stage II to Stage I) as ΔK is decreased. Stage I and stage II fatigue crack paths are shown schematically in Figure A.1. A rough and faceted Stage I crack is illustrated in part (a), while a (relatively) smooth and striated Stage II crack is shown in part (b). Load ratio effects associated with microstructure are not limited to RICC. For example, crack-tip damage during fracture and FCG at elevated K_{max} occurs about microstructural features, *e.g.* particles and dispersoids. The effects of microstructure and K_{max} on FCG rates are discussed further in Section A.3.

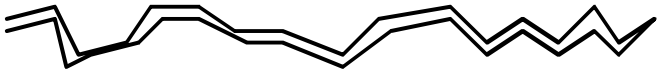

(a) faceted crack surface

(b) striated crack surface

Figure A.1 – Comparison of (a) faceted Stage I and (b) striated Stage II crack paths.

A.1.2 — Environment

Environment affects threshold FCG in several ways. The formation of a voluminous oxide layer in the crack mouth (a product of environment) affects the closure behavior of fatigue cracks. Environment also influences intrinsic (closure-free) FCG threshold behavior. For example, the most damaging component of laboratory air is water vapor. As suggested by Wei [81, 82, 84], oxidation of freshly formed crack surfaces in humid air produces free atomic hydrogen that is drawn into the crack-tip process zone. Hydrogen embrittlement weakens the material ahead of the crack producing accelerated FCG. Additionally, environment can affect the deformation characteristics at the crack-tip (i.e. crack-tip slip behavior) [52, 71], and hydrogen embrittlement increases the effective yield stress of the affected material [85]. Although the influence of environment is important, it is not within the scope of this study and is only discussed here to create a better understanding of threshold FCG behavior and prevent misinterpretation of experimental results (*i.e.* perceiving environmental effects as R effects). The influence of humidity (in laboratory air) on closure-free FCG is examined later in Appendix E.

A.1.3 — Short crack behavior

It has been observed that FCG rates of short cracks are greater than those of long cracks subjected to the same ΔK [20-24, 86]. Short crack FCG behavior was introduced in

Section 1.6.4. There are two explanations for "short crack anomalous" behavior. First, a short crack lacks a significant plastic wake and has lower closure levels than long cracks [87]. Therefore the effective portion of the applied ΔK is greater for short cracks. Cracks are labeled "short" if fatigue crack closure explains all differences related to crack size. However, even considering crack closure, FCG rates of small cracks do not always match those of long cracks subjected to the same ΔK.[31] Because small cracks are only affected by a limited number of grains, continuum mechanics (*i.e.* stress intensity factor) does not adequately describe short crack behavior [86]. Understanding the differences between long and short fatigue crack behavior is important because long crack tests are used to study threshold FCG, which is normally associated with short cracks.

A.2 — THRESHOLD FATIGUE CRACK CLOSURE

Fatigue crack closure occurs when crack faces prematurely contact during cyclic loading. This contact can occur during tensile loading (*i.e.* $R > 0$) and has been shown to produce a load ratio dependency on FCG [7]. It is widely assumed that no crack-tip damage occurs when the crack faces are in contact. Thus, FCG is related to an effective stress intensity range (ΔK_{eff}), as described in Section 1.6.2. FCG threshold closure behavior is especially complicated and poorly understood [88]. The most likely threshold closure mechanisms are plasticity induced crack closure (PICC), roughness induced crack closure (RICC), and oxide induced crack closure (OICC). Each mechanism is discussed in the following paragraphs, followed by a description of closure models found in the open literature. Finally, mode II contact of rough cracks, called sliding mode crack closure (SMCC), and remote closure due to load history, are discussed.

A.2.1 — Crack closure mechanisms

The concept of fatigue crack closure was a conceptual breakthrough for understanding load ratio effects on FCG [7]. Elber proposed that closure occurs because fatigue cracks grow through the plastic strain field generated at the crack-tip. Once in the crack wake, plastic deformation partially fills the crack mouth causing premature contact, *i.e.* crack closure. This closure mechanism has been used to explain the effects of load ratio on FCG rates as well as the influence of load history, including the retardation (or acceleration) behavior following overloads (or underloads) [89]. This closure mechanism was coined plasticity induced crack closure (PICC) as other closure mechanisms were suggested.

Closure due to contact of rough crack surfaces was first proposed by Adams [11], Purushothaman and Tien [12], and Walker and Beevers [8]. This closure mechanism, called roughness induced crack closure (RICC), occurs when misaligned rough crack surfaces contact during unloading. Rough fatigue cracks have a mixed-mode crack-tip stress state resulting in mode II crack face displacements and asperity misalignment. The

[31] A distinction is made here between "short" cracks and "small" cracks. Short cracks are affected by many grains and is well described by ΔK. Differences between short and long crack behavior are explained by fatigue crack closure. Short cracks are affected by a limited number of grains (perhaps only a single grain). Consequently, ΔK may be a poor descriptor of crack-tip driving force.

resulting contact props the crack open, and reduces the effective crack-tip driving force, ΔK_{eff}. Although RICC is not necessarily restricted to threshold conditions, it is most likely a significant contributor at low ΔK because of the tendency for rough (Stage I) crack paths and smaller CTOD.

Sliding mode crack closure (SMCC), also called crack surface interference, occurs when rough crack faces slide into each other during mode II cyclic loading. As first suggested by Tschegg, SMCC was used to explain crack-tip opening behavior for globally applied mode III loading situations [90, 91]. SMCC and RICC are similar, but typically occur under globally applied mode III (or mode II) and mode I loading, respectively. Both SMCC and RICC attenuate the applied ΔK due to contact of rough crack surfaces, however they differ because SMCC reduces the effective (mode II) K_{max}, while RICC increases the effective (mode I) K_{min}. The sliding contact of crack face asperities leads to frictional sliding of crack faces under certain micro-mechanical conditions, and asperity compression or shearing. SMCC reduces the mode II ΔK at the crack-tip, while (potentially) introducing a mode I component. Furthermore, SMCC differs from RICC, and other closure mechanisms, because non-proportional crack-tip loading occurs. This complicates modeling crack-tip plasticity because of the tendency of cross slip, on the microscale, and because the incremental theory of plasticity must be used instead of the simpler deformation theory, on the macroscale.

Oxide induced crack closure (OICC) was first suggested by Walker and Beevers [8], Endo, *et al.* [9], and Suresh, *et al.* [10]. OICC promotes crack face contact when a voluminous oxide layer forms on the crack surfaces, partially filling the crack mouth. Oxide forms in the crack mouth when freshly exposed surfaces in the crack wake react with environmental agents. Because oxide layers are typically small (approximately 10 Å for aluminum [53]), OICC is negligible where crack-tip opening displacements (CTOD) are large, *i.e.* high K_{max}. However, OICC becomes important at threshold as the oxide thickness increases relative to the CTOD [92]. Fretting contact of rough crack surfaces can repeatedly remove portions of the oxide film creating oxide debris in the crack mouth [10]. Oxide debris due to fretting crack surfaces is much thicker than normally expected, resulting in higher closure levels.

Crack face contact is not limited to the crack-tip region. A remote closure mechanism has been proposed such that crack face contact occurs well behind the crack-tip [5, 6]. Here, remote closure occurs when K_{max} is reduced during constant R FCG threshold tests. The larger amounts of plasticity associated with higher K_{max} during the early portion of the test may contact even as the crack-tip remains open. Remote closure occurring during constant R threshold testing is shown schematically in Figure A.2. Typical (constant R) FCG behavior is indicated by the solid curve on the log(da/dN) versus log (ΔK) plot. ΔK reduction is indicated by arrows parallel to the curve. The corresponding crack profile is shown on the right side of Figure A.2; crack wake plasticity is indicated by the shaded regions. Conditions associated with low and high K_{max} are labeled A and B, respectively. As shown here, contact occurs in the crack wake due to plasticity generated at condition B, although the crack-tip (associated with condition A) remains open. Presumably, this remote contact will affect the crack-tip driving force, but

additional crack-tip damage may occur upon further unloading.[32] Paris indicated that the effective crack-tip closure level for remote closure scenarios is only $2/\pi$ of the measured closure load [93].

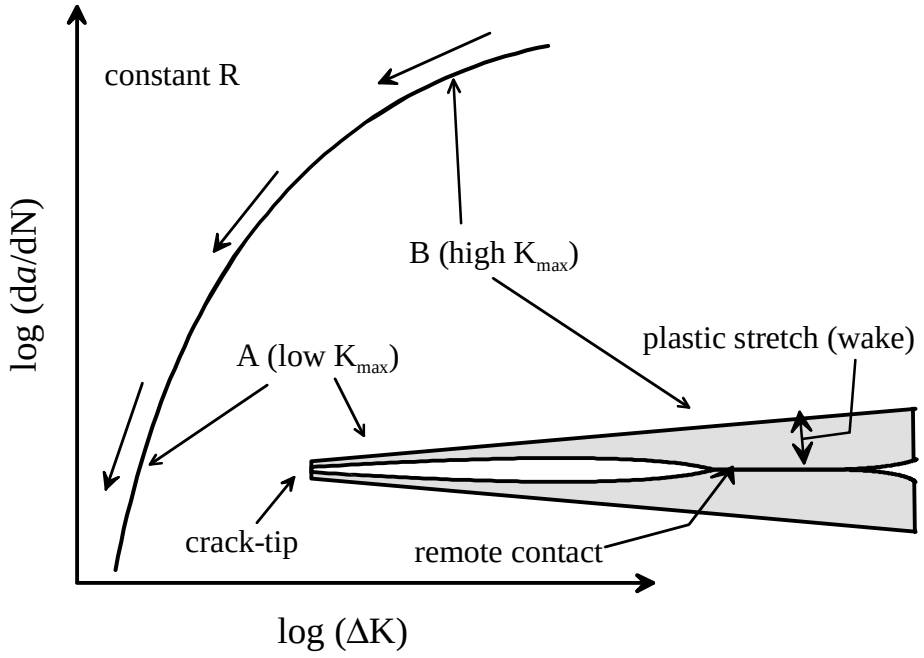

Figure A.2 – Schematic illustrating remote closure due to load history.

A.2.2 — Crack closure models

Budiansky and Hutchinson developed a theoretical PICC model, where the plastic stretch of the crack wake was proportional to the crack-tip opening displacement (CTOD) [34]. A value less than the maximum CTOD was used to account for reversed plasticity during unloading. Although this model provides a good estimate of PICC, as presented it is limited to plane stress conditions. Also, this model is unable to describe load history effects. Numerical strip yield models are able to model load history effects by dividing the crack wake into multiple strips [94]. The initial plastic stretch is determined by the state of loading as the crack-tip propagates through a given strip. In the crack wake, each strip is treated as a separate contact problem, allowing the strips to be compressed individually. More complicated finite element models have also been developed [95-97], but are not discussed in detail here.

Many analytical models exist for RICC that idealize the crack profile as simple geometrical features, *e.g.* triangles, sine curve, or rectangle. RICC has been modeled using a single rectangular asperity [98, 99], and multiple rectangular asperities [100], in the crack wake of an elastic body. Closure occurred when the elastic crack opening

[32] The remote closure mechanism discussed here is considered to be fundamentally different from the contact of the asperity closest to the crack-tip proposed in Chapter 3. Here, remote closure is a product of load history and plastic deformation, occurring far behind the crack-tip. The RICC contact proposed in Chapter 3, is a result of crack face sliding displacements and occurs very close to the crack-tip.

displacement equaled the asperity height. Another geometric model is developed by Suresh and Ritchie, where a rough crack is idealized as a two-dimensional sawtooth, (recall Figure 3.1a) [14]. RICC is caused by an empirical crack-tip sliding displacement (CTSD). Elastic crack face displacements are used to determine closure loads during unloading. Ravichandran has developed a model where crack-tip sliding displacements (CTSD) are produced by crack-tip dislocation emission [37, 62]. This model combines continuum mechanics with the effects of microstructure, *e.g.* influence of grain boundaries on crack-tip slip paths. The Ravichandran model also used a sawtooth profile and predicted closure levels to be a function of microstructural scale (*i.e.* grain size), dislocation density, and yield stress. Here, mode II displacements were the result of a local mode II stress intensity and the resulting dislocation emission. The RICC model of Wang, *et al.*, considers mixed-mode stresses at two-dimensional sawtooth crack-tips [32]. Sliding mode displacements are generated by dislocation emission from the crack-tip along a single slip plane coinciding with the crack direction. Although a useful description of crack-tip events, this model does not allow plastic opening mode displacements, *i.e.* CTOD = 0.

More complicated numerical models have also been developed. As examples, a finite difference model was developed by LLorca [35] and a strip yield model, modified for a sawtooth crack profile, by Chen and Lawrence [36]. LLorca developed a finite difference model, which also idealized the crack profile as a sawtooth wave. The most important variables influencing closure levels for this model were crack tilt angle and average direction of crack growth (for meandering cracks). Furthermore, RICC was discontinuous such that closure was greatest at changes in crack direction (*i.e.* at sawtooth peaks and valleys). Garcia and Seheitoglu modeled rough crack asperities as three-dimensional features randomly distributed along the crack surface. Statistical means were used to evaluate asperity heights and radii. The crack surface was divided into multiple strips, where each strip was treated as a rough surface contact problem. Reverse plasticity (shakedown) occurred due to sliding mode displacements. Chen and Lawrence investigated the combined effects of roughness and plasticity by altering a strip yield model of Newman [101] for sawtooth cracks. The Chen and Lawrence model is among the first to consider multiple closure mechanisms simultaneously.

Several analytical SMCC models exist, most of which idealize the crack as a two-dimensional sawtooth. Ballarini and Plesha considered the effect of SMCC on mode II fracture toughness [102]. The small opening mode load produced by asperity wedging was found to lower the mode II fracture toughness and influence the direction of crack advance. Gross and Mendelsohn studied SMCC and the effects of mode I wedge loading on stress corrosion cracking [103]. Smith, *et al.*, presented a SMCC model where the contacting asperities were allowed to contact during cyclic loading, reducing the effective K_{max} [104]. No mention of mode I wedging was made in the Smith model. Mendelsohn, Gross, Zhang, and Watt (MGZW) developed a SMCC model using profilimetric data from actual fatigue crack surfaces [105]. The applied stress intensity factors differed from those experienced by the crack-tip due to the rough crack path. Furthermore, the MGZW model included friction forces of sliding asperities and the effect of mode I wedge loading on crack-tip stresses. The predictions of the MGZW model were found to

agree with experimental results [72]. Tong, Yates, and Brown (TYB) developed a SMCC model similar to the MGZW model, except the crack was idealized as a two-dimensional sawtooth wave [106]. The TYB model was further modified to include applied mixed-mode loads [107]. Yu and Abel developed a more sophisticated model where non-uniform contact stress distributions are allowed [73]. No SMCC model in the literature includes asperity deformation (*e.g.* compression or shearing), although early experimental studies on asperity deformation exist [108, 109].

Few quantitative models for OICC exist. Suresh and Ritchie developed an analytical OICC model for cracks in elastic bodies [31]. Here, an oxide layer was modeled as a uniform rigid wedge that terminates a finite distance behind the crack-tip. Elastic crack face displacement are calculated and used to determine closure levels, when crack-opening displacements equals the oxide layer thickness. One research paper of historical interest is that of Christensen, where the behavior of wedges in crack mouths were studied years before crack closure was introduced [110]. Although this mechanical wedging was not called crack closure, the application to oxide induced crack closure seems obvious in hindsight.

A.3 — INTRINSIC K_{max} EFFECTS AT THRESHOLD

The concept of fatigue crack closure provided great insight into the mechanisms that cause load ratio effects on FCG rates. However, some researchers have suggested that crack closure does not explain all FCG load ratio effects [15]. Unfortunately, in the decades following the introduction of crack closure, almost all FCG research dealing with load ratio has been closure oriented. Other potential load ratio mechanisms have not received the research intensity of crack closure and, therefore, are poorly understood if even identified. However, a few research papers have dealt with K_{max} effects on FCG. Marci [18] and later Lang, *et al*., [19] reported an "abnormality" in near-threshold FCG at high values of K_{max}. These researchers performed constant K_{max} FCG threshold tests on titanium alloys. At high K_{max} values ($K_{max} > 0.7\ K_c$) and low ΔK ($1\ MPa\sqrt{m} < \Delta K < 2\ MPa\sqrt{m}$), FCG rates were observed to increase with further reduction in ΔK. Careful examination of the data presented in the Lang paper suggests that this phenomenon occurs primarily at long crack lengths, *i.e.* large a/W. No fractography or crack path description was presented to indicate a change in FCG mode although Lang later presented results indicating room temperature creep crack growth was responsible for this abnormal behavior [111].

Several research papers indicate a K_{max} threshold condition exists, in addition to a ΔK threshold condition. In other words, both K_{max} and ΔK must exceed their respective threshold values for FCG to occur. This behavior was discovered while using an indirect technique to determine the presence of fatigue crack closure. Schmidt and Paris, the first to perform such analyses, plotted ΔK_{th} versus load ratio, R [112]. Aluminum alloy 2024 data (from Chapter 4) is presented in Figure A.3a, as suggested by Schmidt and Paris. A sloped line is fit through the low R data (< 0.75) and a horizontal line is fit to the high R (> 0.75) data. (Recall from Chapter 4 that these FCG tests were performed in laboratory air at 11 Hz.) At low values of R ($R < 0.75$), the steep slope in the ΔK_{th} versus R plot is

attributed to closure, while high R data is closure free. An intrinsic ΔK_{th} is assumed to exist so a horizontal line is fit to the high R data. At values of R nearing unity, the deviation from the horizontal line is explained by a static modes mechanism at high K_{max} (see Section 1.6.3). Doker and Bachmann modified this analysis by plotting ΔK_{th} versus K_{max}, as shown in Figure A.3b (for the same data presented in Figure A.3a) [113]. The fitted horizontal line of Figure A.3a, shown in Figure A.3b (horizontal dotted line), does a poor job fitting the data for $K_{max} > 6$ MPa√m. The solid sloped line fits the high Kmax data better suggesting no intrinsic (*i.e.* closure-free) ΔK_{th} exists. Rather, ΔK_{th} is shown to decrease with increasing K_{max}, although this change is subtle relative to closure effects [114, 115].

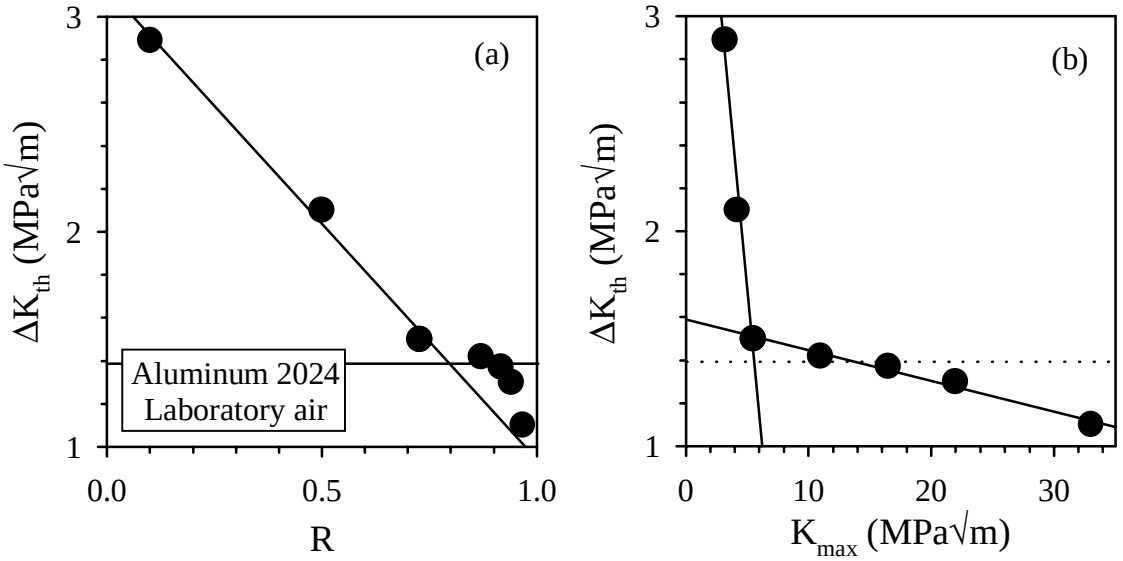

Figure A.3 – FCG threshold, ΔK_{th}, versus (a) R and (b) K_{max} for 2024 aluminum. In part (a) a horizontal line is fitted through the closure-free data, as done by Schmidt and Paris. ΔK_{th} is plotted with K_{max} in part (b), as done by Doker and Bachmann.

Although they provide useful information, such empirical studies of FCG K_{max} effects do not identify the specific mechanism(s) involved, which are likely related to microstructure. Cracks and voids have been found to nucleate at or about included, or second phase particles in several alloys [116-118]. These topics are discussed in the following paragraphs.

A.3.1 — Effects of constituent particles

Microcracking and voiding about included particles occur due to strain localization about microstructural features. Crack-tip plasticity relieves the singular crack-tip stress state predicted by the theory of elasticity. On the microscale, this plasticity is the result of crack-tip dislocation emission. Although the resultant slip occurs on preferential slip planes, several models have been developed that predict crack-tip slip occurring on single

[33], double [119, 120], and multiple slip planes [121, 122] chosen by geometric or continuum criteria. Once emitted from the crack-tip, dislocations travel into the material away from the crack-tip until the energy required for further motion is not available. This may occur when a dislocation travels away from the crack-tip stress field or when the slip path is blocked, for example, by an included particle. Successive dislocations pile-up behind the particle (each contributing to the stress field at the head of the pile-up) shown schematically in Figure A.4a. If stresses are large enough this barrier can be overcome by the following mechanisms (refer to the schematics in Figure A.4); (b) particle shearing, (c) particle fracture, (d) cross slipping, or (e) dislocation looping around the particle. Particle shearing tends to occur when the particle matrix interface is coherent, allowing dislocations to slip through the particle [123, 124]. If the particle is incoherent, the stresses produced by dislocations may break or fracture a brittle particle [125]. If an energetically favorable slip plane is available, the piled up dislocations may cross slip and avoid the particle. Finally, dislocations may loop around the particle forming a void [126], shown schematically in Figure A.4e. Initially (1), the dislocation bows around the particle. Further deformation causes the dislocation to (2) wrap around and (3) eventually create a loop around the particle.

Microcracks tend to nucleate about constituent or second phase particles. This has been demonstrated as a fracture mechanism in 7050 aluminum [127], A357 cast aluminum [125], and 1045 steel [117, 118]. Particle cracking also occurs during FCG, and is influenced by particle size and spacing, especially at FCG threshold [128, 129]. Closely spaced particle clusters have been found to be more damaging because microcracks, form at these particles, and coalesce early in the fatigue process creating large initial flaws [130]. Orientation (with respect to rolling direction) can have a significant influence on fatigue lives [131, 132] because the rolling process breaks large particles into closely spaced particle clusters. These particle clusters are more likely to affect FCG specimens in the S-L or S-T orientations. If particle spacing is not an issue, larger particles are more damaging than smaller particles, in terms of fatigue damage [133].

Voids are known to form about constituent particles during creep deformation (at elevated temperatures). A mechanism for creep crack growth involves (1) void nucleation about particles, (2) void growth, (3) unstable coalescence due to intravoid ligament instability, followed by (4) crack advance [134]. This void sheeting mechanism and other such void growth models primarily address creep crack growth [135-137]. However, void coalescence is also accepted as a room temperature fracture mechanism [117, 118, 138, 139]. Microvoid density on 2024 aluminum fatigue crack surfaces increase with increasing load ratio, or K_{max}, for a given ΔK [116]. Although void coalescence did not occur during FCG, void density increased with increasing K_{max} also occurs for other aluminum alloys [140]. Increases in void density were related to increases in FCG rate. This implies the first two stages of the void growth mechanism occur during room temperature FCG. Increases in void density likely weaken the material at the crack-tip, increasing FCG rates.

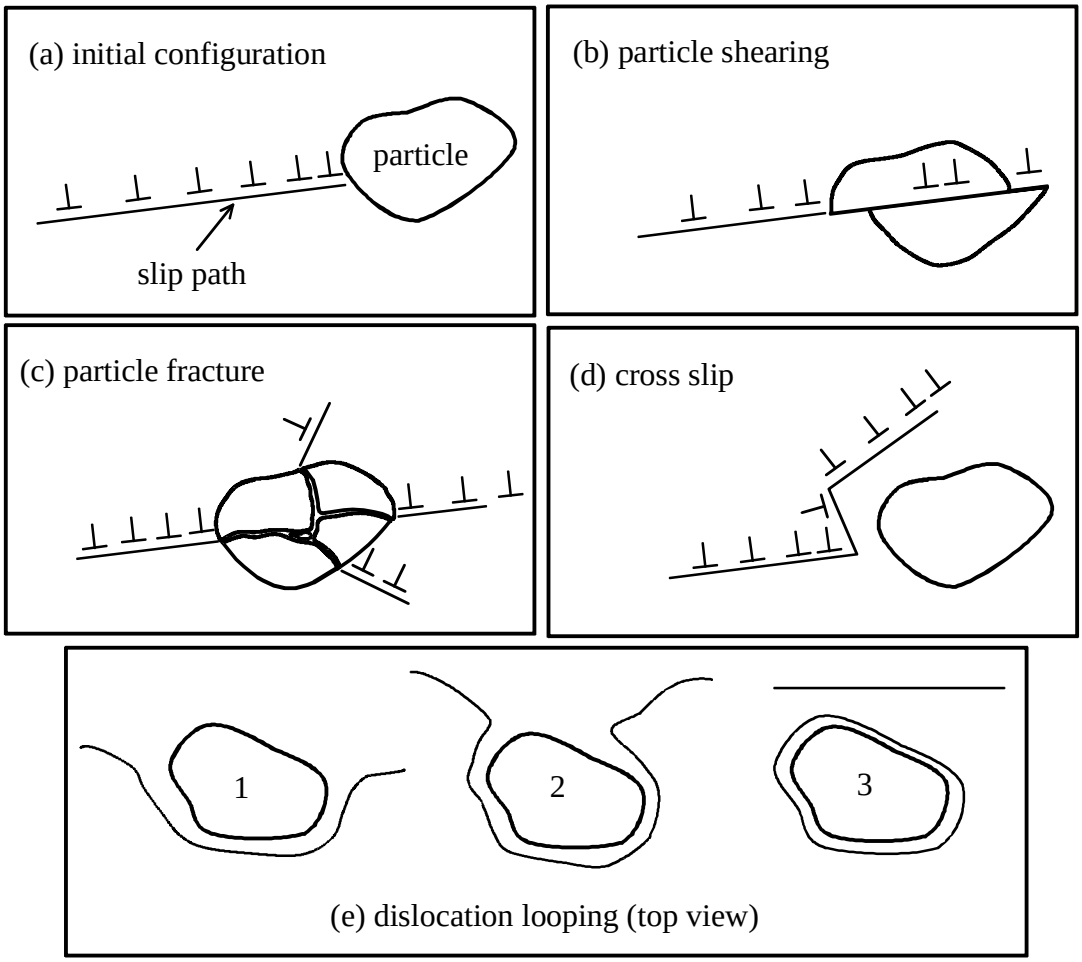

Figure A.4 – Possible ways slip paths interact with constituent particles.

A.3.2 — Effects of grain boundaries

Intergranular crack paths tend to increase FCG rates (because of weaker bonds along grain boundaries) compared with transgranular FCG. Dislocations that pile-up against grain boundaries must generate a sufficiently intense stress state in the neighboring grain to overcome this barrier. Only when the resolved shear stress reaches a critical level will dislocation motion across grain boundaries occur [141]. Because grains are anisotropic on the microscale, deformation tends to be heterogeneous [142] and stage I crack behavior is influenced by the orientation of neighboring grains [76]. Dislocation substructures, such as dislocation cells that form in grain interiors, can restrict the motion of dislocations emitted from a crack-tip [78]. In fine-grained alloys, the probable lack of dislocation cells due to small microstructural scale, combined with the relative ease of intergranular cracking results in interesting deformation behavior. Deformation of fine-grained aluminum alloys is characterized by high yield stress, increased strain rate sensitivity, and unstable plastic deformation resulting from localized deformation about microscopic particles [79, 80, 143].

APPENDIX B — MECHANICAL TESTING PROCEDURES

A detailed description of equipment and procedures used to conduct the mechanical testing (described in Part II of this dissertation) are given here. Unless otherwise stated, these procedures are consistent with ASTM standards (E 647) on fatigue crack growth threshold testing [4].

B.1 — FATIGUE CRACK GROWTH TESTING

FCG tests were performed using closed-loop servo-hydraulic testing machines that applied constant amplitude sinusoidal wave loading. A Fracture Technology Associates (FTA) computer controlled system [144] was used to continuously monitor crack length during testing, using the back-face strain compliance technique [145]. Once crack length was determined, the computer-controlled system calculated the required loads to achieve programmed crack-tip stress intensity factors. Using the FTA system, FCG tests were performed by controlling stress intensity factor (*i.e.* K-control). A photograph of the FTA computer controlled system is shown in Figure B.1. The servo-hydraulic testing machine, specimen, microscope (to verify crack lengths determined by compliance), and the computer used to control the applied loads are indicated in the figure.

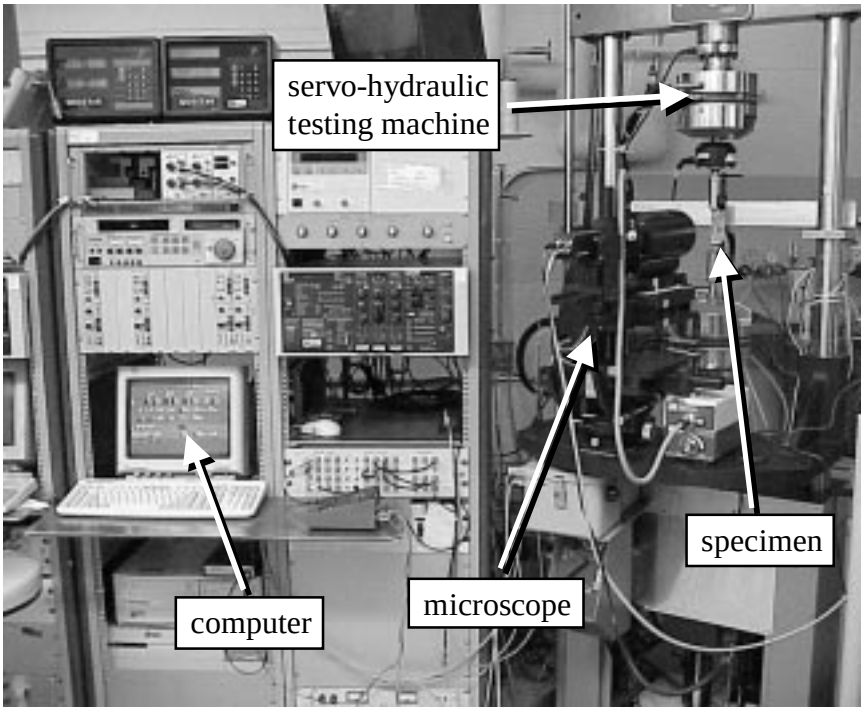

Figure B.1 – Photograph of the equipment and computer system used to perform K-controlled FCG tests. The servo-hydraulic testing machine, microscope, and the computer used to control FCG tests, are indicated.

For a given material and specimen geometry, the crack length is determined using the strain measured at the specimen back face during the load cycle. As crack length increases, the compliance measured by the back face strain gage (dP/dε) decreases, where P is the applied load and ε is the strain measured at the back face.[33] The relation between load and strain (for closure-free conditions; $K > K_{cl}$) is schematically shown in Figure B.2, where curves are shown for three different crack lengths. The arrow labeled '*a*' in the figure indicates a reduction in compliance (dP/dε) with increasing crack length. For a given specimen geometry and material, compliance (dP/dε) corresponds to a unique value of crack length. Figure B.3 is a schematic of compliance (measured at the specimen back face) plotted against crack length. As an example, if the horizontal dotted line in Figure B.3 corresponds to measured compliance, the corresponding crack length is represented by the vertical dotted line.

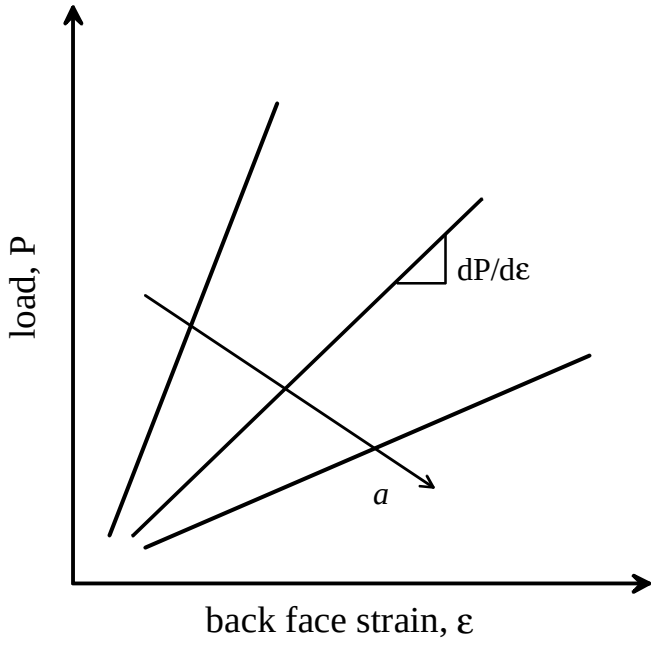

Figure B.2 – Schematic used to show how compliance at the back face (dP/dε) changes with increasing crack length, *a*.

Threshold tests are conducted where ΔK is reduced gradually as the crack grows. FCG threshold is reached when the crack stops growing, or reaches a sufficiently low FCG rate. Two types of threshold tests are discussed here. The first type of test is one where the load ratio, R, is held constant during the test. Constant R threshold tests are the most widely used type of threshold test. The second type of threshold test is performed by holding K_{max} constant. Constant K_{max} threshold tests have two major advantages over constant R threshold tests. First, remote closure is less likely during constant K_{max} threshold testing because the monotonic plastic zone (which is responsible for crack wake plasticity) remains constant during the test. Second, because the effect of load history has

[33] Although dP/dε is a measure of stiffness rather than compliance, it is called compliance for this discussion to be consistent with terminology used in existing literature.

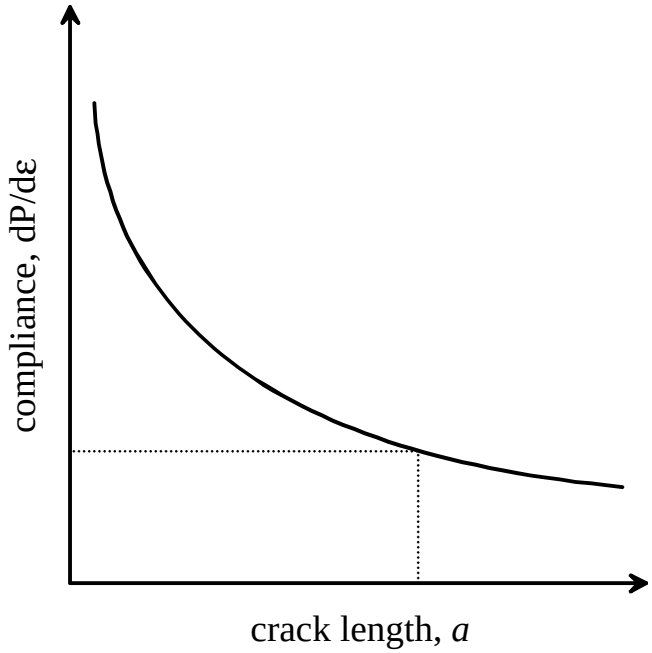

Figure B.3 – A schematic of compliance, dP/dε, as a function of crack length, *a*. Once the compliance is known (indicated by the horizontal dotted line), this relationship is used to determine crack length (indicated by the vertical dotted line).

been eliminated, the load may be shed at a faster rate. For constant K_{max} tests performed in this study, a K-gradient of, C = -0.8 mm^{-1} was used. The K-gradient, C, is defined in Equation B.1. ASTM standards recommend C = - 0.08 mm^{-1} for constant R threshold tests, where the effects of load history are a concern. Schematics of load histories for constant R and constant K_{max} threshold tests are given in Figure B.4. As a constant K_{max} test progresses (Figure B.4a), R increases and fatigue crack closure is eliminated. The horizontal dashed line corresponds to the closure loads. At low ΔK the dashed line was outside the applied range of ΔK, indicating closure-free conditions at threshold. For constant R tests (Figure B.4b) fatigue crack closure was not eliminated as ΔK decreased, indicated by the horizontal dotted line remaining within the range of ΔK. Procedures for determining closure levels are described in Appendix C.

$$C = \frac{1}{\Delta K}\left(\frac{d(\Delta K)}{d\,a}\right) \qquad \text{(B.1)}$$

FCG rates are evaluated after crack growth increments of $a/W = 0.001$. During FCG tests where load reduction occurs as the crack grows (*i.e.* C < 0), determining FCG rates over small increments has been shown to give good results. In other words, the FCG rate from a variable ΔK test matches the result from a constant ΔK test (*i.e.* C = 0). When the FCG rate needs to be determined with great precision, constant ΔK tests are conducted. By plotting crack length versus applied cycles, the FCG rate can be determined by the slope of a line fit through steady state data. Such data is shown for 8009 aluminum subjected

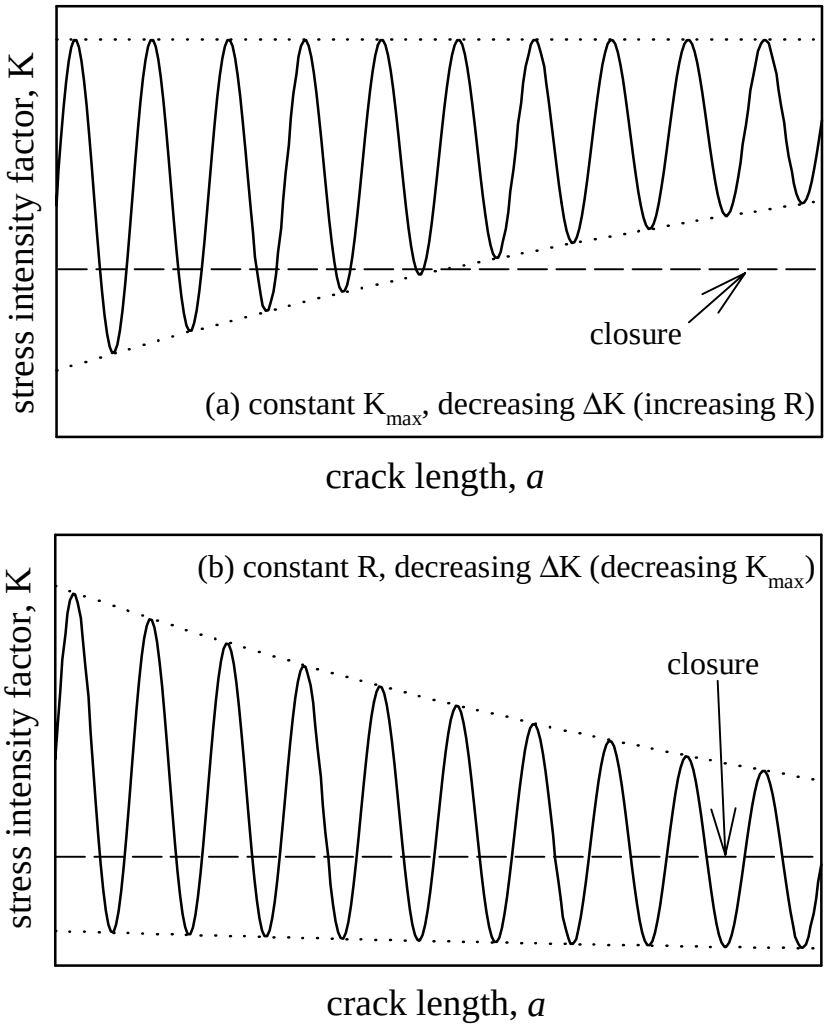

Figure B.4 – A schematic of two types of threshold tests are shown; (a) constant K_{max} and (b) constant R (load ratio).

to K_{max} = 3.3 MPa$\sqrt{m}$ and R = 0.05 (in laboratory air) in Figure B.5. The data is plotted from a crack length of 11.1 mm to 11.7 mm. Steady state FCG occurs when a constant FCG rate is established and the (crack length versus cycle count) data falls along a straight line. Transient behavior occurred in the first 0.2 mm of crack growth, indicated by the deviation from the linear fit to steady state data. Steady state data and transient data are shown in Figure B.5 as closed and open circular symbols, respectively. For this example, the steady state FCG rate (the slope of the fitted line) is 1.203 x 10^{-8} m/cycle.

Periodically, crack lengths were verified by visual measurements. Visual crack lengths, a_{vis}, and compliance crack lengths, a_{comp}, never deviated more than 50 μm, unless otherwise indicated. After testing, FCG rates and stress intensity factors were corrected by considering the deviation between visual and compliance crack length measurements. For the results presented in this dissertation, post-test corrections changed the initial values of ΔK and FCG rates by 5% or less.

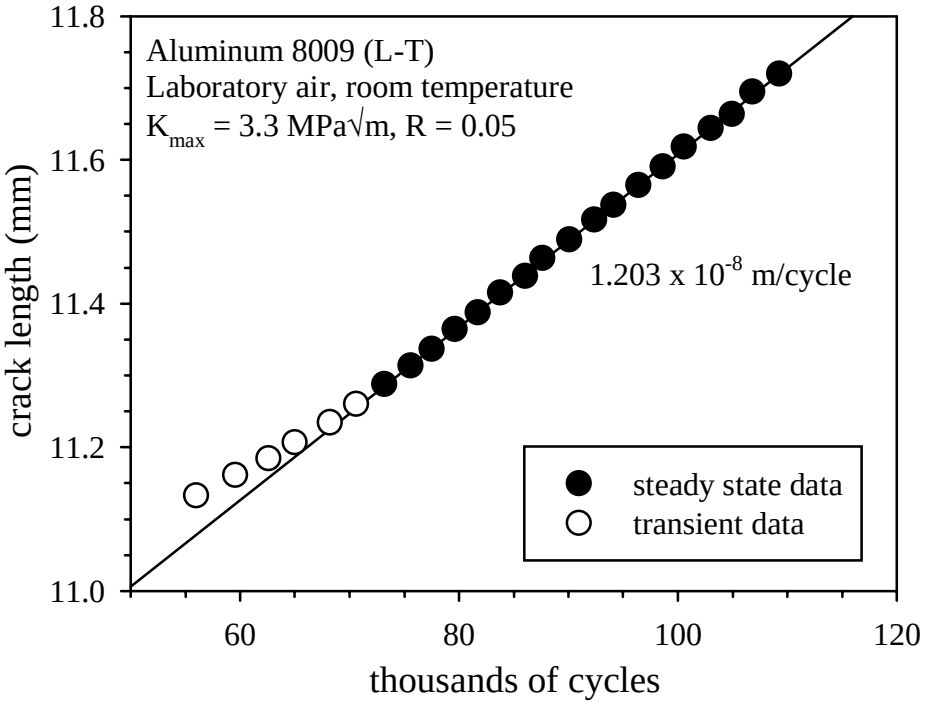

Figure B.5 – Plot of crack length versus applied cycles for aluminum alloy 8009 tested in laboratory air at K_{max} = 3.3 MPa√m and R = 0.05. The slope of the fitted line is the steady state FCG rate.

B.2 — ENVIRONMENT CONTROL

Unless otherwise stated, FCG tests were performed in laboratory air where temperature and relative humidity typically ranged from 18-23°C and 30-70%, respectively. Laboratory air is an aggressive environment that influences FCG behavior of aluminum alloys, especially at threshold. Although the influence of environment on threshold FCG is a topic worthy of much attention, it is examined here only to ensure that environmental influences are not misinterpreted as load ratio effects. To eliminate variation in environmental conditions, some FCG tests were performed in two carefully controlled environments: (1) laboratory air, but with specified relative humidity and (2) ultra-high vacuum (UHV), where the gaseous environment is removed from the specimen. Details of the procedure and setup used to control humid laboratory air are discussed in Appendix E and are not repeated here. FCG tests were performed in vacuum to eliminate the influence of environment from experimental results. A servo-hydraulic testing machine with a vacuum chamber (which enclosed the specimen) was used to perform FCG tests in UHV. A photo of the vacuum chamber is shown in Figure B.6. Indicated in the figure are the vacuum chamber, the door which allows access to the chamber, a specimen mounted in the chamber, an ion gage (used to measure very low absolute pressures), and a "clam shell" oven used to heat the specimen if needed. The actuator and pull rods were extended into the vacuum chamber and sealed by bellows. A series of pumps (including mechanical backing pumps, turbo-molecular pumps, and ion pumps) removed the gaseous environment and reduced the absolute pressure in the vacuum

chamber to approximately 2 x 10^{-7} Pa (1.5 x 10^{-9} Torr). Details and descriptions of vacuum systems are given in reference [146]. The net atmospheric pressure exerted on the bellows is compensated for by pre-setting the zero load to a specified value in laboratory air so that programmed loads are achieved during testing at UHV. Otherwise, FCG tests were performed as previously described in Section B.1.

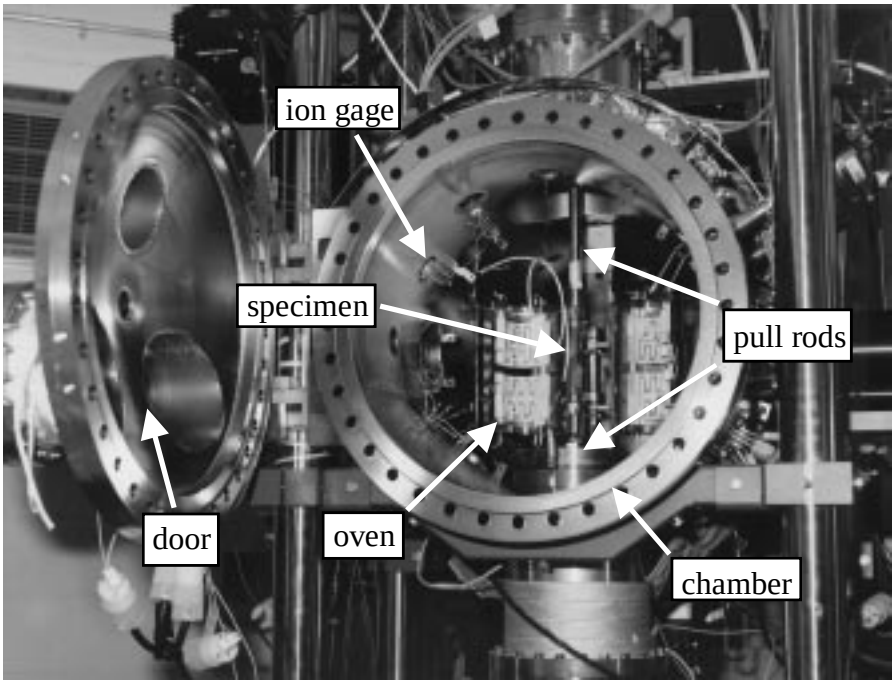

Figure B.6 – A photo of the vacuum chamber is shown here, which is mounted on a servo-hydraulic testing machine.

B.3 — FRACTOGRAPHIC AND ENERGY DISPERSIVE X-RAY SPECTROSCOPY (EDX) ANALYSES

After FCG testing, some crack surfaces were be examined using a scanning electron microscope (SEM). Fractographic examination revealed interesting features on the fatigue crack surfaces, which were correlated with mechanical behavior. For aluminum alloys 2024 and 7050, voiding around particles during constant K_{max} threshold testing were of interest. To determine the chemical composition of these particles, energy dispersive X-ray spectroscopy (EDX) analyses were performed [147, 148]. From the particle chemistry and knowledge of the alloy systems (*e.g.* chemical composition of constituent phases), individual particles were identified.

APPENDIX C — CRACK CLOSURE MEASUREMENT TECHNIQUES

Three techniques are used to determine closure behavior during FCG tests. These techniques are presented in detail along with their corresponding advantages and disadvantages.

C.1 — VISIBLE LIGHT TRANSMITTED THROUGH THE CRACK OPENING

Because aluminum alloy 8009 normally produces a flat and featureless crack surface, light can shine through open fatigue cracks during cyclic loading. Although blockage of light does not prove crack closure occurs, transmitted light does imply that the crack is open (*i.e.* crack faces are not in contact). This technique works best away from the crack-tip where crack opening displacements are larger, and is an effective indicator of the location and likelihood of remote closure. Furthermore, this technique is limited to alloys that produce very flat crack surfaces. A high magnification photograph of light shining through a crack in an 8009 aluminum specimen is shown in Figure C.1. The fatigue crack is indicated as a horizontal feature centered in the photo, where FCG occurred left to right, indicated by the arrow in the legend. The back (opposite) side of the specimen is illuminated, and is the source of the light seen in the crack opening on the right side of the figure. Initially, FCG occurred under constant amplitude loading, K_{max} = 5.5 MPa√m

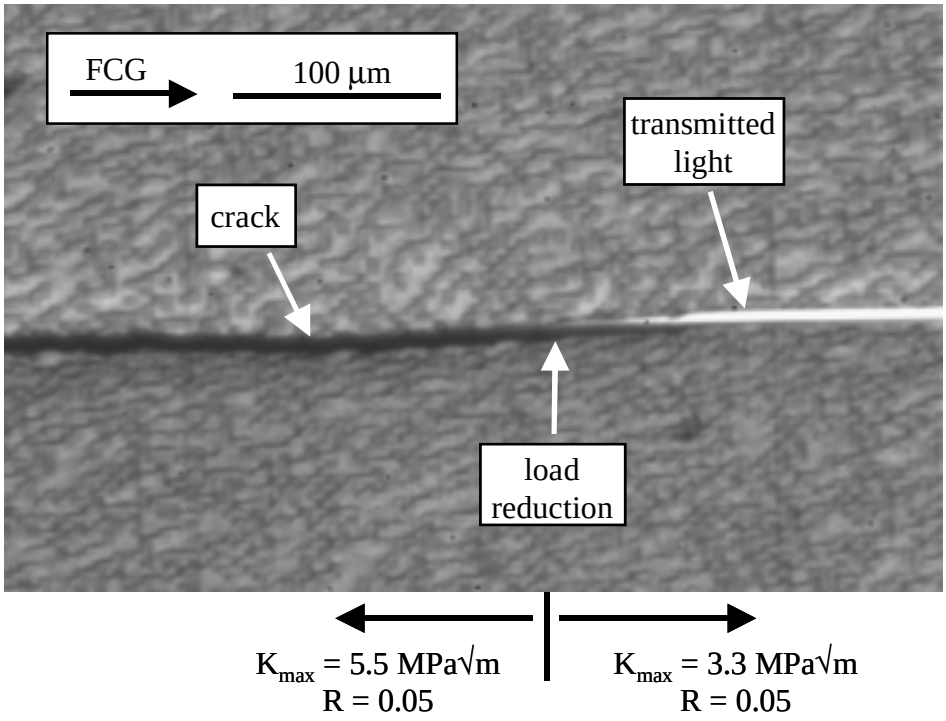

Figure C.1 – A high magnification photograph of light transmitted through the mouth of an 8009 aluminum fatigue crack. Initially, the crack grew at K_{max} = 5.5 MPa√m and R = 0.05. At the location indicated, crack-tip loads were abruptly reduced to K_{max} = 3.3 MPa√m and R = 0.05.

and R= 0.05, on the left side of Figure C.1. Where indicated, the crack-tip loading was abruptly reduced to K_{max} = 3.3 MPa√m and R= 0.05. This 40% reduction in load does not comply with ASTM standards on threshold testing, but is presented as an example to illustrate this technique. The photograph of Figure C.1 was taken after 5 mm of FCG beyond the load reduction, and at peak load (K_{max} = 3.3 MPa√m). Light is seen shining through the crack opening on the right side, where less plastic deformation is expected, but not on the left side (higher plasticity). This observation suggests that remote closure is more likely to occur along the crack faces produced at K_{max} = 5.5 MPa√m (left side of the figure) than at the crack faces produced at K_{max} = 3.3. MPa√m (right side of the figure). This technique does not supply quantitative closure information, but does provide useful qualitative information regarding the location and likelihood of remote closure. This technique was used to ensure remote closure did not affect the quantitative closure measurements (to be discussed in Sections C.2 and C.3) for 8009 aluminum. When the character of light transmitted through the crack mouth indicated remote closure was likely, the offending portion of the crack wake was physically removed. To remove a portion of the crack wake, the specimen was removed from the testing machine and clamped to a table. The portion of the crack wake where remote contact was suspected was removed using a jeweler saw. The slot produced by the saw blade was wide enough (approximately 1 mm) to eliminate crack face contact. A photograph of the crack wake removal procedure is shown in Figure C.2, where the specimen, jeweler saw, and clamp are labeled. A similar procedure was used by Mirzaei and Provan in previous crack closure studies [149, 150]. Great care was taken to ensure the

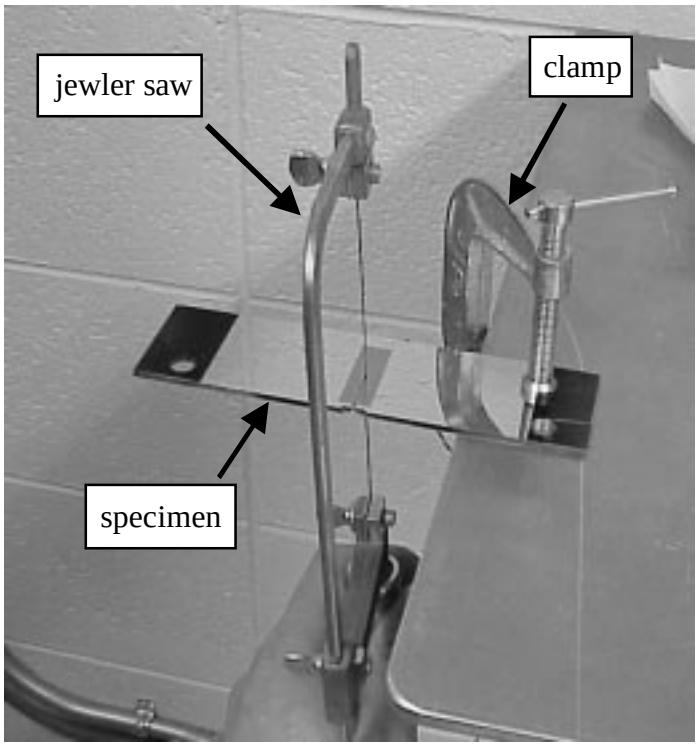

Figure C.2 – Photograph of crack wake removal using a jeweler saw. The specimen, clamp, and jeweler saw are labeled in the figure.

crack-tip was not disturbed. Back face strain was monitored during crack wake removal to ensure the crack-tip was not overloaded and the saw blade never came within 1.5 mm of the crack-tip.

C.2 — COMPLIANCE TECHNIQUES

During FCG testing, crack length is monitored using compliance data from a back face strain gage. Compliance data from the closure-free portion of the load cycle is used to determine crack length, enabling FCG tests to be automated and computer controlled (as discussed in Appendix B). Load versus strain data (both closure-affected and closure-free) can also be used to measure fatigue crack closure events. As a fatigue crack closes, the effective crack length (a_{eff}) is reduced. The effective crack length is defined here as the crack length measured from the starter notch to the closest point where crack face contact occurs. Schematics of changes in a_{eff} due to crack-tip closure are shown in Figure C.3. In Figure C.3a the entire crack is open and a_{eff} is equal to the actual crack length. During unloading the crack partially closes so a_{eff} becomes less than the actual crack length, as indicated in Figure C.3b. The compliance measured at the back face is related to a_{eff} instead of the actual crack length, as indicated in Figure B.3. In other words, the portion of the crack which is closed, behaves as uncracked material, from a compliance standpoint. Therefore, crack-tip closure occurs at the load where compliance first changes during unloading. A schematic of load plotted against back face strain is presented in Figure C.4a. The closure-free compliance is constant, indicated by dP/dε in the upper right portion of the figure. As the load decreases, closure occurs producing a change in compliance (slope change) at point C. In cases where a large portion of the crack face closes at once, or in cases of remote closure, this compliance change is very pronounced and the closure loads are easily determined from these plots. When only a small portion of the crack closes very near the crack-tip, this change in slope may be difficult or impossible to distinguish on a plot of load versus strain. Unfortunately, crack-

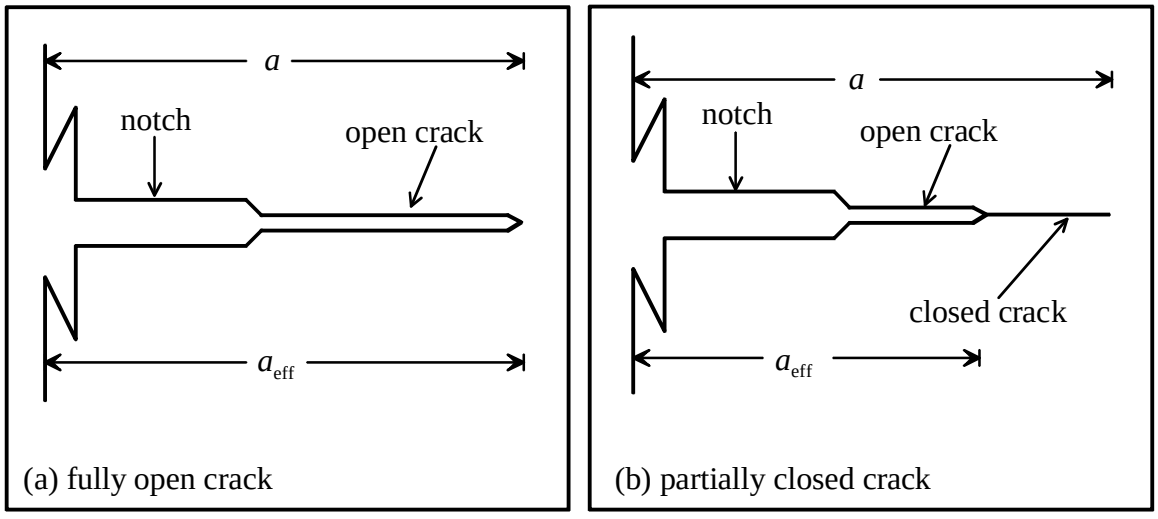

Figure C.3 – A schematic used to illustrate how the effective crack length, a_{eff} changes during crack closure. The schematic in part (a) is of a fully open crack, while part (b) corresponds to a partially closed crack.

tip closure is difficult to detect, but the most significant event affecting the crack-tip driving force (ΔK_{eff}). The reduced compliance technique was developed to improve detection of these subtle compliance changes [151]. The reduced compliance, ε_d, is the deviation from closure-free compliance behavior and is defined in Equation C.1. A plot of load versus ε_d is shown schematically in Figure C.4b. Closure loads are more easily detected from plots of load versus ε_d. Closure-free behavior on these plots becomes a vertical line, making compliance deviations easier to detect. However, the compliance behavior shown in Figure C.4 is exaggerated and does not adequately demonstrate the need for the reduced compliance technique. Plots of actual compliance data, similar to the schematics shown in Figure C.4, are shown in Figure C.5 for steady state FCG of aluminum alloy 8009 at K_{max} = 3.3 MPa$\sqrt{m}$ and R = 0.05 (recall Figure B.5) in laboratory air, and free of remote closure.[34] A plot of the normalized load (P / P_{max}) versus back face strain (ε) is shown in Figure C.5a. These data appear to fall along a straight line, although data corresponding to loads less than 40% of the maximum (open circular symbols) are not used in a linear fit because they are closure-affected (although difficult to detect from Figure C.5). Using the reduced compliance technique, the deviation from the fitted line due to closure is clearly seen; significant deviation at low loads ($P / P_{max} <$ 0.3) is observed in Figure C.5b. Fitting lines through closure-free data ($P / P_{max} > 0.5$) and closed crack data ($P / P_{max} < 0.2$) allows closure to be defined as the load corresponding to the intersection of the fitted lines. For the example shown in Figure C.5b (8009 aluminum at K_{max} = 3.3 MPa$\sqrt{m}$ and R = 0.05), closure occurs at R_{cl} = 0.284. Use of compliance data to measure closure levels is attractive because it is easy to automate by modifying the existing setup to acquire and analyze this data (recall that compliance is already used to determine crack length). However, this technique fails to give information about the location of crack face contact (*e.g.* remote closure or closure

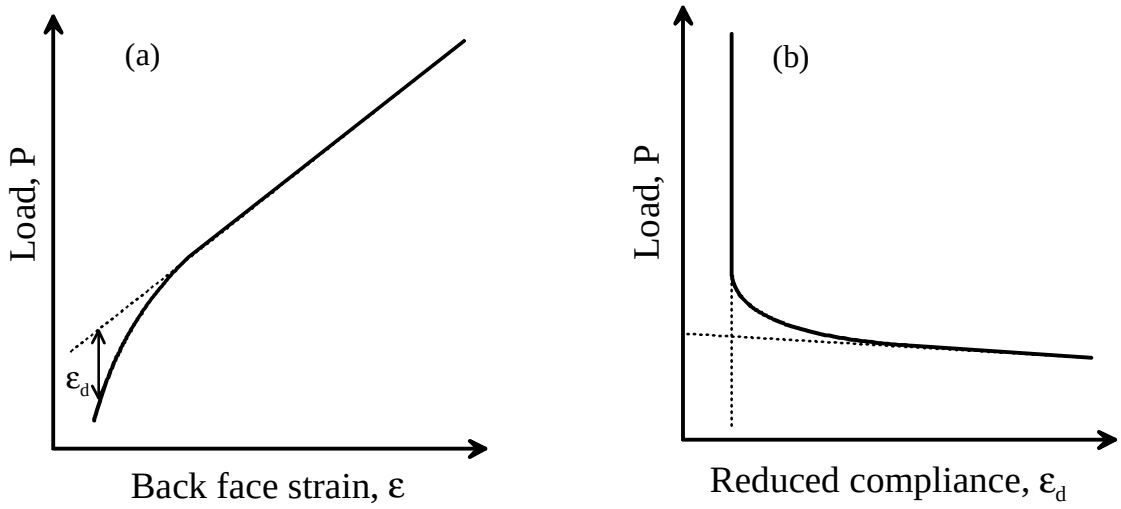

Figure C.4 – Schematics are shown here of the change of (a) compliance during the load cycle and (b) the reduced compliance technique.

[34] Transmitted light through the crack mouth indicated no remote closure occurred (recall Section C.1).

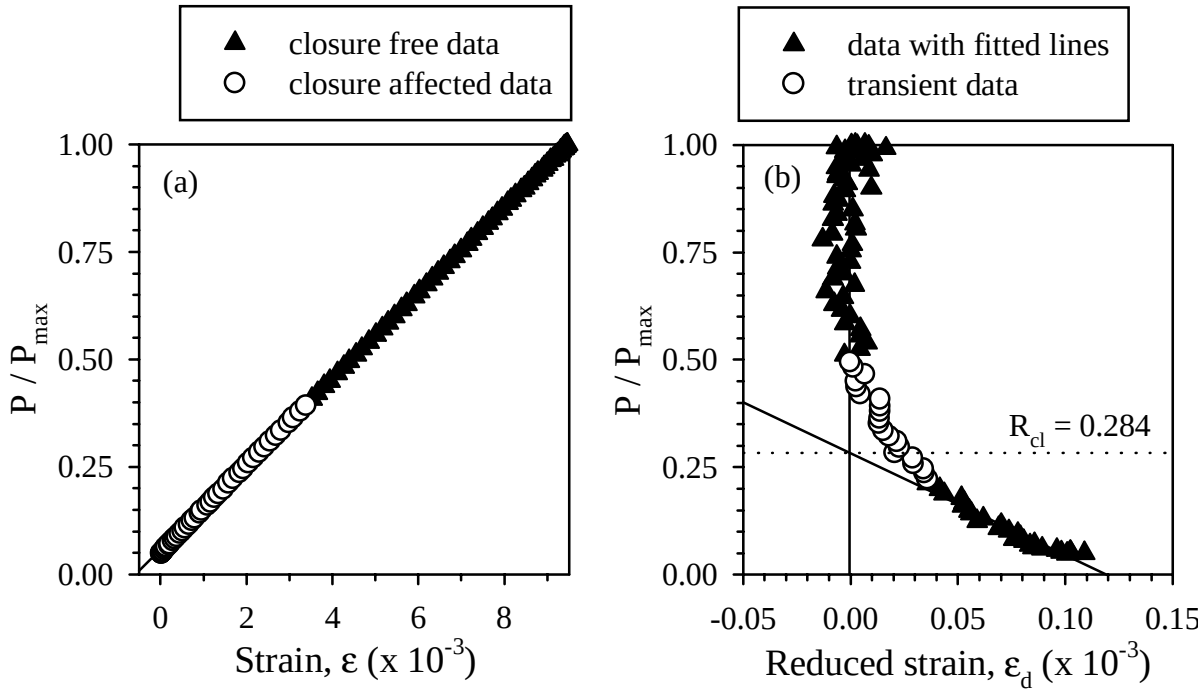

Figure C.5 – Data for aluminum alloy 8009 (K_{max} = 3.3 MPa√m and R = 0.05) used to demonstrate the importance of using reduced compliance.

at the crack-tip). Because this method relies on changes in compliance to determine closure levels, it is more sensitive to remote closure (because it produces larger changes in compliance; large changes in a_{eff}), and is not always a good indicator of crack-tip events.

$$\varepsilon_d = \varepsilon - \frac{P}{\left(dP/d\varepsilon\right)} \qquad \text{(C.1)}$$

C.3 — DIGITAL IMAGE DISPLACEMENT SYSTEM (DIDS)

Compliance techniques are limited and may not be sensitive enough to determine crack-tip closure events at threshold. Therefore, a novel, near-tip, and non-contacting measurement technique, named Digital Image Displacement System (DIDS), was also used to measure closure levels. DIDS determines closure levels by capturing a series of high magnification digital photographs of the cyclically loaded crack-tip region using a long-focal-length microscope [63]. A computer algorithm is used to track image pairs on either side of the fatigue crack [152]. The relative displacements between pairs of images are determined and plotted in relation to applied load. Closure levels are determined by applying the reduced compliance technique (discussed in Section C.2) to the load-displacement data obtained by DIDS. For most DIDS analyses performed here, relative displacements of 0.3 μm could be resolved. Where lower magnification was used the displacement resolution increased to 0.5 μm. Because FCG specimens are polished for

ease of visual crack length measurements, their surfaces lack features distinct enough for DIDS analyses. Therefore, a random pattern of speckles is applied to the surface of the specimen where the fatigue crack is expected to grow.

A photo of the DIDS setup is presented in Figure C.6, where the specimen is shown in the testing machine. The microscope, digital camera, and computer (used to acquire digital images) are also indicated in the figure. A high magnification image of the crack-tip region can be seen on the monitor in the lower left corner of Figure C.6. The random pattern of speckles used for DIDS analyses (at high magnification) can be seen as dark spots on the computer monitor. A photograph of an ESET specimen with a random pattern of speckles in the path of the fatigue crack is shown in Figure C.7, where the notch and location of the back face strain gage are labeled. The speckle pattern is the shaded rectangular region in the center of the specimen. Fatigue cracks grow from the machined notch, through the speckled region, towards the back face strain gage. A high magnification image of a crack growing through a speckled region is shown in Figure C.8. The fatigue crack (a horizontal line in the figure) is labeled and the direction of FCG is indicated by an arrow in the legend. The crack-tip is indicated in the far right of the figure. A typical pair of images used for the DIDS analysis are shown; one image on each side of the crack. As indicated in Figure C.8, both images in a pair were selected the same distance from the crack-tip. By performing DIDS analyses at different distances

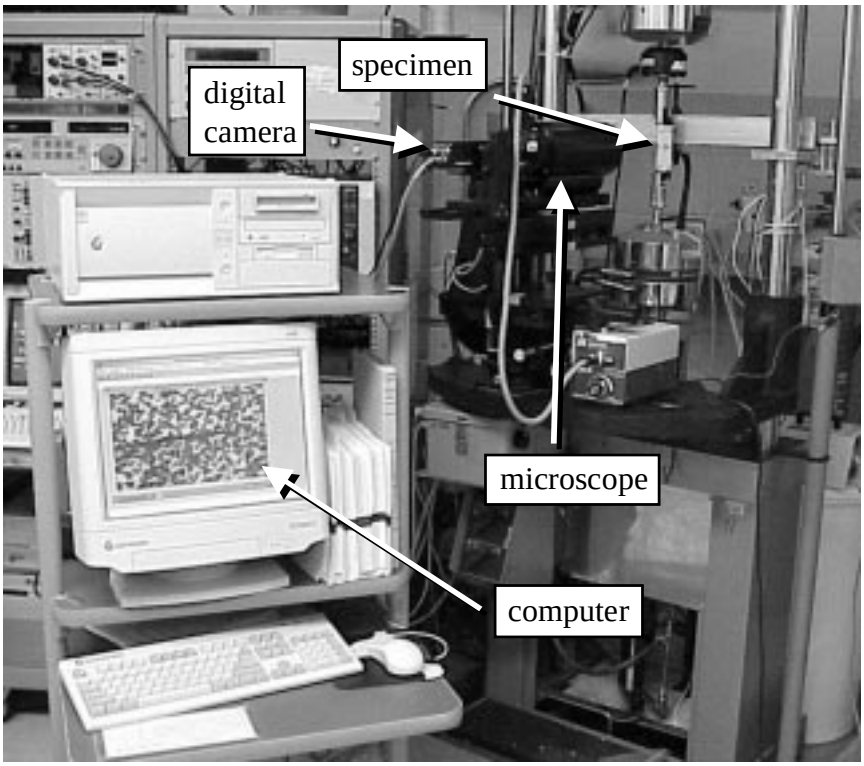

Figure C.6 – A photograph of the DIDS setup. The testing machine, long-focal-length microscope, digital camera, and computer are labeled.

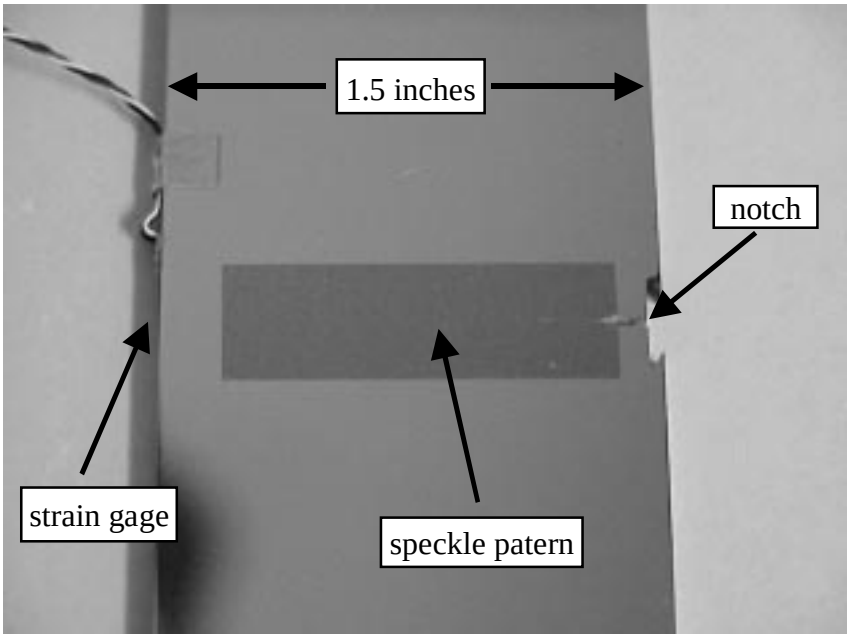

Figure C.7 – Photograph of the speckle pattern on the surface of an ESET specimen. The speckle pattern is oriented perpendicular to the loading axis and centered on the machined notch where crack propagation occurs.

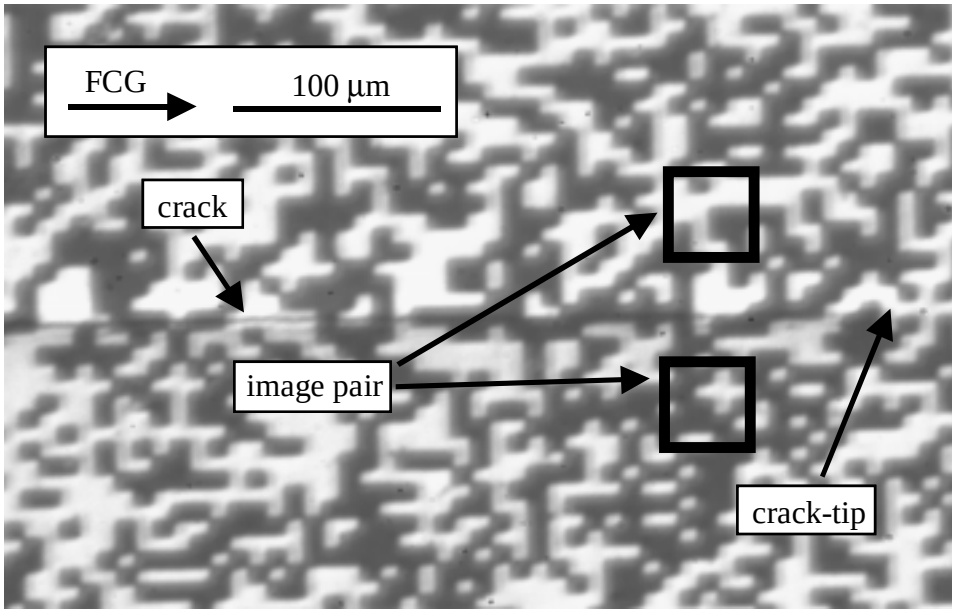

Figure C.8 – A digital image captured during the loading cycle is shown here. The direction of FCG is indicated by an arrow in the legend. The crack-tip is indicated on the right side of the figure. A typical pair of images used for DIDS analyses are also indicated (one on each crack side).

behind the crack-tip, closure behavior can be determined as a function of position along the crack wake. The unique ability of DIDS to evaluate local closure behavior is the most significant advantage of this technique. During the load cycle, the fatigue crack oscillates vertically (for a vertical load axis) as seen under high magnification. Because DIDS analyses are only concerned with the relative displacements between image pairs, translation of the entire crack-tip region is not necessarily of concern. However, all images tracked by DIDS must remain in the digital photographs. A DIDS analysis will fail if any images drift out of view during the load cycle. To prevent this problem, three "rules" are followed. First, the crack is centered in the field of view at mean load. Second, image pairs are selected as close to the crack as practically possible. This allows a greater amount of oscillation to occur before an image drifts out of view. Finally, if the above measures are still insufficient, images are taken at lower magnification. (As mentioned earlier this increases the displacement resolution from 0.3 μm to 0.5 μm.) If (even subtle) specimen movements in line with the microscope occur, the high magnification photographs will become unfocused. Best results were obtained by focusing at mean load. However, images at minimum and maximum loads were sometimes poorly focused, from which DIDS analyses could not produce usable information. Where poor results occurred, the procedure was repeated until good focus quality was obtained. These technical problems (*i.e.* images drifting out of view and focusing problems) made DIDS analyses difficult and were the primary disadvantages of this technique.

Good contrast between the speckles and the base metal are needed for the DIDS technique to be successful. Carbon speckles on polished aluminum worked well and were used for DIDS analyses performed here. Specimens for DIDS measurements were prepared using a six-step procedure described as follows. Schematics illustrating these steps are given in Figures C.9a through C.9f, respectively.

(a) The entire side of the specimen is polished so that the surface reflects light well and remains flat.
(b) A thin layer of photo-resist is applied to the specimen. Any excess amount is removed by spinning the specimen on a wheel before the photo-resist dries.
(c) Once the photo-resist dries, a mask of random speckles is placed over the region where the fatigue crack will grow. The specimen is then subjected to ultra-violet (UV) light. The UV light destroys the photo-resist not protected by the mask.
(d) A chemical rinse removes the UV damaged photo-resist, leaving the random pattern of photo-resist on the specimen surface.
(e) Carbon is vapor deposited (in vacuum) on the specimen surface, covering both the exposed aluminum and the surviving photo-resist. Carbon was selected because it provides good visual contrast with the aluminum specimen. The deposited layer of carbon is only a few angstroms thick; just enough to appear dark and provide good contrast.

(f) Once the specimen has been coated with a thin layer of carbon the entire specimen is subjected to an acetone bath in an ultrasonic cleaner. The acetone penetrates the thin carbon layer and dissolves the remaining photo-resist. The carbon on top of the photo-resist is also removed leaving the inverted random pattern between dark carbon and light (polished) aluminum.

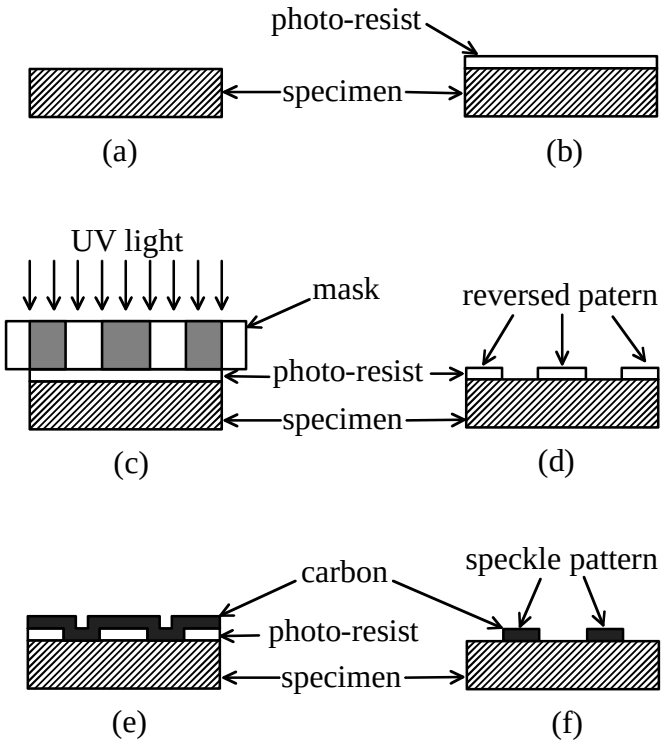

Figure C.9 – Schematics of the required steps to prepare a specimen for DIDS analysis are shown here. Each sketch (a-f) corresponds to events in the respective steps (a-f).

APPENDIX D — ALLOYS AND SPECIMENS

The alloys and specimen configurations used for FCG tests are described in this appendix because it was not convenient to do so in the body of this dissertation. The reasons for selecting each alloy, and specimen configuration are discussed. Physical metallurgical features significant to FCG load ratio effects are discussed for alloys tested here. The first two sections describe aluminum alloys and Nitinol (a shape memory alloy), respectively. Specimen geometry is discussed in the final section, and specimen configurations for all FCG data presented in this dissertation (including data obtained from published literature) are provided.

D.1 — ALUMINUM ALLOYS

Three aluminum alloys (2024, 7050, and 8009) were selected for study based on their threshold FCG characteristics. Aluminum alloy 7050 was selected because load ratio effects have been observed that are not explained by fatigue crack closure [67]. This implies intrinsic (closure-free) load ratio effects exist for 7050 aluminum. Additionally, 7050 aluminum exhibits low fracture toughness in the S-L orientation (for thick plates), possibly due to cracking along grain boundaries. This "weak" orientation will likely exaggerate any intrinsic (closure-free) load ratio effects. Aluminum alloy 8009 was selected for two reasons. First, unusual FCG threshold behavior suggests intrinsic load ratio effects may exist for this alloy [60]. Second, the fine microstructure (average grain diameter is 0.5 μm) of 8009 aluminum produces smooth and nearly featureless fatigue crack surfaces. Therefore, roughness-induced crack closure (RICC) is minimized or eliminated for 8009 aluminum.[35] Aluminum alloy 2024 was selected because it is well behaved at threshold (*i.e.* load ratio effects are well explained by closure). Additionally, the crack surfaces of 2024 aluminum are sufficiently rough for RICC to occur (and contrast with the smooth crack surfaces of 8009 aluminum). Finally, because 2024 aluminum is so widely used and studied, it provides a known quantity with which to compare and contrast the effects of load ratio. Mechanical properties relevant to this research project are given in Table D.1 for aluminum alloys 2024, 7050, and 8009. Included are elastic modulus (E), yield stress (σ_o), plane-strain fracture toughness (K_{Ic}), as-tested fracture toughness (K_c), and grain size. A description of physical metallurgy is given for each alloy, although limited to features significant to threshold FCG behavior.

D.1.1 — Aluminum alloy 2024

Aluminum alloy 2024 is a commercial wrought alloy commonly used in the aerospace industry. As tested, the material was rolled into a sheet with a final thickness of 2.3 mm

[35] In a recent study by McEvily it was observed that increases in closure at threshold corresponded with increased texture of 8009 aluminum crack surfaces [57]. From these observations it was concluded that RICC became significant at threshold. McEvily approached threshold by periodically stepping down the load in increments not greater than 10% of the maximum load. In this dissertation, remote closure was occurred after stepping reductions in load (see Figure C.1) and increased closure levels produce textured crack surfaces in 8009 (see Figure 3.43). Therefore, increases in crack surface texture were probably due void production at high R threshold FCG conditions.

Table D.1 – Mechanical properties of aluminum alloys.

	Alloy (orientation)		
	2024-T3 (L-T)	7050-T6 (S-L)	8009 (L-T)
E (GPa)	72	72	88
σ_o (MPa)	350	250	420
K_{IC} (MPa$\sqrt{m}$)	35	29	30
K_C (MPa$\sqrt{m}$)	42	25	35
grain size (μm)	70-150	30-100	0.3-1.0

and had a temper designation of T3. For rolled sheets and plates, the longitudinal direction (L) corresponds to the rolling direction. The short-transverse (S) direction is normal to the surface of the sheet product (*i.e.* in the thickness direction), while the long-transverse (T) direction is normal to both (L) and (S) directions. A surface is described by the material direction normal (perpendicular) to that surface (*e.g.* L, T, and S indicate surfaces normal to the longitudinal, long-transverse, and short-transverse directions, respectively). Micrographs of the three material orientations (for 2024 aluminum) are cropped and arranged so an observer appears to be looking at a cube of the material as shown in Figure D.1. Micrographs arranged in this way are called orthogonal

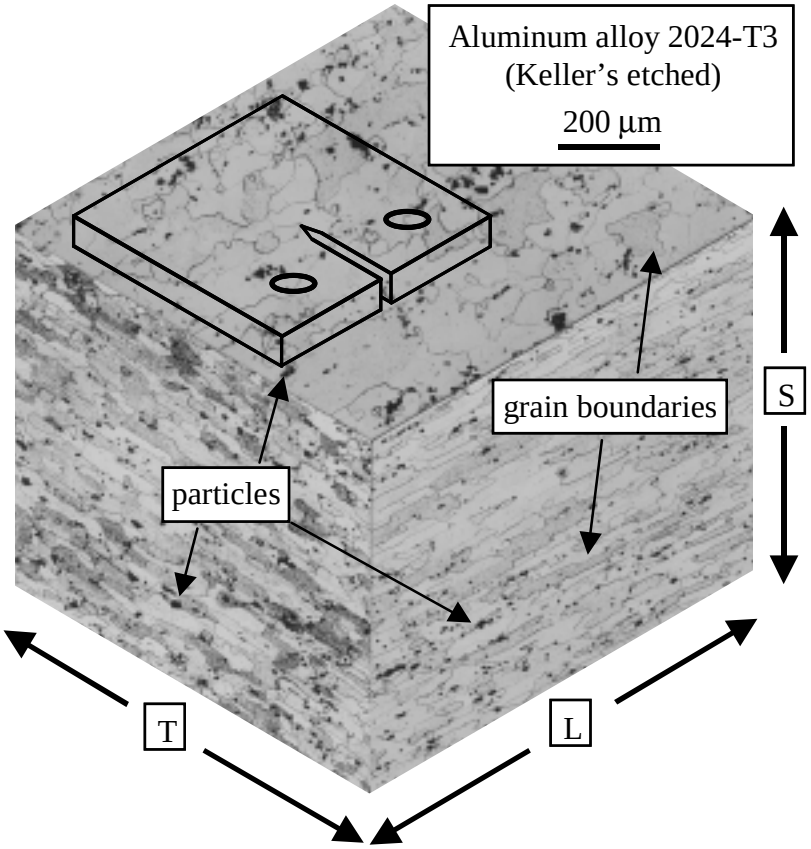

Figure D.1 – Orthogonal metallurgical cube for aluminum alloy 2024-T3.

metallurgical cubes. The micrographs of Figure D.1 were polished and etched (exposed to Keller's reagent for 10 seconds) to highlight metallurgical features such as grain boundaries and particles. Due to the rolling process, grains are elongated in the rolling direction (L), and to a lesser extent in the long-transverse direction (T). The grains are very thin in the short-transverse (S) direction, so grains in this sheet alloy have a "pancake" shape. Scale is indicated in the legend, and material directions are shown as arrows. When describing the orientation of FCG specimens, two orientations are used. The first orientation corresponds to the direction of applied loads, while the second describes the direction of FCG. Aluminum alloy 2024 FCG specimens were of the L-T orientation, as indicated by the FCG specimen schematic in Figure D.1. For the orientation used here, the longitudinal plane (L) is the plane of the fatigue crack surface (as presented in Figures 4.7). The nominal composition of 2024 is 4.4% Cu (by weight), 0.6% Mn, and 1.5% Mg. The hardening phase, $Cu_2Mn_3Al_{20}$, is a complex mixture of aluminum, copper, and magnesium consisting of particles approximately 5 μm in diameter [153, 154]. These particles appear as black dots in Figure D.1, a few of which are labeled. Voids formed at these particles during high K_{max} FCG tests (see Chapter 4).

D.1.2 — Aluminum alloy 7050

Like 2024, aluminum alloy 7050 is a commercial wrought aluminum alloy commonly used in the aerospace industry. Considered to be a variant of 7075 aluminum, 7050 contains more copper and zinc than the former and has better resistance to corrosion and corrosion cracking. The nominal composition of 7050 is 2.3% Cu (by weight), 2.2% Mg, 6.2% Zn, and 0.12 Zr% [153, 154]. Due to higher copper and zinc content, aluminum alloy 7050 has a higher percentage of Al_2CuMg as a brittle second phase that tends to reduce fracture toughness. The 7050 aluminum specimens tested here were made from a plate 1.5 inches thick. An orthogonal metallurgical cube for aluminum alloy 7050 is shown in Figure D.2, where each of the three orientations (L, T, and S) is labeled. Scale is indicated in the legend. The micrographs of Figure D.2 were polished and etched (exposed to Keller's reagent for 10 seconds) to highlight metallurgical features such as grain boundaries and particles. A few grain boundaries and (Al_2CuMg) particles are indicated in the figure. During constant K_{max} threshold testing, voids formed around these particles (see Chapter 4). Similar to 2024 aluminum, 7050 aluminum grains also have a "pancake" shape. Because 7050 aluminum FCG specimens are of the S-L orientation, fatigue cracks are more likely to grow along grain boundaries. Constituent particles, which exist primarily at grain boundaries, are more likely to affect FCG behavior in the S-L or S-T orientations. Furthermore, the short grain dimension in the short-transverse (S) direction allows fatigue cracks to follow grain boundaries with less out of plane crack deflection. Thus, cracking along grain boundaries is a likely explanation for the low fracture toughness associated with this orientation. Any unusual FCG behavior exhibited by this alloy, especially at high K_{max}, would likely be enhanced in the S-L orientation.

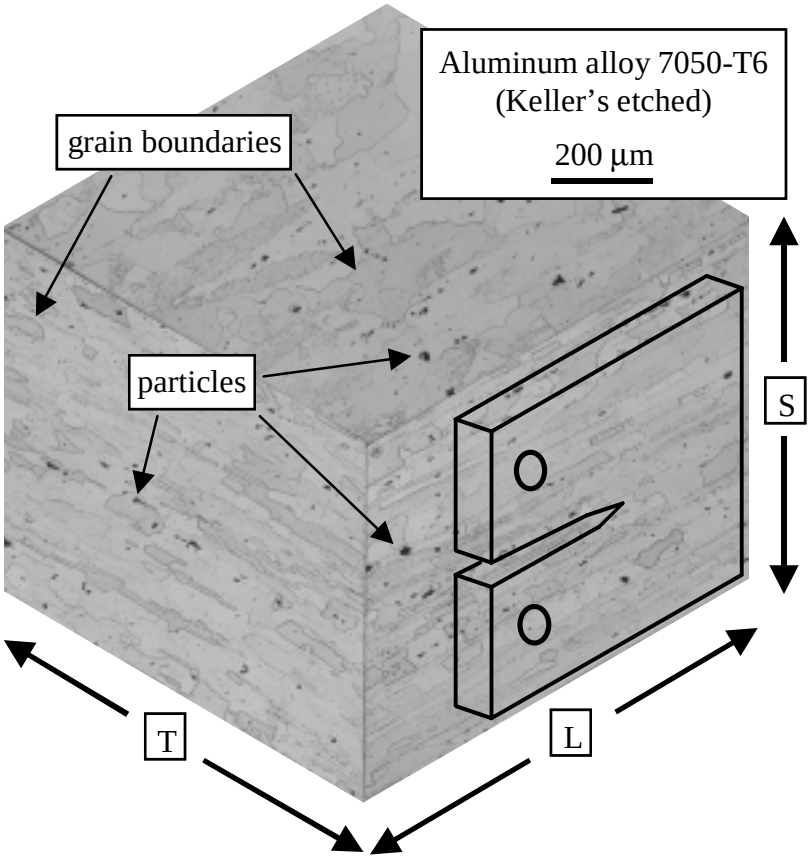

Figure D.2 – Orthogonal metallurgical cube for aluminum alloy 7050-T6.

D.1.3 — Aluminum alloy 8009

Aluminum alloy 8009 is a non-heat-treatable powder metallurgy (PM) alloy with extremely fine grain microstructure and a nominal composition of 8.5% Fe - 1.3% V - 1.7% Si (numbers in percent by weight). The material was planar flow casted, followed by ribbon comminution, vacuum hot pressing, extrusion, and either rolling or forging [60, 69, 155]. The resulting microstructure has a very fine microstructure consisting of grains about 0.5 μm in diameter and $Al_{12}(Fe, V)_3Si$ dispersoids of average diameter 400-800 Å. These silicide dispersoids consume about 27% of the total volume. In general, PM alloys (including 8009) have inferior FCG properties compared with other engineering alloys. Specimens tested here were fabricated from rolled sheets 2.3 mm thick. An orthogonal metallurgical cube of 8009 aluminum is shown in Figure D.3. Each of the three material orientations (L, T, and S) are indicated by arrows and labeled. Scale is indicated in the legend. The micrographs are shown for un-etched polished surfaces. Etching highlights grain boundaries by allowing an reactive solution to attack the polished surface, preferentially at grain boundaries. Because of the fine grain size (*i.e.* large density of grain boundaries), 8009 aluminum was especially reactive to etching. No significant features can be seen in Figure D.3 due to the extremely fine microstructure of aluminum alloy 8009. FCG specimens are of the L-T orientation, indicated by the specimen schematic in Figure D.3.

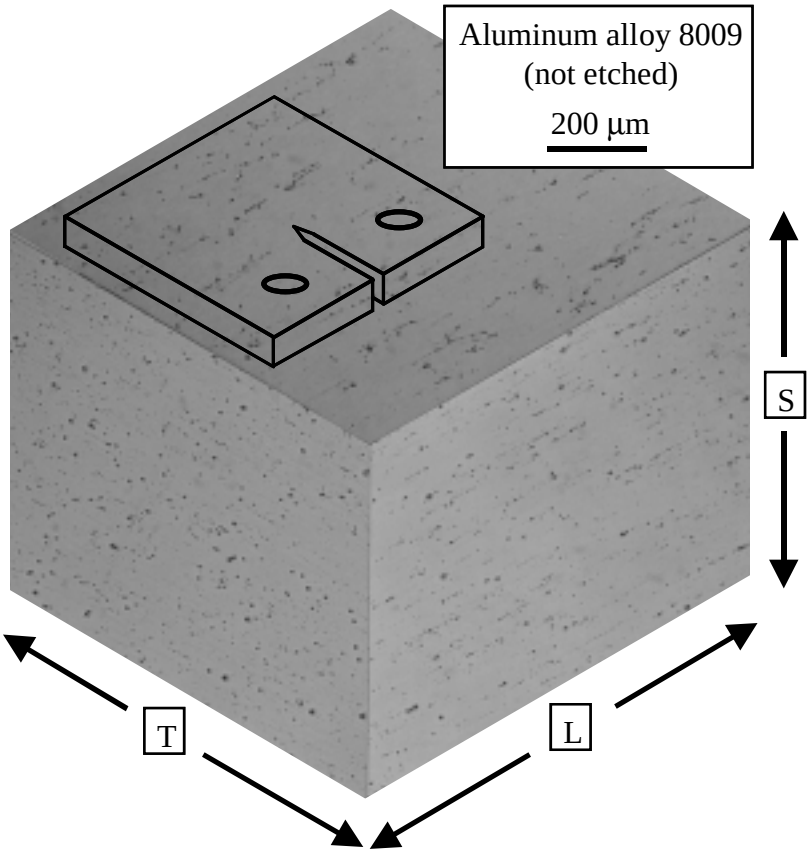

Figure D.3 – Orthogonal metallurgical cube for aluminum alloy 8009.

D.2 — NITINOL (SHAPE MEMORY ALLOY)

Nearly equi-atomic titanium-nickel alloys, commonly called Nitinol, are the most widely studied shape memory alloys. Shape memory alloys are characterized by the ability to return to their original shape after plastic (or psuedo-plastic) deformation[36], as if the material "remembers" its original configuration. The Nitinol alloy studied here is called Nitinol 50-50 because the molar content of nickel and titanium are each 50%. Other Nitinol alloys have different amounts of nickel and titanium, and may contain other elements (such as copper, Cu). Due to the composition of Nitinol studied here (50% molar content for both Ni and Ti), it is called "Nitinol 50-50." Shape memory alloys may allow recovery of crack wake plasticity, thus, eliminating PICC. However, the shape memory effect can be destroyed by intense cyclic deformation [64]. It is not known if crack-tip cyclic plasticity will destroy (or damage) the shape memory effect. If the shape memory effect is damaged, perhaps enough crack wake plasticity can be recovered to eliminate PICC.[37]

[36] Here plastic deformation refers to deformations that occur under mechanical loading, but are not recovered by unloading. Because these deformations can be recovered using the shape memory effect, they are called psuedo-plastic deformations.

[37] Recall from Figure 3.4 that the residual crack wake plasticity only needs to be reduced to 75% of the CTOD to eliminate PICC during tensile loading (for a straight crack).

The production and recovery of plastic strains are achieved with a thermo-plastic phase transformation cycle. Unstrained material at room temperature is primarily composed of a martensitic phase. Applied tensile stress, or increasing temperature, transforms martensite to an austenitic phase. A stress induced transformation, rather than dislocation movement (as in typical engineering metals), is responsible for the psuedo-plastic strains. Psuedo-plastic strains are recovered by heating and cooling a deformed specimen (a process called annealing). This shape memory effect is a result of a thermo-plastic hysteresis loop occurring near ambient temperature. A schematic of a typical thermo-plastic hysteresis loop is shown in Figure D.4. Here, (psuedo-plastic) strain is plotted against temperature. The solid curves indicate the behavior of the material with temperature. On the extreme left side of Figure D.4, at temperatures below M_f (the temperature at which the transformation to martensite is finished), martensite exists as the only stable phase, *i.e.* no austinite. On the right side of the figure, above A_f (the temperature at which the transformation to austenite is finished), austenite is the only stable phase so no martensite exists. Between the temperatures M_f and A_f, a hysteresis loop exists allowing for shape memory behavior. Nitinol alloys are designed for service temperatures near M_f.

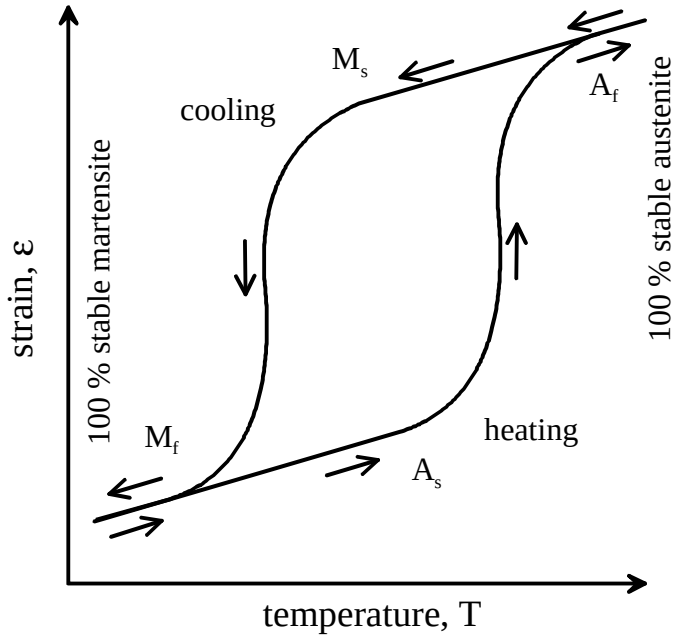

Figure D.4 – Schematic of thremo-plastic hysteresis loop for typical shape memory alloys, including Nitinol 50-50.

As stable (unstressed) martensite is heated above M_f, the material remains in the martensite phase even though stable austenite can exist. (This phase-temperature relation is indicated at the bottom of the hysteresis loop; the arrows indicate movement along this curve.) When heated above the temperature A_s (where transformation to austenite starts), some of the martensite phase is transformed to austenite. All of the martensite is transformed to austensite, as the temperature is increased to A_f. When stable austenite (at temperatures greater than A_f) is cooled below A_f, austenite initially remains unchanged,

although stable martensite can exist. This phase-temperature relation is indicated at the top of the hysteresis loop; the arrows indicate movement along this curve. When cooled below the temperature M_s (start of transformation to martensite), some of the austensite transforms to martensite. By the time the material is cooled to M_f, all austenite has transformed to martensite.

The psuedo-plastic deformations can be recovered by annealing (heating above A_f and cooling to the ambient temperature) resulting in the material returning to its original configuration. In general, the operating conditions for shape memory alloys lie just below the hysteresis loop (*i.e*. below M_f). For Nitinol 50-50, the temperatures A_f, A_s, M_f, and M_s are 78°C, 48°C, 28°C, and 37°C, respectively [156]. However, these temperatures are extremely sensitive to changes in alloy composition. The reference shape (for the shape memory effect) can be reset by heating the specimen above the shape-setting temperature, 850°C.

Schematics of stress-strain curves for Nitinol 50-50 are shown in Figure D.5 for (a) martensite and (b) austenite phases. For tensile loading of martensite, linear behavior is initially observed until approximately 90 MPa. At this stress (at room temperature) the martensite begins to transform to austenite. The increase in strain is a result of the transformation, but appears to be a linear-elastic/perfectly-plastic response (*i.e*. behaves as if yielding). Strains of approximately 4% occur if all martensite is transformed to austenite. Further loading will lead to permanent deformation not recoverable by annealing, which destroys the shape memory effect [64]. Stress-strain behavior of martensite is approximated by a tri-linear curve (three line segments), as shown in Figure D.5a. Initially, martensite has an elastic modulus of 69 GPa, until reaching the stress corresponding to phase transformation. After the transformation the elastic modulus increases to 82-103 GPa. Considering the effects of the phase transformation, a

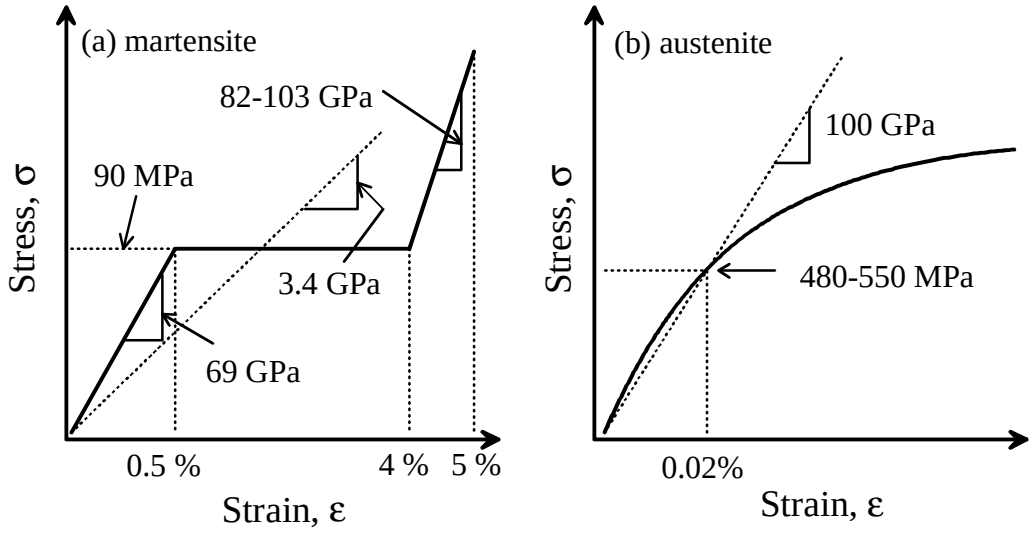

Figure D.5 – Schematics of stress-strain plots are shown here for Nitinol 50-50 in (a) martensite and (b) austenite phases.

secant modulus can be used, typically about 3.4 GPa. The behavior after the phase transformation in part (a) is, in reality, the stress-strain response of austenite. A schematic of the stress-strain behavior of austenite is presented in part (b). Here, no obvious linear behavior (or deviation from linear behavior) is suggested. Elastic modulus, determined at a 0.02% strain offset, is typically 100 GPa. Because no, phase transformation occurs due to applied stress, all plastic strains are permanent and are not recoverable by annealing [64]. In this way, intense deformation can destroy the shape memory effect. Cyclic loading can damage the shape memory effect [64], but it is not known how cyclic crack-tip strains will affect recovery of crack wake plasticity.

An orthogonal metallurgical cube of Nitinol 50-50 is shown in Figure D.6. Because Nitinol is produced as a cast billet (and then forged), only two material orientations exist: parallel (forging, F) and perpendicular (transverse, T) to the forging direction. Three orientations in Figure D.6 are labeled F, T_1, and T_2 (for forging direction and two transverse directions, respectively). FCG growth specimens used here are oriented as indicated by the FCG specimen schematic in Figure D.6 (*i.e.* a T_1-T_2 specimen orientation). The polished Nitinol surfaces presented in Figure D.6 were etched (10 seconds exposed to Kroll's reagent) before photographing. The grain dimension in both transverse directions is approximately 200 μm, as indicated in the figure.

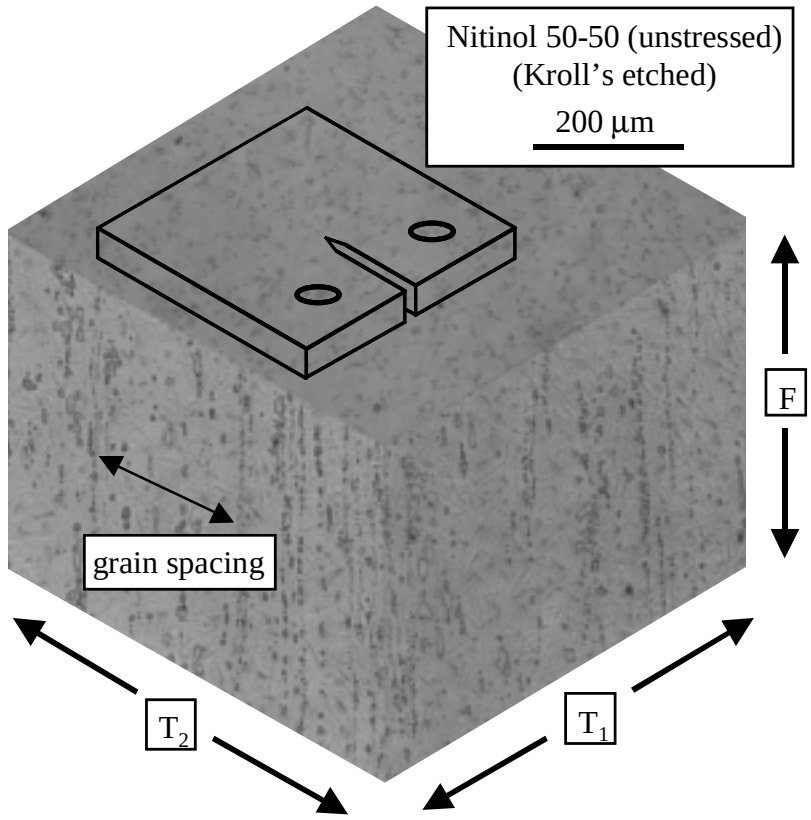

Figure D.6 – Orthogonal metallurgical cube for Nitinol 50-50 (as tested).

D.3 — FATIGUE CRACK GROWTH SPECIMENS

FCG experiments were performed using compact tension, (CT) [4] or eccentrically loaded single edge notch tension (ESET) specimens[38]. Photographs of CT and ESET specimens are shown in Figures D.7a and D.7b, respectively. For both specimen configurations, pin-holes, the back-face strain gage, and machine notch are labeled. A U.S. nickel is also shown for scale. The ESET specimen shown is 1.5 inches wide, while the CT specimen has a dimension W = 1.2 inches (total width of 1.5 inches). Specimen dimensions, for both specimen configurations, are prescribed by two variables: specimen width, W, and specimen thickness, B. Both CT and ESET specimens are loaded by pins, at pin-holes shown in Figure D.7. A sharp notch is machined in the side of both specimen configurations. The high stress concentration around the sharp notch ensures fatigue crack initiation at the notch root and FCG normal to applied loads. Aluminum 2024 specimens were of the ESET configuration because the material was available in large sheets. Because 7050 aluminum specimens were tested in the S-L orientation, and constructed from a plate 1.5 inches thick, ESET specimens were not

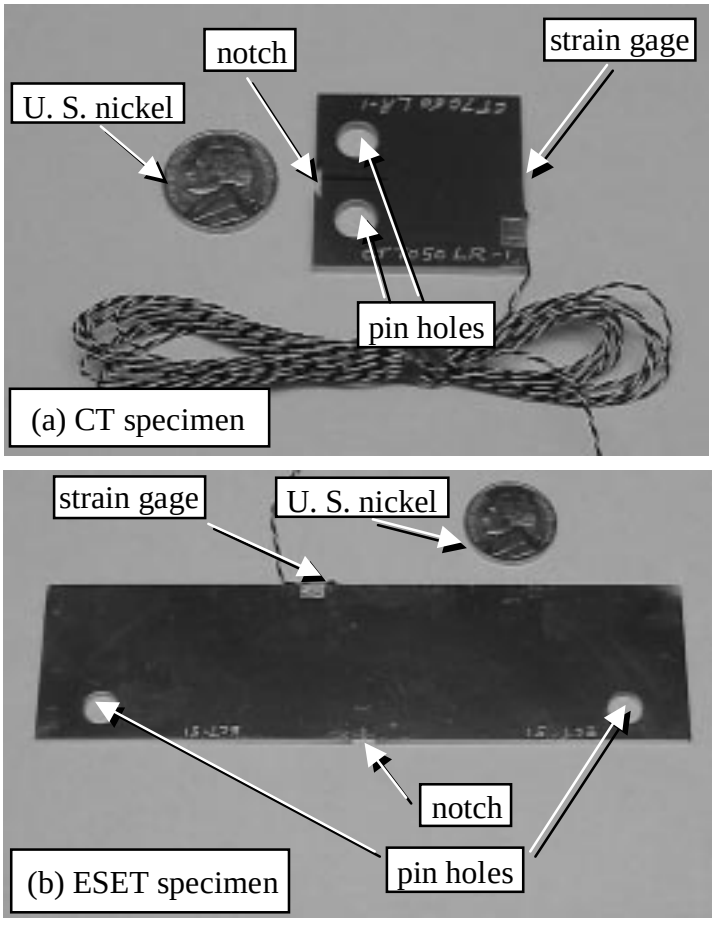

Figure D.7 – Photographs of (a) compact tension (CT) and (b) eccentrically loaded edge notch tension (ESET) specimen configurations.

[38] The ESET specimen was formerly called the extended compact tension (ECT) specimen [157].

practical. Instead sub-size CT specimens were used. Due to the small quantity of available material, the CT configuration was used for Nitinol specimens. FCG data presented in this dissertation were generated using specimen configurations as summarized in Table D.2. This includes the specimen configuration, width, and thickness. Information is given for alloys tested as part of this dissertation and those of results published in existing literature that were used here to verify the PRO closure model (developed in Chapter 3).

Table D.2 – Specimen configuration and geometry of FCG specimens.

Alloy	Specimen configuration	Specimen width W (mm)	Specimen thickness B (mm)
Tests performed here			
2024-T3 (L-T) aluminum	ESET	38.1	2.28
7050-T6 (S-L) aluminum	CT	30.5	2.54
8009 (L-T) aluminum	ESET	38.1	2.28
Nitinol 50-50	CT	44.5	2.54
Data from literature			
8009 aluminum [1]	CT	57.2	6.35
AISI 1080 steel (CG) [2]	CT	63.5	6.35
AISI 1080 steel (FG) [2]	CT	63.5	6.35
INCONEL 718 (CG) [3]	CT	38.0	3.80
INCONEL 718 (FG) [3]	CT	38.0	3.80
Grade E Drill Pipe Steel [4]	CT	63.0	6.30

[1] From McEvily [57] (T-L orientation)

[2] From Gray [58]

[3] From Drury [59]

[4] From Ruppen [54]

APPENDIX E — THRESHOLD FATIGUE CRACK GROWTH HUMIDITY EFFECTS

The effect of humidity on threshold FCG is studied in this appendix. Variations in humidity levels during FCG testing are believed to cause some scatter in aluminum 7050 FCG data (presented in Chapter 4, Figure 4.3). Constant-ΔK FCG tests are performed on aluminum 7050 in carefully controlled humid air environments to evaluate the influence of humidity on threshold FCG.

E.1 — INTRODUCTION

Aluminum 7050 constant K_{max} FCG data was presented in Chapter 4 (Figure 4.3). Although accelerated FCG rates were associated with increasing K_{max}, the data in Figure 4.3 appeared to contain more scatter than the other aluminum alloys, under similar conditions. For example, the aluminum 7050 data indicates FCG rates for K_{max} = 5.5 MPa√m are greater than for K_{max} = 11.0 MPa√m, about ΔK = 2.0 MPa√m. Furthermore, little difference between FCG rates at K_{max} = 16.5 MPa√m and K_{max} = 22.0 MPa√m is observed. Because increases in crack-tip driving forces (ΔK and K_{max}) are expected to increase FCG rates, the scatter seen in Figure 4.3 is likely a result of an external influence. Humidity variations in ambient air are considered a likely source of this scatter. Because the aluminum 7050 data contains more scatter, this alloy is likely more sensitive to humidity than the other aluminum alloys (2024 and 8009).

The humidity level and temperature of the laboratory air environment were monitored for one week.[39] Relative humidity (RH) and temperature data of ambient air are plotted against time in Figure E.1.[40] Horizontal dotted lines bound the humidity and temperature data and are used to determine ambient conditions. As seen in Figure E.1a, ambient RH varies from 30% to 70% (lower and upper horizontal dotted lines, respectively). The ambient range of temperature is 20°C to 25°C, as shown in Figure E.1b. Temperature variations in this range are not expected to significantly affect FCG behavior because the melting point of aluminum is much higher (approximately 600°C). However, variations in humidity between 30% and 70% RH might be significant. The influence of water vapor on FCG has been studied in detail by other researchers, and details of water vapor interactions with FCG can be found in the literature [81, 82, 84, 85, 158-165]. However, details of water vapor (humidity) effects on FCG are not within the scope of this dissertation. Rather, humidity effects are studied to ensure that the accelerated FCG rates reported in Chapter 4 are a result of increasing K_{max} and not changes in RH.

[39] Ambient humidity and temperature were monitored (in an indoor laboratory) for one week in April 2000 at NASA-Langley Research Center in Hampton, VA. The humidity and temperature data presented in Figure E.1 is considered typical of indoor conditions, although seasonal variations in laboratory air humidity have not been examined.

[40] Humidity measurements are reported here in percent relative humidity (RH). RH is the ratio of water vapor in the air divided by the saturation water vapor (maximum amount of water vapor). For example, the RH of dry air and saturated air are 0% and 100%, respectively.

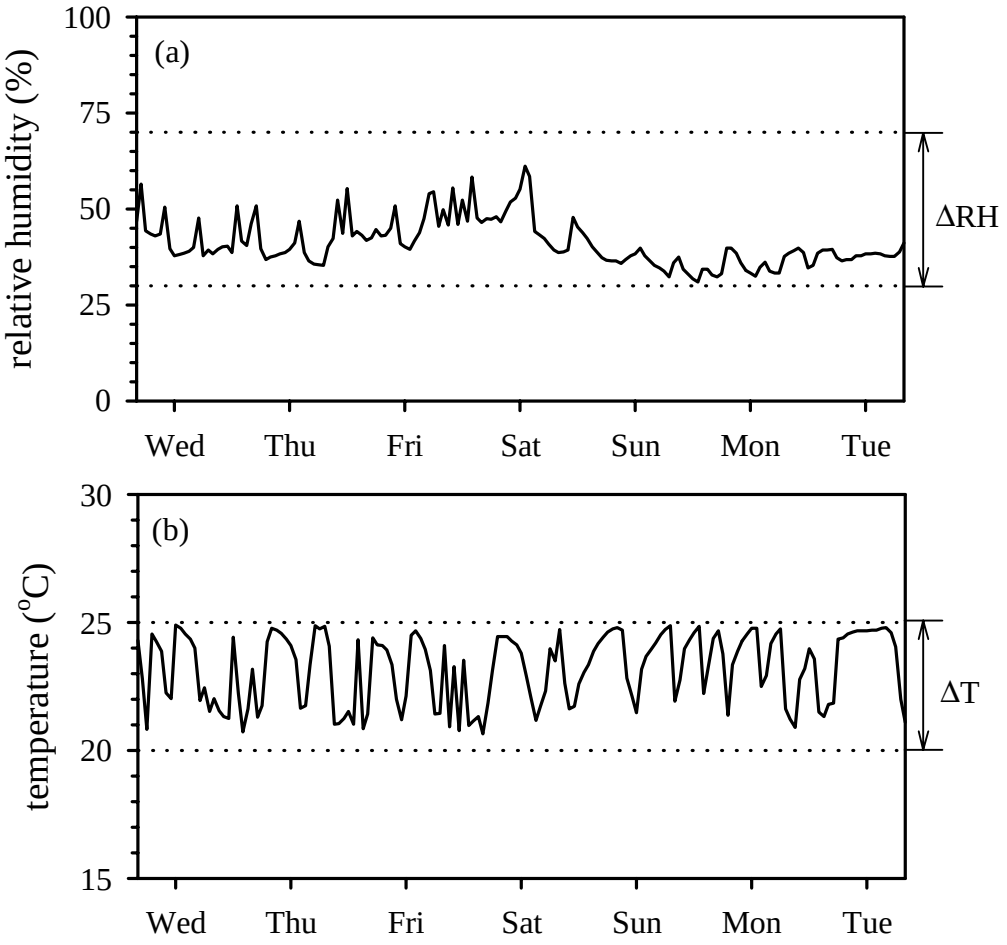

Figure E.1 – Humidity and temperature measurements of laboratory air. RH and temperature, measured for one week, are plotted in parts (a) and (b), respectively. These data were used to determine the ambient range of humidity and temperature (ΔRH and ΔT, respectively), bounded by horizontal dotted lines in the plots.

E.2 — TEST PROCEDURE AND RESULTS

FCG tests were performed in laboratory air at specified RH levels to determine humidity effects on FCG rates. Based on (closure-free) FCG data presented in Chapter 4, FCG load ratio effects were (primarily) associated with K_{max}. Other factors, like variations in humidity, are believed to be smaller secondary effects. Therefore, resolving (potentially) small humidity effects may be difficult, and were considered when planning FCG tests. Aluminum alloy 7050 is used exclusively for constant RH tests because humidity effects are likely large (relative to other aluminum alloys) and more easily detected. Constant ΔK tests are used because FCG rates can be determined with greater accuracy. Because threshold FCG is of interest in this dissertation, a (constant) ΔK of 1.0 MPa$\sqrt{m}$ is used. Finally, FCG experiments were performed in laboratory air at constant RH levels. Performing constant ΔK tests in constant RH environments is the best method to resolve subtle humidity effects at FCG threshold.

FCG tests were performed in laboratory air at constant (controlled) RH levels by enclosing FCG specimens in a humidity chamber. RH levels were controlled in the humidity chamber by mixing dry and humid air. The flow rates of dry and moist air were controlled with flowmeters, adjusted to achieve prescribed RH levels. A humidity probe in the chamber was used to monitor RH levels during testing. Otherwise, FCG testing was performed as described in Appendix B. Compressed air, with less than 0.4% RH, was used as a source of dry air. The small amount of water vapor measured in the compressed air (0.4% RH) is within the error of the humidity probe (4% RH) and considered negligible. Humid air was obtained by bubbling the compressed air through a beaker of warm water. The measured RH level of humidified air was greater than 98%.

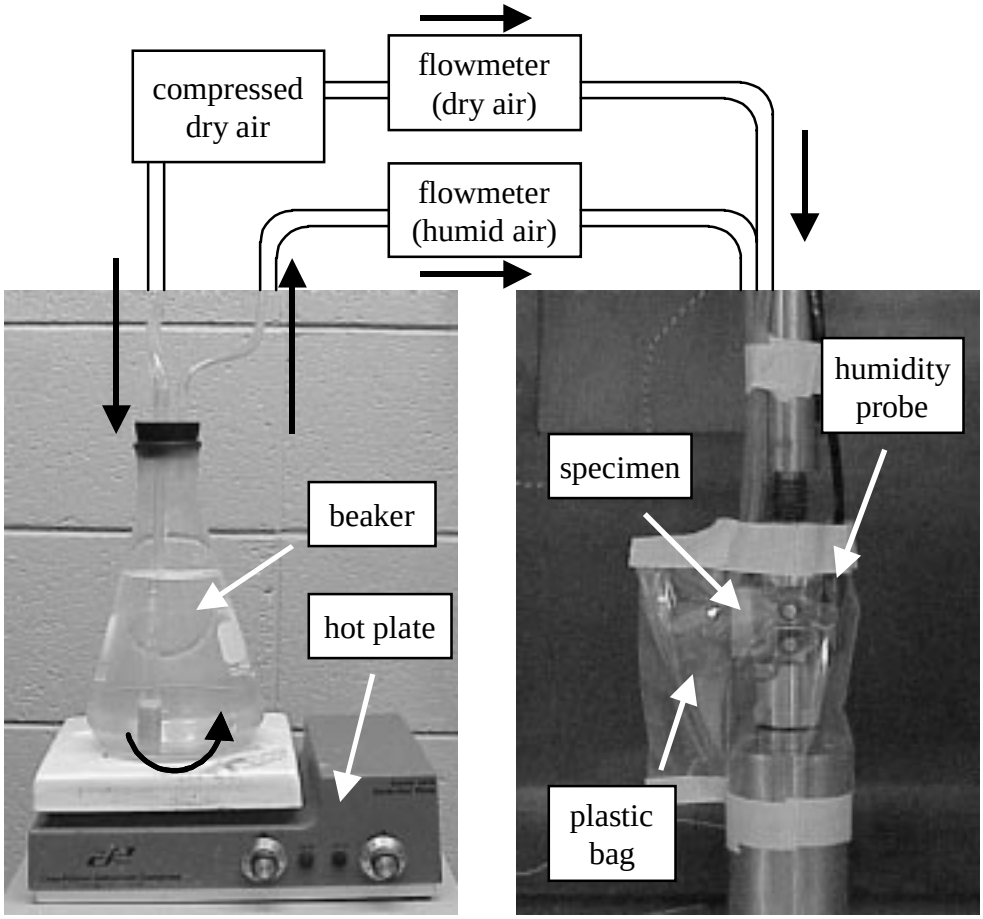

Figure E.2 – Photograph of test setup to perform FCG tests in controlled RH. The specimen is shown inside a plastic bag where two air hoses, a humidity probe, pullrods, and a strain gage wire are allowed to penetrate the bag. Holes in the bag are sealed with tape. A warm beaker of water is used to humidify the compressed air, as shown.

Controlling flow rates of dry and humid air into the humidity chamber enabled RH levels to be specified within 4% for any RH value between 0.4% and 98%. In Figure E.2, a

combination of photographs and schematics illustrate the setup used to control RH levels. A plastic bag around the specimen was used as a humidity chamber, indicated in the lower right photograph in the Figure E.2. The specimen and humidity probe are labeled in the lower right corner of the figure. Plastic bags were sealed with masking tape, but small leaks were allowed, permitting air to flow through the chamber. In the lower left corner of the figure, a beaker of water on a hotplate is shown. The flow of dry and humid air to the humidity chamber is shown schematically above the photographs in Figure E.2.

During threshold testing (decreasing ΔK), FCG rates are determined by dividing a small increment of crack growth by the number of cycles occurring during a small increment of crack growth. Although ΔK continuously changes as the crack grows, changes in ΔK are small when small crack increments are analyzed. FCG rates can be determined with greater accuracy over larger increments of crack growth. However, smaller crack growth increments reduces the error in ΔK. For FCG threshold testing, smaller crack growth increments allows ΔK to be known with greater precision, but larger increments increases the precision of FCG rate. (The increments of crack growth used to evaluate FCG rates in this dissertation are 0.04 mm.)

Constant ΔK tests permit FCG rates to be determined with greater precision than threshold tests because crack-tip loads (*i.e.* ΔK and K_{max}) are constant. For specified test conditions, FCG rate is determined from crack length and cycle count data. As an example, consider the aluminum 7050 FCG data presented in Figure E.3 for $\Delta K = 1.0$

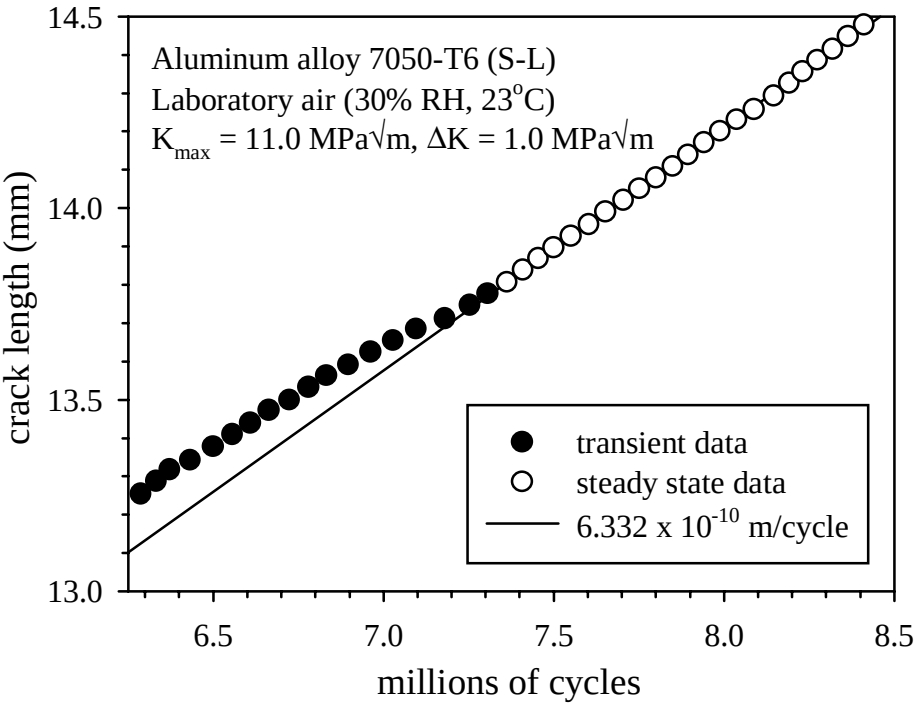

Figure E.3 – Plot of crack length versus cycle count used to determine steady state FCG rate.

MPa√m, K_{max} = 11.0 MPa√m, and 30% RH. Crack length and cycle count data are indicated along vertical and horizontal axes, respectively. Approximately 1.2 mm of FCG occurred during this test (crack length increased from 13.3 mm to 14.5 mm) requiring 2.2 million load cycles (from 6.3 to 8.5 million cycles). Nearly 0.5 mm of transient FCG (closed circular symbols in lower left corner of the figure) occurred before a steady state was achieved.[41] Steady state FCG occurred for 0.7 mm (between crack lengths of 13.8 mm and 14.5 mm), more than three MPZ radii.[42] A least squares line is fit to the steady state data (open circular symbols in the upper right corner of Figure E.3). The slope of this fitted line is the steady state FCG rate: 6.332 x 10^{-10} m/cycle. Steady state FCG rates are determined for other loading conditions and RH levels using constant ΔK FCG data. Using the technique illustrated in Figure E.3, much FCG data (23 data points for this example) are reduced to a single data point (FCG rate) with increased accuracy. Because FCG tests were performed at 11 Hz, the data in Figure E.3 required approximately 56 hours of test time.

A series of constant ΔK = 1.0 MPa√m tests were performed at two K_{max} levels (5.5 MPa√m and 11.0 MPa√m) in laboratory air with controlled RH levels. Steady state FCG rates are determined for each condition using constant ΔK data as shown in Figure E.3. Steady state FCG rates are plotted against RH (for ΔK = 1.0 MPa√m) in Figure E.4. (Note that linear axes are used in Figure E.4.) The FCG data for each constant ΔK test (*e.g.* the data in Figure E.3) are reduced to individual data points in Figure E.4. That is, each data point shown in Figure E.4 represents an entire FCG test similar to that shown in Figure E.3. Steady state FCG data for K_{max} levels of 5.5 MPa√m and 11.0 MPa√m are plotted as open circular and closed triangular symbols, respectively. The range of ambient RH, shown in Figure E.1a, is indicated in the center of Figure E.4 between two vertical dotted lines. The ASTM suggested threshold rate of 10^{-10} m/cycle is shown as a horizontal dashed line near the bottom of the figure.

Because humidity history effects were a concern, FCG tests were not done in order of increasing or decreasing RH. Rather, RH levels were chosen in random order. A few tests were reproduced with different humidity histories. For example, two tests at 70% RH for K_{max} = 5.5 MPa√m were performed immediately following tests at RH levels of 0% and 90%. Although the FCG rate following the 90% RH test was approximately 10% greater than that following the 0% RH test, no such trend was shown to exist in general. (The opposite "humidity history effect" was shown in other cases. Humidity history effects on transient data will be discussed later.) For convenience, FCG rate (on the vertical axis) is scaled by 10^{-10} m/cycle. Relative humidity is shown in percent (%) along the bottom horizontal axis. The corresponding partial pressure of water vapor (at 23°C) is shown along the top horizontal axis. The ambient range of RH is indicated between two vertical dotted lines near the center of the figure. Data for K_{max} levels of 5.5 MPa√m and 11.0 MPa√m are plotted as open circular and closed triangular symbols, respectively. As seen in the figure, FCG rates for both sets of data increase from nearly 10^{-10} m/cycle

[41] For comparison, the plane-strain MPZ size for this example is calculated as 0.2 mm using Equation 5.9b.
[42] During threshold testing, ΔK would have been reduced from 3 MPa√m to 2.84 MPa√m and 1.73 MPa√m for K-gradients (C) of -80 m^{-1} and -800 m^{-1}, respectively, after 0.7 mm of crack growth.

to 6.5 x 10^{-10} m/cycle as RH increases from 0% to 100%. These plots are divided into three portions, each approximated by a line. In the figure, solid and dash-dot lines approximate the data for K_{max} levels of 5.5 MPa√m and 11.0 MPa√m, respectively. FCG rates for K_{max} = 11.0 MPa√m are greater in all cases (for RH < 95%) than for K_{max} = 5.5 MPa√m. Between RH levels of 0% and 30%, FCG rates increase with increasing RH. For K_{max} = 5.5 MPa√m, the FCG rate increases from (approximately) 10^{-10} m/cycle to 4 x 10^{-10} m/cycle (factor of 4 increase). The K_{max} = 11.0 MPa√m data indicate an increase in FCG rate from (approximately) 1.5 x 10^{-10} m/cycle to 6 x 10^{-10} m/cycle (also a factor of 4 increase) in the same RH range. The lines fit through the data in this region (left side of figure) are slopped, indicating an increase in FCG rate with increasing RH. Fatigue crack growth rates are nearly independent of humidity between RH levels of 30% and 90%. Horizontal lines are shown to approximate the FCG behavior in this RH range.

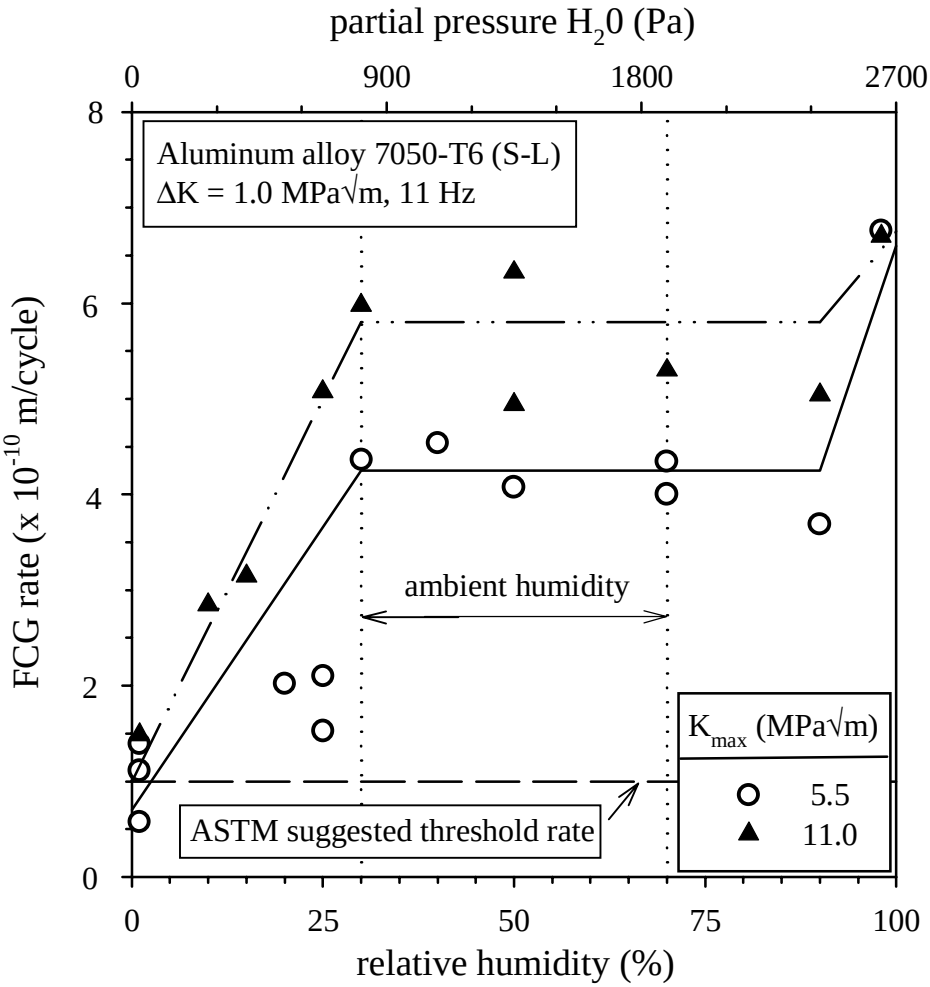

Figure E.4 – Steady state FCG rate plotted as a function of RH for aluminum alloy 7050-T6. Test results correspond to ΔK = 1.0 MPa√m and K_{max} = 5.5 (closed symbols) or 11.0 MPa√m (open symbols). The FCG data are plotted (on a linear plot) against RH (bottom horizontal axis). The corresponding partial pressure of water vapor is shown along the top horizontal axis.

Variations in this region are thought to be associated with statistical scatter (likely associated with microstructure) rather than humidity. Because this region coincides with the ambient RH range, humidity effects on FCG data in Chapter 4 are likely small. However, RH levels were shown in Figure E.1a near 30%. The data in Figure E.4 indicate that further reduction in RH will produce significant reduction in FCG rates.

Although the data plotted in Figure E.4 correspond to steady state FCG, two interesting observations are made from transient data immediately following sudden changes in RH. First, no transient FCG occurs when RH levels suddenly increase. Here, FCG rates immediately increase from steady state value at low RH to the steady state value at high RH. Second, sudden decreases in RH produce transient FCG until the crack grows (approximately) through the monotonic plastic zone (MPZ) associated with high RH. After growing through the MPZ produced at higher humidity, steady state FCG occurs at low RH.

Data showing FCG behavior after a sudden increase, and a sudden decrease, in RH are shown in Figures E.5 and E.6, for K_{max} levels of 5.5 MPa$\sqrt{m}$ and 11.0 MPa$\sqrt{m}$, respectively. FCG tests were performed at ΔK = 1.0 MPa$\sqrt{m}$ and 11 Hz. Where indicated in the figures, RH suddenly changed from one value to another. Steady state and transient data (plotted as crack length versus applied cycles) are indicated by open and closed symbols, respectively. In Figure E.5a, crack growth data is shown as the RH level decreases from 30% to 0%. In the lower left corner of the plot, steady state FCG data is indicated by open circular symbols. The RH level is suddenly reduced from 30% to 0% at a crack length of approximately 14.5 mm, indicated by the lower horizontal dashed line. The upper horizontal dashed line corresponds to the edge of the plane-strain MPZ as RH was reduced. Transient FCG data at 0% RH is indicated by closed triangular symbols. The steady state FCG rate for 30% RH persists after the RH level is reduced to 0%. In the figure, closed triangular symbols continue along the same linear relation of the open circular symbols until the crack grew approximately through the MPZ that existed at the higher humidity level. FCG rate (slope of the data) gradually decreased after the crack grew through the MPZ (upper horizontal dashed line). FCG rates at 0% RH approached the steady state value after approximately 0.15 mm of crack growth, indicated by the open triangular symbols. Similar data for an increase in RH level is shown in Figure E.5b. As seen by the open triangular data in the lower left corner of the figure, steady state FCG at 0% RH occurred until the RH level was abruptly increased from 0% to 30% at a crack length of approximately 15.13 mm. No transition was observed after this increase in RH. FCG rates abruptly changed from the steady state at 0% RH to the steady state at 30% RH.

Transient FCG data for ΔK = 1.0 MPa$\sqrt{m}$ at K_{max} = 11.0 MPa$\sqrt{m}$ is shown in Figure E.6. Data is plotted similar to Figure E.5 for (a) a sudden increase and (b) a sudden decrease in RH. Steady state FCG data at 90% RH are indicated in the lower left of Figure E.6a. The RH level was abruptly decreased to 0% at a crack length of approximately 17.12 mm, indicated by the lower horizontal solid line. The upper horizontal line corresponds the edge of the MPZ at the decrease in RH. Transient FCG data are shown as closed triangular symbols. The steady state FCG rate of 90% RH persists for approximately

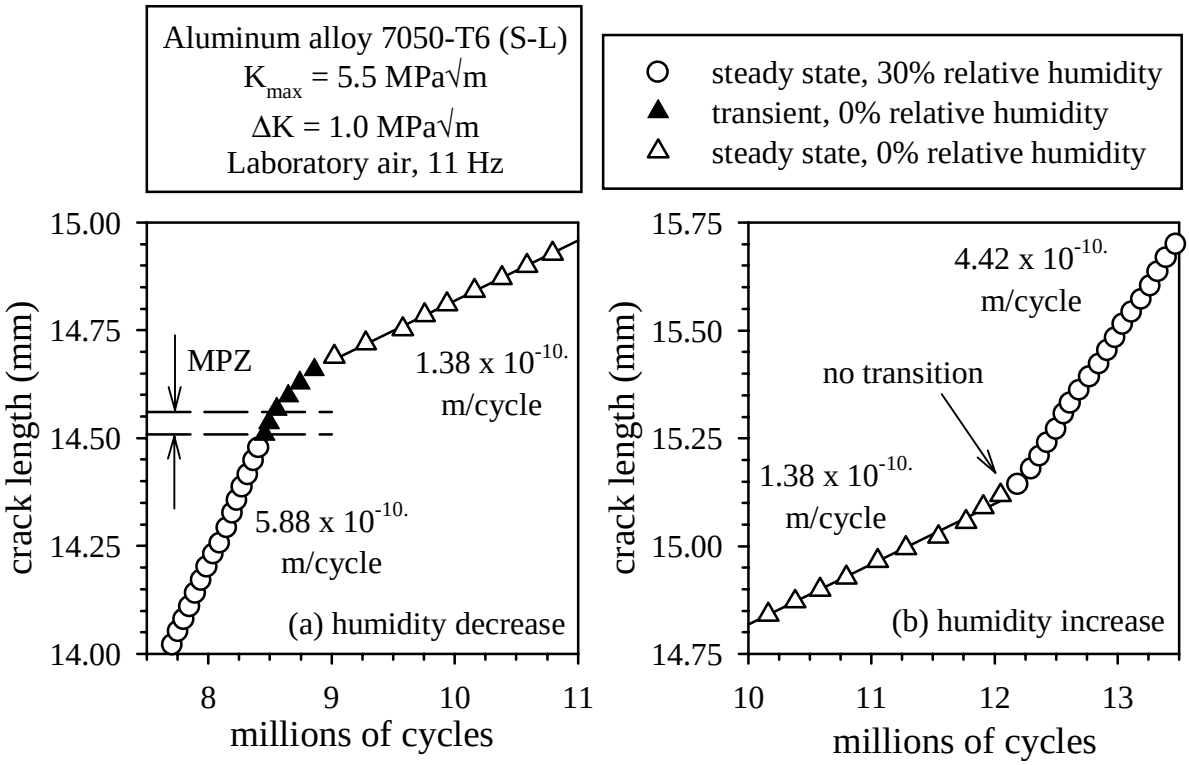

Figure E.5 – Plots of crack length versus cycle count for K_{max} = 5.5 MPa√m as humidity was (a) decreased and (b) increased. Transient behavior occurred until the crack grew approximately one MPZ in part (a). No transition was observed in part (b).

0.1 mm. Steady state FCG is established after the fatigue crack grew through the MPZ produced at 90% RH (an increase in crack length of 0.205 mm). Steady state data at 0% RH is indicated as open triangular symbols in the upper right corner of Figure E.6a.

FCG data is shown in Figure E.6b as the RH level was abruptly increased from 0% to 70% (at a crack length of 18.05 mm). Steady state data for 0% RH is shown in the lower left corner of the figure as open triangular symbols. No transition in FCG rate occurred after the increase in RH. Rather, FCG rates changed abruptly to steady state values for 70% RH. Steady state FCG data generated at 70% RH are shown as open square symbols in the upper right corner of the figure.

E.3 — HYDROGEN DIFFUSIVITY

For aluminum alloy 7050 tested at ΔK = 1 MPa√m and two values of K_{max} (5.5 and 11.0 MPa√m), the intrinsic (closure-free) FCG behavior was not significantly affected for ambient RH conditions (30% to 70% RH). This suggests K_{max} test data presented in Chapter 4 is not significantly affected by variations in humidity. Because other aluminum alloys had less scatter in their FCG data they are less likely affected by variations in RH. Furthermore, the effects of ambient RH on FCG rate are small, at least

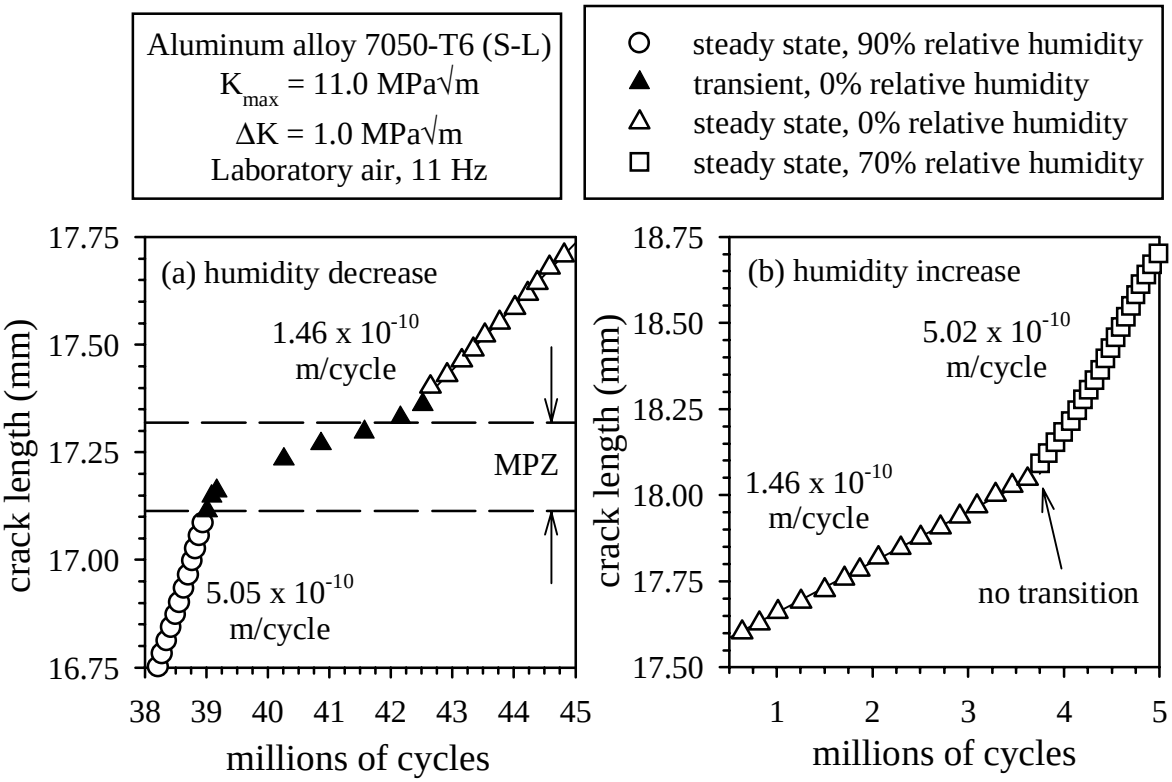

Figure E.6 – Plots of crack length versus cycle count for K_{max} = 11.0 MPa√m as humidity was (a) decreased and (b) increased. Transient behavior occurred until the crack grew approximately one MPZ in part (a). No transition was observed in part (b).

for 7050 aluminum. However, extreme values of RH (*e.g.* rain forest or desert) may influence FCG behavior differently than laboratory air results suggest. It is important to know the service conditions a cyclically loaded member will endure and the effects that variations in conditions will bring. A discussion of hydrogen diffusion (the likely cause of RH effects) in aluminum is discussed in this section. It will be shown that bulk diffusion is an unlikely transport mechanism in the MPZ. A dislocation-assisted diffusion mechanism is proposed as a likely hydrogen transport mechanism.

Presumably, hydrogen (a component of water vapor) in the MPZ produced the accelerated FCG rates at high humidity. Hydrogen is likely transported into the MPZ by one of two mechanisms, (1) bulk diffusion or (2) dislocation-assisted diffusion [166]. Consider, a clean piece of metal with a smooth surface that is suddenly exposed to a gaseous species. This configuration is shown schematically in Figure E.7a. The exposed metal surface is labeled as a vertical line with the metal and environment indicated on right and left sides, respectively. The concentration of the gaseous species at the metal interface is C_o. Because the metal is initially clean, a concentration gradient exists, and the net mass flux of the gaseous species is into the metal (to the right, as indicated in the figure). The concentration of the gaseous species for this case is a function of depth from

the free surface, x, and exposure time, t,[43] as shown in Equation E.1 where the concentration in the interior, C(x,t), is normalized by the concentration at the surface, C_o, and D is the mass diffusivity [166]. The 'erf' in Equation E.1 indicates use of the error function.

$$\frac{C(x,t)}{C_o} = 1 - \mathrm{erf}\left(\frac{x}{2\sqrt{Dt}}\right) \tag{E.1}$$

The configuration shown in Figure E.7a is modified to analyze diffusion rates in the MPZ of a fatigue crack. This configuration is shown in Figure E.7b, where the crack-tip and MPZ are indicated. The gaseous concentration at the crack-tip is indicated as C_o. The distance from the crack-tip to the edge of the MPZ is labeled r_p. For plane-strain conditions the MPZ radius, r_p, is approximated in Equation 5.9b. The time required for a fatigue crack to propagate through one MPZ is a function of FCG rate, r_p, and loading frequency (*f*), as shown in Equation E.2. Hydrogen must diffuse $2r_p$ ahead of the crack-tip in this time to outpace a propagating fatigue crack.

$$t = \frac{r_p}{f\left(da/dN\right)} \tag{E.2}$$

Because the environment/metal interface in Figure E.7b is not a flat plane, the crack-tip diffusion is not a one-dimensional problem. As an approximation, diffusion ahead of the crack-tip is assumed to occur as described in Equation E.1. This assumption will result in an overprediction of concentration. Substituting $2r_p$ for x (in Equation E.1) provides an approximation for concentration ahead of the crack-tip under steady state conditions, as shown in Equation E.3. (Recall, t is specified by Equation 6.11.) Bulk and dislocation-assisted diffusivities of hydrogen in aluminum, D_H, are given in Equations E.4a and E.4b, respectively [167]. Recall from Figures E.4 through E.6 that FCG rates in aluminum alloy 7050-T6 (S-L) at $\Delta K = 1.0$ MPa$\sqrt{m}$ are approximately 10^{-10} m/cycle and 6×10^{-10} m/cycle, for low (0% RH) and high (>30% RH) humidity levels, respectively, for both K_{max} levels (5.5 MPa$\sqrt{m}$ and 11.0 MPa$\sqrt{m}$).

$$\frac{C(x,t)}{C_o} = 1 - \mathrm{erf}\left(\frac{r_p}{\sqrt{Dt}}\right) \tag{E.3}$$

$$D_H = 10^{-14}\ m^2/s \quad \text{(bulk diffusion)} \tag{E.4a}$$

$$D_H = 2.25\times10^{-12}\ m^2/s \quad \text{(dislocation-assisted diffusion)} \tag{E.4b}$$

[43] For this discussion the symbol 't' refers to time, instead of oxide layer thickness.

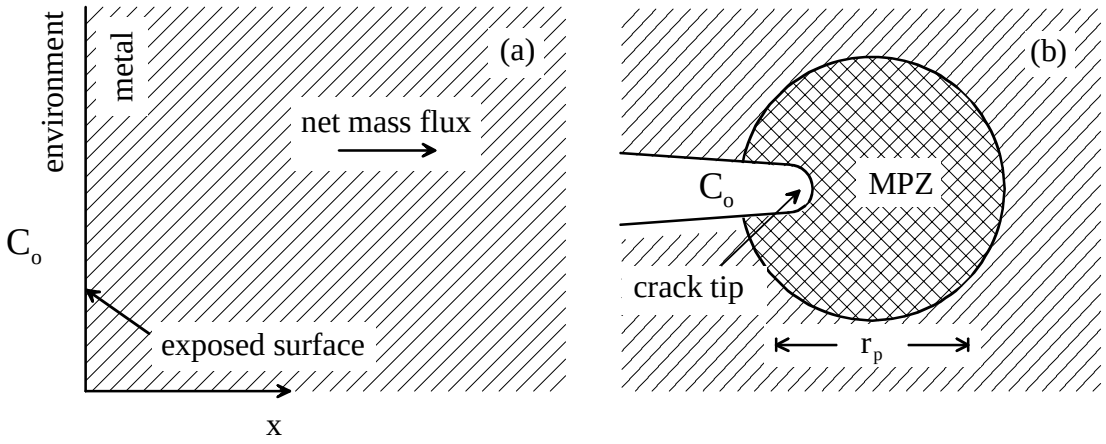

Figure E.7 – Schematics of (a) planar interface of environment and clean metal surface and (b) interaction of environment at a crack-tip. These configurations are used to model the concentrations of hydrogen in the MPZ of a fatigue crack.

The normalized concentration expected at the edge of the MPZ under steady state conditions (Equation E.3) is computed for K_{max} levels of 5.5 MPa√m and 11.0 MPa√m, and high and low humidity. Values of normalized concentrations are presented in Table E.1 for bulk diffusion (not in parentheses) and dislocation-assisted diffusion (in parentheses). As seen in the table, the expected concentrations associated with bulk diffusion are nearly zero in all cases. Although the hydrogen concentration required for accelerated FCG rates is unknown, the low bulk diffusion concentrations suggest higher diffusivity is needed. Because intense deformation (dislocations on the microscopic level) occurs at the crack-tip, a dislocation-assisted diffusion process might occur. The (normalized) concentrations expected for dislocation-assisted diffusion are shown in parentheses in the table. Because these values are much greater than bulk diffusion, dislocation-assisted diffusion is a more likely hydrogen transport mechanism in the MPZ.

Table E.1 – Expected hydrogen (normalized) concentration at edge of MPZ.

K_{max} (MPa√m)	Low RH (10^{-10} m/cycle)	High RH (6×10^{-10} m/cycle)
5.5	8×10^{-4} (0.826)	0 (0.582)
11.0	0 (0.654)	0 (0.272)

E.4 – SUMMARY

Scatter in constant K_{max} test data was noted for aluminum alloy 7050 in laboratory air environments. Variation in ambient humidity was investigated as a likely explanation for this behavior. Constant ΔK = 1.0 MPa√m tests were performed at K_{max} = 5.5 MPa√m and 11.0 MPa√m in controlled RH environments to investigate humidity effects on threshold FCG. These test results (see Figure E.4) indicated that FCG rates were nearly

constant over the ambient range of humidity in laboratory air (30% to 70% RH) and RH effects on the FCG data presented in Chapter 4 were small. However, outside of ambient RH conditions, FCG rates were strongly affected by humidity, and FCG rates increased with increasing RH. Transient FCG data indicated humidity-related crack-tip damage occurred in the MPZ. Analysis of hydrogen diffusion through an aluminum matrix suggested that bulk diffusion was an unlikely transport mechanism. Rather, a dislocation-assisted diffusion mechanism was proposed as the most likely hydrogen transport mechanism in the crack-tip MPZ.

APPENDIX F — BASIC COMPUTER CODES FOR MODEL EVALUATION

Models were developed in Chapters 3 and 4 to quantify the effects of fatigue crack closure and crack-tip damage, respectively. BASIC computer programs, created to evaluate the model results, are presented here.

F.1 — FATIGUE CRACK CLOSURE MODEL

The following BASIC program was used to evaluate the results of the PRO closure model developed in Chapter 3. The lines of code shown below consist of six parts described as follows:

(a) Input of model parameters – User input of model parameters such as elastic modulus and yield stress.

(b) Calculation of stress intensity factors and displacements – The stress intensity factors (due to roughness and meandering) are computed along with the elastic crack face displacements at the first asperity behind the crack-tip.

(c) Crack tip plasticity – The plastic crack face displacements are calculated using the angles of shear extrema and plastic zone size. The residual plasticity in the crack wake is also calculated.

(d) Calculation and output of closure levels at asperity – The closure levels corresponding to the first kink behind the crack-tip are given.

(e) Calculation and output of closure levels at crack-tip – The closure levels corresponding to the crack-tip are given.

```
'    A MODEL FOR PICC, OICC, AND RICC DEVELOPED BY:
'     J. A. Newman
CLS
CTODp = 0
CTSDp = 0
pi = 4 * ATN(1!)
DIM x(5900)
DIM f(5900)
DIM sig(5900)
DIM r(5)
DIM b(5)
DIM th(5)
n = 1

'       INPUT OF MODEL PARAMETERS

PRINT "Input alpha (degrees)"
INPUT adeg
a = adeg * pi / 180
a2 = .5 * a
```

```
PRINT "Input kink length, g (micrometers)"
INPUT gmm
g = gmm / 1000000
PRINT "Input E (GPa)"
INPUT Egpa
E = Egpa * 1000000000
PRINT "Input Poisson ratio (dimensionless)"
INPUT nu
PRINT "Input t (nanometers)"
INPUT tmm
t = tmm / 1000000000
PRINT "Yield stress (MPa)"
INPUT sigympa
sigy = sigympa * 1000000
PRINT "Input gamma (degrees)"
INPUT gamdeg
gam = gamdeg * pi / 180
PRINT "Input K1g (MPa m^0.5)"
INPUT k1gmpa
k1g = k1gmpa * 1000000
PRINT "Input K2g (MPa m^0.5)"
INPUT k2gmpa
k2g = k2gmpa * 1000000
PRINT "Input applied R"
INPUT Rapp

'      CALCULATION OF STRESS INTENSITY FACTORS AND DISPLACEMENTS

k1l = k1g * (COS(gam)) ^ 1.5 - 2 * k2g * SIN(gam) * (COS(gam)) ^ .5
k2l = k1g * SIN(gam) * (COS(gam)) ^ .5 + k2g * (2 * (COS(gam)) ^ 1.5
        - (COS(gam)) ^ -.5)
k1 = k1l * (COS(a2)) ^ 3 - 3 * k2l * SIN(a2) * COS(a2) * COS(a2)
k2 = k1l * SIN(a2) * COS(a2) * COS(a2) + k2l * COS(a2) * (1 - 3 * SIN(a2) * SIN(a2))
up = 4 * (1 - nu * nu) * k2 * (1 / E) * ((g / (2 * pi)) ^ .5)
vp = 4 * (1 - nu * nu) * k1 * (1 / E) * ((g / (2 * pi)) ^ .5)
u = up * COS(a) - vp * SIN(a)
v = up * SIN(a) + vp * COS(a)

'      FINDING ANGLES OF SHEAR EXTREMA

 FOR k = 1 TO 3599
   x(k) = (1800 - k) * pi / 1800
   x2 = .5 * x(k)
   f(k) = k1 * COS(x2) * (1 - 3 * SIN(x2) * SIN(x2))
        - k2 * SIN(x2) * (7 - 9 * SIN(x2) * SIN(x2))
   sig(k) = SGN(f(k))
```

```
 NEXT k
 FOR j = 1 TO 3598
   IF (sig(j) = 0) THEN th(n) = x(j) AND n = n + 1
   IF (sig(j) = 0) GOTO 775
   IF ((sig(j + 1) / sig(j)) = 1) GOTO 775
   th(n) = .5 * (x(j) + x(j + 1))
   n = n + 1
775 NEXT j

'      CRACK TIP PLASTICITY

FOR i = 1 TO n - 1
  m1 = (COS(.5 * th(i)) ^ 2) * (3 * (SIN(.5 * th(i)) ^ 2) + (1 - 2 * nu) ^ 2)
  m2 = 3 + (SIN(.5 * (th(i))) ^ 2) * ((1 - 2 * nu) ^ 2 - 9 * (COS(.5 * (th(i))) ^ 2))
  m3 = 2 * COS(.5 * (th(i))) * SIN(.5 * (th(i))) * (3 * (COS(.5 * th(i)) ^ 2
          - SIN(.5 * th(i)) ^ 2) - (1 - 2 * nu) ^ 2)
  r(i) = (k1 * k1 * m1 + k2 * k2 * m2 + k1 * k2 * m3) / (2 * pi * sigy * sigy)
  r(i) = 1.828 * r(i)
  dum = k1 * COS(.5 * th(i)) * COS(.5 * th(i)) * SIN(.5 * th(i))
          + k2 * COS(.5 * th(i)) * (1 - 3 * SIN(.5 * th(i)) * SIN(.5 * th(i)))
  b(i) = sigy * r(i) * pi * (1 - nu * nu) / E * SGN(dum)
   CTODp = CTODp + b(i) * SIN(th(i))
   CTSDp = CTSDp + b(i) * COS(th(i))
NEXT i

 CTOD = CTODp * COS(a) + CTSDp * SIN(a)
 CTSD = -CTODp * SIN(a) + CTSDp * COS(a)

  x = .8561 + .0205 * Rapp + .1438 * Rapp ^ 2 + .2802 * Rapp ^ 3 - .3007 * Rapp ^ 4

'      CALCULATION AND OUTPUT OF CLOSURE LEVELS AT ASPERITY

c1 = -.25 * CTOD * COS(a) + .25 * ABS(CTSD * SIN(a))
c2 = 2 * v * COS(a) + .5 * CTOD * COS(a) - 2 * ABS(u * SIN(a))
          - .5 * ABS(CTSD * SIN(a))
c3 = .75 * CTOD * COS(a) - .75 * ABS(CTSD * SIN(a)) - (2 * t)
          - (x * CTOD / COS(a))

cons = c2 * c2 - 4! * c1 * c3
Rcl1 = (-c2 + SQR(ABS(c2 * c2 - 4! * c1 * c3))) / (2 * c1)
Rcl2 = (-c2 - SQR(ABS(c2 * c2 - 4! * c1 * c3))) / (2 * c1)
PRINT "Rcl at asperity =", Rcl1, "or", Rcl2

'      CALCULATION AND OUTPUT OF CLOSURE LEVELS AT CRACK TIP

ct1 = 1
```

```
ct2 = -2
ct3 = .44 + (8 * t / CTODp)

cont = ct2 * ct2 - 4! * ct1 * ct3
Rcl1t = (-ct2 + SQR(ABS(ct2 * ct2 - 4! * ct1 * ct3))) / (2 * ct1)
Rcl2t = (-ct2 - SQR(ABS(ct2 * ct2 - 4! * ct1 * ct3))) / (2 * ct1)
PRINT "Rcl at crack tip =", Rcl1t, "or", Rcl2t

999 END
```

F.2 — K_{max} DAMAGE MODEL

The following BASIC program was used to evaluate the results of K_{max} damage model developed in Chapter 4. The lines of code shown below consist of three parts described as follows:

(a) Input of model results – The user inputs all needed parameters.
(b) Crack growth by increments – The stress intensity factor of the main crack is calculated and the corresponding FCG rate is calculated. The fatigue crack is allowed to grow by a small increment at this rate. The process is continued until fracture occurs and the main crack coalesces with the microcrack.
(c) Calculation and output of results – The baseline and effective FCG rates are calculated and output.

```
'       A MODEL TO PREDICT THE EFFECT OF CRACK TIP DAMAGE,
'       ASSOCIATED WITH HIGH Kmax, ON FATIGUE CRACK GROWTH BY:
'       J. A. Newman

'       INPUT OF PARAMETERS

PRINT "Input applied K1 (MPa m^.5)"
INPUT k1
PRINT "Input Kc (MPa m^.5)"
INPUT kc
PRINT "Input microcrack half-length (micrometers)"
INPUT c
PRINT "Input distance between centers of microcracks (micrometers)"
INPUT di

logdk = LOG(k1) / LOG(10)
pi = 3.1415927#
d = di - 2 * c
deltad = d / 250
n = 1
```

```
'              CRACK GROWTH BY INCREMENTS
FOR i = 1 TO 249

cnst = (c * c / (64 * d * d))
cnst2 = SQR((di / (pi * c)) * TAN(pi * c / di))
k1true = cnst2 * k1 * (1 + 16 * cnst)

IF (k1true > kc) GOTO 300
   logdkt = LOG(k1true) / LOG(10)
IF (logdkt > .5514) GOTO 110

ldadn = -33.62 + 317.35 * logdkt - 1617.25 * logdkt ^ 2 + 4099.79 * logdkt ^ 3
          - 5136.09 * logdkt ^ 4 + 2540.74 * logdkt ^ 5

GOTO 120
110 ldadn = -10.37 + 3.69 * logdkt

120 dadn = 10 ^ ldadn
ni = deltad / (dadn * 1000000)
n = n + ni
d = d - deltad
'PRINT i, k1true, ni, dadn
NEXT i

'              CALCULATION AND OUTPUT OF RESULTS

300 dadne = di / (n * 1000000)
'PRINT n
'PRINT "Effective da/dN =", dadne

logdk = LOG(k1) / LOG(10)
IF (logdk > .5514) GOTO 210

ldadnb = -33.62 + 317.35 * logdk - 1617.25 * logdk ^ 2 + 4099.79 * logdk ^ 3
          - 5136.09 * logdk ^ 4 + 2540.74 * logdk ^ 5

GOTO 220
210 ldadnb = -10.37 + 3.69 * logdk
220 dadnb = 10 ^ ldadnb

PRINT "Baseline da/dN = ", dadnb
PRINT "Crack growth ratio = ", dadne / dadnb
PRINT "Ktrue/Kapplied =", k1true / k1
END
```

APPENDIX G — REFERENCES

[1] N. E. Dowling, *Mechanical Behavior of Materials*, 2nd Edition, Prentice Hall, Upper Saddle, New Jersey (1999).

[2] G. R. Irwin, "Analysis of Stresses and Strains Near the End of a Crack Traversing a Plate," *Journal of Applied Mechanics*, v. 24 (1957), pp. 361-364.

[3] P. C. Paris and F. Erdogan, "A Critical Analysis of Crack Propagation Laws," *Journal of Basic Engineering*, Dec. (1963), pp.528-534.

[4] ASTM, *Annual Book of ASTM Standards*, v. 3.01, "E-647 – Standard Test Method for Measurement of Fatigue Crack Growth Rates," American Society for Testing and Materials, West Conshohocken, PA (1999).

[5] J. C. Newman Jr., "Analyses of Fatigue Crack Growth and Closure Near Threshold Conditions for Large-Crack Behavior," *Fatigue Crack Growth Thresholds, Endurance Limits, and Design*, ASTM STP 1372, J. C. Newman Jr. and R. S. Piascik, eds., American Society for Testing and Materials, West Conshohocken, PA (2000), pp. 227-251.

[6] R. C. McClung, "Analyses of Fatigue Crack Closure During Simulated Threshold Testing," *Fatigue Crack Growth Thresholds, Endurance Limits, and Design*, ASTM STP 1372, J. C. Newman, Jr. and R. S. Piascik, eds., American Society for Testing and Materials, West Conshohocken, PA (2000), pp. 209-226.

[7] W. Elber, "Fatigue Crack Closure under Cyclic Tension," *Engineering Fracture Mechanics*, v. 2 (1970), pp. 37-45.

[8] N. Walker and C. J. Beevers, "A Fatigue Crack Closure Mechanism in Titanium," *Fatigue of Engineering Materials and Structures*, v. 1 (1979), pp. 135-148.

[9] K. Endo, K. Komai, and Y. Matasuda, "Mechanical Effects of Corrosion Products in Corrosion Fatigue Crack Growth of a Steel," *Bulletin of the JSME*, v. 24 (1981), pp. 1319-1325.

[10] S. Suresh, G. F. Zaminski, and R. O. Ritchie, "Oxide Induced Crack Closure: An Explanation for Near-Threshold Corrosion Fatigue Crack Growth Behavior," *Metallurgical Transactions*, v. 12A (1981), pp. 1435-1443.

[11] N. J. Adams, "Fatigue Crack Closure at Positive Stresses," *Engineering Fracture Mechanics*, v. 4 (1972), pp. 543-554.

[12] S. Purushothaman and J. K. Tien, "A Fatigue Crack Growth Mechanism for Ductile Materials," *Scripta Metallurgica*, v. 9 (1975), pp. 923-926.

[13] J. C. Newman Jr. and W. Elber, eds., *Mechanics of Fatigue Crack Closure*, ASTM STP 982, American Society for Testing and Materials, Philadelphia, PA (1988).

[14] S. Suresh and R. O. Ritchie, "A Geometric Model for Fatigue Crack Closure Induced by Surface Roughness," *Metallurgical Transactions*, v. 13A (1982), pp. 1627-1631.

[15] D. Gan and J. Weertman, "Crack Closure and Crack Propagation Rates in 7050 Aluminum, *Engineering Fracture Mechanics*, v. 15 (1981), pp. 87-106.

[16] C. J. Beevers, "Fatigue Crack Growth Characteristics at Low Stress Intensities of Metals and Alloys," *Metal Science*, Aug./Sept. (1977), pp. 362-367.

[17] R. O. Ritchie and J. F. Knott, "Mechanisms of Fatigue Crack Growth in Low Alloy Steel," *Acta Metallurgica*, v. 21 (1973), pp. 639-648.

[18] G. Marci, "Failure Mode Below 390K with IMI 834," *Proceedings of the 6th International Fatigue Congress*, Berlin, Germany, May 6-10 (1996), v. 1, pp. 493-498.

[19] M. Lang, G. A. Hartman, and J. M. Larsen, "Investigation of an Abnormality in Fatigue Crack Growth Curves – The Marci Effect," *Scripta Metallurgica*, v. 38 (1998), pp. 1803-1810.

[20] S. Pearson, "Initiation of Fatigue Cracks in Commercial Aluminum Alloys and the Subsequent Propagation of Very Small Cracks," *Engineering Fracture Mechanics*, v. 7 (1975), pp. 235-247.

[21] H. Kitagawa and S. Takahashi, "Applicability of Fracture Mechanics to Very Small Cracks or the Cracks in the Early Stage," *Proceedings of the 2nd International Conference on Mechanical Behavior of Materials*, Boston, MA (1976), pp. 627-631.

[22] R. O. Ritchie and J. Lankford, eds., *Small Fatigue Cracks*, Proceedings of the 2nd Engineering Foundation International Conference, Santa Barbara, CA, Jan. 5-10 (1986).

[23] K. S. Ravichandran, R. O. Ritchie, and Y. Murakami, eds., *Small Fatigue Cracks: Mechanics, Mechanisms and Applications*, Proceedings of the 3rd Engineering Foundation International Conference, Oahu, HI (1998).

[24] R. O. Ritchie and J. Lankford, "Overview of the Small Crack Problem," *Small Fatigue Cracks*, Proceedings of the 2nd Engineering Foundation International Conference (1996), pp. 1-5.

[25] K. Tokaji, T. Ogawa, and Y. Kameyama, "The Effects of Stress Ratio on the Growth Behavior of Small Fatigue Cracks in an Aluminum Alloy 7075-T6 (With Special Interest in Stage I Crack Growth)," *Fatigue and Fracture of Engineering Materials and Structures*, v. 13 (1990), pp. 411-421.

[26] J. C. Newman Jr., Personal communication with (2000).

[27] J. K. Donald, G. H. Bray, and R. W. Bush, "Introducing the K_{max} Sensitivity Concept for Correlating Fatigue Crack Growth Data," *High Cycle Fatigue of Structural Materials*, W. O. Soboyejo and T. S. Srivatsan, eds., The Minerals, Metals, and Materials Society (1997), pp. 123-141.

[28] R. W. Bush, J. K. Donald, and R. J. Bucci, "Pitfalls to Avoid in Threshold Testing and its Interpretation," *Fatigue Crack Growth Thresholds, Endurance Limits, and Design*, ASTM STP 1372, J. C. Newman Jr. and R. S. Piascik, eds., American Society for Testing and Materials, West Conshohocken, PA (2000), pp. 269-284.

[29] R. A. Everett Jr. and W. Elber, “Damage Tolerance Issues Related to Metallic Rotorcraft Dynamic Components,” *Journal of the American Helicopter Society*, v. 45 (2000), pp. 3-10.

[30] T. Swift, “Technical Evaluation Report,” *An Assessment of Fatigue Damage and Crack Growth Prediction Techniques*, 77th Meeting of the AGARD Structures and Materials Panel, Bordeaux, France, 29-30 September, (1993), pp. T1-T4.

[31] S. Suresh and R. O. Ritchie, "Some Considerations on the Modeling of Oxide-Induced Fatigue Crack Closure Using Solutions for a Rigid Wedge Inside a Linear Elastic Crack," *Scripta Metallurgica*, v. 17 (1983), pp. 575-580.

[32] S. H. Wang, C. Muller, and H. E. Exner, "A Model for Roughness-Induced Fatigue Crack Closure," *Metallurgical and Materials Transactions*, v. 29A (1998), pp. 1933-1939.

[33] B. A. Bilby, A. H. Cottrell, and K. H. Swinden, "The Spread of Plastic Yield from a Notch," *Proceedings of the Royal Society of London*, v. A272 (1963), pp. 304-314.

[34] B. Budiansky and J. W. Hutchinson, "Analysis of Closure in Fatigue Crack Growth," *Journal of Applied Mechanics*, v. 45 (1978), pp. 267-276.

[35] J. LLorca, "Roughness-Induced Fatigue Crack Closure: A Numerical Study," *Fatigue and Fracture of Engineering Materials and Structures*, v. 15 (1992), pp. 655-669.

[36] N. Chen and F. V. Lawrence, "An Analytical Model for Studying Roughness-Induced Crack Closure," *Fatigue and Fracture Mechanics*, 29th Volume, ASTM STP 1321, T. L. Panontin and S. D. Sheppard, eds., American Society for Testing and Materials1(1998).

[37] K. S. Ravichandran, "A Theoretical Model for Roughness Induced Crack Closure," *International Journal of Fracture*, v. 44 (1990), pp. 97-110.

[38] G. C. Sih, *Handbook of Stress Intensity Factors*, Institute of Fracture and Solid Mechanics, Lehigh University, Bethlehem, PA (1973).

[39] H. Tada, P. Paris, and G. Irwin, *The Stress Analysis of Cracks Handbook*, 2nd Edition, Del Research Corporation, Saint Louis, MO (1985).

[40] F. Erdogan and G. C. Sih, "On the Crack Extension in Plates Under Plane Loading and Transverse Shear," *Journal of Basic Engineering*, Dec. (1963), pp. 519-527.

[41] D. S. Dugdale, “Yielding of Steel Sheets Containing Slits,” *Journal of the Mechanics and Physics of Solids*, v. 8 (1960), pp. 100-104.

[42] A. J. Wilkinson and S. G. Roberts, “A Dislocation Model for the Two Critical Stress Intensities Required for Threshold Fatigue Crack Propagation,” *Scripta Materialia*, v. 35 (1996), pp. 1365-1371.

[43] J. Weertman, *Dislocation Based Fracture Mechanics*, World Scientific Publishing Co., River Edge, NJ (1996).

[44] J. Dundurs, and T. Mura, "Interaction Between and Edge Dislocation and a Circular Inclusion," *Journal of the Mechanics and Physics of Solids*, v. 12 (1964), pp. 177-189.

[45] R. Pippan, "The Condition for the Cyclic Plastic Deformation of the Crack Tip: The Influence of Dislocation Obstacles," *International Journal of Fracture*, v. 58 (1992), pp. 305-318.

[46] H. W. Liu, "A Dislocation Barrier Model for Fatigue Limit – As Determined by Crack Non-initiation and Crack Non-propagation," *International Journal of Fracture*, v. 96 (1999), pp. 331-344.

[47] H. Gao, N. Alagok, M. W. Brown, and K. J. Miller, "Growth of Fatigue Cracks Under Combined Mode I and Mode II Loads," *Multiaxial Fatigue*, ASTM STP 853, K. J. Miller and M. W. Brown, eds., American Society for Testing and Materials, Philadelphia, PA (1985), pp. 184-202.

[48] R. E. Reed-Hill, *Physical Metallurgy Principles*, 2nd Edition, PWS Publishers, Boston, MA (1973), pp. 171-173.

[49] J. D. Eshelby, F. C. Frank, and F. R. N. Nabarro, "The Equilibrium of Linear Arrays of Dislocations," *Philisophical Magazine*, v. 42 (1951), pp. 351-364.

[50] J. C. Newman Jr., "Analyses of Fatigue Crack Growth and Closure Near Threshold Conditions for Large-Crack Behavior," NASA-TM-1999-209133 (1999).

[51] P. K. Liaw, "Overview of Crack Closure at Near-Threshold Fatigue Crack Closure Levels," *Mechanics of Fatigue Crack Closure*, ASTM STP 982, J. C. Newman, Jr. and W. Elber, eds., American Society for Testing and Materials, Philadelphia, PA (1988), pp. 62-92.

[52] S. Suresh, A. K. Vasudevan, and P. E. Bretz, "Mechanisms of Slow Fatigue Crack Growth in High Strength Aluminum Alloys: Role of Microstructure and Environment," *Metallurgical Transactions*, v. 15A (1984), pp. 369-379.

[53] M. S. Hunter and P. Fowle, "Natural and Thermally Formed Oxide Films on Aluminum," *Journal of the Electrochemical Society*, v. 103 (1956), pp. 482-485.

[54] J. A. Ruppen and R. Salzbrenner, "The Effect of Environment on Crack Closure and Fatigue Threshold," *Fatigue of Engineering Materials and Structures*, v. 6 (1983), pp. 307-314.

[55] P. A. Wawrzynek and A. R. Ingraffea, "FRANC2D: A Two-Dimensional Crack Propagation Simulator," NASA-CR-4572 (1994).

[56] I. S. Raju and K. N. Shivakumar "An Equivalent Domain Integral Method in the Two-dimensional Analysis of Mixed Mode Crack Problems," *Engineering Fracture Mechanics*, v. 37 (1990), pp. 707-725.

[57] A. J. McEvily "Fatigue Fracture-Surface Roughness and the K-opening Level," *International Journal of Fatigue*, v. 19 (1997), pp. 629-633.

[58] G. T. Gray III, J. C. Williams, and A. W. Thompson, “Roughness Induced Crack Closure: An Explanation for Microstructurally Sensitive Fatigue Crack Growth,” *Metallurgical Transactions,* v. 14A (1983), pp. 421-433.

[59] W. J. Drury, A. M. Gokhale, and S. D. Antolovich, “Effect of Crack Surface Geometry on Fatigue Crack Closure,” *Metallurgical and Materials Transactions*, v. 26A (1995), pp. 2651-2663.

[60] A. P. Reynolds, “Constant Amplitude and Post-Overload Fatigue Crack Growth Behavior in PM Aluminum Alloy AA 8009,” *Fatigue and Fracture of Engineering Materials and Structures*, v. 15 (1992), pp. 551-562.

[61] G. H. Bray, A. P. Reynolds, and E. A. Starke Jr., “Mechanisms of Fatigue Crack Retardation Following Single Tensile Overloads in Powder Metallurgy Aluminum Alloys,” *Metallurgical Transactions*, v. 23A (1992), pp. 3055-3066.

[62] K. S. Ravichandran, "Further Results on 'A Theoretical Model for Roughness Induced Crack Closure': Effect of Yield Strength and Grain Size," *International Journal of Fracture*, v. 44 (1990), pp. R23-R26.

[63] M. A. Sutton, W. Zhao, S. R. McNeill, J. D. Helm, R. S. Piascik, and W. T. Riddell, "Local Crack Closure Measurements: Development of a Measurement System Using Computer Vision and a Far Field Microscope," *2nd Symposium on Crack Closure Measurement and Analysis*, ASTM STP 1343, R. C. McClung and J. C. Newman, eds., American Society for Testing and Materials, West Conshohocken, PA (1999).

[64] Y. Furuya, H. Shimada, M. Matsumoto, and T. Honma, “Fatigue and Degradation of Shape Memory Effect in Ti-Ni Wire,” Proceedings of the MRS International Meeting on Advanced Materials Tokyo, Japan, May 31-June 3 (1988), v. 9, *Shape Memory Alloys*, M. Doyama, *et al.*, eds., Materials Research Society, Pittsburgh, PA, pp. 269-274.

[65] R. H. Dauskardt, T. W. Duerig, and R. O. Ritchie, “Effects of *in-situ* Phase Transformation on Fatigue-Crack Propagation in Titanium-Nickel Shape-Memory Alloys,” Proceedings of the MRS International Meeting on Advanced Materials, Tokyo, Japan, May 31-June 3 (1988), v. 9, *Shape Memory Alloys*, M. Doyama, *et al.*, eds., Materials Research Society, Pittsburgh, PA, pp. 243-249.

[66] S. Miyazaki, M. Suizu, K. Otsuka, and T. Takashima, “Effect of Various Factors on Fatigue Crack Propagation Rate in Ti-Ni Alloys,” Proceedings of the MRS International Meeting on Advanced Materials Tokyo, Japan, May 31-June 3 (1988), v. 9, *Shape Memory Alloys*, M. Doyama, *et al.*, eds., Materials Research Society, Pittsburgh, PA, pp. 263-268.

[67] NASA-Johnson Space Center, *Derivation of Crack Growth Properties of Materials for NASA/FLAGRO – 2.0*, v. 1, JSC-26254 (1994).

[68] S. S. Kim, M. J. Haynes, and R. P. Gangloff, “Localized Deformation and Elevated-Temperature Fracture of Submicron-grain Aluminum with Dispersoids,” *Materials Science and Engineering*, v. A203 (1995), pp. 256-271.

[69] K. V. Jata, D. Maxwell, and T. Nicholas, “Influence of Environment and Creep on Fatigue Crack Growth in a High Temperature Aluminum Alloy 8009,” *Journal of Engineering Materials and Technology*, v. 116 (1994), pp. 45-53.

[70] S. A. Meguid, P. E. Gaultier, and S. X. Gong, “A Comparison between Analytical and Finite Element Analysis of Main Crack-Microcrack Interaction,” *Engineering Fracture Mechanics*, v. 38 (1991), pp. 451-465.

[71] B. R. Kirby and C. J. Beevers, “Slow Fatigue Crack Growth and Threshold Behavior in Air and Vacuum of Commercial Aluminum Alloys,” *Fatigue of Engineering Materials and Structures*, v. 1 (1979), pp. 203-215.

[72] T. S. Gross, Y. Zhang, and D. W. Watt, "Fracture Surface Interference in Shear - II. Experimental Measurements of Crack Tip Displacement Field Under Mode II Loading in 7075-T6 Al," *Acta Metallurgica et Materialia*, v. 43 (1995), pp. 901-906.

[73] X. Yu and A. Abel, "Modeling of Crack Surface Interference Under Cyclic Shear Loads," *Fatigue and Fracture of Engineering Materials and Structures*, v. 22 (1999), pp. 205-213.

[74] X. Yu and A. Abel, "Mixed-Mode Crack Surface Interference Under Cyclic Shear Loads," *Fatigue and Fracture of Engineering Materials and Structures*, v. 23 (2000), pp. 151-158.

[75] P. J. E. Forsyth, "A Two Stage Process of Fatigue Crack Growth," *Crack Propagation: Proceedings of the Cranfield Symposium* (1962), Her Majesty's Stationary Office, London, pp. 76-94.

[76] M. Shimojo, Y. Uchida, S. Yuruoka, and Y. Higo, "Fatigue Striation Formation in an Fe-3%Si Alloy - Effects of Crystallographic Orientation and Neighboring Grains," *Fatigue and Fracture of Engineering Materials and Structures*, v. 22 (1999), pp. 153-159.

[77] X. D. Li, “Dislocation Pile-up Model of Fatigue Thresholds for 2024 and 7075 Alike Aluminum Alloys,” *Theoretical and Applied Fracture Mechanics*, v. 24 (1996), pp. 165-179.

[78] J. P. Lucas and W. W. Gerberich, "A Proposed Criterion for Fatigue Threshold: Dislocation Substructure Approach," *Fatigue of Engineering Materials and Structures*, v. 6 (1983), pp. 271-280.

[79] D. J. Lloyd, "Deformation of Fine-Grained Aluminum Alloys," *Metal Science*, May (1980), pp. 193-198.

[80] H. Westengen, "Tensile Deformation of a Fine-Grained Al-Alloy," *Strength of Metals and Alloys*, R. C. Gifskins, ed., Permagon Press, 1983, pp. 461-466.

[81] R. P. Wei, “Synergism of Mechanics, Mechanisms and Microstructure in Environmentally Assisted Crack Growth,” *Fracture: Interactions of Microstructure, Mechanisms and Mechanics*, J. M. Wells and J. D. Landes, eds. (1984), pp. 75-88.

[82] R. P. Wei and G. W. Simmons, “Recent Progress in Understanding Environment Assisted Fatigue Crack Growth,” *International Journal of Fracture*, v. 17 (1981), pp. 235-247.

[83] S. Suresh, *Fatigue of Materials*, Cambridge University Press (1991), Cambridge, UK.

[84] R. P. Wei and M. Gao, “Reconsideration of the Superposition Model for Environmentally Assisted Fatigue Crack Growth,” *Scripta Metallurgica*, v. 17 (1983), pp. 959-962.

[85] D. L. Davidson and J. Lankford, “The Effect of Water Vapor on Fatigue Crack Tip Mechanics in 7075-T651 Aluminum Alloy,” *Fatigue of Engineering Materials and Structures*, v. 6 (1983), pp. 241-256.

[86] J. C. Newman Jr., "Fracture Mechanics Parameters for Small Fatigue Cracks," *Small-Crack Test Methods*, ASTM STP 1149, J. Larsen and J. E. Allison, eds., American Society for Testing and Materials, Philadelphia, PA (1992), pp. 6-33.

[87] W. A. Herman, R. W. Hertzberg, and R. Jaccard, "A Simplified Laboratory Approach of the Prediction of Short Crack Behavior in Engineering Structures," *Fatigue and Fracture of Engineering Materials and Structures*, v. 11 (1988), pp. 303-320.

[88] A. J. McEvily, "On Crack Closure in Fatigue Crack Growth," *Mechanics of Fatigue Crack Closure*, ASTM STP 982, J. C. Newman and W. Elber, eds., American Society for Testing and Materials, Philadelphia, PA (1988), pp. 35-43.

[89] C. M. Ward-Close and R. O. Ritchie, "On the Role of Crack Closure Mechanisms in Influencing Fatigue Crack Growth Following Tensile Overloads in Titanium Alloy: Near Threshold Versus Higher ΔK Behavior," *Mechanics of Fatigue Crack Closure*, ASTM STP 982, J. C. Newman, Jr. and W. Elber, eds., American Society for Testing and Materials, Philadelphia, PA (1988), pp. 93-111.

[90] E. K. Tschegg, "Mode III and Mode I Fatigue Crack Propagation Behavior Under Torsional Loading," *Journal of Materials Science*, v. 18 (1983), pp. 1604-1614.

[91] E. K. Tschegg, "Sliding Mode Crack Closure and Mode III Fatigue Crack Growth in Mild Steel," *Acta Metallurgica*, v. 31 (1983), pp. 1323-1330.

[92] A. K. Vasudevan and S. Suresh, "Influence of Corrosion Deposits on Near-Threshold Fatigue Crack Growth Behavior in 2XXX and 7XXX Series Aluminum Alloys," *Metallurgical Transactions*, v. 13A (1982), pp. 2271-2280.

[93] P. C. Paris, H. Tada, and J. K. Donald, “Service Load Fatigue Damage – A Historical Perspective,” *Proceedings of Fatigue Damage of Structural Materials II*, Cape Cod, MA, Sept. 7-11 (1998).

[94] J. C. Newman Jr., "A Crack-Closure Model for the Fatigue Behavior of Notched Specimens," *Methods and Models for Predicting Fatigue Crack Growth Under Random Loading*, ASTM STP 748, American Society for Testing and Materials, Philadelphia, PA (1983), pp. 53-84.

[95] J. C. Newman Jr., “FASTRAN II – A Fatigue Crack Growth Structural Analysis Program,” NASA-TM 104159 (1992).

[96] R. C. McClung, “Finite Element Modeling of Crack Closure During Simulated Fatigue Threshold Testing,” *International Journal of Fracture*, v. 52 (1991), pp. 145-157.

[97] K. N. Shivakumar and J. C. Newman Jr., "ZIP3D - An Elastic and Elastic-Plastic Finite-Element Analysis Program for Cracked Bodies," NASA-TM-102753 (1990).

[98] W. L. Morris, M. R. James, and O. Buck, "A Simple Model of Stress Intensity Range Threshold and Crack Closure Stress," *Engineering Fracture Mechanics*, v. 18 (1983), pp. 871-877.

[99] C. J. Beevers, "A Model for Fatigue Crack Closure," *Engineering Fracture Mechanics*, v. 19 (1984), pp. 93-100.

[100] R. L. Carlson and C. J. Beevers, "A Multiple Asperity Fatigue Crack Closure Model," *Engineering Fracture Mechanics*, v. 20 (1984), pp. 687-690.

[101] J. C. Newman Jr., “A Crack-Closure Model for Predicting Fatigue Crack Growth under Aircraft Spectrum Loading,” *Methods and Models for Predicting Fatigue Crack Growth Under Random Loading*, ASTM STP 748, J. B. Chang and C. M. Hudson, eds., American Society for Testing and Materials, Philadelphia, PA (1981), pp. 53-84.

[102] R. Ballarini and M. E. Pleasha, "The Effects of Crack Surface Friction and Roughness on Crack Tip Stress Fields," *International Journal of Fracture*, v. 34 (1987), pp. 195-207.

[103] T. S. Gross and D. A. Mendelsohn, "Mode I Stress Intensity Factors Induced by Fracture Surface Roughness under Pure Mode III Loading: Application to the Effect of Loading Modes on Stress Corrosion Crack Growth," *Metallurgical Transactions*, v. 20A (1989), pp. 1989-1999.

[104] M. C. Smith and R. A. Smith, "Modeling the Unlocking and Slip of Crack Surfaces Under Mode II Loading," *Advances in Fracture Research (Fracture 84)*, Proceedings of the 6th International Conference on Fracture (1984), New Delhi, India, S. R. Valluri, *et al*., eds.

[105] D. A. Mendelsohn, T. S. Gross, and Y. Zhang, "Fracture Surface Interference in Shear - I. A Model Based on Experimental Surface Characterizations," *Acta Metallurgica et Materialia*, v. 43 (1995), pp. 893-900.

[106] J. Tong, J. R. Yates, and M. W. Brown, "A Model for Sliding Mode Crack Closure, Part I: Theory for Pure Mode II Loading," *Engineering Fracture Mechanics*, v. 52 (1995), pp. 599-611.

[107] J. Tong, J. R. Yates, and M. W. Brown, "A Model for Sliding Mode Crack Closure, Part II: Mixed Mode I and II Loading and Application," *Engineering Fracture Mechanics*, v. 52 (1995), pp. 613-623.

[108] A. P. Green, "Friction Between Unlubricated Metals: A Theoretical Analysis of the Junction Model," *Proceedings of the Royal Society of London*, v. 228A (1955), pp. 191-204.

[109] C. M. Edwards and J. Halling, "Experimental Study of the Plastic Interaction of Model Surface Asperities During Sliding," *Journal of Mechanical Engineering Science*, v. 10 (1968), pp. 121-132.

[110] R. H. Christensen, "Fatigue Crack Growth Affected by Metal Fragments Wedged Between Opening-Closing Crack Surfaces," *Applied Materials Research*, Oct. (1963), pp. 207-210.

[111] M. Lang, "Explanation of an Apparent Abnormality in Fatigue Crack Growth Rate Curves in Titanium Alloys," *Acta Materialia*, v. 47 (1999), pp. 3247-3261.

[112] R. A. Schmidt and P. C. Paris, "Threshold for Fatigue Crack Propagation and the Effect of Load Ratio and Frequency," *Progress in Flaw Growth and Fracture Toughness Testing*, ASTM STP 536, American Society for Testing and Materials, Philadelphia, PA (1973), pp. 79-94.

[113] H. Doker and V. Bachmann, "Determination of Crack Opening Load by use of Threshold Behavior," *Mechanics of Fatigue Crack Closure*, ASTM STP 982, J. C. Newman Jr. and W. Elber, eds., American Society for Testing and Materials, Philadelphia, PA (1988), pp. 247-259.

[114] T. R. Clark, W. A. Herman, R. W. Hertzberg, and R. J. Jaccard, "A Technical Note: Influence of Mean Stress on Fatigue in Several Aluminum Alloys Utilizing $K_{c\ max}$ Threshold Procedures," *Fatigue and Fracture of Engineering Materials and Structures*, v. 19 (1996), pp. 949-954.

[115] S. W. Smith and R. S. Piascik, "Determining Closure Free Fatigue Crack Growth Behavior in the Near Threshold Regime," *Fatigue Crack Growth Thresholds, Endurance Limits, and Design*, ASTM STP 1372, J. C. Newman and R. S. Piascik, eds., American Society for Testing and Materials, West Conshohocken, PA (2000).

[116] W. T. Riddell and R. S. Piascik, "Stress Ratio Effects on Crack Opening Loads and Crack Growth Rates in Aluminum Alloy 2024," NASA-TM-1998-206929 (1998).

[117] A. S. Argon and J. Im, "Cavity Formation from Inclusions in Ductile Fracture," *Metallurgical Transactions*, v. 6A (1975), pp. 825-837.

[118] A. S. Argon and J. Im, "Separation of Second Phase Particles in Spheroidized 1045 Steel, Cu-0.6% Cr Alloy, and Maraging Steel in Plastic Straining," *Metallurgical Transactions*, v. 6A (1975), pp. 839-851.

[119] J. Weertman, I. H. Lin, and R. Thomson, "Double Slip Plane Crack Model," *Acta Metallurgica*, v. 31 (1983), pp. 473-482.

[120] C. A. Caracostas, H. M. Shodja, and J. Weertman, "The Double Slip Plane Model for the Study of Short Cracks," *Mechanics of Materials*, v. 20 (1995), pp. 195-208.

[121] C. F. Qian, and J. C. M. Li, "Edge Dislocations Emitted along Multiple Inclined Slip Planes from a Mode I Crack – Part I. Sequential Emission," *Mechanics of Materials*, v. 24 (1996), pp. 1-10.

[122] C. F. Qian, and J. C. M. Li, "Edge Dislocations Emitted along Multiple Inclined Slip Planes from a Mode I Crack – Part II. Simultaneous Emission," *Mechanics of Materials*, v. 24 (1996), pp. 11-17.

[123] A. Misra and R. Gibala, "Slip Transfer and Dislocation Nucleation Processes in Multiphase Ordered Ni-Fe-Al Alloys," *Metallurgical and Materials Transactions*, v. 30A (1999), pp. 991-1001.

[124] G. Terlinde and G. Luetjering, "Influence of Grain Size and Age-Hardening on Dislocation Pile-Ups and Tensile Fracture for a Ti-Al Alloy," *Metallurgical Transactions*, v. 13A (1982), pp. 1283-1292.

[125] L. Mishnaevsky Jr., N. Lippmann, S. Schauder, and P. Gumbsch, "In-situ Observation of Damage Evolution and Fracture in $AlSi_7Mg_{0.3}$ Cast Alloys," *Engineering Fracture Mechanics*, v. 63 (1999), pp. 395-411.

[126] C. Schmitt, P. Lipinski, and M. Berveiller, "Micromechanical Modeling of the Elastoplastic Behavior of Polycrystals Containing Precipitates - Application to Hypo- and Hyper-Eutectoid Steels," *International Journal of Plasticity*, v. 13 (1997), pp. 183-199.

[127] A. M. Gokhale, N. U. Deshpande, D. K. Denzer, and J. Liu, "Relationship Between Fracture Toughness, Fracture Path, and Microstructure of 7050 Aluminum Alloy: Part II. Multiple Micromechanisms-Based Fracture Toughness Model," *Metallurgical and Materials Transactions*, v. 29A (1998), pp. 1203-1210.

[128] D. Sigler, M. C. Montpetit, and W. L. Haworth, "Metalography of Fatigue Crack Initiation in an Overaged High-Strength Aluminum Alloy," *Metallurgical Transactions*, v. 14A (1983), pp. 931-938.

[129] C. Y. Kung and M. E. Fine, "Fatigue Crack Initiation and Microcrack Growth in 2024-T4 and 2124-T4 Aluminum Alloys," *Metallurgical Transactions*, v. 10A (1979), pp. 603-610.

[130] E. A. DeBartolo and B. M. Hillberry, "Effects of Constituent Particle Clusters on Fatigue Behavior of 2024-T3 Aluminum Alloy," *International Journal of Fatigue*, v. 20 (1998), pp. 727-735.

[131] A. Zabett and A. Plumtree, "Microstructural Effects on the Small Fatigue Crack Behavior of an Aluminum Alloy Plate," *Fatigue and Fracture of Engineering Materials and Structures*, v. 18 (1995), pp. 801-809.

[132] A. D. Wilson, "Fractographic Characterization of the Effect of Inclusions on Fatigue Crack Propagation," *Fractography and Materials Science*, ASTM STP 733, L. N. Gilbertson and R. D. Zipp, eds., American Society for Testing and Materials (1981), pp. 166-186.

[133] P. J. Laz and B. M. Hillberry, "Fatigue Life Prediction from Inclusion Initiated Cracks," *International Journal of Fatigue*, v. 20 (1998), pp. 263-270.

[134] M. J. Haynes and R. P. Gangloff, "Temperature-Dependent Void-Sheet Fracture in Al-Cu-Mg-Ag-Zr," *Metallurgical and Materials Transactions*, v. 29A (1998), pp. 1599-1613.

[135] T. Shibutani, T. Kitamura, and R. Ohtani, "Creep Cavity Growth Under Interaction Between Lattice Diffusion and Grain-Boundary Diffusion," *Metallurgical and Materials Transactions*, v. 29A (1998), pp. 2533-2542.

[136] A. C. F. Cocks and J. Pan, "Void Growth Ahead of a Dominant Crack in a Material which Deforms by Coble Creep," *International Journal of Fracture*, v. 60 (1993), pp. 249-265.

[137] M. D. Thouless, C. H. Hsueh, and A. G. Evans, "A Damage Model of Creep Crack Growth in Polycrystals," *Acta Metallurgica*, v. 31 (1983), pp. 1675-1687.

[138] P. F. Thomason, "A View on Ductile-Fracture Modeling," *Fatigue and Fracture of Engineering Materials and Structures*, v. 21 (1988), pp. 1105-1122.

[139] H. G. F. Wilsdorf, "The Ductile Fracture of Metals: A Microstructural Viewpoint," *Materials Science and Engineering*, v. 59 (1983), pp. 1-39.

[140] J. A. Newman, W. T. Riddell, and R. S. Piascik, "Effects of K_{max} on Fatigue Crack Growth Threshold in Aluminum Alloys," *Fatigue Crack Growth Thresholds, Endurance Limits, and Design*, ASTM STP 1372, J. C. Newman Jr. and R. S. Piascik, eds., American Society for Testing and Materials, West Conshohocken, PA (2000), pp. 63-77.

[141] V. Doquet, "Micromechanical Simulations of Microstructure-Sensitive Stage I Fatigue Crack Growth," *Fatigue and Fracture of Engineering Materials and Structures*, v. 22 (1999), pp. 215-223.

[142] J. Harder, "A Crystallographic Model for the Study of Local Deformation Processes in Polycrystals," *International Journal of Plasticity*, v. 15 (1999), pp. 605-624.

[143] P. A. Friedman and A. K. Ghosh, "Microstructural Evolution and Superplastic Deformation Behavior of Fine Grain 5083Al," *Metallurgical and Materials Transactions*, v. 27A (1996), pp. 3827-3839.

[144] Fracture Technology Associates, *User's Reference Manual for Automated Fatigue Crack Growth (Compliance)*, v. 2.43, Fracture Technology Associates, Bethlehem, PA (1984).

[145] W. F. Deans, C. B. Jolly, W. A. Poyton, and W. Watson, "A Strain Gauging Technique for Monitoring Fracture Mechanics Specimens During Environmental Testing," *Strain*, v. 13 (1977), pp. 152-154.

[146] J. F. O'Hanlon, *A User's Guide to Vacuum Technology*, 2nd Edition, John Wiley & Sons, Inc., New York (1989).

[147] L. C. Feldman and J. W. Mayer, *Fundamentals of Surface and Thin Film Analysis*, Elsevier Science Publishing Co., Inc., New York (1986), pp. 125-153.

[148] M. H. Loretto, *Electron Beam Analysis of Materials*, Chapman and Hall, New York (1984).

[149] M. Mirzaei and J. W. Provan, "The Effect of Crack Wake Characteristics on Fatigue Crack Closure: Part I - A Crack Wake Removal Study," *Theoretical and Applied Fracture Mechanics*, v. 18 (1993), pp. 179-183.

[150] M. Mirzaei and J. W. Provan, "The Effect of Crack Wake Characteristics on Fatigue Crack Closure: Part II - A Non-Uniform Wake Study," *Theoretical and Applied Fracture Mechanics*, v. 18 (1993), pp. 185-191.

[151] W. Elber, "Crack Closure and Crack Growth Measurements in Surface-Flawed Titanium Alloy Ti-6Al-4V," NASA-TN-D-8010 (1975).

[152] M. A. Sutton, Y. J. Chao, and J. S. Lyons, "Computer Vision Methods for Surface Deformation Measurements in Fracture Mechanics," *Novel Experimental Techniques in Fracture Mechanics*, v. 176 (1993), American Society for Mechanical Engineers, pp. 203-217.

[153] J. E. Hatch, ed., *Aluminum: Properties and Physical Metallurgy*, American Society for Metals, Metals Park, OH (1984).

[154] J. R. Davis, ed., *Aluminum and Aluminum Alloys*, ASM International (1993).

[155] W. C. Porr and R. P. Gangloff, "Elevated Temperature Fracture of RS/PM Alloy 8009: Part I. Fracture Mechanics Behavior," *Metallurgical and Materials Transactions*, v. 25A (1994), pp. 365-379.

[156] B. Strnadel, S. Ohashi, H. Ohtsuka, T. Ishihara, and S. Miyazaki, "Cyclic Stress-Strain Characteristics of Ti-Ni and Ti-Ni-Cu Shape Memory Alloys," *Materials Science and Engineering*, v. A202 (1995), pp. 148-156.

[157] R. S. Piascik, J. C. Newman Jr., and J. H. Underwood, "The Extended Compact Tension Specimen," *Fatigue and Fracture of Engineering Materials and Structures*, v. 20 (1997), pp. 559-563.

[158] A. Hartman, "On the Effect of Oxygen and Water Vapor on the Propagation of Fatigue Cracks in 2024-T3 Alclad Sheet," *International Journal of Fracture Mechanics*, v. 1 (1965), pp. 167-188.

[159] F. J. Bradshaw and C. Wheeler, "The Influence of Gaseous Environment and Fatigue Frequency on the Growth of Fatigue Cracks in Some Aluminum Alloys," *International Journal of Fracture Mechanics*, v. 5 (1969), pp. 225-268.

[160] R. P. Wei, "Some Aspects of Environmental-Enhanced Fatigue-Crack Growth," *Engineering Fracture Mechanics*, v. 1 (1970), pp. 633-651.

[161] P. K. Liaw, S. J. Hudak Jr., and J. K. Donald, "Influence of Gaseous Environments on Rates of Near-Threshold Fatigue Crack Propagation in NiCrMoV Steel," *Metallurgical Transactions*, v. 13A (1982), pp. 1633-1645.

[162] D. L. Davidson and J. Lankford, “Fatigue Crack Tip Mechanics of a Powder Metallurgy Aluminum Alloy in Vacuum and Humid Air,” *Fatigue of Engineering Materials and Structures*, v. 7 (1984), pp. 29-39.

[163] D. L. Dicus, “The Effect of Water Vapor on Fatigue Crack Growth in 7475-T651 Aluminum Alloy Plate,” NASA-TM-84477 (1984).

[164] R. S. Piascik and R. P. Gangloff, “Environmental Fatigue of an Al-Li-Cu Alloy: Part I-Intrinsic Crack Propagation Kinetics in Hydrogenous Environments,” *Metallurgical Transactions*, v. 22A (1991), pp. 2415-2428.

[165] R. S. Piascik and R. P. Gangloff, “Environmental Fatigue of an Al-Li-Cu Alloy: Part II. Microscopic Hydrogen Cracking Process,” *Metallurgical Transactions*, v. 24A (1993), pp. 2751-2762.

[166] P. Shewmon, *Diffusion in Solids*, The Minerals, Metals, and Materials Society, Warrendale, PA (1989).

[167] S. W. Smith, *Hydrogen Trapping in Al-Li-Cu-Zr Alloys*, Ph.D. Dissertation, University of Virginia (1995).

VITA

John Andrew Newman

John Andrew Newman (called “Andy”) was born in Newport News, Virginia on February 24, 1971. Andy was raised in Hampton, Virginia and graduated from Kecoughtan High School in 1989. In the fall of 1989, he became an engineering student at Virginia Tech. He earned a Bachelor of Science degree in Engineering Science and Mechanics in 1994 and a Master of Science degree in Engineering Mechanics in 1996. Andy is currently working as an Aerospace Engineer for the U. S. Army Research Laboratory (Vehicle Technology Directorate) at NASA-Langley Research Center in Hampton, Virginia. Andy is married (to Lisa), and has a daughter (Sydney).